Laser Photoionisation Spectroscopy of Silver Dimer

James William Macdonald

A thesis presented for the degree of
Doctor of Philosophy in the
Faculty of Science at the
University of Edinburgh
1993

He joined up for just three years
It seemed a small amount
But they didn't tell him that
The first two didn't count

J. Burns

Abstract

A number of experimental techniques have been brought together to create a powerful investigative tool. This laser vaporisation, supersonic expansion, laser ionisation mass spectrometry amalgam has allowed the study of two distinct types of molecular species.

Many heteronuclear diatomic species have been prepared and investigated for the first time. These novel molecules are of interest due to their utility as bulk phase alloys. Mass spectra are presented for many such combinations.

Homonuclear diatomic species have been analysed using these techniques for some time. In particular, this work has focussed on transition metal species as this is one of the few methods which permits such study. Spectroscopic investigations of the A, B and C states of the silver dimer (Ag_2) molecule are presented here. The analysis of this work has provided the following rotational constants for these states;

X state $B_e = 0.04878$ cm^{-1}
A state $B_e = 0.04432$ cm^{-1}
B state $B_e = 0.04544$ cm^{-1}
C state $B_0 = 0.04851$ cm^{-1}.

All values are for the $^{107,109}Ag_2$ isotopomer.

The first ionisation potential (I.P.) of any molecular system is an important parameter in the understanding of that species. The value of the I.P. has been evaluated for the silver dimer molecule under differing experimental conditions. It is reported here both under the influence of a potential field (I.P. = 61658.4 cm^{-1}) and under field free conditions (I.P. = 61740.0 cm^{-1}).

Acknowledgements

The completion of this thesis would not have been possible without the help of the following people and organisations.

Firstly, thanks go to my supervisor Dr. P.R.R. Langridge-Smith for introducing me to the subject area, and to the Science and Engineering Research Council for bearing some of the cost. Coupled to this is the support and tuition offered to me by the past members of the research group. In particular Kevin Costello, Andrew James and George Keenan were of great help, and Trevor Ridley was always willing to spare me some time. My period in the group also coincided with that of two post-doctoral assistants; I am indebted to George Lemire, with whom I spent many late nights on the silver work, and to Pierre-Francois Brevet, with whom the mixed species work was undertaken. I would also like to mention two of the present members of this group, Jon Miller and Mike Dale, who have done much to keep me sane in the latter stages of this work.

In the course of this work it was necessary to call upon the variety of services offered within the Chemistry department from time to time. In particular, I would like to thank Stuart Mains (Mechanical Work Shop) and Derek Burgess (Stores) for their help and friendship on and off the football field.

My time in Edinburgh would not have been nearly as enjoyable without the friendship of Jimmy Thomson. I hope this will continue to be the case in the years ahead.

Away from work, I owe more than these few lines to the support given to me by my parents, Helen and Jim. They have made many sacrifices so that I could reach this point, and I hope they think it has been worthwhile. I am forever in their debt.

Finally, I want to thank my wife, Ruth. She has given me a great deal of support over the past four years, and without her belief and drive this thesis may never have been finished. It is to her that this work is dedicated.

Table of Contents

List of Figures

List of Tables

Chapter 1

Introduction

1.1 Introduction

The chemical and physical properties of any given substance are of great importance. These properties are determined, to a great extent, by the electronic structure of the particular species. This structure has historically been measured at the extreme limits of the molecular scale - the atom and the bulk phase. The reason for this polarisation was principally the lack of suitable experimental techniques to prepare and probe the intermediate species.

During the past ten years, however, much interest has been shown in these intermediates [1]. This interest has been both experimental and theoretical; experimental studies have been carried out on these systems both in terms of their discrete electronic structure, and with regard to their potential role as models for heterogeneous catalysis, while various theoretical models have been used to calculate the predicted role of various s and d electron combinations in bond formation.

These species, known as clusters, have been studied as a result of the development of a new experimental technique. This technique, or more accurately, amalgam of techniques, will be described in detail later in this thesis.

The term cluster requires to be defined more clearly at this juncture. Consider a typical, 'inorganic' cluster M_nX_y. This contains n metal atoms connected, via some bonding network, with y ligands occupying bridging or terminal sites in such a way that the valencies of all the species present are filled, or at least stabilised, by such interactions. Many of these clusters have been studied, and much valuable

structural information collected [2] [3]. However, this body of work gives little information on the molecular core, which can be considered as a builing block for the bulk phase metallic properties. If, however, the ligand free cluster, M_n, is considered, then a study of a family of clusters as their size, n, increases would provide an opportunity to observe the change from atomic to bulk properties, leading to a deeper understanding of these species.

A cluster has already been described as a number of metal atoms bound together without the presence of any ligating species. Again considering the M_n system, then clearly when n = 1, the species under consideration is simply the metal atom. While n = 2 could be considered as a simple diatomic species, it is also generally considered to be the smallest of the cluster series, being justified in that they represent prototypical systems whose characteristics appear, to varying extents, in larger clusters. Typically, the properties of any given cluster are size dependent, as a result of the gradual change from the discrete atom to the bulk phase. A well documented example of this is the fall in ionisation potential as cluster size increases [4] - [6]. Here, the diatomic species is a most important member of the series, as many of the observed discontinuities in these trends are most noticeable for small clusters [7].

Given the range of cluster species available, the lower members of the transition metals are of particular interest due to the presence of filled, or partially filled, d orbitals. These orbitals become more heavily contracted, with respect to the valence shell, as a transition period is crossed. Thus the part played in bonding varies from species to species - a spectroscopic investigation of di- and triatomic species should yield information on this d orbital participation in the metal-metal bond, while an investigation of larger clusters would give an indication of the electronic structure of species believed to be involved in catalysis [8].

Much experimental work had been carried out on diatomic metal species prior to the explosion of ligand free cluster work [9]. This work was clearly split into two experimental approaches, and by considering each in turn their strengths and weaknesses may be assessed.

Many spectroscopic studies had used a matrix isolation technique [1]. Here,

the vapour of the species under investigation was co-condensed with an inert gas and cooled to some very low temperature, commonly 4K. This resulted in the metalic atoms and molecules being effectively separated from each other - all they could 'see' were their neighbouring inert gas atoms - and as a result were long lived species. As their thermal motion had been effectively removed, these species were frozen in space and available for investigation. Such investigation could be carried out using a variety of techniques including extended xray absorption fine structure (EXAFS) [10], electron spin resonance (ESR) [11], magnetic circular dichroism (MCD) [12], Raman spectroscopy [13] and electronic adsorption [14].

The limitations of this type of work are fourfold. As the metal vapour is co-condensed, there is no way to determine its true composition in terms of cluster mass. Hence any spectroscopic information obtained has no definite origin. Conditions may be weighted in the favour of diatomic production, but a spread of constituents is unavoidable, due to the long aggregation periods which can result in high cluster formation. A comparison of these results with those obtained elsewhere might allow an unambiguous assignment of such spectra. Unfortunately this situation is further complicated by the fact that matrix spectra are displaced relative to the true transitions, due to metal-matrix interactions. This can lead to movement of up to 1000 cm^{-1}. However, this effect is well documented, and can usually be overcome during the analysis of results. A further complication can arise due to the variety of matrix sites that can be occupied. Hence identical species can generate different spectra due to their geometric environment. A final consideration is that of resolution. While the metal-matrix interactions result in a broadening of transitions, the nature of these experiments means they are limited to the investigation of electronic bands, such that no vibronic or rovibronic structure can be resolved.

In terms of gas phase studies, two approaches had been used historically. Hot oven sources found utility in the investigation of the lower boiling point metals such as the alkalis [15], where the vapour pressure of the species was sufficient to allow molecular beam formation by expansion through an orifice. The use of inert carrier gas to both aid cluster growth and cool the molecules during expansion

allowed molecular beams of large, cold clusters to be produced. For the more refractory species like transition metals, however, these ovens produced vapour pressures that were too low for such growth. Despite this, several of the coinage dimers were investigated via emission from thermally populated electronic excited states, and these results formed a useful guide for some of the work reported later in this thesis. Thermal sources have proved more useful in the determination of cluster dissociation energies, using Knudsen effusion mass spectrometry [16].

Thermal emission spectroscopy has also proved of limited success in the investigation of transition metal dimers. The Boltzmann population in all but the lowest excited states is too small to be of significant use, while those systems which are populated are usually of such low intensity that little useful information can be recorded. The complementary technique of absorption spectroscopy offers more scope, but is limited by the low level of sensitivity that is available. While discharge sources can circumvent the problems of low excited state populations, transition metal dimers are not easily produced in this manner, and the resulting spectra are usually complicated by congestion. This means that the ability to assign particular bands to a specific host can be lost. There are two other points of consequence concerning the resolution of such spectra.

The rotational constant of a rigid, diatomic rotor is defined as [17],

$$B_e = h/8\pi^2 c^* \mu {r_e}^2 \tag{1.1}$$

As the mass of the species increases, so does the reduced mass, μ. Hence the rotational constant becomes progressively smaller as mass increases. This proves problematic in the second and third transition metal periods, where consecutive rovibronic lines become tightly packed at low J, due to their relationship with the rotational constant. However, an even greater barrier to rotational resolution exists. Most elements are a mixture of two or more naturally ocurring isotopes. Each of these is incorporated in the resulting diatomic species under consideration, such that each combination is present according to the relative abundances of its constituents. In turn, each of these diatomic isotopomers gives rise to a unique spectroscopic signature. The problem arises due to the fact that these spectra are

only displaced from each other by the ratio of the reduced masses of the respective species. Hence such spectra are reduced to an impenetrable mass of lines, due to their physical overlap.

It became clear that in order to overcome all of the above problems, a new experimental direction was required. Any new technique needed to allow the preparation of the most refractory materials, preferably in such a way that they were spectroscopically cold. It also required to not only allow for the small energy differences between successive lines in the rotational spectra of high mass species, but also to permit the unambiguous assignment of spectroscopic spectra to these species.

Such a system was developed by Smalley *et al.* [18], and has since been utilised by a wide variety of research groups, perhaps most notably by Morse and co-workers [19]. The clusters were prepared by laser vaporisation of the appropriate target material. In the initial design this consisted of an elemental rod. However, this meant that only homonuclear species could be investigated. Some of the more recent studies have incorporated a modified source consisting of a disc target, allowing heteronuclear species to be prepared and studied [20]. Both these designs resolved the problem encountered with refractory species by means of the extremely high local temperatures produced. The resulting plasma was quenched thermally by a pulse of inert gas, which also provided collisional cooling as the beam species were expanded supersonically into vacuum. Hence the beam was spectroscopically cooled. The spectroscopy itself was performed using etalon narrowed dye laser radiation, helping to remove the problems of the small rotational constants. The identification of particular species was achieved via time-of-flight mass spectrometry, with associated fast detection and electronics, thus removing the final problem of spectral blending. Hence this system was able to improve on all the problem areas identified earlier.

The availability of the above experimental package meant that many of the diatomic transition metal species were open to study. Earlier in this discussion it was stated that a primary interest in such transition metal species was the participation of the d orbital electrons in the metal-metal bond. It may come as

something of a surprise, therefore, to find that the experimental work reported in this thesis concerns the disilver species. With a $4d^{10}5s^1$ ground state electronic configuration, the silver atom bonds primarily through the valence s atomic orbital, with the filled d orbital cores playing little part. However, some justification for studying this relatively simple system comes from the overwhelming electronic complexity of the transition metal dimer species with open d shells, many examples of which are to be found in the literature [1]. This complexity arises from the numerous ways in which the d core 'holes' can correlate in the molecule. This simplification holds for theoretical models also, where systems with weak d orbital interaction and low multiplicity of states are described more satisfactorily. In disilver, the contracted d cores can be treated outwith the valence space, leading to greatly simplified calculations. Hence any satisfactory theoretical model should be able to give good agreement with experimental values for these, the simplest valence-bonded transition metal clusters.

Since first described, the new experimental technique has been used in many studies. These have focussed mainly on the previously inaccessible transition metal cluster species. Perhaps surprisingly, then, there is still much that is unknown concerning the coinage dimers. Accordingly, the early work in this group centred on copper [21] [22], silver [22] [23] and the mixed species copper - silver [23]. Despite these endeavours, only one electronically excited state of the silver dimer molecule had been investigated at the onset of this work. It was hoped, therefore, to continue this work on the A state, before moving on to work on the higher excited states. Chapter 4 of this thesis describes all the work carried out on the A, B and C states of this molecule.

As well as these spectroscopic studies of high mass species, this technique has also proved useful in the recording of threshold ionisation spectra. Here the utility lies mainly in two points. The use of resonant two-photon ionisation results in such limits being routinely accessable for all transition dimers. Coupled to this is the relative ease of massive ion collection, as opposed to the stringent requirements of electron analysis apparatus. Again, previous work in this group centred on the

coinage species Cu_2 and CuAg. Chapter 5 of this thesis describes the recording and analysis of such threshold spectra of the Ag_2 system.

Many diatomic systems have been investigated using these experimental techniques. Of these, the vast majority have been homonuclear. Indeed, in a recent review article it was noted that of all the possible transition metal heteronuclear dimers that were possible, only some 59 out of 435 had been investigated at all, with most of these studies being fragmentary [1]. While no spectroscopic studies have yet been carried out, Chapter 3 of this thesis presents mass spectra for various heteronuclear species, all of which have been recorded for the first time during the course of this work. Before these results are presented, a full description of the experimental apparatus used in this work is given in Chapter 2.

Bibliography

[1] Morse M.D., Chem. Rev., 1986, **86**, 1049.

[2] Cotton F.A. and Wilkinson G. *Advanced Inorganic Chemistry*, Third Edition, Interscience Publishers, New York, 1972.

[3] Purcell K.F. and Kotz J.C., *Inorganic Chemistry*, Holt-Saunders International Editions, Philadelphia, 1977.

[4] Rohlfing E.A., Cox D.M. and Kaldor A., Chem. Phys. Lett., 1983, **99**, 161.

[5] Rohlfing E.A., Cox D.M. and Kaldor A., J. Phys. Chem., 1984, **88**, 4497.

[6] Whetten R.L., Zakin M.R., Cox D.M., Trevor D.J. and Kaldor A., J. Chem. Phys., 1986, **85**, 1697.

[7] Powers D.E., Hansen S.G., Geusic M.E., Michalopolous D.L. and Smalley R.E., J. Chem. Phys., 1983, **78**, 2866.

[8] Kaldor A., Cox D.M. and Zakin M.R., Adv. Phys. Chem., 1988, **70(2)**, 211.

[9] Huber K.P. and Herzberg G., *Molecular Spectra and Molecular Structure* IV*: Constants of Diatomic Molecules*, Van Nostrand Reinhold, New York, 1979.

[10] Montano P.A., Zhao J., Ramanathan M., Shenoy G.K., Schulze W. and Urban J., Chem. Phys. Lett., 1989, **164**, 126.

[11] van Zee R.J. and Weltner W. Jnr., Chem. Phys. Lett., 1989, **162**, 437.

[12] Grinter R., Armstrong S., Jayasooriya U.A., McCombie J., Norris D. and Springall J.P., Faraday Symp. Chem. Soc., 1980, **14**, 14.

[13] Schulze W. and Abe H., Faraday Symp. Chem. Soc., 1980, **14**, 87.

[14] Ozin G.A., Huber H., McIntosh D., Mitchell S., Norman J.G.Jnr. and Noodleman L., J. Am. Chem. Soc., 1979, **101**, 3504.

[15] Herrmann A., Leutwyler S., Schumacher E. and Wöste L., Helv. Chim. Acta., 1978, **61**, 453.

[16] Hilpert K., Ber. Bunsenges. Phys. Chem., 1979, **83**, 161.

[17] Atkins P.W., *Physical Chemistry*, Third Edition, Oxford University Press, 1986.

[18] Dietz T.G., Duncan M.A., Powers D.E. and Smalley R.E., J. Chem. Phys., 1981, **74**, 6511.

[19] Fu Z., Lemire G.W., Hamrick Y.M., Taylor S., Shui J-C. and Morse M.D., J. Chem. Phys., 1988, **88**, 3524.

[20] O'Brien S.C., Liu Y., Zhang Q., Heath J.R., Tittel F.K., Curl R.F. and Smalley R.E., J. Chem. Phys., 1986, **84**, 4074.

[21] Cartwright P.C., *PhD. Thesis*, University of Edinburgh, 1989.

[22] Butler A.M., *PhD. Thesis*, University of Edinburgh, 1989.

[23] James A.M., *PhD. Thesis*, University of Edinburgh, 1991.

Chapter 2

Experimental Apparatus

2.1 Introduction

All of the experimental results described in the following chapters of this thesis were obtained using one of two home built molecular beam machines. In this chapter a detailed description of these machines is given together with details of the other apparatus used in the collection of these results. To distinguish readily between the two machines, they will from now on be referred to as MB1 and MB2, respectively.

2.2 Molecular Beam Apparatus MB1

The MB1 apparatus is shown schematically in Figure 2-1. It consisted of three chambers, each fabricated from 16 mm, 304 stainless steel, and each achieving high vacuum status from their dedicated pumping system. This so called 'differential pumping' resulted in the loads on the pumps in the latter chambers being much reduced compared to a single chamber system [1]. Each of the three chambers will be described in detail.

2.2.1 Main (M) Chamber

The M chamber was cuboid in shape, with outer dimensions of 635 mm x 370 mm x 370 mm, resulting in an internal volume of 69 l. There were two, rectangular

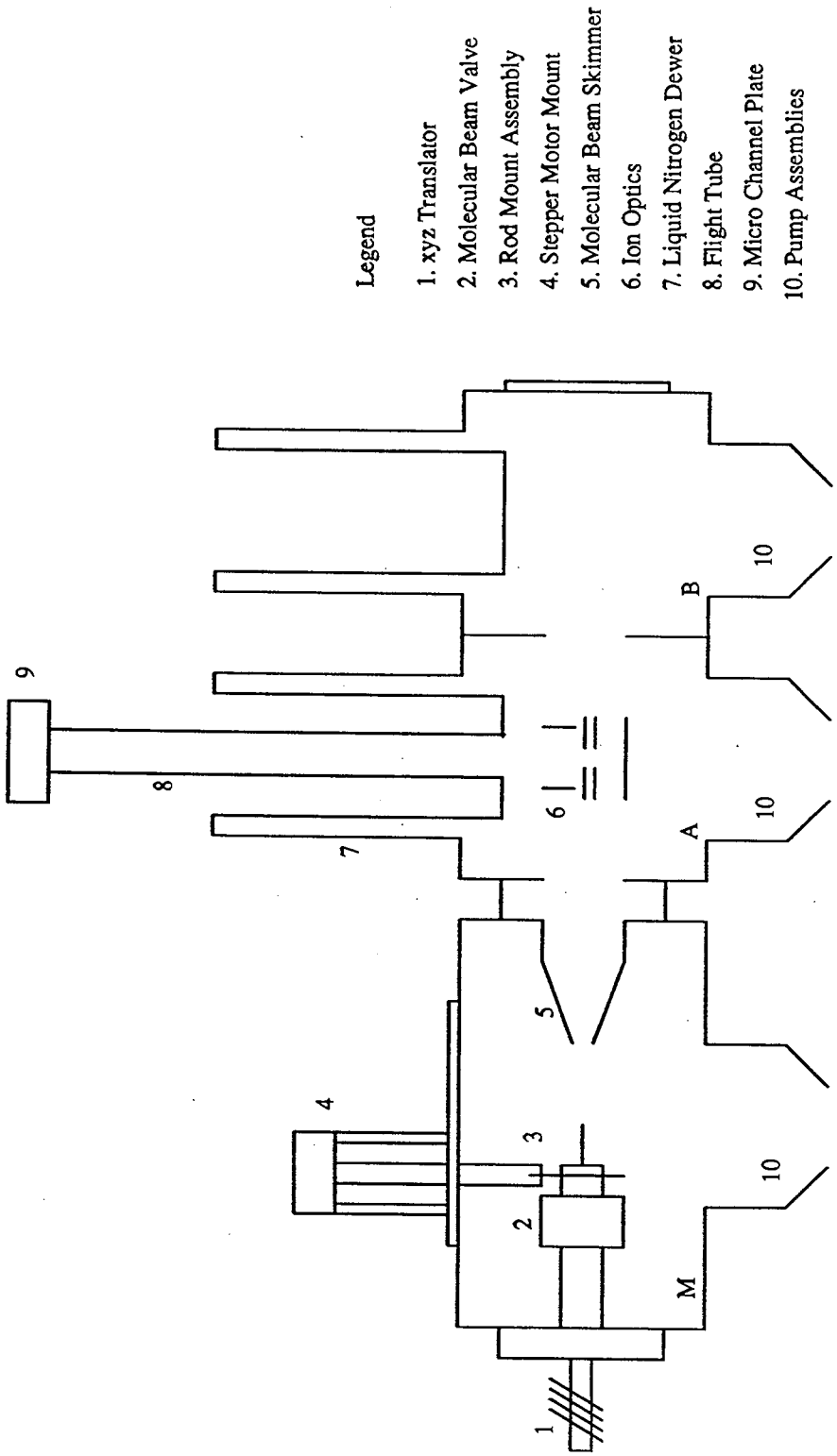

Figure 2–1: Schematic diagram of molecular beam apparatus MB1

side flanges which could be removed to allow facile access to the internal working area. These flanges, made of aluminium, were provided with two circular perspex viewing ports on each side (135 mm diameter), to permit visual access to the chamber, and a quartz window to allow the introduction of the vaporisation laser. This latter window had to be mounted on the end of a stand-off tube (270 mm long) to avoid the deposition of vaporised material.

The M chamber was pumped by a CVC PBA 1000 diffusion pump, charged with Convoil 20 fluid (1000ml). The system incorporated a water cooled, half-chevron baffle which reduced the pumping speed from 5300 ls^{-1} to 2690 ls^{-1}, for air, up to 10^{-3} mbar. The diffusion pump was backed by a rotary pump (Edwards E2M40) fitted with a mechanical booster pump (Edwards EH250), resulting in a combined pumping throughput of 8.5 mbar ls^{-1} at a foreline pressure of 0.1 mbar. These values are as given in the manufacturer's literature [2]. This pump combination allowed a base pressure of 1 x 10^{-6} mbar and a running pressure of 1 x 10^{-4} mbar to be achieved. As the main chamber was frequently required at atmospheric pressure, it could be isolated from the pumping system and the A/B chambers by two pneumatically operated valves (Vacuum Research Corporation and Airco Temescal respectively).

The top flange supported the drive mechanism for the rod/ disc source, and the end flange supported an XYZ translation mechanism to allow accurate positioning of the molecular beam valve. The final component present in the main chamber was the molecular beam skimmer. These will be described in greater detail elsewhere. Pressure measurements were made by a combination of an Edwards PRL 010 Pirani and an Edwards CP25-K Penning gauge.

2.2.2 A Chamber

This chamber was cubic, with an outside dimension of 285 mm, resulting in an internal volume of 16 l. It was pumped by an Edwards E09 diffusion pump and backed by an Edwards E2M18 rotary pump. The vacuum chamber was equipped with two circular, 280 mm diameter, stainless steel side flanges. Both these flanges

were provided with a central quartz window (50 mm diameter) to allow laser access. One flange also supported four high voltage MHV feed throughs which supplied the ion optics for the time-of-flight mass spectrometer, described later. The top flange of the chamber supported a double-skinned dewar which was filled with liquid nitrogen during operation. This cryopumping achieved an order of magnitude reduction in base pressure. The dewar also extended into the chamber by some 6.4 cm where it was used to support the ion optics mount. Centrosymmetric with the dewar was the flight tube for the mass spectrometer. It was 132 cm in length, had an internal diameter of 4 cm and was fabricated from stainless steel. The lower 66 cm of its length lay within the dewar. Pressure measurements in this chamber were made by a Balzers TPR 010 Pirani (100 - 5.6 x 10^{-4} mbar) and Balzers IKR 020 cold cathode ionisation gauge (5 x 10^{-3} - 4 x 10^{-10} mbar). Typical values were 1.2 x 10^{-7} mbar as base pressure, rising to 6 x 10^{-6} mbar in operation.

2.2.3 B Chamber

This chamber was identical to the A chamber in capacity. It was pumped by an Edwards 160/700C Diffstak, backed by an Edwards E2M18 rotary pump. This rotary pump was linked in parallel with that of the A chamber, such that either could be removed without necessitating an entire shut down of the system. The foreline pressure was measured by another Balzers TPR 010 pirani gauge. As an end chamber, the B chamber was equipped with three removeable flanges, and a similar cryo-dewar was mounted atop the chamber. Pressures were measured using a similar arrangement as in the A chamber, with typical pressures now being 7.2 x 10^{-8} mbar at base and 3 x 10^{-6} mbar during operation. The principal use of this chamber was as a dump for the molecular beam.

2.3 Molecular Beam Apparatus MB2

This apparatus also consisted of three vacuum chambers constructed from 16 mm 304 stainless steel. A schematic diagram showing both plan and side elevation is given in Figure 2-2

2.3.1 Main (M) Chamber

The main chamber consisted of a cube of external dimension 370 mm, resulting in an internal volume of 39 l. The circular side flanges were made of aluminium, and provided with laser access ports. The chamber was pumped by a CVC PMC-10 10″ diffusion pump with water cooled half-chevron baffle. The diffusion pump was backed by an Edwards EH250/E2M40 mechanical booster/rotary pump combination, as for MB1, the only difference being that the main chamber could be isolated from the rest of the vacuum system by two manually operated valves between the PMC-10 and the A/B chambers. The top flange supported the stepper motor for the target source, and the end flange incorporated an XYZ translator. A molecular beam skimmer was again present. Pressure measurements were made by an Edwards PRL 010 Pirani and an Edwards CP25-EK Penning gauge.

2.3.2 A Chamber

The A chamber was again cubic, with an internal volume of 16 l. It was pumped by an Edwards 160/700l Diffstak backed by an Edwards E2M18 rotary pump. The chamber was equipped with two side flanges supporting access windows and electrical feedthroughs. The chamber was also fitted with a cryodewar and flight tube as before. One additional feature were two bed bars which were used to support and locate the ion optics in this apparatus. These bed bars ran parallel to the molecular beam axis, and the optics assembly was secured via a bar and tightbolt assembly. This allowed the ion optics to be mounted either parallel or perpendicular to the molecular beam axis and rapid interchanges between either

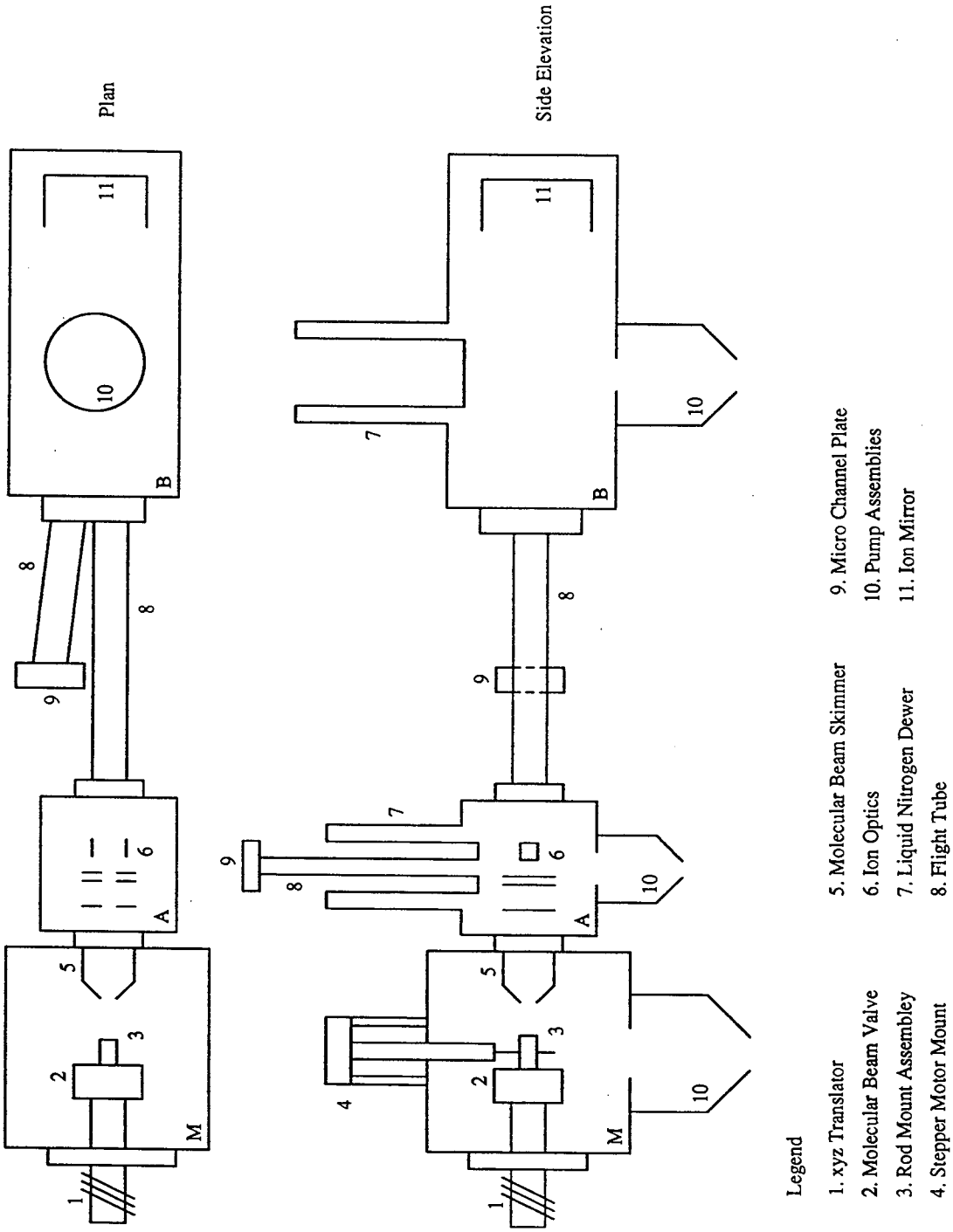

Figure 2–2: Schematic diagram of molecular beam apparatus MB2

configuration. The importance of this facility will be discussed later. Pressures were measured by an Edwards PRL 010 Pirani and an Edwards CP25-K Penning gauge.

2.3.3 B Chamber

The B chamber consisted of a main cylindrical section with two, smaller cylindrical adjuncts, creating a V-shaped configuration. The reason for the V-shaped configuration of this chamber was that it housed the flight tubes of a reflectron type time-of-flight mass spectrometer. This system will be described in more detail in the following chapter. The B chamber was pumped by an Edwards CR160/700 Diffstak incorporating an integral liquid nitrogen cooled baffle, and backed by an Edwards E2M18 rotary pump. Pressure readings in this chamber were made by an Edwards PRM 010 Pirani and an Edwards CP25-K Penning gauge. The A and B chambers shared a single rotary backing system but could be isolated from one another by means of two foreline valves. The foreline pressure was again measured using a PRM 010 Pirani guage.

2.4 Cluster Source

In both of the previously described molecular beam machines, the means of production of the chemical species to be studied, the "cluster source", was housed in the main chamber. Two distinct types of cluster source have been used in this work; a rod source and a disc source. In both cases, motion of the target was achieved via a stepper motor mounted on top of the main chamber and coupled via an O-ring seal into the vacuum chamber.

2.4.1 Rod Source

The rod source was the simpler of the two designs. A rod (5 mm diameter, 50 - 90 mm length) of the desired target species was located, near tangentially, to the

output channel of the molecular beam valve in a brass mount. This mount had three mutually perpendicular channels, allowing the passage of laser beam, rod and expansion gas. The rod was suspended via a series of universal joints from the stepper motor (Clannan HS34, 1.8° step, MB1) housed on the top flange of the chamber. This motor allowed the rod to be rotated and translated, via a screw thread mechanism, while under investigation. The importance of this motion was to continually expose a fresh portion of the rod surface to the laser beam - this was found to be a necessary requirement for stable operation over any period of study.

In chapters 4 and 5 of this thesis the spectroscopic studies carried out on the silver dimer molecule are described. The silver target used in all of these studies was a rod, using a source design similar to that described by Powers *et. al.* [3]. This source has proved to be extremely useful for studies of species which can be fabricated into rods and exhibit a degree of tensile strength. Hence much work has focussed on metallic systems [4] - [8].

However, this source has precluded the study of materials that cannot be produced in rod form. It has meant that soft metals like sodium were unsuitable, as the continual rotation of the target innevitably led to these weak rods being broken and wedged inside the mount. Perhaps more importantly, there was little opportunity to expand into the field of mixed metal species. As alluded to in chapter 1, very few of the mixed transition metal dimers have been studied. As alloys form an impotant class of materials, the study of these materials is clearly of interest. Unfortunately, the requirement of a rod format meant that only a few such combinations were accessible. One novel approach worth noting involved two vaporisation lasers acting on separate rods [9]. The mixing of the two entrained beams resulted in mixed species formation. However, this approach still required the constituent species to be available in rod format and was heavily resource dependent.

One previous study undertaken in this group focussed on the mixed species CuAg [10]. As this type of mixture is generally unavailable commercially in rod form, the source had to be fabricated in house. This was achieved by melting

alternate slugs of the two elements in a quartz tube under an inert atmosphere. Once cooled, the rod was turned down to the required 5 mm diameter. The rod appeared homogeneous, and was gold-like in colour. A typical mass spectrum of the cluster species, obtained using this target, is shown in Figure 2-3. Clearly mixed species had been formed in the clustering process.

It was found, however, that other such combinations of metals were not as successful. The reasons for this have not been rigourously studied, but the following general observations have been made. The best rods were formed from combinations of species with similar melting points and densities, and which were available in an extended bulk phase format. When melting points varied substantially, the initial liquid component dropped to the bottom of the tube long before the other had melted. This resulted in poor mixing and a rod with little homogeneity. A similar situation arose when the species had widely varying densities. This precluded the use of powders/ground crystals. Not only did mixtures of such species suffer from the two previous points, but they were also found to form rods of little mechanical strength. This was thought to be due to the high level of suface contamination that was present in such surface rich species, resulting in poor quality binding between the elemental partners.

To date, the CuAg rod is the only mixed species to be fabricated successfully in our laboratory. This is due mainly to the adoption of a new and somewhat universal technique for mixed species fabrication.

2.4.2 Disc Source

The disc source was first described in the late eighties [11]. It involved simply exchanging the target rod to a target disk - all other experimental conditions remaining as before. This source was mounted inside the chamber in the same manner as the rod source (i.e. bolted to the XYZ translator), but was more complex in terms of design. The necessary motion of the target disc was achieved by coupling the output of the stepper motor (Radio Spares 332-082, 1.8° step MB2) to two off-centre cam shaft and belt drive assemblies, which resulted in the

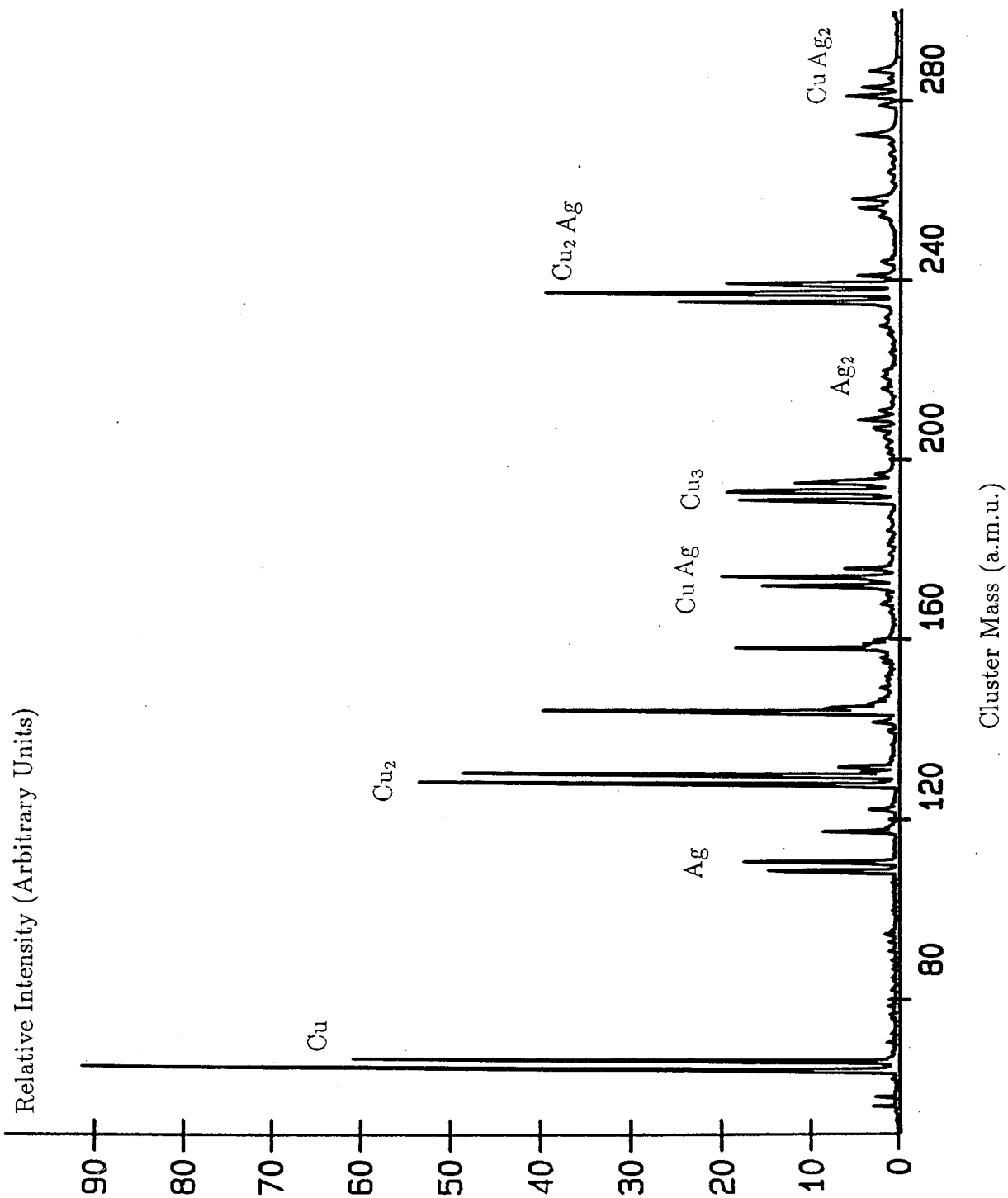

Figure 2–3: Time-of -flight mass spectrum of cluster species obtained using a mixed Cu/Ag target in the rod source

point of interrogation of the vaporisation laser on the disc surface tracing out a spiral pathway during the course of an experiment. The target discs were held in place by a spring and grub screw assembly.

Fabrication of the required target discs was achieved in-house. The selected mixture of powders, ground if necessary, were placed in a home-built stainless steel press and die assembly. The mixture was then pressed, using a maximum pressure of 30 tons/inch^2, for several seconds. It was found that increasing this time did not affect the properties of the disc in any way. On release of the pressure, a disc was recovered. The outward physical properties of such discs varied with their parental mixtures; their appearance and mechanical strength being dependent on the relative particle size and density of the materials used. In general, transition metal combinations gave a durable disc that could be repeatedly polished to produce a smooth and lustrous finish, whilst other metallic or non-metallic mixtures gave quite delicate discs which required sensitive handling. While the latter were only of use for a limited experimental period, the former could be used over extensive periods. Many such mixtures were prepared and investigated during the course of this work. Some of the mass spectra and preliminary optical spectra obtained for these species are discussed in the final section of the following chapter. Figure 2-4 shows a time-of-flight mass spectrum recorded using a Cu/Ag disc under similar experimental conditions used to obtain the spectrum shown in Figure 2-3.

2.5 Molecular Beam Valves

The end flanges of the main chambers on both MB1 and MB2 supported a tubular mount which extended into the main chambers themselves. There were two reasons for this; the mount acted as a coarse XYZ translator, to permit motion of the target in any required direction. This was important to allow alignment of the cluster source instrument. Secondly, the fact that the mount was hollow allowed the inclusion of the molecular beam valve such that the valve shell was at atmospheric pressure, but the valve output was directed into the high vacuum region. During

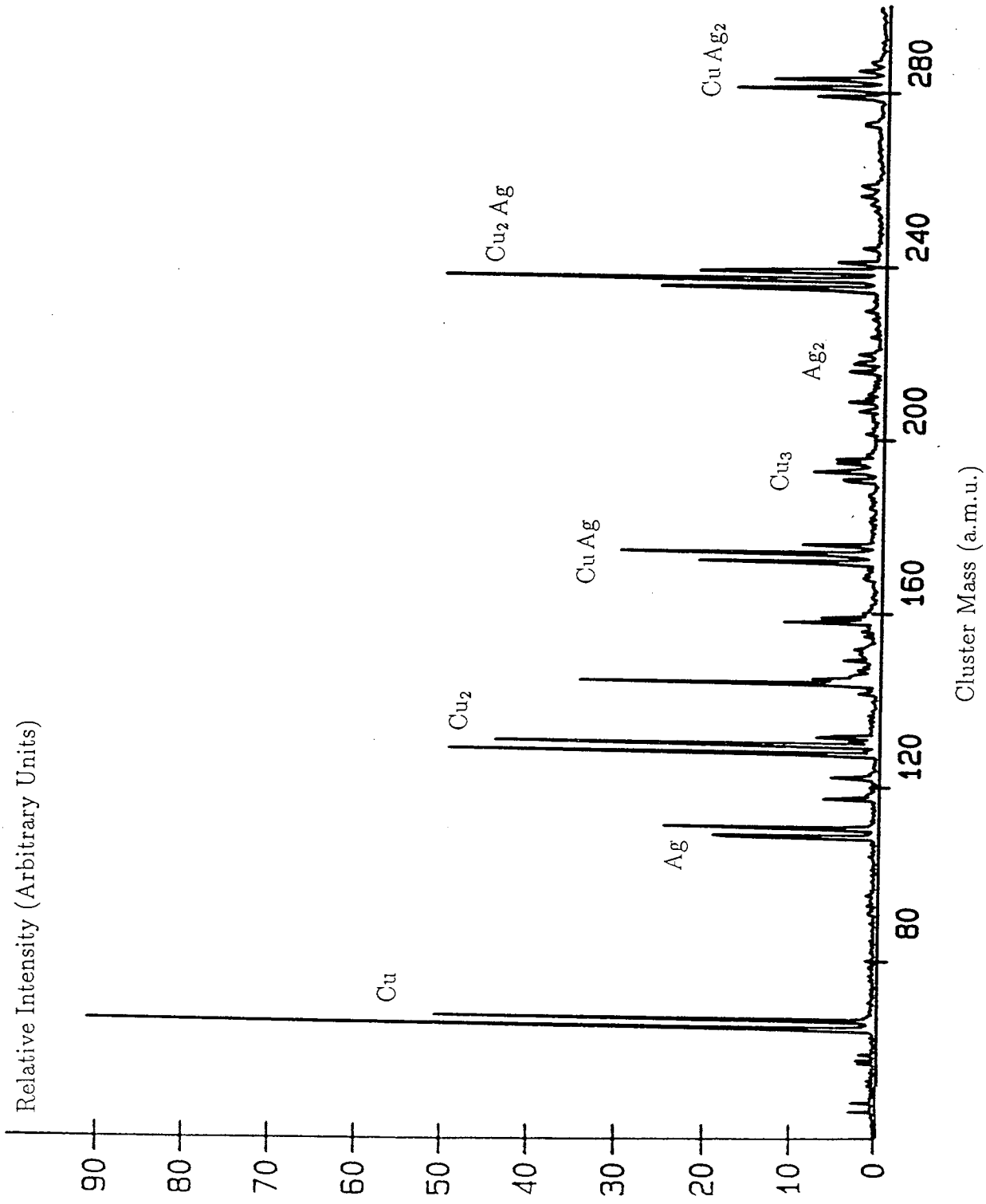

Figure 2–4: Time-of-flight mass spectrum obtained using a Cu/Ag target in the disc source.

the course of this work, two commercially available pulsed valves were used. As each operated according to a different principle, they will be described separately.

2.5.1 Newport BV-100V

This valve was of a double-solenoid type [12]. The valve consists of two coils - an 'open' and a 'close' coil - held at a fixed separation. Between these coils sits a soft iron actuator which is connected to a rubber tip-seal. This acts as the sealing mechanism. When a voltage pulse is applied to the coils, a magnetic field is induced at right angles to the coil. Hence the valve can be opened and closed by applying an appropriate voltage to the required coil. A typical gas pulse profile from this valve is shown in Figure 2-5.

While pulses of shorter duration were available, the typical pulse durations employed were of the order of 900 μs.

2.5.2 General Valve Corporation Series 9/Iota One

This valve consisted of a single solenoid and spring assembly. The tension of the spring is used to keep a plastic 'poppet' positioned such that the valve is in the closed position. When a voltage is pulsed across the coil, the induced magnetic field forces the iron actuator to open the valve. When the voltage is removed, the valve snaps shut. A typical gas pulse profile from this valve is shown in Figure 2-6.

In general terms, the Newport valve gave a gas profile which was more intense and had sharper rising and falling edges. This had implications for the clustering and cooling of beam species, which rely on many collisions. However, the General Valve was the more reliable valve, and was used in the majority of this work. That it produced lower gas densities was reduced in importance by the fact that the work reported here only required to produce diatomic species, which require fewer collisions.

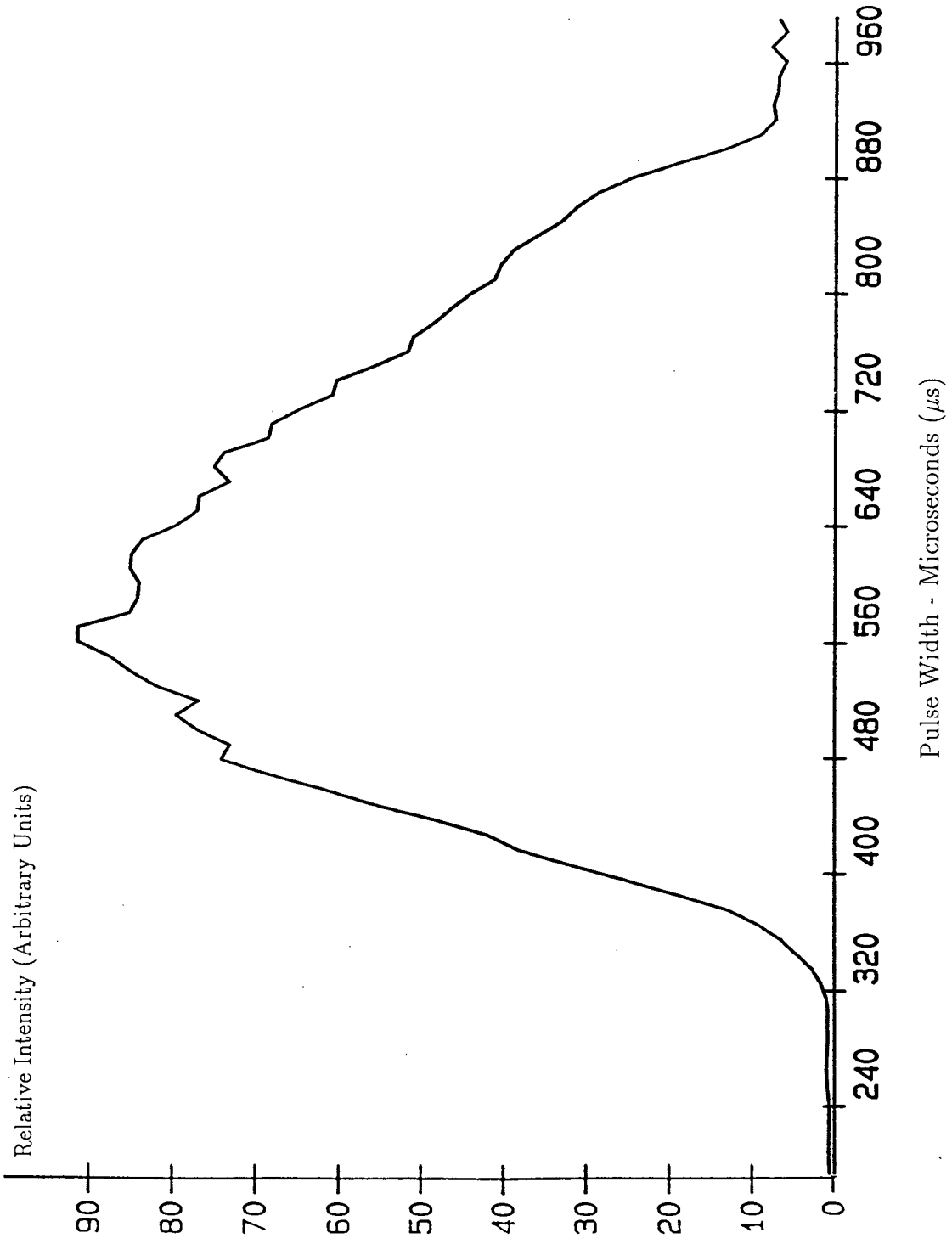

Figure 2–5: Helium pulse profile from the Newport valve

Figure 2–6: Helium pulse profile from the General Valve Corporation valve

2.5.3 Molecular Beam Skimmer

Regardless of which molecular beam valve was in use, the resulting molecular beam had to negotiate a skimmer [13] before passing from the Main to A chambers. The skimmer consisted of a cone fabricated by electroplating nickel (or some other metal) onto a template. The skimmer was used to remove (skim) the outer portion of the molecular beam, which consisted mainly of helium, and so reduce the amount of gas passing into the A/B chambers. Hence it was positioned on the common Main/A chamber wall, set-off at some distance to reduce the effect of perturbations, due to reflection of the gas pulse from the Main chamber bulkhead wall [14] [15]. This reduction of beam size, along with the fact that the chambers were differentially pumped, meant that the pumping requirements for the later chambers were much reduced. Two sizes of skimmer were used in the course of this work; the skimmer on MB1 had a 5 mm diameter orifice and 30° included angle, whilst that on MB2 had a 3 mm diameter orifice with a 50° included angle. While these were fully interchangeable, they were generally kept on a single machine due to their delicate nature.

2.6 Ion Optics

The A chambers of both systems contained the ion optics for the time-of-flight mass spectrometers [16]. Although the concepts behind the operation of time-of-flight mass spectrometers will be discussed in greater detail in the following chapter, the basic design of the ion optics housed in this chamber will be described here.

The ion extraction optics consisted of a set of parallel metallic plates, as shown in Figure 2-7.

In MB1, the three main plates were 72 mm square, 0.5 mm thick and constructed from stainless steel. For MB2, the sizes were similar but the plates were made of 1.7 mm thick gold plated aluminium. The plates were held apart by spacers, manufactured from Delrin rod. The three plates are commonly known as

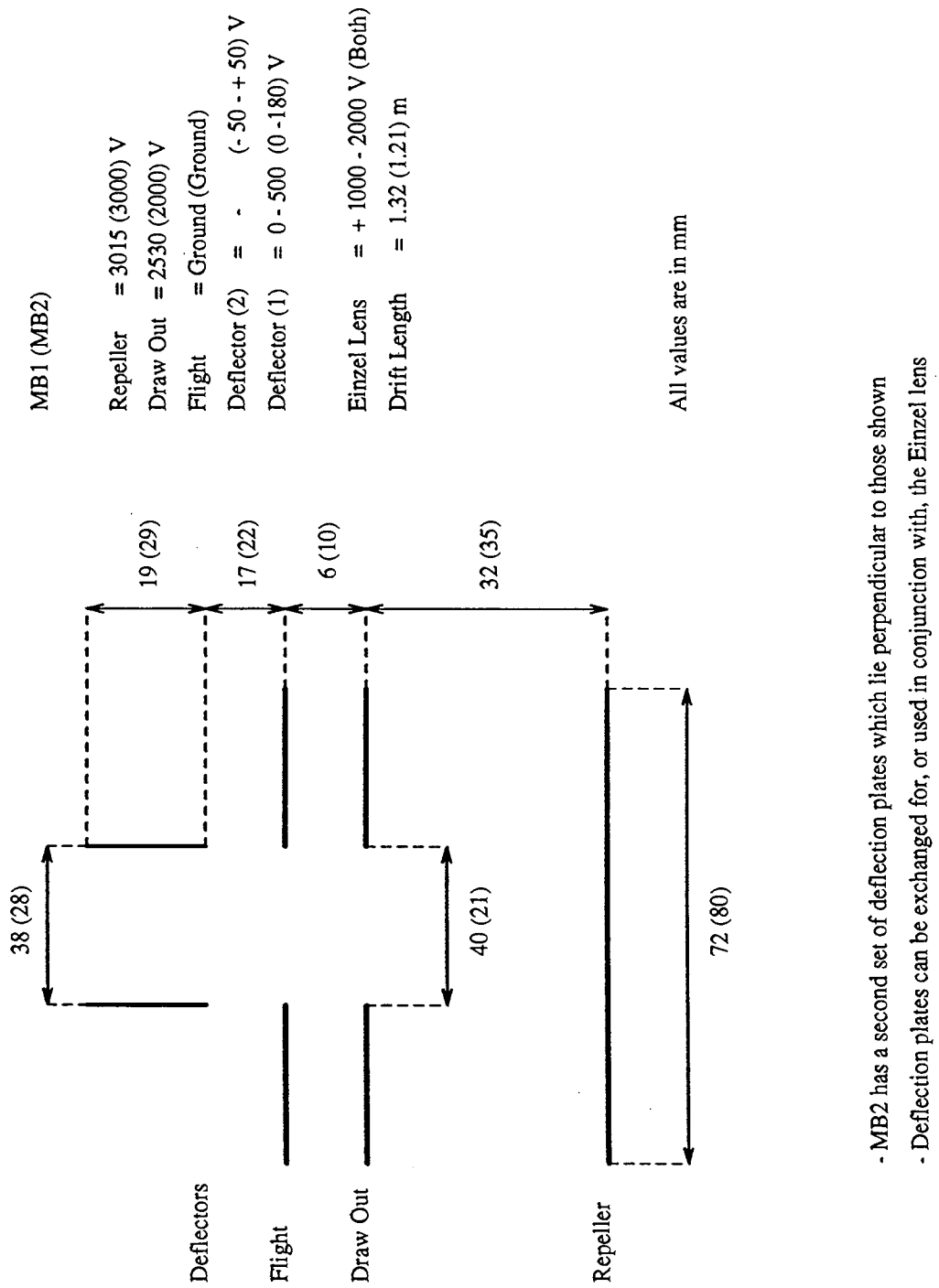

Figure 2–7: Schematic diagram of the ion extraction optics in the A chambers of MB1 and MB2.

repeller, draw-out grid and flight grid. On MB1, the repeller consisted of a solid plate, whilst the other two had 40 mm diameter, centrally located holes cut in them to permit the passage of the ion beams. In order to reduce the perturbations in the electric fields associated with these plates, the holes were covered by a nickel mesh (Buckbee Mears 90% transmission) affixed with silver conducting paint. Sitting above the field plate were two sets of mutually perpendicular 'deflection plates', which were used to compensate for any off-axis energy that the ions possessed - the axis being that of the time-of-flight instrument in use at that time. These plates were made from 1/4″ aluminium plate.

Despite these similarities, the A chambers on MB1 and MB2 possessed some subtle differences. In MB1, the ion optics were supported from the bottom of the cryogenic dewar which was re-entrant into the vacuum chamber, and were housed inside a copper box which was cryocooled via thermal conduction from the double skinned dewar. This helped reduce any background signal from pump fluid constituents etc. Hence the time-of-flight axis was always perpendicular to that of the original molecular beam. In MB2, however, the ion optics were supported on two horizontal rails attached to the floor of the vacuum chamber. This allowed the optics to be oriented perpendicular or parallel to the molecular beam axis. Hence MB2 had two sets of interchangeable ion optics; one set had a solid repeller plate and was used for perpendicular extraction, while the other had a repeller containing a centrally located hole, and was used in a linear extraction mode. The reason for this difference lay in the utilisation of the B chambers. On MB1, the B chamber acted only as a beam dump. On MB2, however, the B chamber housed the ion mirror and flight tube of a reflectron-type time-of-flight mass spectrometer [17]. Again, a detailed discussion of this type of mass analyser will appear in the next chapter, but essentially the ions in this case were reflected by a pair of potential fields set up near the vertex of the V shaped chamber. The optics themselves are shown in Figure 2-8. They consisted of six stainless steel toroidal rings with outer diameters of 120 mm and apertures of 60 mm. The first and second rings were covered by mesh, as described previously, with the others left

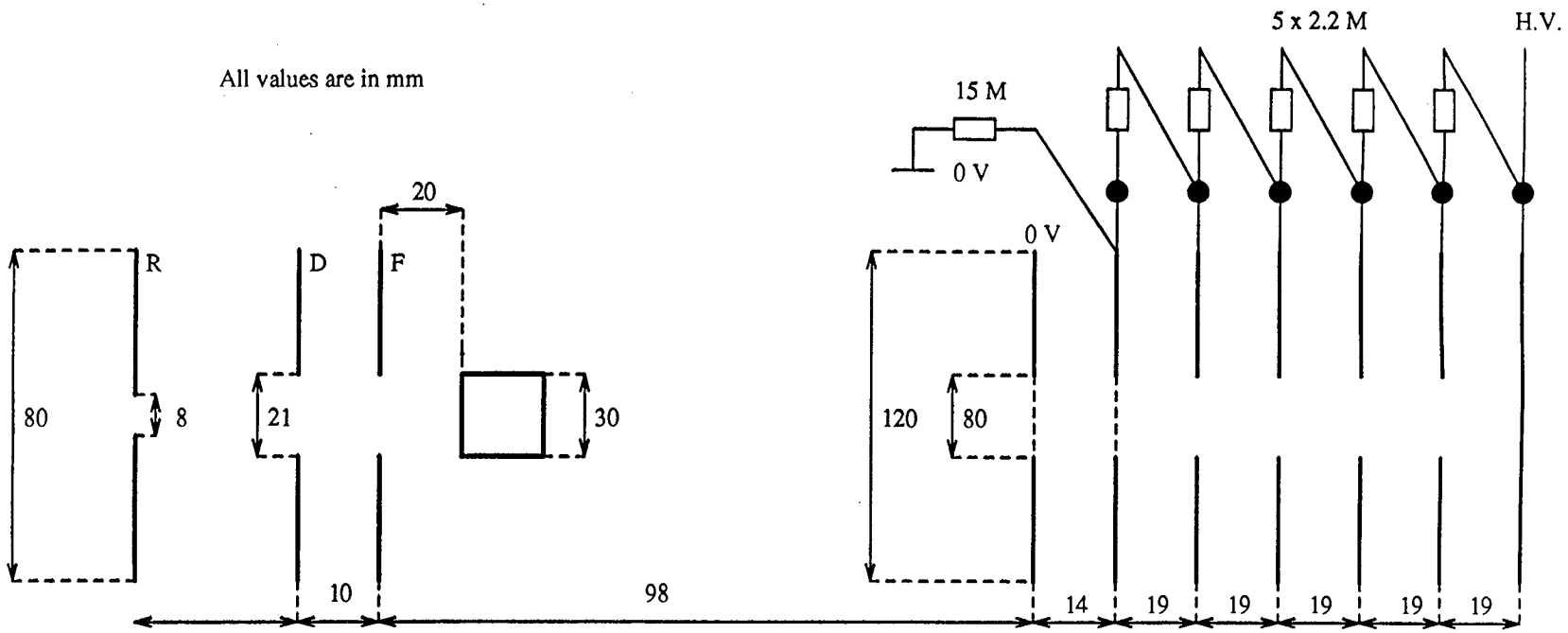

Repeller (R)	= 3000 V	Deflectors (Vertical)	= - 30 V - + 30 V
Draw Out (D)	= 2115 V	Deflectors (Horizontal)	= - 50 V - + 50 V
Flight (F)	= Ground (0 V)	Mirror (H.V.)	= 3082 V

- H.V. Mirror was inclined at an angle of 4 degrees to the extraction axis
- An Einzel lens could be mounted downstream of the deflection plates
- The distance from the mirror ground plate to the detector was 72 cm

Figure 2–8: Schematic diagram of the ion mirror in the B chamber of MB2

open. These rings were connected by a resistor chain such that a stepped potential field was introduced.

2.7 Ion Detection and Signal Enhancement

The ions, having been separated in the mass spectrometer, now need detection. This can be thought of as encompassing two distinct operations. Firstly, there was the actual detection of the species themselves. This was followed by the amplification of these, often weak, signals such that they were of suitable intensity for further data processing.

2.7.1 Jordan Microchannel Plate (MCP) Detector

Both molecular beam machines employed the same detection system, namely an MCP device. These items were purchased commercially, and have been well documented [18]. Briefly, the MCP consisted of two active micro channel plates and an impedance matched 50 Ω anode. Each plate contained many thousands of channels (10 μm diameter, 12.5 μm between centres) which ran parallel to one another and perpendicular to the plate itself. The plates were fabricated from a lead glass material (Galileo MCP-18B) with an active detection area of 2.48 cm^2 per plate. The plates were supplied by a simple, homebuilt unit which consisted of a resistor chain, which divided the input voltage, and also incorporated high value capacitors to prevent any gain 'droop' by enhancing the nanosecond recovery time between successive ion packets. The exact amplification obtained from the MCP depended on the length/diameter ratio of the channels and the exact voltage at which they were driven. Typical literature values are of the order of 10^3 at 1000 V per plate [19]. Usual operating conditions were 700 V per plate, resulting in an approximate gain of 10^2 per plate. One other point of note is that both MCPs were used in a grounded anode configuration. This made for simpler connection to subsequent equipment, as there was no need to decouple the signal from a high voltage anode.

2.7.2 Signal Amplifiers

The output from the MCP could now be transferred to the data acquisition equipment described in the next section. In some cases, as in the spectroscopic experiments, however, the output signal was still very weak, and it was often desirable to utilise a further amplification stage [20]. This was achieved using one of two preamplifiers. A Pacific Video Amplifier was used in some work. This provided a gain of 20, and whilst useful in some applications, due to its portability, it suffered due to electronic noise in some locations in the laboratory. The second unit, a LeCroy Research Systems Corp. Model 134 linear amplifier, provided two circuits each of gain 10. These were often used in series to effect a gain of 100 for weak signals. This NIM unit was rack-based, and used in the majority of the work described in the later chapters.

2.8 Experimental Control and Data Acquisition

All the experiments reported in this thesis were performed, with the above equipment, under computer control using a suite of programs which were written and developed in-house by a previous member of this research group [21]. These programs ran on a mini computer (IBM PC-AT). In addition to this software, a variety of data acquisition and control equipment was also required to ensure that these experiments could be performed. Both the hardware and the software are described in the next two sections.

2.8.1 Experimental Hardware

Many of the units to be described were housed in a standard CAMAC (Computer Automated Measurement and Control) crate (WES) which conformed to the internationally accepted standards [22]. The crate contained a parallel data bus of 24 bits for reading from and writing to any of the individual CAMAC modules it housed [23]. The crate was controlled by a double width CAMAC unit (Transiac

6002 Crate Controller) which could serve as either a master or an auxilliary unit. It was always used in the master configuration, and as such occupied the rightmost station of the crate. It also acted as a Dataway Display Module, and was used in conjunction with a Microcomputer Interface Card (IBM PC004), cable and software driver which permitted input and output and DMA transfers of up to 700 Kb per second. The unit provided external registers to hold CAMAC commands (N,F,A) and transfer data to and from the CPU. Figure 2-8 shows a schematic representation of how this crate exercised control over the other electronic hardware required for the experimental work.

All experimental timing control was achieved via accurate trigger pulses produced by one of two timing delay modules. The less critical timing delays were provided by an eight channel timing pulse generator (Kinetic Systems Model 3655) housed within a single width CAMAC unit. It contained a 16 bit counter and 8 x 16 bit set point registers and used an internal crystal clock, set to 1 MHz time-base frequency. The output signals were at TTL level, and of 200 ns duration with a jitter of $\pm$ 0.025% ($\pm$ 0.05 ns). The output from this module was used to trigger the vaporisation and ionisation lasers, along with the molecular beam valve. One of these channels was used to trigger the second delay module. This module was a much higher accuracy/precision pulse generator (LeCroy Model 4222), again housed in a single CAMAC unit, providing 4 x 5V outputs, but now with 1 ns accuracy and 150 ps jitter. Each pulse was 100 ns wide. This pulser was employed to trigger the spectroscopic/resonant ionisation lasers, the transient digitiser and the high voltage pulser unit used in zero-field threshold photoionisation experiments.

The output signals from both of these timing modules were often insufficient to drive the required items of apparatus. To overcome this, their outputs could be fed into a multichannel line driver. These units, built in-house, boosted the output signals from the pulse generators and were capable of driving twelve output channels at either 5 or 15 V amplitude, as required.

Two other CAMAC units were available to provide control signals. Firstly, a digital to analogue converter (Bi Ra Model 5408) which was capable of supplying eight output voltages of 0 - 10 V at 5 mA. Each channel had a 12 bit register.

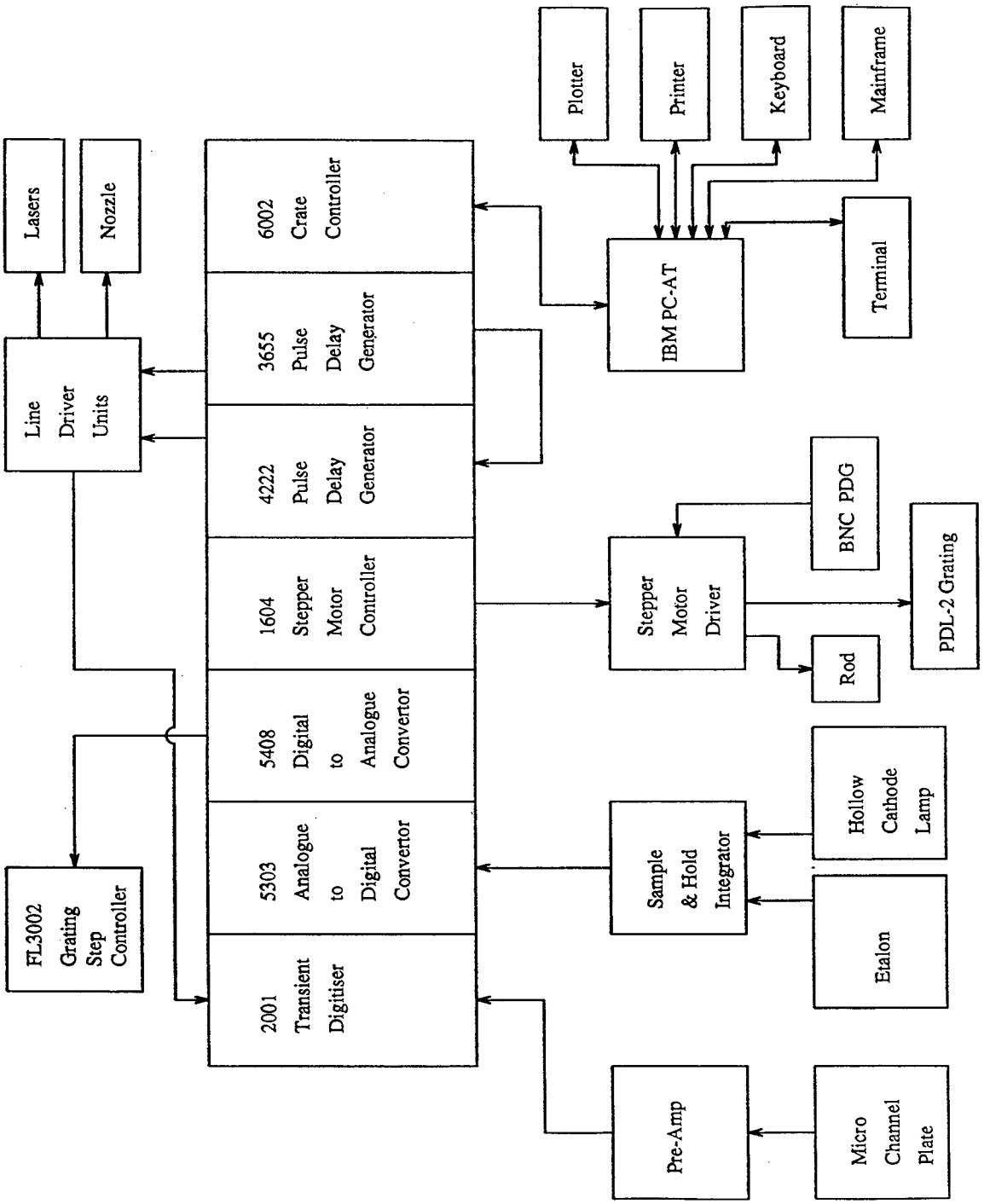

Figure 2–9: Schematic of hardware control structure

This module was used to trigger the in-built microprocessor controlling the operation of the Lambda Physik dye laser. Secondly, a four channel stepper motor controller (Hytec SMC 1604), which provided independantly controlled channels for generating step and direction signals for the various other stepper motors used in the experiments. The SMC 1604 supplied pulses to chopped, bipolar drive cards (M^{c}Lennan TM 162C) located in a 19″ rack unit, which were used to control the stepper motors driving the rod/disc sources and the stepper motor driving the grating on the Quanta Ray PDL-2 dye laser.

The output waveform from the MCP detector, following preamplification if necessary, was digitised using a CAMAC-based 100 MHz, 8 bit transient digitiser (Transiac 2001). This was capable of storing 32 K (32768) samples at a 100 MHz (10 ns) sampling rate. The analogue signal was sampled, converted to a digital number and stored in memory. After a stop trigger was received, the stored data was read by the computer.

A second method of providing input was from an analogue to digital signal converter (Bi Ra Model 5303). This module accepted up to eight analogue signals and converted them to their digital eqivalents, providing the input was at least 6μs in duration. This unit was used for recording laser power levels and etalon fringes via monitoring photodiodes, the output from which was sent to the ADC via NIM-housed gated integrators (Stanford Research Systems SR 250).

The CAMAC crate was also equipped with a programmable high voltage supply (LeCroy Model 2415) housed in a double width CAMAC module. The output could be varied up to either 3.5 or 7 kV maximum, and set to the required value using the potentiometer settings on the front panel. It was never used in a computer controlled mode. Accuracy was of the order of $\pm$ 1V. The above unit was used to supply the repeller plate voltage on MB1. The other high voltage requirements, i.e. for draw-out grid, deflection plates and MCP detector were provided by three different models of 19″ rack mounting high voltage supplies manufactured by Power Designs, namely;

Draw-out grid Model 1570 1-3012V,40MA Calibrated.

Deflection plates	Model 2K20A 1-2000V,20MA Regulated
MCP Detector	Model 1556C 1-6000V,20MA Calibrated

Each unit featured a temperature stabilised, all silicon transistorised control amplifier which drove a vacuum tube series regulator. This resulted in superior operating characteristics over other designs, with output voltage stability of 0.25%.

For MB2, all the required voltages were also supplied by rack mounted units. While the repeller plate used a 2500 V supply (Stanford Research Systems Inc. Model PS325), the draw out grid, detector, deflection plates and ion mirror all used 5000V supplies (Stanford Research Systems Inc. Model PS350). All were programmable with digital display, providing accurate resetability, and had a $\pm$ 1 V accuracy.

For some of the threshold photoionisation experiments described in chapter 5, a pulsed potential supply was required. Here, a prototype factory model (Kentech Instruments) was obtained which supplied a fast rise-time (25 ns) pulse (100 μs) to both repeller (3000 V) and draw out grid (2000 V) on the arrival of a trigger pulse from the computer controller. This allowed photoionisation to occur in a field free environment, with subsequent ion extraction as before. The detailed electronics of this model are not in the public domain and cannot be reported here. However, a fast acting pulser which is readily available has been recently reported, and is shown schematically in Figure 2-10 [24].

One other experimental alteration required for the threshold ionisation studies was the introduction of a pair of nickel/aluminium scavanging plates into the Main chamber. These were placed above and below the molecular beam and had a small d.c. voltage applied to them continuously. The reason for this was that many of the original ions survive the quenching and clustering stages intact. Previously, these would have been removed by the repeller voltage or field. However, without this barrier, they could enter the time of flight tube and swamp the detector. A potential of 60 V was applied, from a battery pack, across the scavenging plates

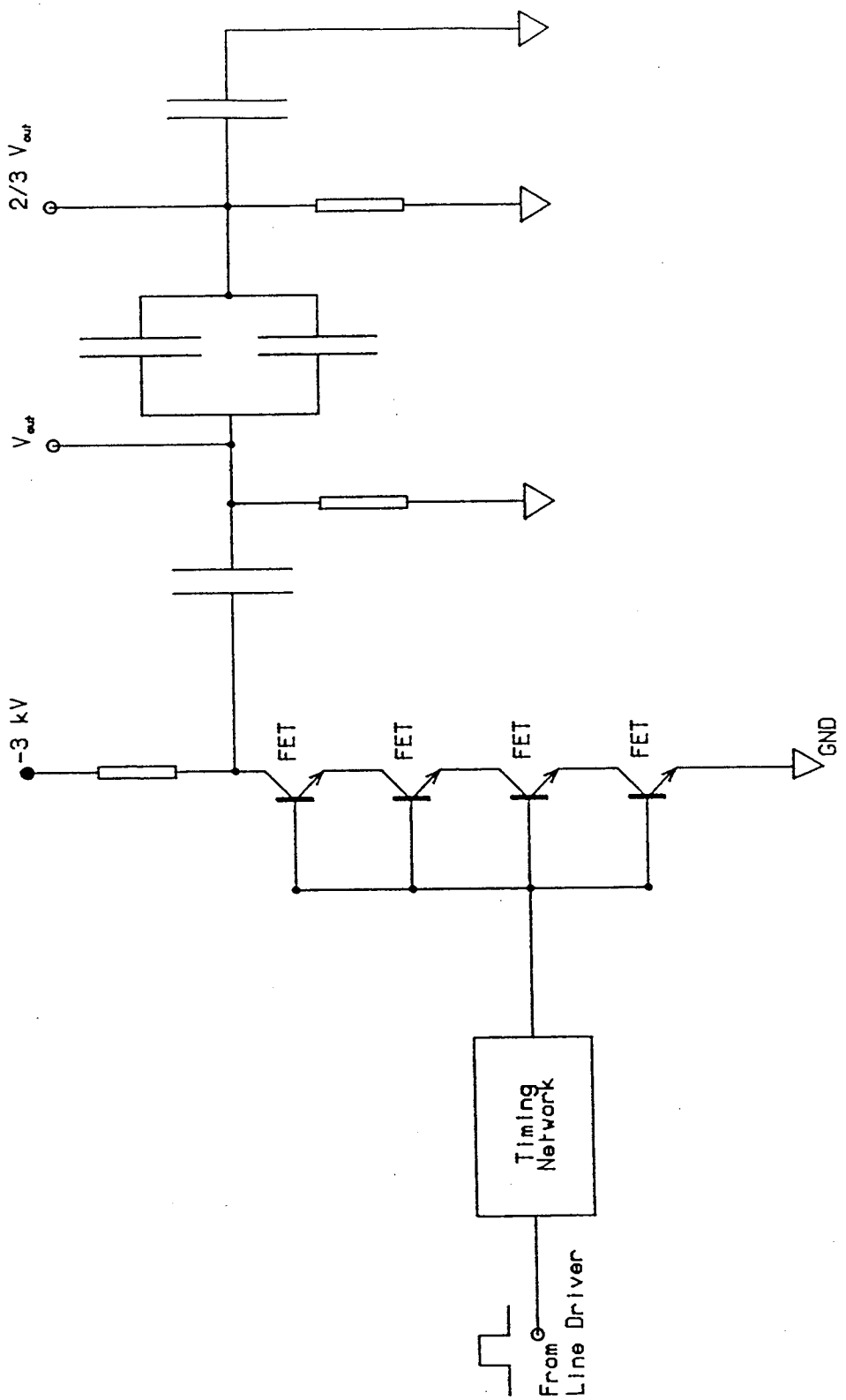

Figure 2–10: Schematic of fast pulser circuit

such that all ions up to around mass 250 were swept out of the beam, and those of higher masses were less likely to negotiate both skimmer and repeller openings.

2.8.2 Experimental Software

There are essentially two programs that need to be described here. The first, known as THOR provided experimental control and data collection. The second, for data analysis, was called ODIN. Although the detailed workings of both these programs have been documented by their author [21], it is useful to describe their operating characteristics in order to give the reader a flavour of the experimental procedures involved.

The THOR program

This program was comprised of a variety of sub-routines. All were written in either the C programming language (Microsoft v5.0) or in low level assembler code required to access the units in the CAMAC crate. The program offered screen menu drive and a variety of single key commands to effect changes while the program was running. The key to this action were two sub-routines, the so called TIC and TOC routines. When the TIC function was called, all timing delays were set for the forthcoming data cycle, which was run at a constant repetition rate of 10 Hz. A typical timing sequence, as used in one of these experiments, is shown in Figure 2-11.

The TOC function was then called to read the data from the transient digitiser, and the ADC if used, for loading into the computer where it could be displayed on screen and recorded. There were three main modes of operation of the THOR program: the mass scan mode, the time scan mode and the frequency scan mode.

The mass scan mode displayed all the peaks that had been recorded in an intensity versus mass screen. Calibration of the mass axis was achieved using known mass peaks. This was the most commonly used mode of operation as it allowed for the qualitative assessment of beam species. Depending on the transient digitiser time-base setting (e.g 10 ns or 50 ns) and any delay inserted in the computer

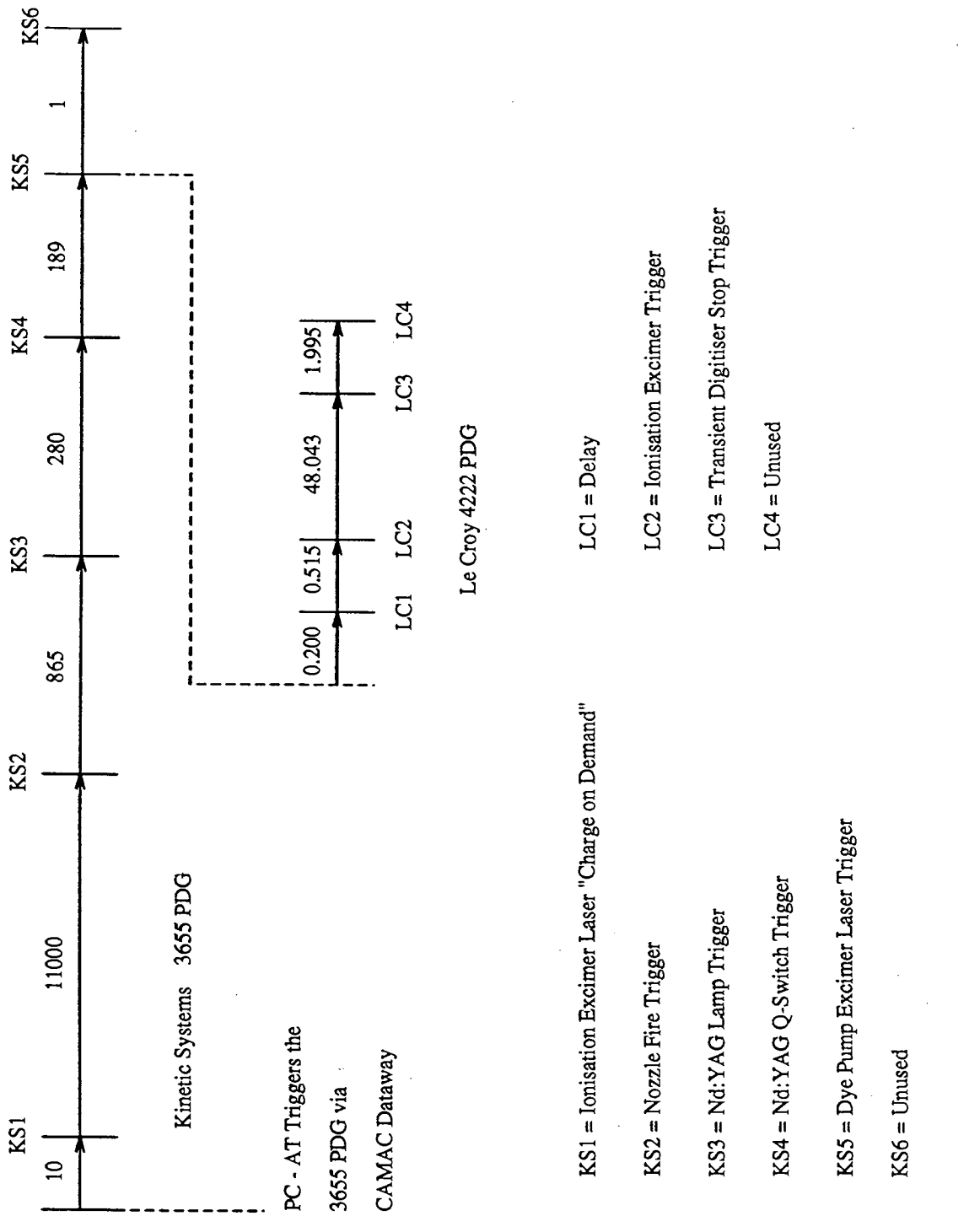

Figure 2–11: Schematic of typical experimental timings

function, the mass spectrum could display a wide or narrow mass window. This should not be confused with simply expanding the mass axis scale.

In order to optimise any given signal in a mass scan, it was necessary to move to the time scan mode. The channels of the mass spectrum which contained the peaks of interest were measured and entered into the appropriate menu. These channels could then be monitored whilst another parameter, for example the Q-switch delay of the vaporisation laser, was scanned between defined limits. This allowed the experimentalist to select the time-delay for the Q-switch that resulted in the most intense peak signal. This value could then be measured and entered back into the required timing menu. The gas pulse profiles shown earlier in this chapter, see Figures 2-5 and 2-6, were obtained in this way by monitoring the He mass channels while scanning the nozzle-ionisation laser time delay.

Having now optimised the desired signal, the frequency scan mode could be envoked. This allowed the intensity of these measured channels to be monitored as the frequency of a dye laser was scanned. All of the spectroscopic data reported in the later chapters was produced in this way. Again, screen driven menus ensured that the limits of the scan were appropriate and that the dye laser grating was driven synchronously. With data now recorded, some form of analysis could be applied.

The ODIN program

This program was written entirely in the C programming language. Its main functions were to allow the accurate measurement of any desired areas of data, and to facilitate the production of hard copy. In terms of spectral measurement, the program incorporated a peak finding routine [25] which employed well documented procedures. Once measured, these peak files could be transferred to a mainframe computer where they were assigned and fitted. All of the spectral figures in this thesis were produced by the ODIN plotting routine using a Hewlett Packard Colour Pro plotter, HP7440A.

2.9 Laser Systems

All the experiments carried out involved the use of at least two laser systems, and often three, simultaneously. Each system had a different set of properties which lent themselves to their appointed task.

2.9.1 Lumonics TE-861T-4

Excimer, or exciplex, lasers are capable of generating intense pulses of radiation, at a variety of wavelengths covering a wide range of the electromagnetic spectrum [26]. The precise wavelength of radiation emitted by any one system is determined by the gas phase species present in the laser cavity. This mixture is held in a reservoir at a few atmospheres pressure, along with an electrode assembly. When electrical discharge (40kV) takes place, the species present in the gas mix are able to form molecules which have bonding character in their excited states, but are non-bonding in their electronic ground states. These EXCIted diMERS or EXCIted comPLEXES then emit radiation as they fall apart and return to the ground state equilibria.

The particular laser used in these experiments was a single table top mounting comprising of resevoir, electrode assembly, transverse gas recirculation and water cooling system all in the one unit [27]. This configuration helped to combat loss mechanisms at the excitation stage. Only three gas mixes were used in the course of this work; ArF, KrF and F_2. While all three provide output in the ultraviolet region of the spectrum, only the F_2 line required any special arrangements. Lying at 157 nm, the output on the F_2 line was heavily absorbed by molecular oxygen and so a purge tube flushed continually with nitrogen was required.

The excimer laser ran at 10Hz, with external (computer) triggering in the stable resonator (divergent beam) mode with a fully reflecting back optic and a fully transmitting front optic.

One, in-house, modification was made to the basic factory model. It was found that the output (on ArF in particular) could be sustained for greatly enhanced periods of time by circulating the reservoir gasses via a diaphragm pump (Air Dimensions Inc. Model 19313VYPR) and copper tubing connections [28]. This tubing was coiled in one section and immersed in a liquid nitrogen bath. The main loss mechanisms in the ArF system are due to the production of non-lasing chemical species, which can be removed by low temperature trapping. Although used only occasionally, this modification did result in longer and sustained sessions of work.

The output characteristics of the laser vary depending on the system of operation. Typical working conditions were;

ArF 10 ns (FWHM) 60 mJ/pulse at 193 nm = 6.4 eV
KrF 10 ns (FWHM) 90 mJ/pulse at 238 nm = 5.0 eV

Due to the high energy nature of the output of this laser system, it was ideal for ionisation purposes as most species require only two photons to effect ionisation.

2.9.2 JK HyperYAG HY750 Nd^{3+}:YAG Laser

While the pevious section described the workings of a gas phase laser system, this section describes a solid state laser. The gain medium here consists of rod shaped crystals of neodymium-doped yttrium aluminium garnet (Nd^{3+}:YAG) [29]. These crystals are housed in such a way that they are efficiently excited by the output of a xenon flashlamp [30]. The lasing action itself is a result of a subsequent electronic relaxation in the neodinium ions. The output wavelength of this system is at 1064 nm, but the system is easily adapted to allow generation of second or higher harmonics. All work discussed here used second harmonic generation (SHG) at 532 nm.

The laser consisted of two Nd^{3+}YAG rods, mounted in an oscillator/amplifier configuration. The oscillator contained a 3″ Nd^{3+}:YAG rod 4 mm in diameter

and pumped by a single xenon flashlamp. This rod was contained inside a cavity consisting of a plane output coupler and a 5 m radius of curvature, concave, maximum reflectivity rear mirror. A Galilean telescope (2 x magnification) was focussed such that it compensated for the thermal lensing effects of the YAG rod. The final oscillator component was a Pockels cell / polariser Q-switch assembly which contained a dielectric polariser and a dry mounted Brewster angled KD*P crystal with a rhomb to correct for beam deviation. This system claimed to work better than the alternative which was a crystal immersed in a refractive index matching fluid. Timing of the opening of the Pockels cell was achieved via an avalanche transistor string. In the amplifier section, the oscillator output passed through a 3″ long 8 mm YAG diameter rod in a similar flashlamp pumped chamber. Again a telescope (2 x magnification) was used for compensation. Finally the output passed through a harmonic generation assembly (HGA). Although 2^{nd}, 3^{rd} and 4^{th} harmonic outputs could be achieved, all the work reported here used only the 2^{nd}. Another birefringent (non-centrosymmetric) CD*A or KD*P crystal was used to create these higher components, with the required output separated by a pair of gull winged prisms. Typical operating parameters were;

Nd:YAG 10 ns (FWHM)	532 nm	320 mJ/pulse
	355 nm	170 mJ/pulse

As the output energy of this system was very easily controlled by manipulation of the Q-switch delay, it was ideal for the production of beam species by vaporisation.

2.9.3 Quanta Ray PDL-2 Pulsed Dye Laser System

This was a fully portable dye laser system which consisted of a conventional oscillator - amplifier arrangement with an optional pre - amplifier stage for low gain dyes [31]. The system could be used either in a longitudinal or transverse pumped configuration and also allowed for a 2.5 ns optical delay path for use with dyes which displayed a high amplified spontaneous emission (ase). The diffraction grating was driven under computer control, and could be tuned through the range

380 - 900 nm. This control could be disengaged to allow for manual adjustment when required. Although the bandwidth of the output radiation was too large (0.4 cm^{-1} at 500 nm) for any work at rotational resolution, this instrument was used consistently as described in chapter 5 to pump the A $\leftarrow$ X transition during our investigation of the threshold ionisation of Ag_2.

2.9.4 Lambda Physik Excimer Pumped Dye Laser

This system was used for all of the high resolution spectroscopy reported in this thesis [32]. It consisted of two distinct parts; the excimer laser (EMG201MSC) which acted as the pump source and the dye laser itself (FL3002EC), the output of which was used to perform the experiments [33].

EMG201MSC Excimer Laser

The excimer used in this system was essentially the same as that described earlier. It was thyratron switched and ran at an experimental repetition rate determined by the external computer clock. This system was always run on the XeCl (308 nm) line and gave the following performance;

XeCl (308 nm)	400 mJ/pulse at 1 Hz
	200 mJ/pulse at 10 Hz

All laser pulse energy measurements were made using a pyroelectric joulemeter (Gentec ED200) displayed on a 150 MHz oscilloscope (Tektronic 2445A).

FL3002EC Dye laser

This system consisted of three dye cuvettes arranged near colinearly on a set of optical rails. The first, oscillator, cuvette was housed inside a Hänsch type cavity [34]. A portion of the excitation radiation was focussed into the cuvette. The resulting fluorescense passed through a set of beam expansion prisms before encountering the diffraction grating (600 lines/mm). This beam expansion not only

reduced power density for component protection, but also increased resolution, which is proportional to the number of grating lines illuminated by the beam. The selected frequencies, which were determined by the angle of the grating, then passed back through the oscillator cuvette and then on through the remaining two cuvettes which had been excited by the remainder of the pump beam. In this mode of operation, a bandwidth of 0.18 cm^{-1} at 480 nm was available. Spectral calibration was achieved by use of a solid quartz etalon of around 3.3 cm^{-1} free spectral range (FSR), as described in Chapter 4. In order to increase resolution, the bandwidth of the radiation had to be reduced. This was achieved by use of an etalon positioned inside the oscillator cavity. Here, an air spaced etalon (finesse = 25 - 30, FSR = 1 cm^{-1}) was routinely mounted. The resulting bandwidth was reduced to approximately 0.04 cm^{-1} at 480 nm. Spectral calibration was now achieved using an air spaced monitor etalon (finesse = 25, FSR = 0.1 cm^{-1}). In both the above cases the reference fringes from the etalon were simultaneously recorded with the spectra. This dye laser system also allowed for a further reduction in bandwidth by use of an additional, extracavity, etalon coupled to pressure tuning of the grating block. This facility was never utilised. Typical output values from this laser were of the order of 12 mJ/pulse of output narrowed radiation, subject to the dye in use at any given time.

Although the dye laser could produce output continuously from 300 nm to 1000 nm, it was often desireable to produce radiation of higher energy. This was accomplished by means of a second harmonic generator or doubling crystal. This was mounted towards the end of the optical path and consisted of two motorised tables which were driven synchronously in opposite directions. On the first was mounted the crystal itself, and on the second a quartz block of similar refractive index to compensate for any beam movement through the crystal. The crystals used in the work reported were either potassium dihydrogen phosphate (KD*P) or β-barium borate (BBO). Each had a different efficiency / frequency curve and were selected accordingly. All movements of grating, etalon and doubling crystal were synchronised under the control of a dedicated micro processor installed in the laser

system itself. The timings of the grating steps, however, were externally controlled by the microcomputer signals to ensure total experimental synchronisation.

Bibliography

[1] Fluendy M.A.D. and Lawley K.P. *Chemical Applications of Molecular Beam Scattering*, Chapman and Hall, London, 1973.

[2] Edwards High Vacuum *Instruction Manual*, Crawley, England, 1982-86.

[3] Powers D.E., Hansen S.G., Geusic M.E., Puiu A.C., Hopkins J.B., Dietz T.G., Duncan M.A., Langridge-Smith P.R.R. and Smalley R.E., J. Phys. Chem., 1982, **86**, 2556.

[4] Powers D.E., Hansen S.G., Geusic M.E., Michalopoulos D.L. and Smalley R.E., J. Chem. Phys., 1983, **78**, 2866.

[5] Michalopoulos D.L., Geusic M.E., Hansen S.G., Powers D.E. and Smalley R.E., J. Phys. Chem., 1982, **86**, 3914.

[6] Hopkins J.B., Langridge-Smith P.R.R., Morse M.D. and Smalley R.E., J. Chem. Phys., 1983, **78**, 1627.

[7] Morse M.D., Hansen G.P., Langridge-Smith P.R.R., Zheng L-S., Geusic M.E., Michalopoulos D.L. and Smalley R.E., J. Chem. Phys., 1984, **80**, 5400.

[8] Langridge-Smith P.R.R., Morse M.D., Hansen G.P., Smalley R.E. and Merer A.J., J. Chem. Phys., 1984, **80**, 593.

[9] Nonose S., Sone Y., Onodera K., Sudo S. and Kaya K., J. Phys. Chem., 1990, **94**, 2744.

[10] James A.M. *PhD Thesis*, University of Edinburgh, 1991.

[11] O'Brien S.C., Liu Y., Zhang Q., Heath J.R., Tittel F.K., Curl R.F. and Smalley R.E., J. Chem. Phys., 1986, **84**, 4074.

[12] Adams T.E., Rockney B.H., Morrison R.J.S. and Grant E.R., Rev. Sci. Instrum., 1981, **52**, 1469.

[13] Gentry, W.R. and Giese, C.F., Rev. Sci. Instrum., 1975, **46**, 104.

[14] Campargue R., Rev. Sci. Instrum., 1964, **35**, 111.

[15] Brucat P.J., Zheng L-S., Pettiette C.L., Yang S. and Smalley R.E., J. Chem. Phys., 1986, **84**, 3078.

[16] Wiley W.C. and M°Laren I.H., Rev. Sci. Instrum., 1955, **26**, 1150.

[17] Mamyrin B.A., Karataev V.I., Schmikk D.V. and Zagulin V.A., Sov. Phys. JETP, 1973, **37**, 45.

[18] Wiza, J.L., Nuc. Inst. & Methods, 1979, **162**, 587.

[19] Hellsing M., Karlsson L., Andren H-O. and Norden H., J. Phys. E: Sci. Instrum., 1985, **18**, 920.

[20] Adams T.E., Morrison R.J.S. and Grant E.R., Rev. Sci. Instrum., 1980, **51**, 141.

[21] Butler, A.M., *PhD. Thesis*, University of Edinburgh, 1989.

[22] Costrell L., IEEE Trans. Nuc. Sci., 1973, **20**, 557.

[23] Horelich D. and Larsen R.S., IEEE Spectrum, 1976, **13**, 50.

[24] Gandhi S.R. and Bernstein R.B, J. Chem. Phys., 1990, **93**, 4024.

[25] Savitzky A. and Golay M.J.E., Anal. Chem., 1964, **36**, 1627.

[26] Rhodes C.K. (Ed.) *Topics in Applied Physics*, Vol. 30, Springer Verlag, Berlin, 1979.

[27] *TE-861T-4 Excimer Laser Instruction Manual*, Lumonics Inc., Kanata, Canada, 1984.

[28] Lemire G.W., *Private Communication*

[29] Hollas J.M., *High Resolution Spectroscopy*, Butterworths, London, 1982.

[30] *JK HyperYAG Laser Instruction Manual*, Lumonics Ltd., Rugby, England, 1986.

[31] *Quanta-Ray Pulsed Dye Laser (PDL-2) Instruction Manual*, Mountain View, USA, 1984.

[32] Demtröder W., *Laser Spectroscopy: Basic Concepts and Instrumentation*, Springer Series in Chemical Physics 5, Springer Verlag, Berlin, 1984.

[33] *Lambda Physik FL3002EC Instruction Manual*, Lambda Physik, Göttingen, Germany, 1986.

[34] Hänsch T.W., Appl. Optics, 1972, **11**, 895.

Chapter 3

Experimental Techniques

3.1 Introduction

In the previous chapter (Chapter 2: Experimental Apparatus) all of the equipment required to perform the experiments described in Chapters 4 and 5 was described in some detail. In this chapter, the so called 'experimental cycle' will be described, followed by a detailed description of each of the key components in the experimental cycle.

3.2 The Experimental Cycle

The Q-switched output from the JK HY750 Nd^{3+}:YAG laser (30 mJ/pulse) was focussed (BK7 plano-convex pyrex 100 cm lens) onto the surface of the desired target material. This vaporisation laser pulse was timed to coincide with the maximum gas density of a pulse from the General Valve or Newport molecular beam valve. The resulting plasma, generated due to target absorption of the laser radiation, was quenched and entrained in the gas pulse. This seeded beam then passed into a high vacuum region, resulting in supersonic expansion and associated cooling of the beam species. After skimming, the beam entered the ionisation region of a time-of-flight mass spectrometer (TOFMS). Ionisation was achieved by the absorption of two or more photons from the Lumonics and/or Lambda Physik dye laser, depending upon the particular experiment. The resulting ions travelled

along the flight tube of the TOFMS to the microchannel plate detector. They were then amplified and passed to the PC-AT via the transient digitiser.

The above is a brief description of the experimental cycle. All experiments reported in this thesis were run at a repetition rate of 10 Hz. Any given cycle is easily broken down into a variety of discrete processes, and each of the following sections is dedicated solely to one of these processes.

3.3 Laser Vaporisation

The principal experimental barrier to examining clusters of refractory species in the gas phase was one of production. In the past, techniques such as sputtering, ligand stripping and high temperature ovens had been used, but these had all proved unsuitable as general sources. This problem was overcome by the introduction of the laser vaporisation technique. Since first reported, it has become a much used route to cluster production over the past decade [1].

When laser radiation is directed onto a desired target, some of the energy of that radiation is absorbed by the surface. The gas phase species produced depend heavily on the power density of the incident beam. Several distinct material removal processes have been identified [2]. Below 10^5 Wcm^{-2}, the main mechanism is the melting of the target surface, resulting in the ejection of liquid droplets. From 10^6 - 10^8 Wcm^{-2} material is removed mainly as a vapour, whilst powers greater than 10^9 Wcm^{-2} result in plasma formation. The least acceptable scenario for our purposes would be the production of liquid droplets. These species act as nucleation centres and efficiently prohibit cluster production [3]. Hence the use of high power, Q-switched radiation to produce the vapour phase species. However, this was not an ideal solution as only the initial portion of any pulse removed material from the target. The remainder of the pulse was absorbed by the vapour and quickly formed an opaque, super-heated plasma. This plasma was quenched by collisional cooling, as described in the next section. One other point of note is that if a target was interrogated for a period of time, the cluster signal was seen to

drop off. This was due to the creation of a deep hole and the subsequent inability of the species created to become entrained in the gas pulse. To overcome this, the target was continually moved such that a fresh area was exposed to the laser every second.

The physical alignment and choice of pulse energy for the vaporisation laser beam were optimised by observing the plasma itself along the molecular beam axis from the B chamber. When a good plasma was being formed, a distinct colour change took place from the green colour of the vaporisation beam to one which was related to an energy change within the plasma material itself.

A second means of optimisation was that of 'hole burning'. The vaporisation laser pulse was timed to coincide with the maximum gas density produced by the molecular beam valve. This resulted in a sharp reduction of beam gas intensity in this region of space/time due to the plasma 'blowing' the beam gas out of its path. Figure 3-1 clearly shows this sharp reduction on the plateau region of the He pulse profile. The width and depth of the dip could be crudely controlled by varying the energy of the laser pulse.

3.4 Cluster Formation

The high density of He present when the plasma was produced resulted in the so-called quenching of the plasma. This was essentially a two-body process, whereby the highly energetic target species were relaxed by energy transfer collisions with the highly abundant beam species [4]. The resulting seeded beam was of almost room temperature. Further three-body collisions, now between two metallic species and one gas species resulted in the process of metallic condensation or cluster production - the excess energy being removed as translational energy of the third body. The creation of these clusters is believed to proceed via a stepwise addition pathway [5];

$$M_n + M + X \rightarrow M_{n+1} + X \tag{3.1}$$

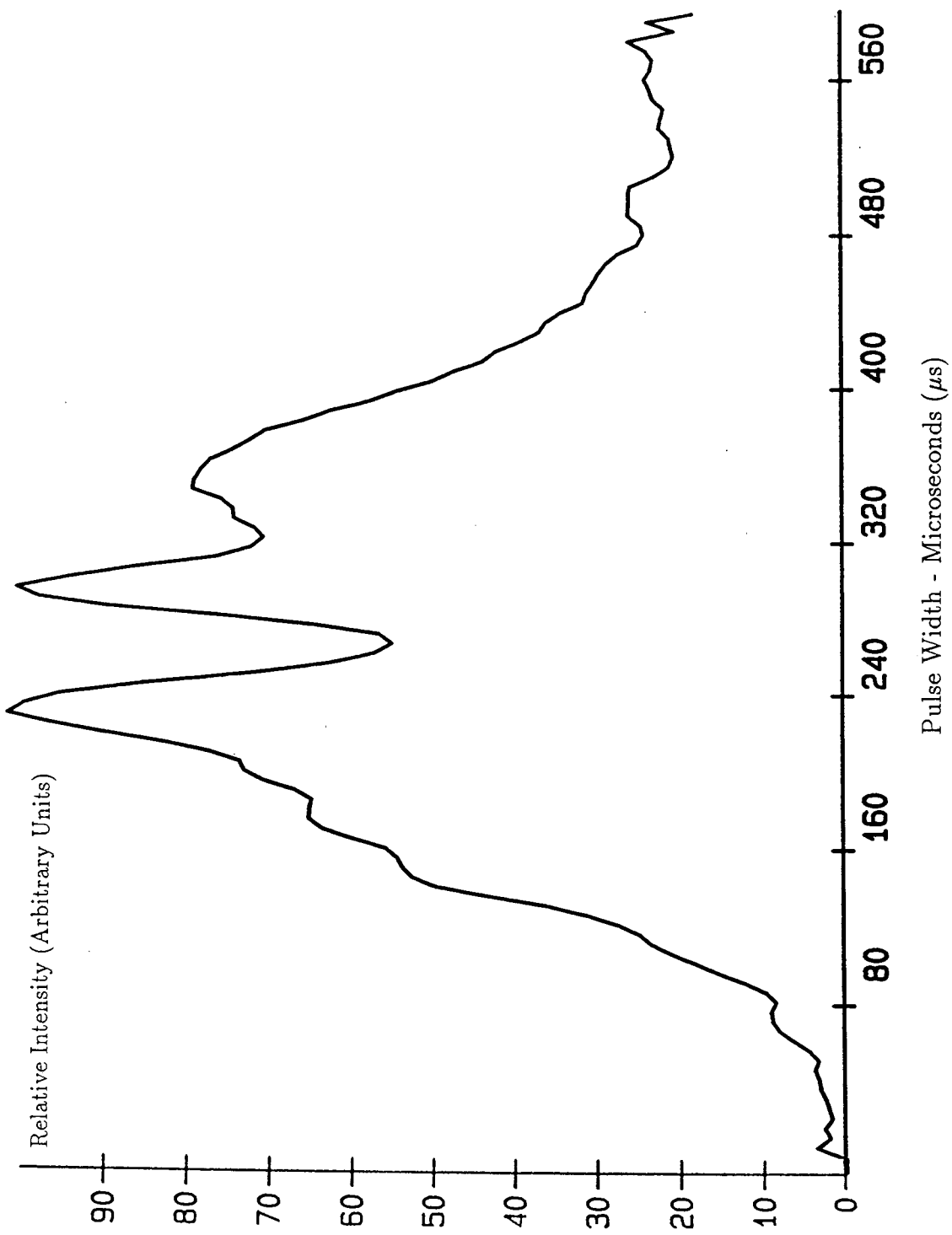

Figure 3–1: Helium pulse profile with 'hole-burning' on plateau.

To this end, it seemed logical that for the preparation of larger clusters, the retention time in the high pressure region should be maximised. To facilitate this, extension channels were routinely fixed to the front plate of the source. They were of a variety of lengths (15 - 40 mm) and bore diameters (0.5 - 1.0 mm). It was even possible to alter the internal geometry of the channel [6], in order to create funnels and so-called waiting rooms. Some of the mass spectra obtained using different target materials are shown in Figures 3-2 to 3-4.

Variation of the backing gas pressure could also be utillised to influence the size of clusters produced, a typical range being 2 - 10 atm. However, for the silver cluster work, 10 atm backing pressure and 40 mm extension channels were typically used.

3.5 Supersonic Expansion

When the seeded beam leaves the high density clustering region it enters a region of high vacuum. In the area surrounding this pressure interface, one of two processes can take place [7]. If the diameter of the orifice is smaller than the mean free path of the beam species, then the beam components on either side of the orifice have essentially the same bulk properties as, on average, no collisions have taken place in this region. However, if the diameter is much larger than the mean free path, many collisions can take place in this region. This results in a conversion of the energy of internal motion i.e. vibration and rotation, and that of random translation, into directed mass flow [8] [9]. The translational temperature of the carrier gas falls dramatically and the expansion is said to be supersonic [10]. This effect is shown in Figure 3-5, where the velocity distribution of the expanded gas has been substantially narrowed with respect to the reservoir gas from which it came.

It should be noted that the term supersonic, which is defined in terms of the Mach number, M, (the quotient of the flow velocity and the local speed of sound), arises mainly from the reduction of the local speed of sound rather than

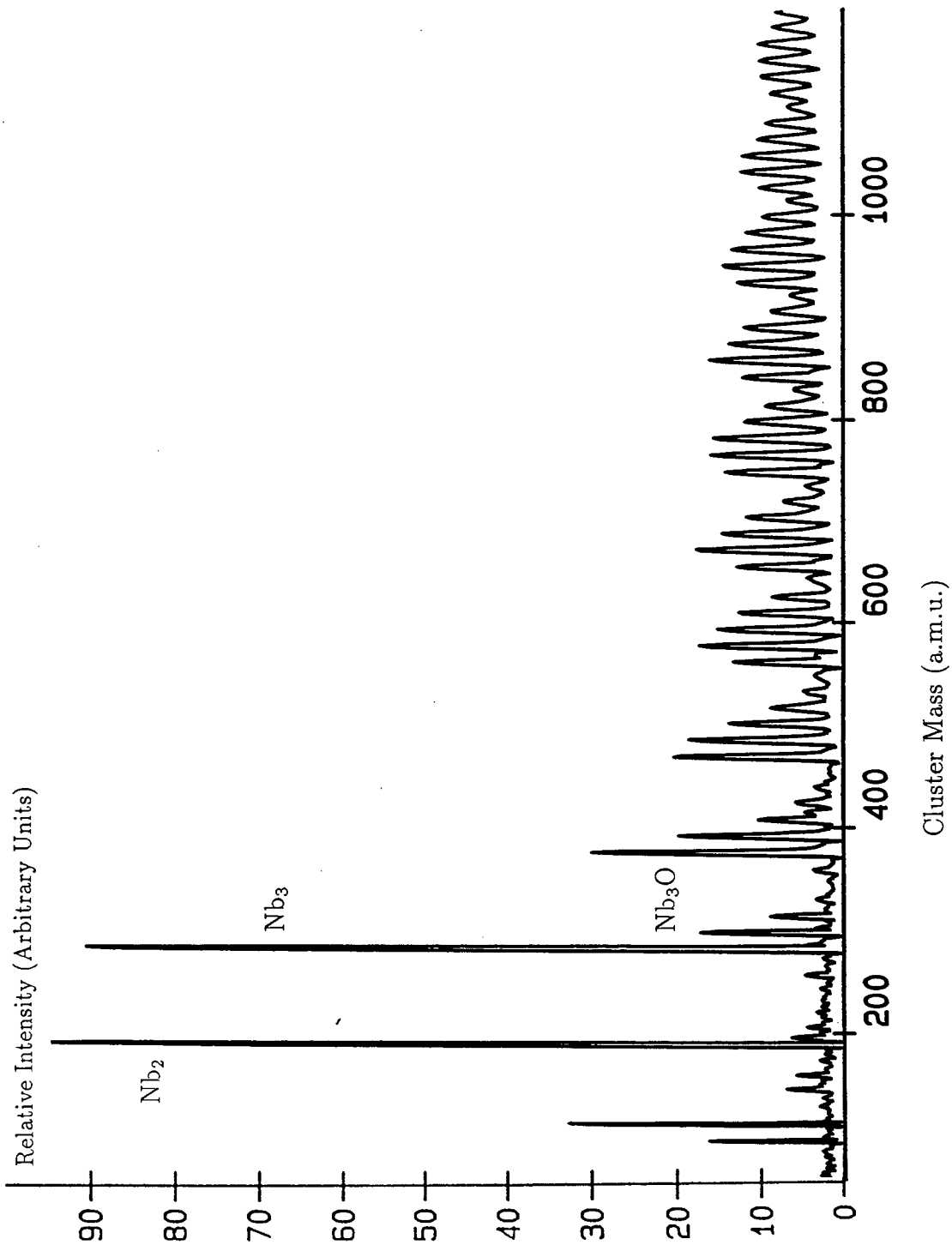

Figure 3–2: Mass spectrum of a Niobium target

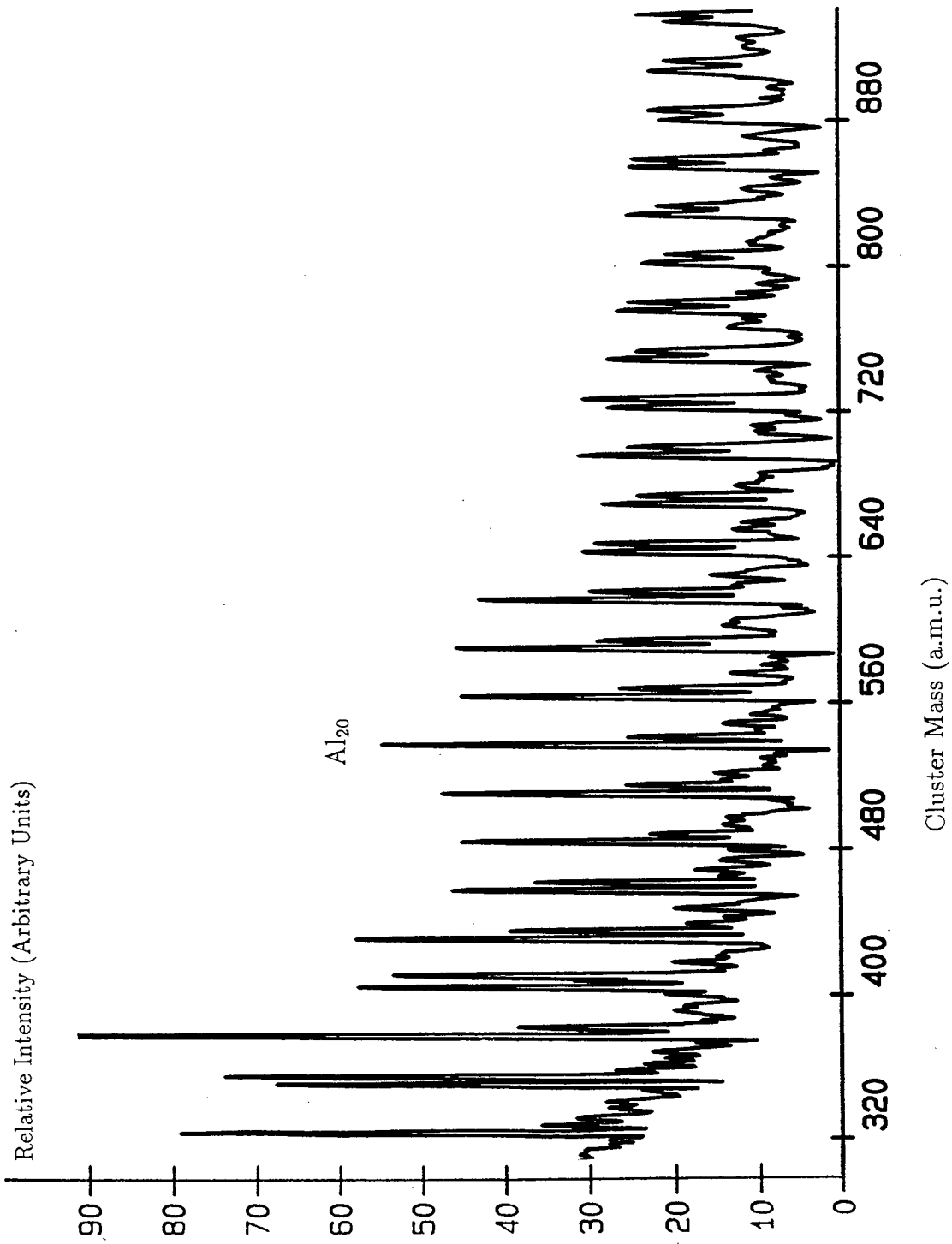

Figure 3–3: Mass spectrum of a Aluminium target

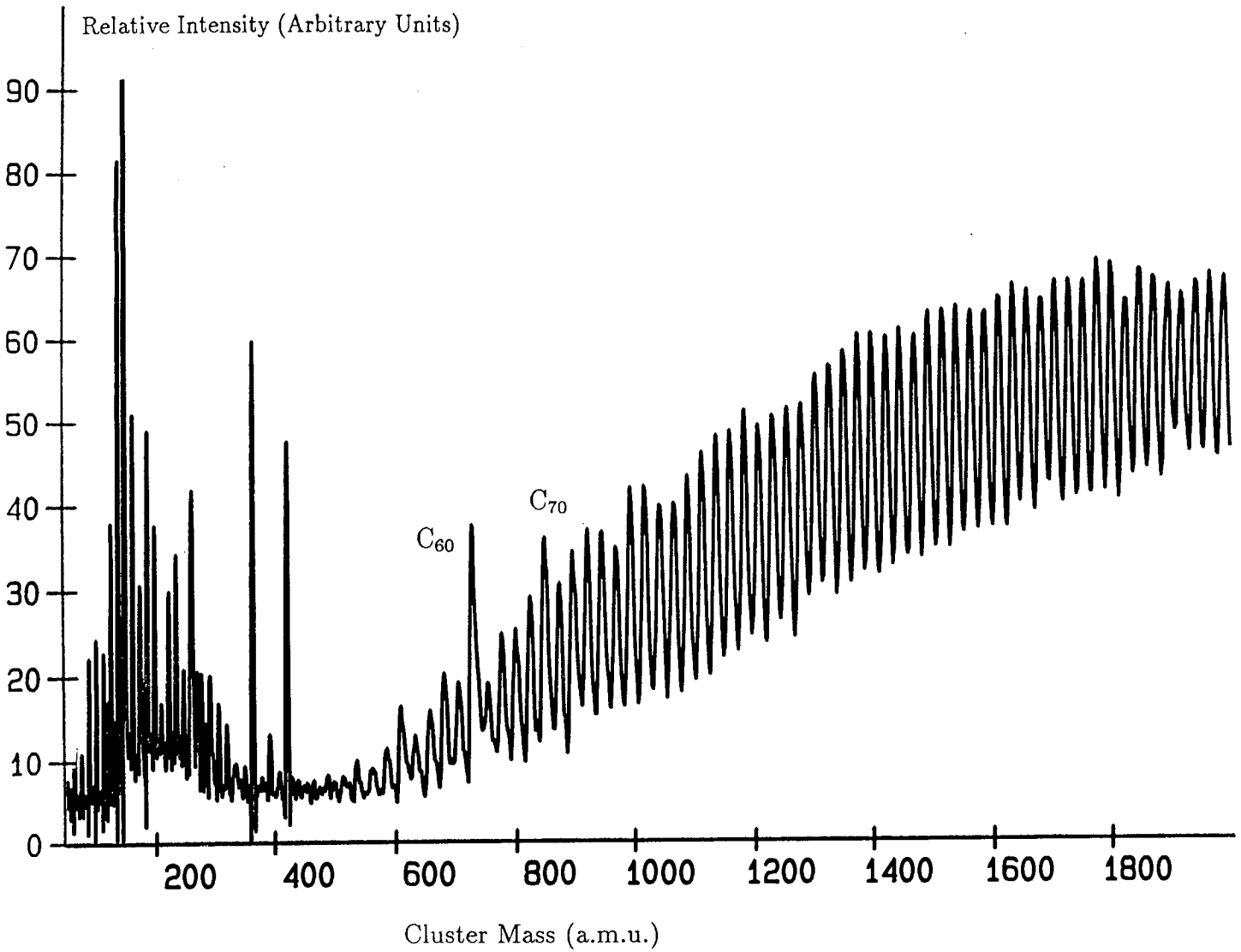

Figure 3–4: Mass spectrum of a Graphite target

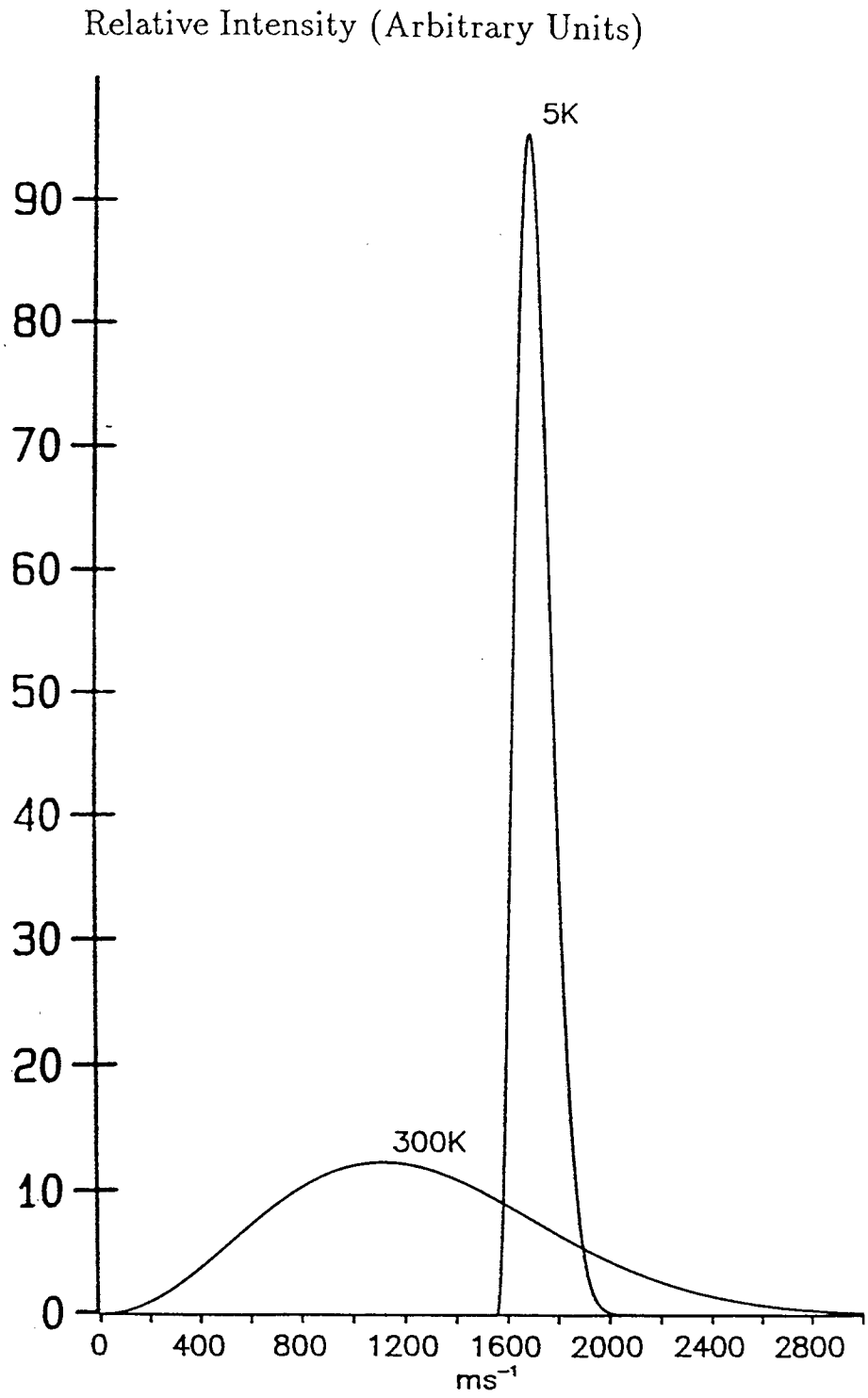

Figure 3–5: Velocity distributions for He at 5K and 300K

from an increase in the average beam velocity [11]. The metal clusters seeded in the carrier beam undergo a similar expansion, but do not attain the full beam velocity due to mass slippage. As the expansion proceeds, collisions with the He carrier gas continue until the density of the beam falls to the point such that no further collisions can take place. At this point the internal energy manifolds of the beam species are effectively frozen [12]. This is important as the translational, vibrational and rotational 'temperatures' do not fall at the same rate. These modes equilibrate depending upon the efficiency with which the energy can be transferred in rotational-translational, vibrational-translational and translational-translational collisions. As the rotational quanta are coupled more closely to the translational temperature than are the vibrational quanta, a typical range of temperatures would be;

$$\begin{aligned} T_{trans} &= 1 \rightarrow 20 \text{ K} \\ T_{vib} &= 10 \rightarrow 100 \text{ K} \\ T_{rot} &= 2 \rightarrow 50 \text{ K} \end{aligned}$$

Thus it is possible to produce a source of low temperature, isolated cluster species. This is an ideal sample for spectroscopic studies, as any signals should be free from collisional perturbations, and the resulting spectra should not be over-congested, as only the lowest quantum states will be populated. In all of the experiments described in this thesis, helium was used as the expansion gas. Although lower temperatures can be achieved by the use of heavier expansion species, e.g. Ar, these are more polarisable and have a greater tendancy to self-cluster or 'snowball'. Hence to avoid such van der Waals clusters, helium was always used.

3.6 Laser Photoionisation

The molecular beam now consistsed of cold, isolated clusters of various sizes [28]. However, they were still electrically neutral, carrying no overall charge. In order to analyse them in a mass spectrometer, they had to become charged species. This was easily accomplished by photoionisation [14] from one of the laser sources, described later. Ionisation is defined as the process by which an electron is given enough energy to remove it from its localised orbit to an infinite distance from the nucleus [15]. In terms of photons, this energy is available in quanta which are related to the wavelength of the radiation [16]. Hence for ionisation to take place, the energy of the absorbed photon must exceed the required energy of ionisation. This is shown in Figure 3-6 (a). In the case of Ag_2, for example, the ionisation potential is of the order of 7.5 eV, which is equivalent to approximately 60000 cm^{-1}, and so single-photon ionisation can take place for radiation of wavelength less than 165 nm. Although it is possible to generate laser radiation in this wavelength region via a variety of non-linear optical schemes, broadly tunable sources are not routinely available.

Fortunately, photoionisation is not restricted to single photon absorption [17]. In general, ionisation can be achieved by the simultaneous absorption of any number of photons such that the sum of their energies is in excess of the ionisation potential [18] [19]. However, as the number of photons increases, so does the required photon density to sustain such processes, following the equation

$$W_n = \sigma_n I^n \tag{3.2}$$

where;

W_n= rate of n-photon process,

σ_n = cross section for n-photon process ($cm^{2n}s^{n-1}$),

I = instantaneous photon flux (photons $cm^{-2}s^{-1}$) and

n = order of the process.

Typical cross-section values are 10^{-17} cm^2 and 10^{-50} cm^{4}s for one- and two-photon ionisation [20]. Pulsed laser sources are capable of supplying photon densities in the region of 10^{28} photons cm^{-2}s^{-1}, and so both processes should be available, with those of higher order being less likely.

There are a large number of possible multi-photon processes, and to review all of them would be time consuming and unnecessary [21]. Therefore, only some of those processes involving two-photon absorption will be considered further. Those of direct relevance to this work are shown in Figure 3-6 (b)-(d).

Two-photon absorption occurs, of necessity, via an intermediate level or state. The relative energetics and nature of this state have important ramifications for the ionisation process concerned. When the intermediate level lies more than halfway to the ionisation limit, then the second photon can come from the same source. A common example of this is the routine ionisation by the ArF excimer. If the intermediate level lies less than halfway to ionisation, then the second photon must come from a separate source. The spectroscopic studies of the A $\leftarrow$ X electronic transition in Ag_2 described in this thesis involved the use of this type of excitation scheme. Another important factor is in the nature of the intermediate level. When this level is a real state of the species under investigation, the lifetime of the level is greatly enhanced. This in turn increases the probability of ionisation taking place, and the process undergoes a resonance enhancement, leading to increased photoion production, whenever this first excitation step is resonant with an allowed transition between the initial and intermediate step. Hence by monitoring the photoion yield as a function of laser wavelength, the rovibronic structure of the transition between these two states can be obtained. This resonantly enhanced two-photon ionisation (R2PI) scheme was employed for all the spectroscopic studies of Ag_2 described in Chapter 4.

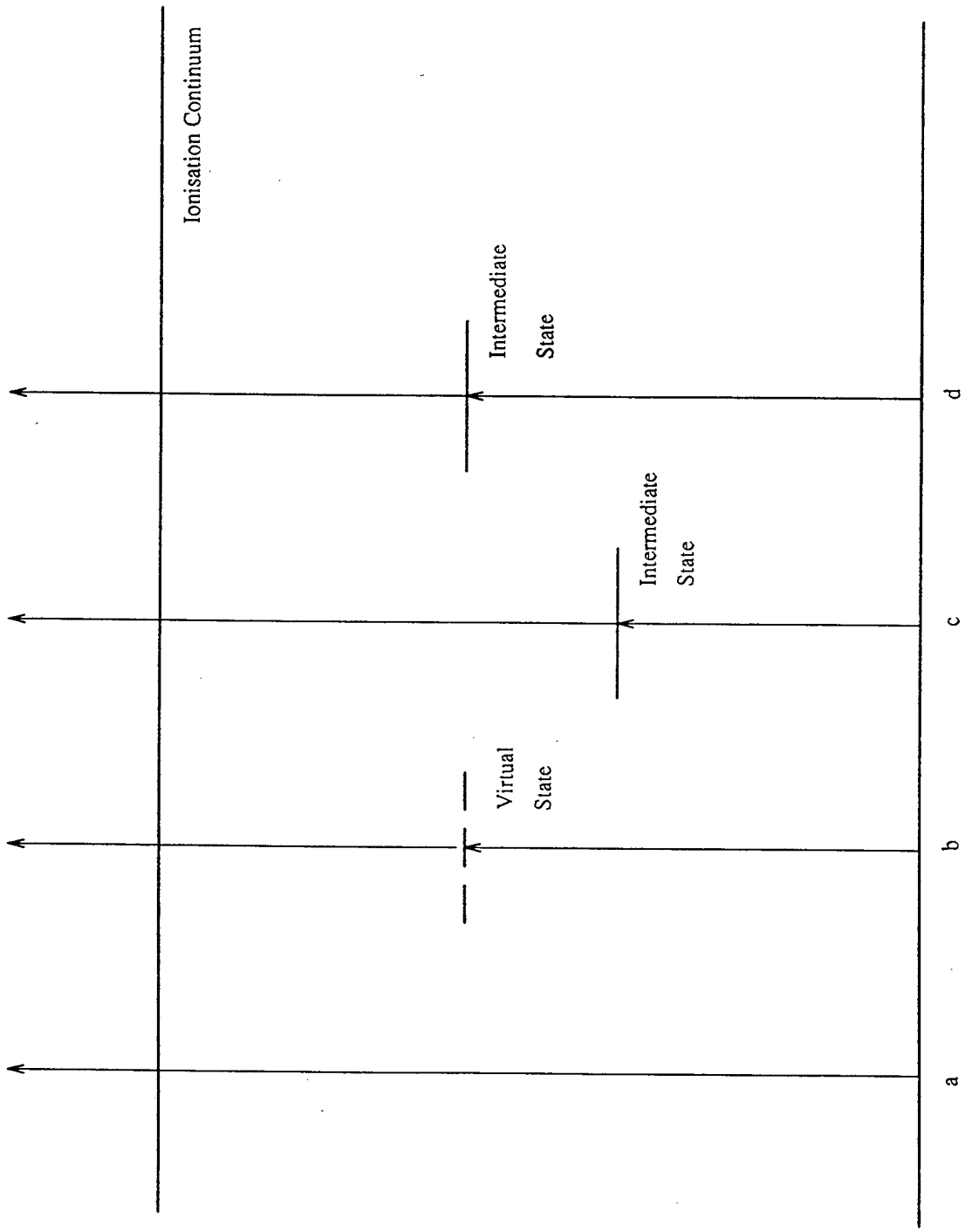

Figure 3–6: Photoionisation schemes

3.7 Time-of-Flight Mass Spectrometry (TOF-MS)

The operating principle behind mass spectrometry is very simple indeed; in a distribution of chemical species, each is likely to have a unique molecular mass. Hence separation by mass allows the contents of any such sample to be fully analysed [22]. Just how, and to what extent, this separation is achieved is very much technique dependent. Although an in depth discussion of all mass spectrometry techniques will not be presented here, some areas where these compare and contrast with time-of-flight mass spectrometry will be discussed.

Consider the system shown in Figure 3-7. If we assume that all ions are formed in region s, they will feel the effect of the potential field E_s. As the energy obtained by each species is dependent on charge and not mass, all species enter the field free region, D, with the same energy. Using Newton's equations of motion, it is easily shown that the time taken to reach the detector is proportional to $m^{1/2}$. Thus as mass increases, the adjacent peaks arrive with smaller and smaller time differences between them. In this ideal system, with infinitely narrow peaks and infinitely short response times from the detection electronics, the system has effectively an infinite resolution. However, it is the deviations from this idealised system that result in the loss of resolution. The main sources of this loss of ideality can be summarised very simply; all ions are not formed at the same point in space and time, and they will not all possess equal values of initial kinetic energy. These departures from ideality can be investigated by considering a few simple examples [23].

3.7.1 Spatial Resolution.

Consider the situation shown in Figure 3-7 (a). If two ions of identical mass/charge ratio and zero kinetic energy are formed at different distances from the field free region, these species will now extract differing amounts of energy from the static

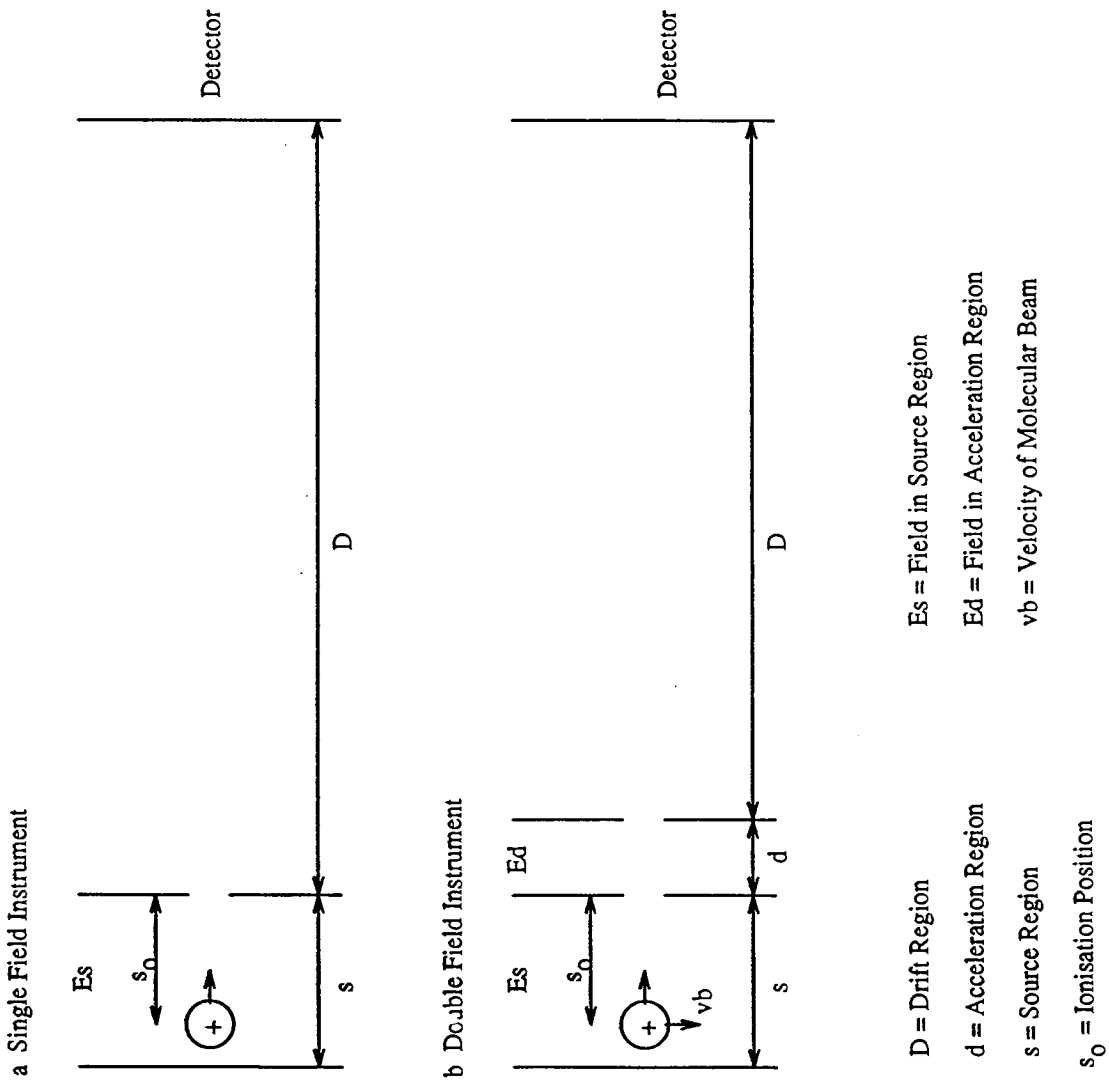

Figure 3–7: Source regions of simple time-of-flight mass spectrometers

field and hence will travel with different final velocities. Ion A will enter the drift region first, but will travel slower, while ion B will move faster, but emerge later. At some point in the drift region, these species will catch up with each other. For maximum resolution, any detector has to be situated at this point. It can be shown that for this single field type instrument, the point at which this occurs is a function of the geometry of the system. That is to say, if the position of ionisation changes, then the point of focus will also change. In fact, it can be shown that this focus length is equal to twice the value of s_0. This results in flight times that are far too short to allow the packets of differing masses to resolve themselves in space. While the problem of differing positions of ionisation can be reduced by using a slit iris, the lack of resolution is still an inhibiting factor for most applications.

3.7.2 Energy Resolution

Consider the same two ions A and B which are now formed at the same place and time but now have a velocity component parallel to the spectrometer axis. If these ions have equal but opposite velocities, then they will arrive at any given point in the drift region separated by the so called turn-around time. Although this time can be reduced by increasing the potential field, this results in longer drift region requirements to ensure adequate peak resolution. The application of molecular beams as a source for time-of-flight mass spectrometry has helped reduce this energy broadening, as the skimmed beam that is interrogated by the laser will contain only those species with the smallest off-axis velocities.

3.7.3 Time Resolution

Consider ions A and B formed at the same place with identical mass/charge ratio and velocity components. Whatever means is used to create these ions, the event will correspond to a finite time. Thus we can consider the case where one ion is formed at the beginning of the source pulse, and the other formed at its end. Clearly these two ions will again arrive at any given detection point separated by a time delay proportional to the difference in original ion formation time. This

proved an important limiting factor in early time-of-flight mass spectrometers; obtaining a short pulse from an electron gun was non-trivial. Indeed, it was not until the advent of laser ionisation that very short (10 ns) pulses were achieved, and this problem could be substantially eliminated.

3.7.4 Wiley and McLaren "Linear" TOFMS

In a detailed analysis of the problems mentioned above, Wiley and McLaren provided mathematical solutions for improving the resolution of a spectrometer [24]. They did this, in the main, by introducing a second accelerating region and creating the so-called double field mass spectrometer, as shown in Figure 3.7 (b). It can be shown quite simply that the spatial focussing condition now relies on the ratio of the accelerating fields E_d/E_s. This has two important results. Firstly, this condition is no longer a simple geometric one. Should the point of ionisation change, then the ratio of these fields can be altered slightly to bring the ions A and B back into coincidence at the detector. Secondly, and perhaps more importantly, the resolving power of the instrument is increased substantially, as the flight times of the ions themselves are increased. This improved resolution is illustrated in Figures 3-8 and 3-9. Here, the different isotopomers in the mass spectra of Ag_2 and Ag_3 can clearly be identified in their predicted isotopic ratios ($^{107}Ag_2$: $^{107}Ag^{109}Ag$: $^{109}Ag_2$ at 1 : 2 : 1 and $^{107}Ag_3$: $^{107}Ag_2{}^{109}Ag$: $^{107}Ag^{109}Ag_2$: $^{109}Ag_3$ at 1 : 3 : 3 : 1 respectively). This degree of mass resolution proved vital for the interpretation of the electronic spectra described in the following chapter.

Wiley and McLaren also discussed another mechanism for improving the energy resolution of the system. This involved introducing a time lag between ionisation and the onset of application of the extraction voltages. This method was not used as it involved a trade off between spatial and energy resolution. However, this problem was reduced by arranging the two fields such that the first field accounted for a smaller portion of the overall energy than the second. Thus the difference in total energies of two ions formed at different positions in the source region was reduced.

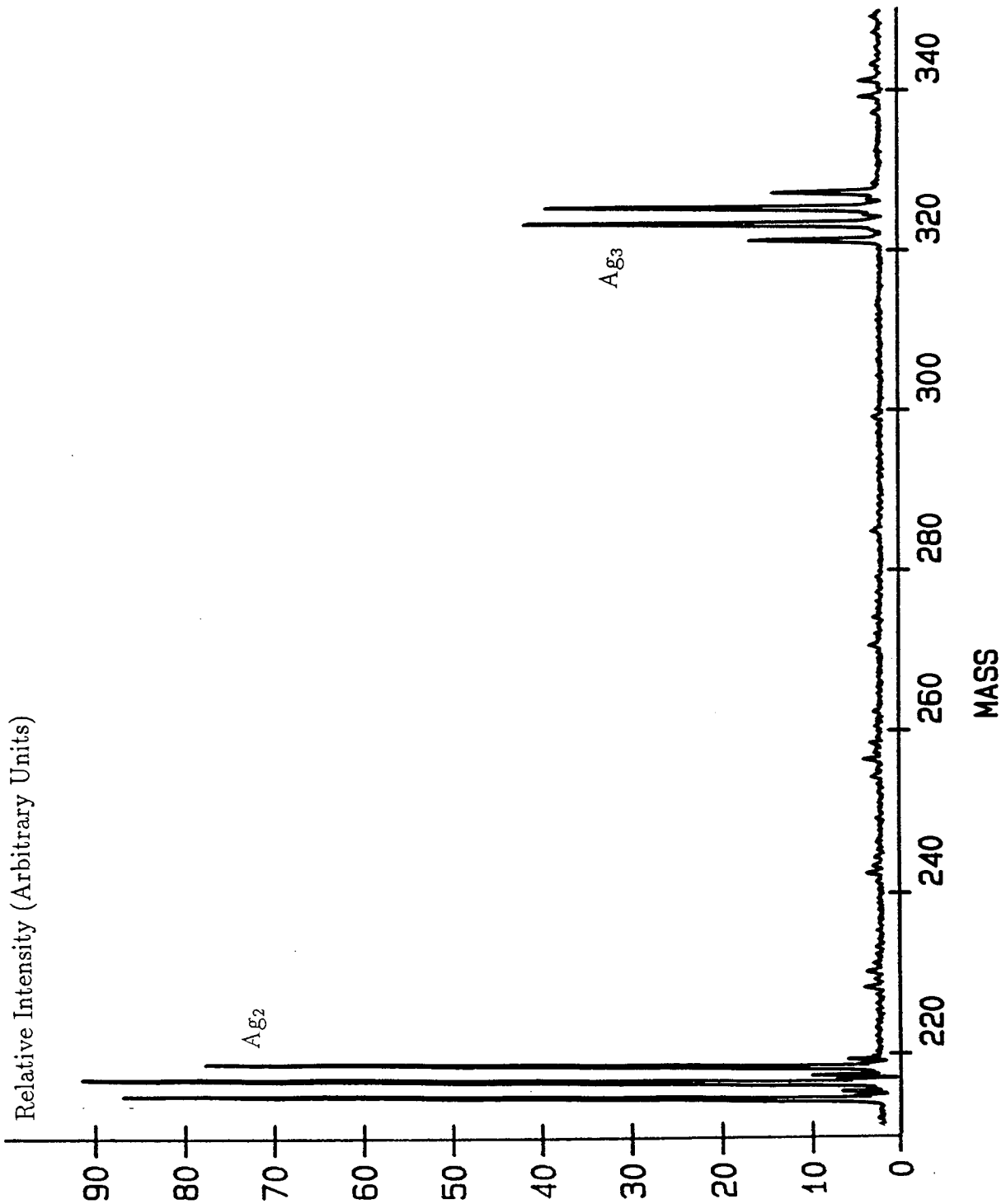

Figure 3–8: Time-of flight mass spectrum of Ag_2 and Ag_3

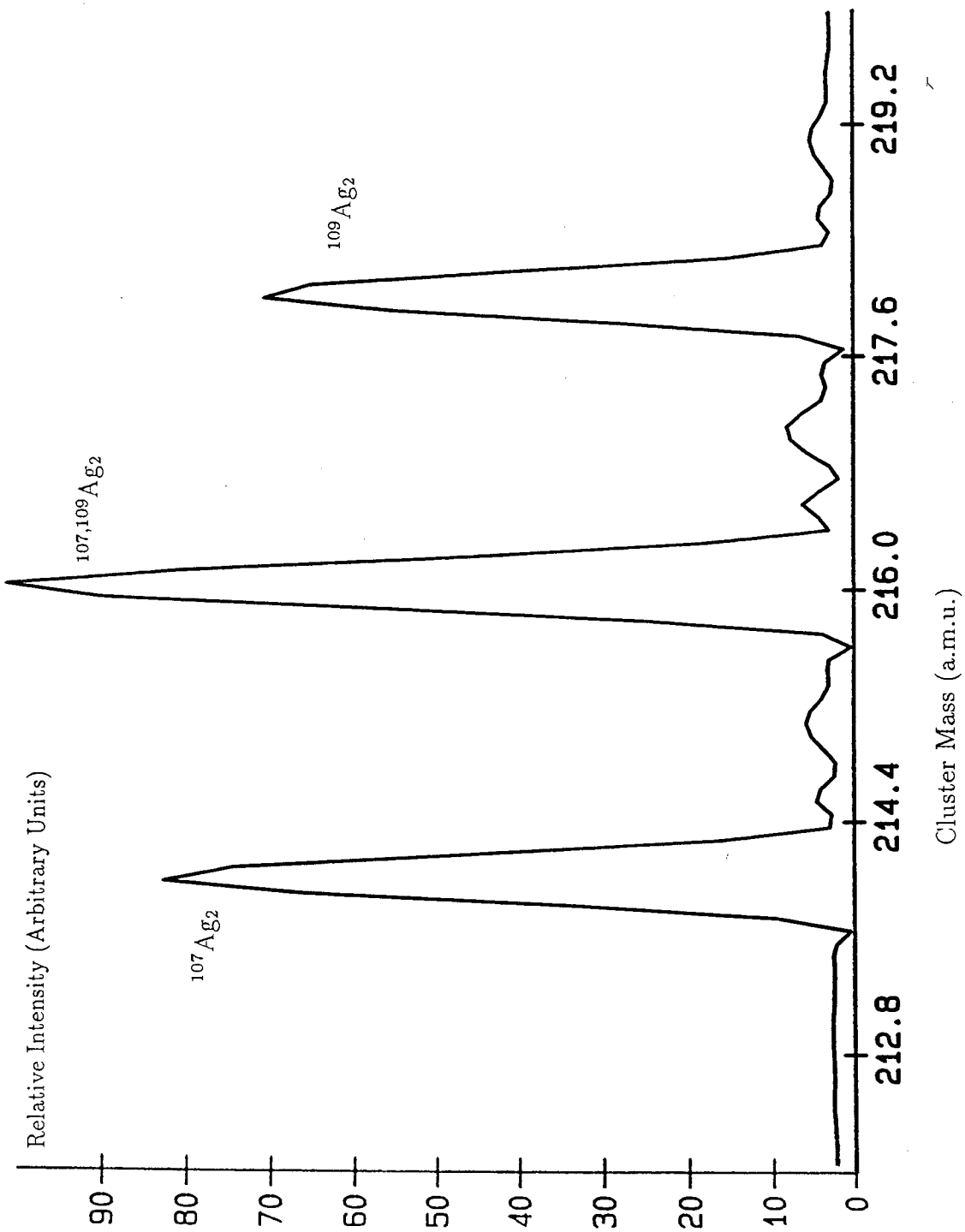

Figure 3–9: Time-of-flight mass spectrum of Ag_2 at high resolution showing resolved isotopomers.

3.7.5 Mamyrin "Reflectron" TOFMS

A further improvement in instrument design was introduced by Mamyrin and coworkers [25] [26]. This involved the addition of another set of potential fields where the detector would have originally been placed on a conventional, linear TOFMS. After passing the spatial focus point, two ions, A and B, of the same nominal mass/charge ratio, but created at two different positions in the source region, will begin to move apart in space - as they have different kinetic energies. If, however, they enter an area of increasing potential gradient, the ion with the greater energy will penetrate the field further than the less energetic species. By careful selection of these fields, this difference in flight times can be used to refocus the ions at the detector, which is now placed at the end of the second flight tube. The importance of this extra stage is that while the ion packets arrive in a spatially focussed manner, their total flight times have been greatly increased. Thus the time between successive ion packets is increased, leading to a marked increase in resolution. While the initial geometry of such instruments resulted in a V-shaped ion trajectory, a further improvement was realised in the form of a linear reflectron [27], such that the ions were now detected behind the source region. This allowed a reduction of size in such instruments while retaining their high sensitivity [28].

3.7.6 Space Charge and Detector Effects.

It has been calculated that space charge effects in the ionisation region begin to have an effect on the constituent ions at a density of around 10^6 - 10^7 ions cm^{-3}. In a typical experiment on MB1 or MB2, the densities were no higher than 10^3 cm^{-3}. Thus there was little broadening due to this mechanism.

In terms of detectors, any electrical circuit will have a finite response time to an incoming signal. Microchannel plate detectors have been shown to possess sub-nanosecond risetimes, and have thus found much use in this field [29]. While it is known that transfer and analysis can introduce broadening and corruption of data, these mechanisms are not believed to play a significant role in this work.

3.8 Mass and Frequency Spectra

Using the above experimental techniques, many experiments were performed using a variety of source combinations. While Chapters 4 and 5 of this thesis describe the spectroscopic studies carried out on the Ag_2 molecule, some of the mass spectra and preliminary electronic spectra obtained for a variety of other species are summarised here. Figures 3-10 - 3-21 show some of these mass and frequency spectra, obtained using either the disc or rod source. A rigorous comparison of the mass spectra recorded using the disc source versus the rod source would have been most instructive. Unfortunately, it has been possible to obtain only a few selected species in powder form for fabrication into discs. The performance of the disc source is therefore something that requires further characterisation in any future work. Of those species where direct comparison can be made, perhaps the work on silver is again the most instructive. Not only were similar mass spectra achieved, but a full rovibronic R2PI spectrum for the A $\leftarrow$ X transition of Ag_2 was recorded. This is shown in Figure 3-10, and demonstrated the durability of the metallic disc and the stability of the disc source - a typical full rovibronic experiment taking in the order of twelve hours to complete. Clearly, the disc source was capable of producing the required quality of spectra with single metal systems.

However, as stated earlier, the principal reason for the development of the disc source was to allow investigation of, erstwhile unavailable, mixed species, and in particular mixed metal systems, where the bulk phase alloy may prove to be of some interest.

The species NiCu has been investigated in the bulk phase [30] and in the gas phase [31]. The latter study involved an experimental set up very similar to that employed in the present work. A 1:1 molar ratio disc was prepared as described earlier, and the resulting mass spectrum obtained is shown in Figure 3-11. Clearly the mixed species is present.

From the previous gas phase R2PI spectroscopic study by Fu and Morse [31], it was immediately possible to scan the region containing the known E $\leftarrow$ X and F

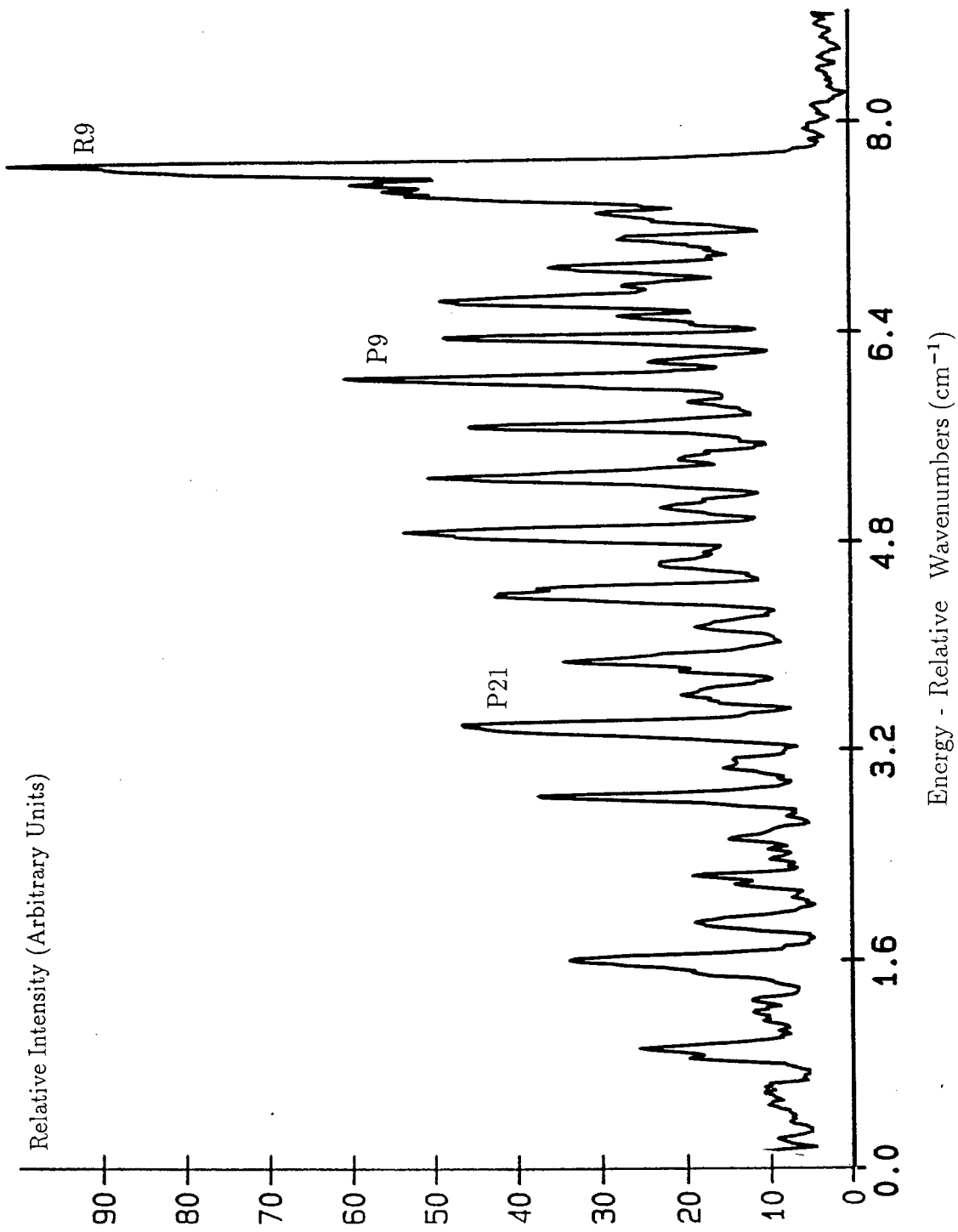

Figure 3–10: Frequency Spectrum of $^{107}Ag_2$ A←X (0-0)

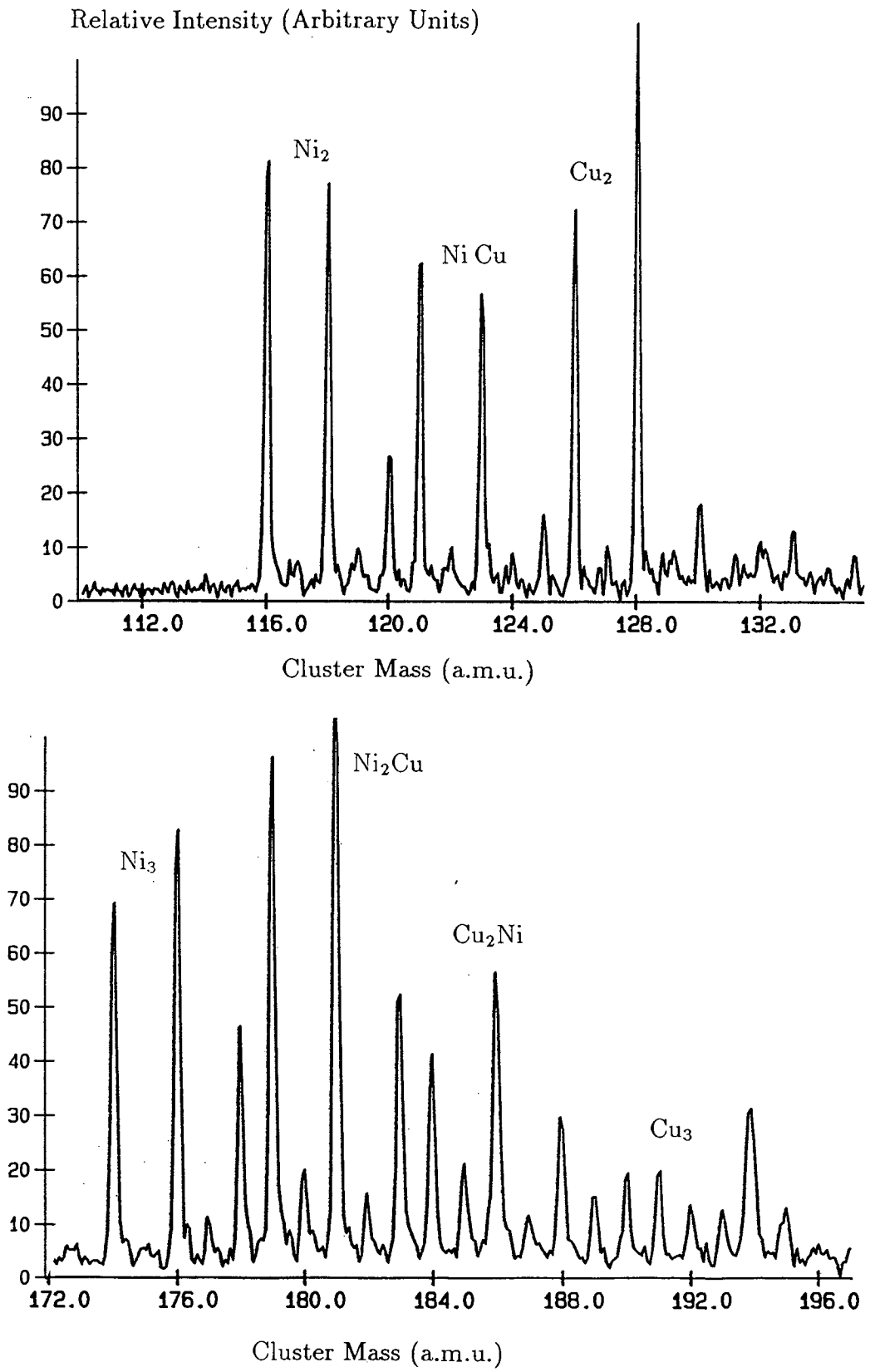

Figure 3–11: Mass Spectrum of a 1:1 Ni:Cu Disc

$\leftarrow$ X electronic transitions. This was carried out using an R2PI excitation scheme similar to that employed for the work on Ag_2, with the dye laser using LDS 698 dye in the 707 nm - 720 nm region. The resulting spectrum is shown in Figure 3-12.

The absolute wavelength calibration of this spectrum could not be evaluated, as no optogalvanic lines were recorded simultaneously. However, the fact that these features had been reported previously allowed facile determination. A more detailed description of spectral calibration is given in Chapter 4.

The periodic table derives much of its value from the great predictive powers of its structure. Consider the following. Table 3.1 shows some spectroscopic data for the Cr_2, Mo_2 and CrMo systems [32] [33], as well as data from Ni_2, NiCu [31], Cu_2 [34], CuAg [35] and Ag_2 [34].

It is clear that the electronic transitions for the mixed species lie close to the arithmetic mean, or at least between, the values for the corresponding homonuclear dimers. Clearly then, there were strong grounds for assuming that the transitions in the mixed species NiAg could be predicted to a close degree using the existing knowledge on the Ni_2, Ag_2, Cu_2 and NiCu systems. While the species NiAg had been the subject of one bulk phase study [30], there has been no work reported on this molecule in the gas phase. Figure 3-13 shows the mass spectrum obtained for NiAg using the disc source and a 1:1 molar target fabricated from Ni and Ag powders.

The mass spectrum shows both atomic peaks and the mixed species in the appropriate ratio. This species was then investigated in the 610 - 765 nm region, a not dissimilar area to that of the previous gas phase study. Although mostly barren, Figure 3.14 shows some of the weak structure that was recorded for this species.

This structure is real and reproducible. The spacing between neighbouring features is of the order of 70 cm^{-1}. If, as with the NiCu species, these represent two feathered progressions, then the vibrational constant has nearly twice this value. Although this would represent a fall of some 60 cm^{-1} from NiCu to NiAg,

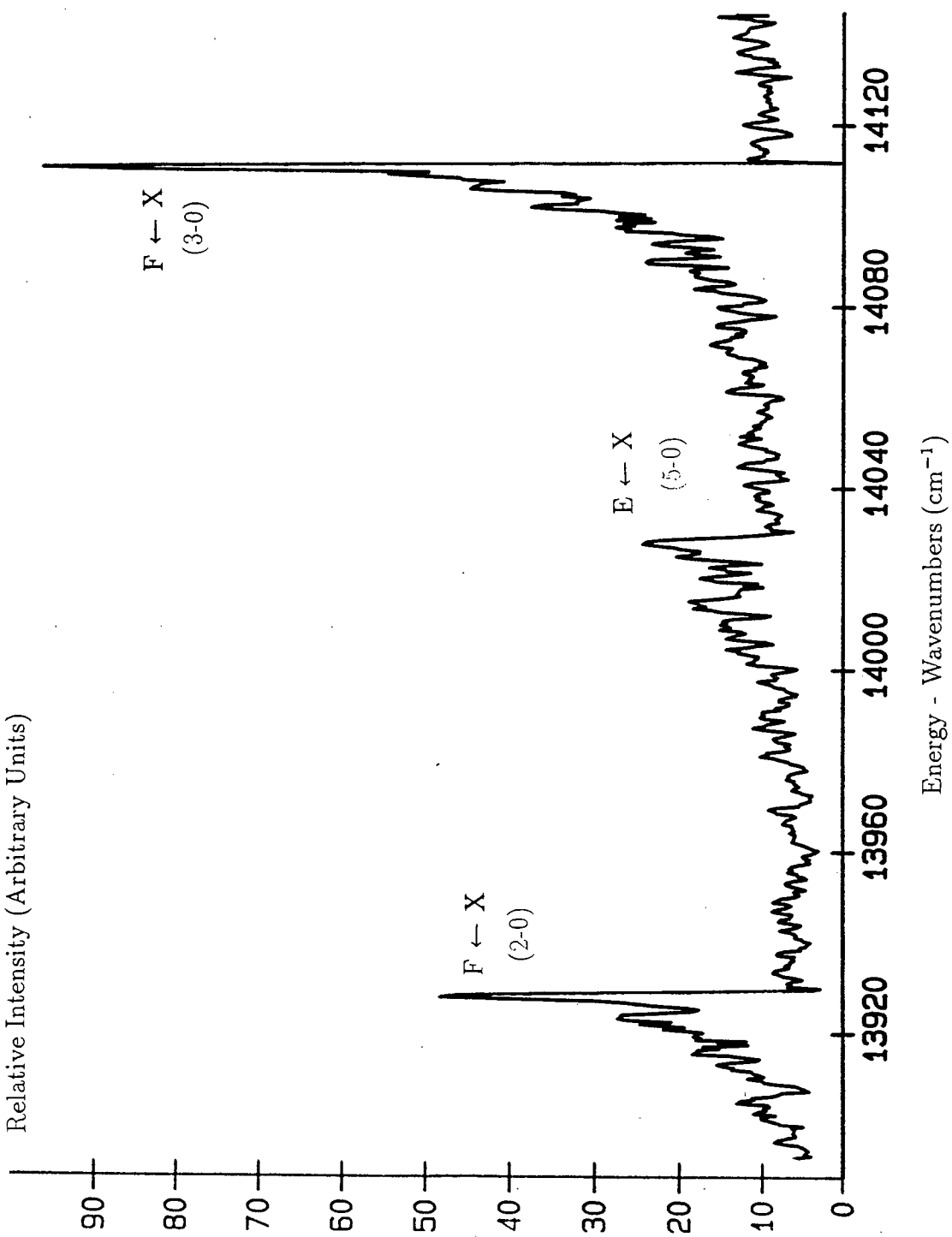

Figure 3–12: Frequency Spectrum of $^{58}Ni^{63}Cu$ Disc

Table 3–1: Some Spectroscopic Details of Mixed Metal Dimers

Species	Transition	ν_{00} (cm^{-1})	ω''_e (cm^{-1})	B''_e (cm^{-1})	r''_e (Å)
Cr_2	$A\ ^1\Sigma^+ \leftarrow X\ ^1\Sigma^+$	21751.4	452.34[a]	0.2303	1.6788
CrMo	$A\ ^1\Sigma^+ \leftarrow X\ ^1\Sigma^+$	20526.8	-	0.1503	1.8182
Mo_2	$A\ ^1\Sigma^+ \leftarrow X\ ^1\Sigma^+$	19303.7	477.10	0.0916	1.938
Cu_2	$A\ ^1\Sigma_u^+ \leftarrow X\ ^1\Sigma_g^+$	20433.2	266.43	0.1087	2.2197
CuAg	$A\ 0^+ \leftarrow X\ ^1\Sigma^+$	20807.2	229.17[a]	0.07556[b]	2.3732[c]
Ag_2	$A\ 0_u^+ \leftarrow X\ ^1\Sigma_g^+$	22996.4	192.4	0.05121	2.480
Ni_2	$A\ \Omega' = 5 \leftarrow X\ \Omega'' = 4$	11427.3	380.9	0.1203[b]	2.200[c]
NiCu	$A \leftarrow X\ ^2\Delta_{5/2}$	11485.5	273.01	0.112	2.2330
Cu_2	$A\ ^1\Sigma_u^+ \leftarrow X\ ^1\Sigma_g^+$	20433.2	266.43	0.10874	2.2197

(a) Values are $\Delta G''_{1/2}$

(b) Values are B''_0

(c) Values are r''_0

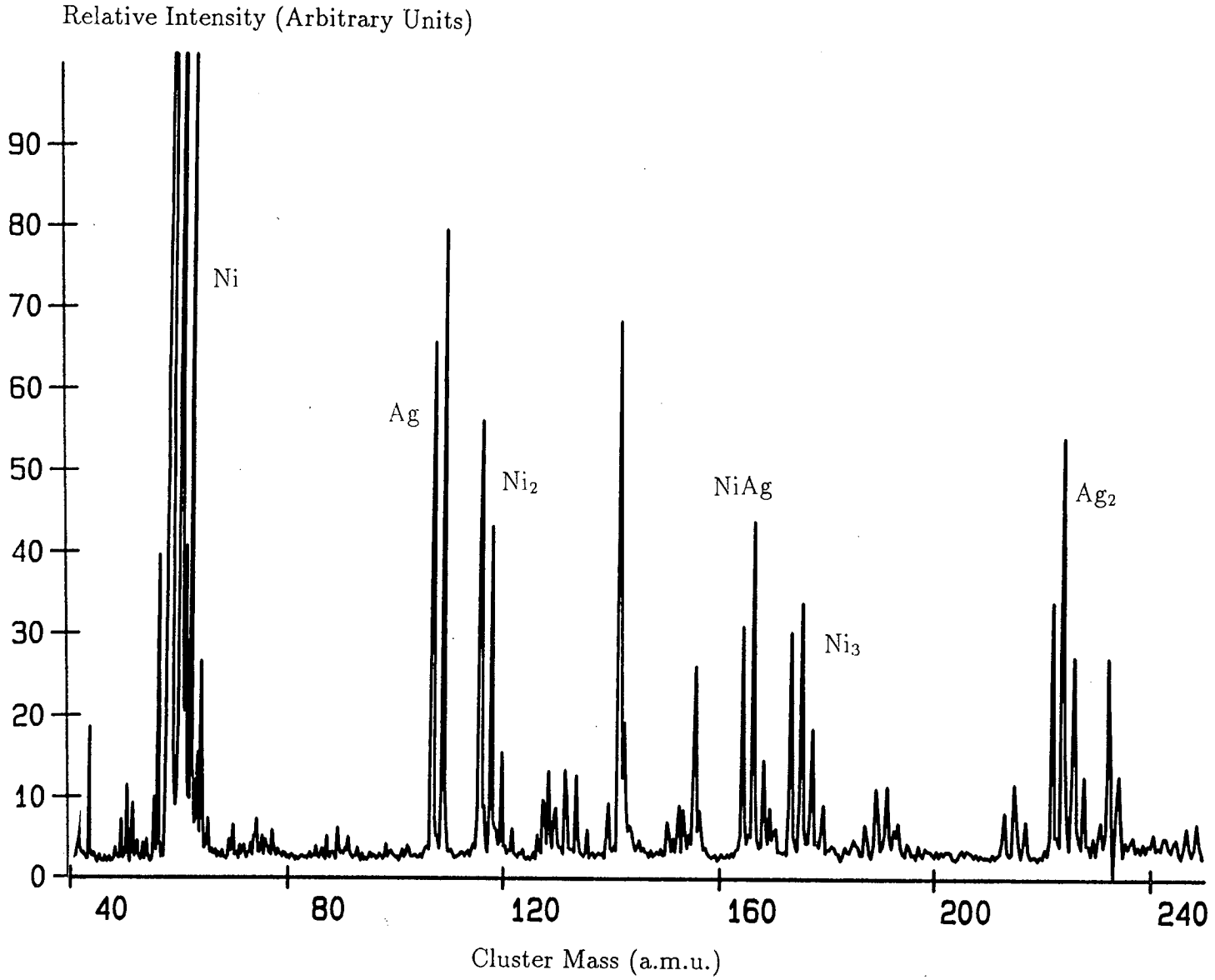

Figure 3–13: Mass spectrum of the NiAg species

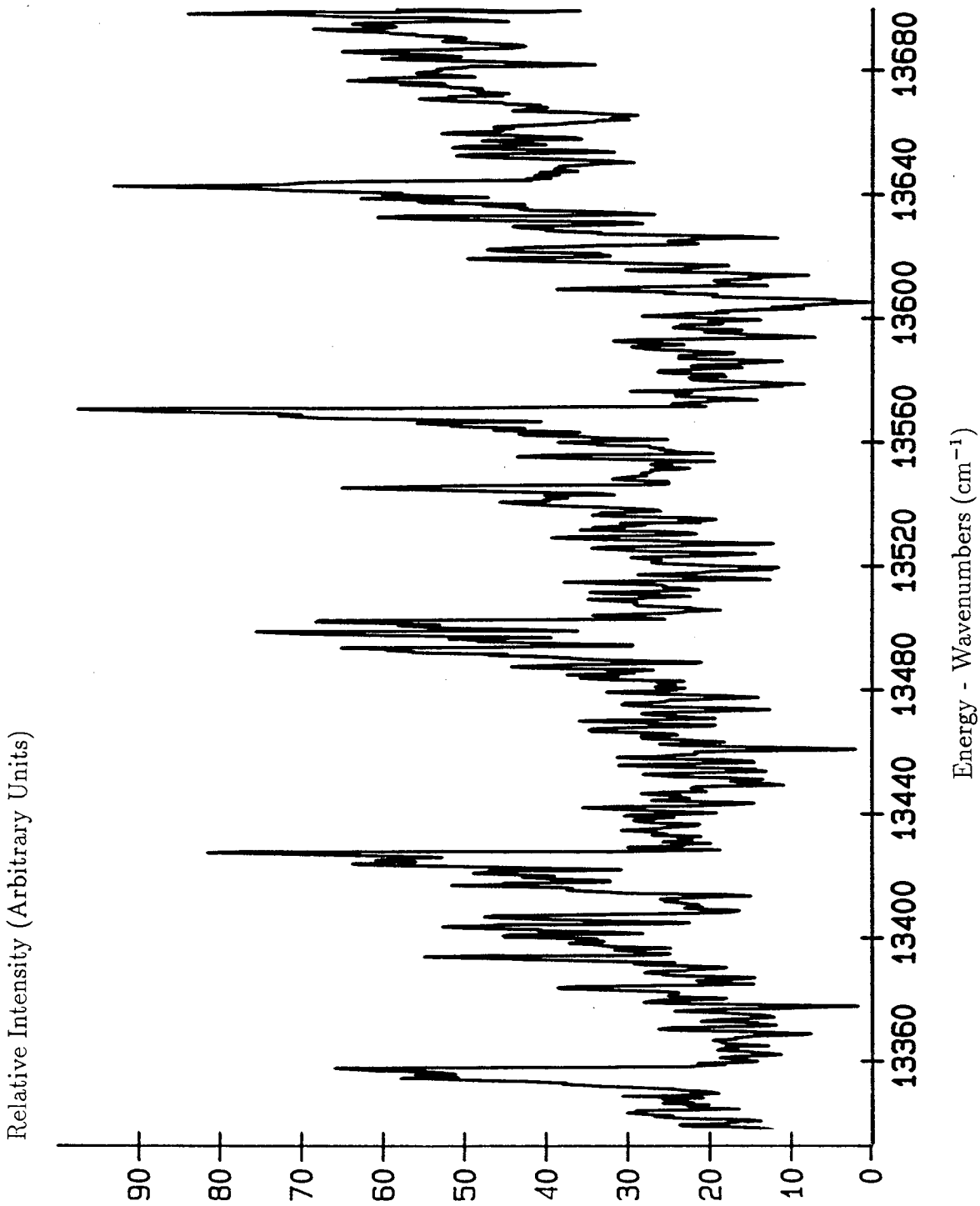

Figure 3–14: Vibronic scan of the $^{58}Ni^{107}Ag$ species

one explanation could be that the 4d orbitals on Ag play less part in bonding than the 3d on copper. This is due to their reduction in relative size, Hence, any resulting molecular bond is weaker in the heavier species, with weaker bonds being characterised by smaller vibrational constants. As to why much of the scanned region contained no spectral information is unclear, and should form the basis for a future, and more comprehensive, study of this species.

Several novel combinations involving aluminium were also studied in the course of this work. Figures 3.15 - 3.17 show mass spectra of AlNi, AlAg and AlCu respectively.

Again, all appear to be present in the ratios expected from isotope considerations. Of these species, AgAl does not appear to have been studied previously - neither as a bulk alloy, a molecular system or even given a theoretical treatment. The AlNi alloy has been previously reported [36], while the CuAl has been studied as a molecular alloy [37] [38] and has undergone theoretical calculations [39] [40]. Table 3.2 shows the ranges covered in these experiments. One of the weak transitions recorded from these spectra is shown in Figures 3.18.

As stated in an earlier chapter, one reason that coinage and alkali systems have been so heavily studied was that they could be regarded as pseudo hydrogen systems - each with one bonding electron, forming a single σ bond. Combining this idea with the freedom of the disc source should allow the study of a new collection of such pseudo molecules. The first of these studies is reported here.

The LiCu combination is a known alloy in the bulk phase [41]. It is an important system, particularly due to the migration of the Li species to the alloy surface. The species has also been considered theoretically at the molecular level [42] and has been observed in the gas phase [43]. Thus a comprehensive experimental study of the system would be of interest.

Fabrication of LiCu proved difficult as the lithium was much less dense than the copper. Having mixed and pressed the powders several times, the resulting discs were clearly non uniform. The mass spectra recorded this fact with wide intensity alterations in the corresponding mass channels. This problem was overcome by

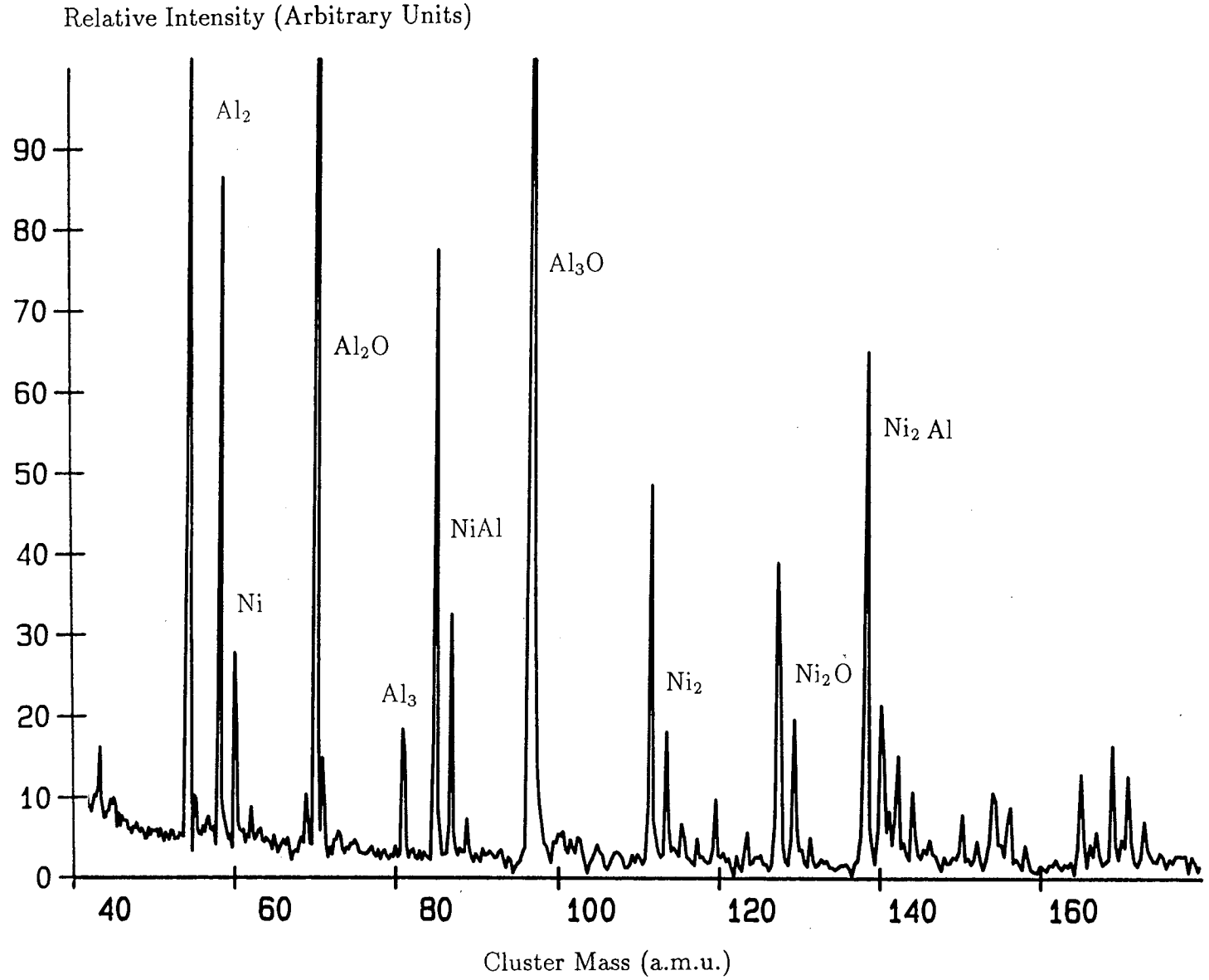

Figure 3–15: Mass Spectrum of the AlNi Disc.

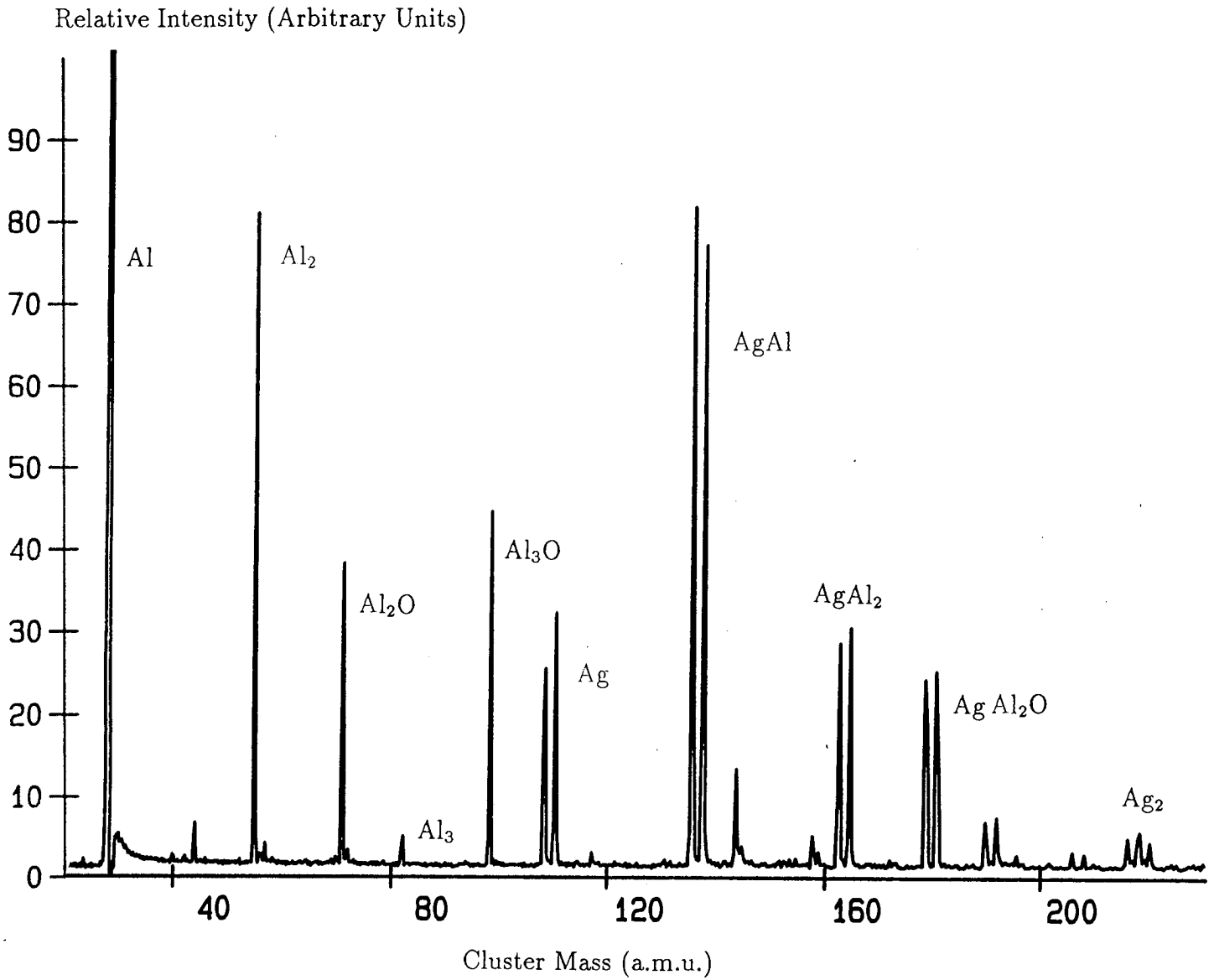

Figure 3–16: Mass Spectrum of the AlAg Disc.

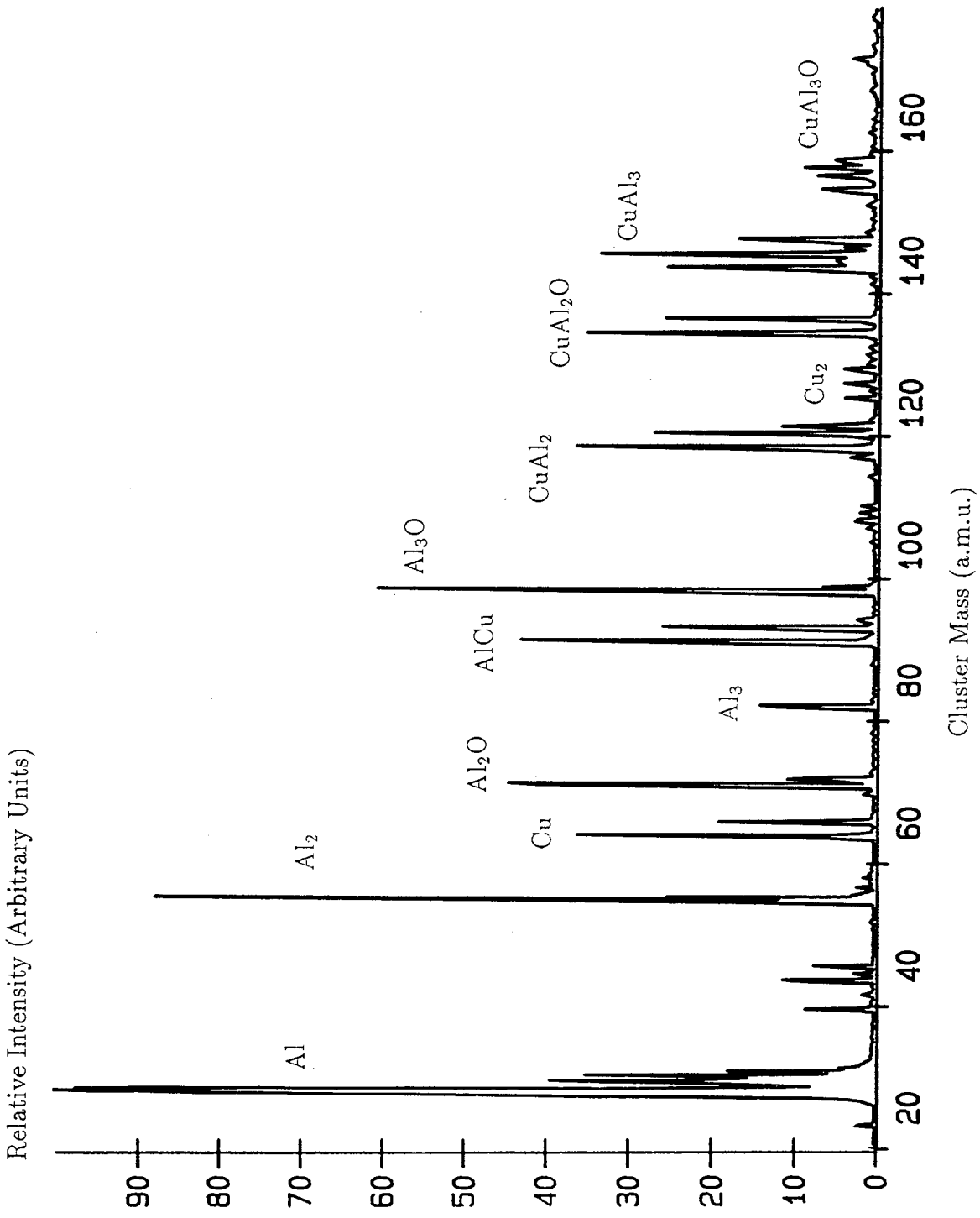

Figure 3–17: Mass Spectrum of the AlCu Disc.

Table 3–2: Frequency Ranges of Mixed Metal Dimer Studies

Species	Range covered (nm)
NiAg	610 - 765
AgAl	387 - 402
CuAl	386 - 420
CuNi	707 - 720
NiAl	412 - 550
	610 - 760
LiCu	462 - 497

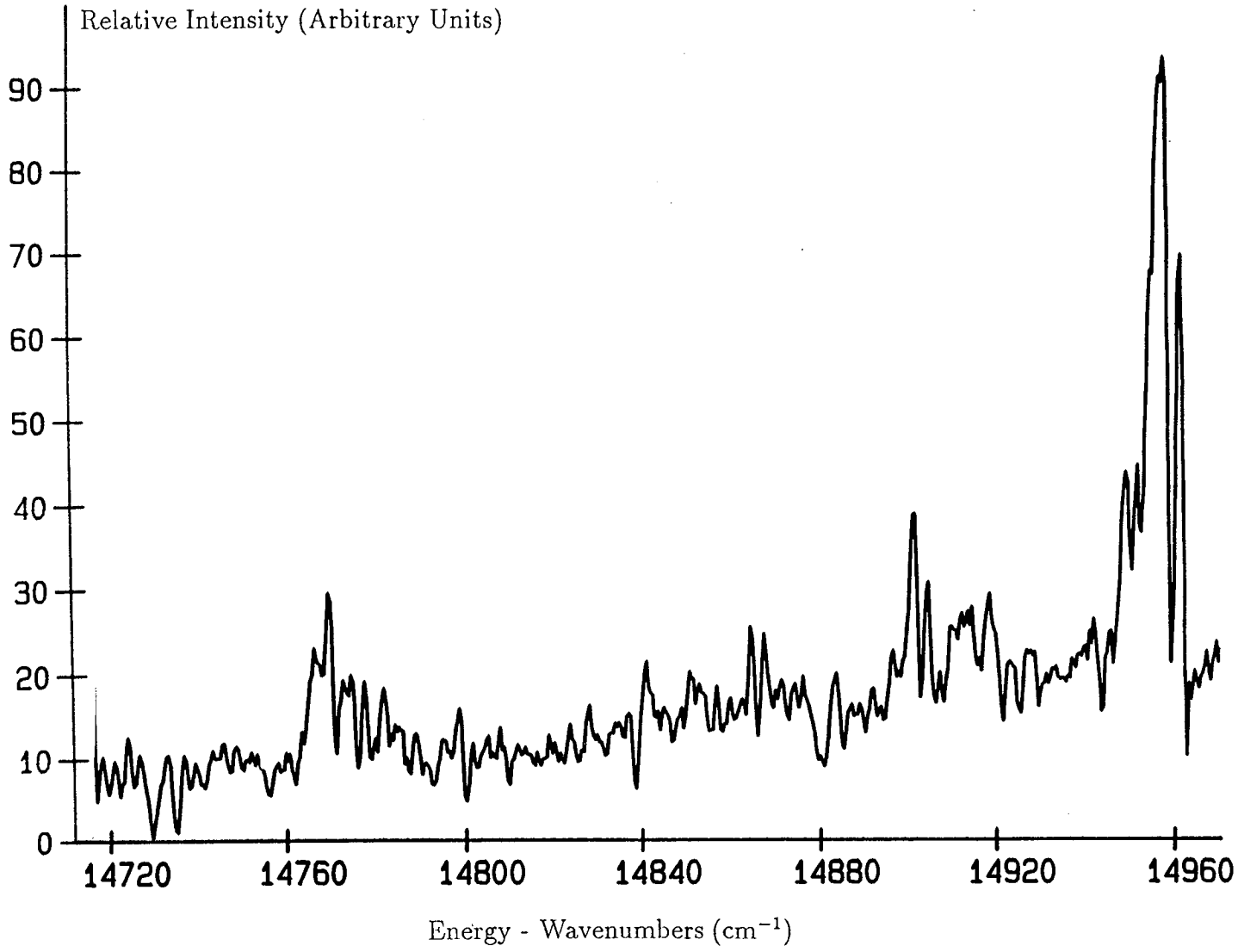

Figure 3–18: Frequency Spectrum of the $^{27}Al^{58}Ni$ Disc

a process of disc fabrication, grinding and repressing. After several repetitions of such a cycle a more stable source was produced. Unfortunately, this specimen was mechanically weak. Despite several attemps to improve its strength with the inclusion of a halowax binding additive, all the work reported here was achieved with the bare disc.

A typical mass spectrum is shown in Figure 3.19. Lithium is a mixture of two naturally occuring isotopes: ^{6}Li at 7.52% and ^{7}Li at 92.48%. Copper also exists in two guises: ^{63}Cu at 69.1% and ^{65}Cu at 30.9%. Hence one would expect a mass spectrum of the mixed species to contain a multiplet of four peaks in the ratios 2:29:1:13. In fact, the actual spectra show only two peaks at masses 70 and 72 in the ratio 2:1 - the two statistically disadvantaged combinations being lost in the spectal noise.

Such spectra have been recorded at a variety of fixed frequencies ; 193 nm (ArF, 6.4 eV), 248 nm (KrF, 4.98 ev) and 308 nm (XeCl, 4.0 eV) as well as a variety of fixed and scanning frequencies from the dye laser. These are also summarised in Table 3.2. No molecular transitions were observed in any of this work.

One final experimental note is to point out the fact that this system is not limited to the mixing of two species. Figure 3.20 shows the resulting mass spectrum when lithium, aluminium and copper are mixed together. Not only are there atomic and diatomic peaks present, but also those of higher clusters. It would seem that this technique has no limit in this respect, and has the potential to permit the study of some quite unlikely molecular combinations.

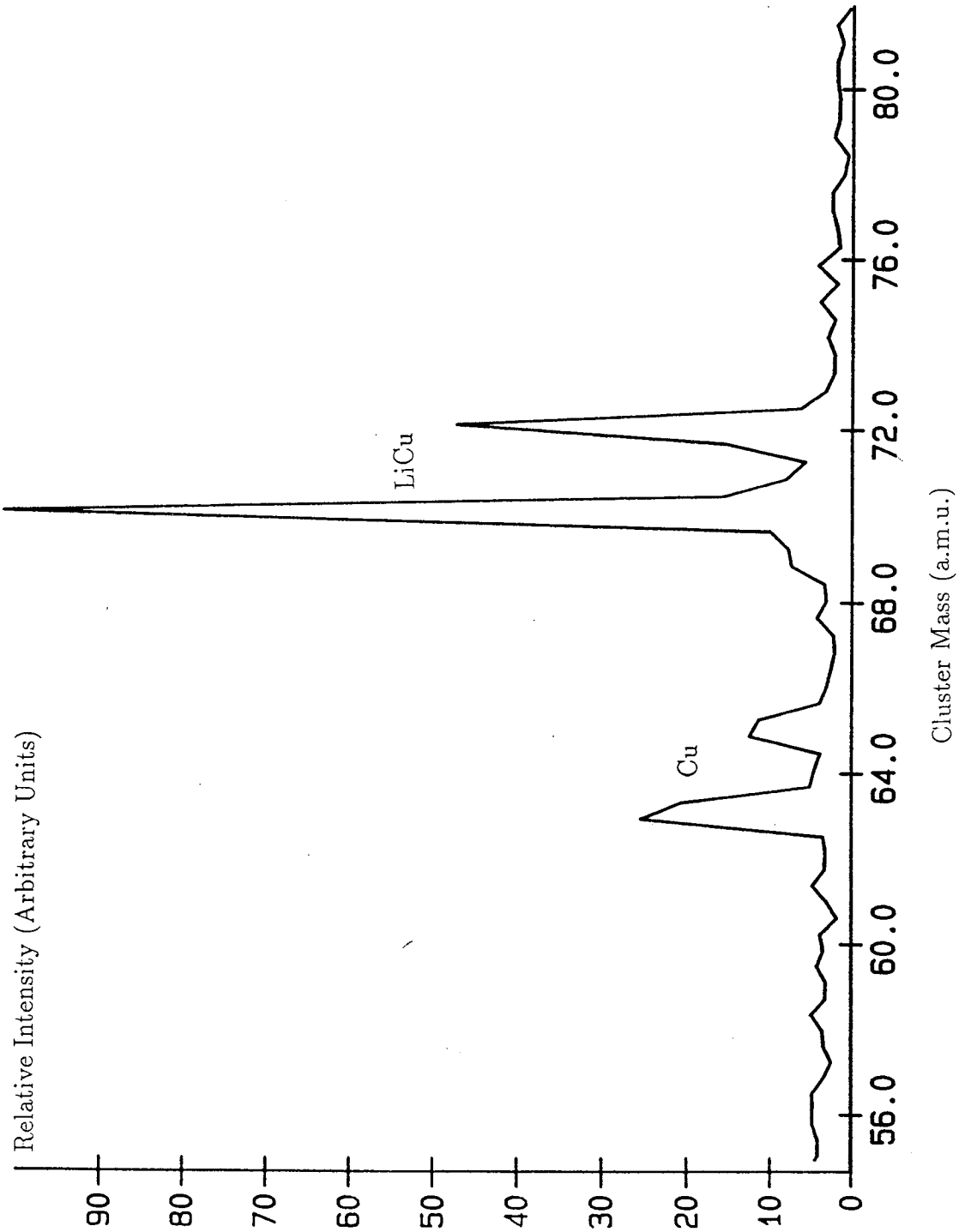

Figure 3–19: Mass Spectrum of the LiCu Disc

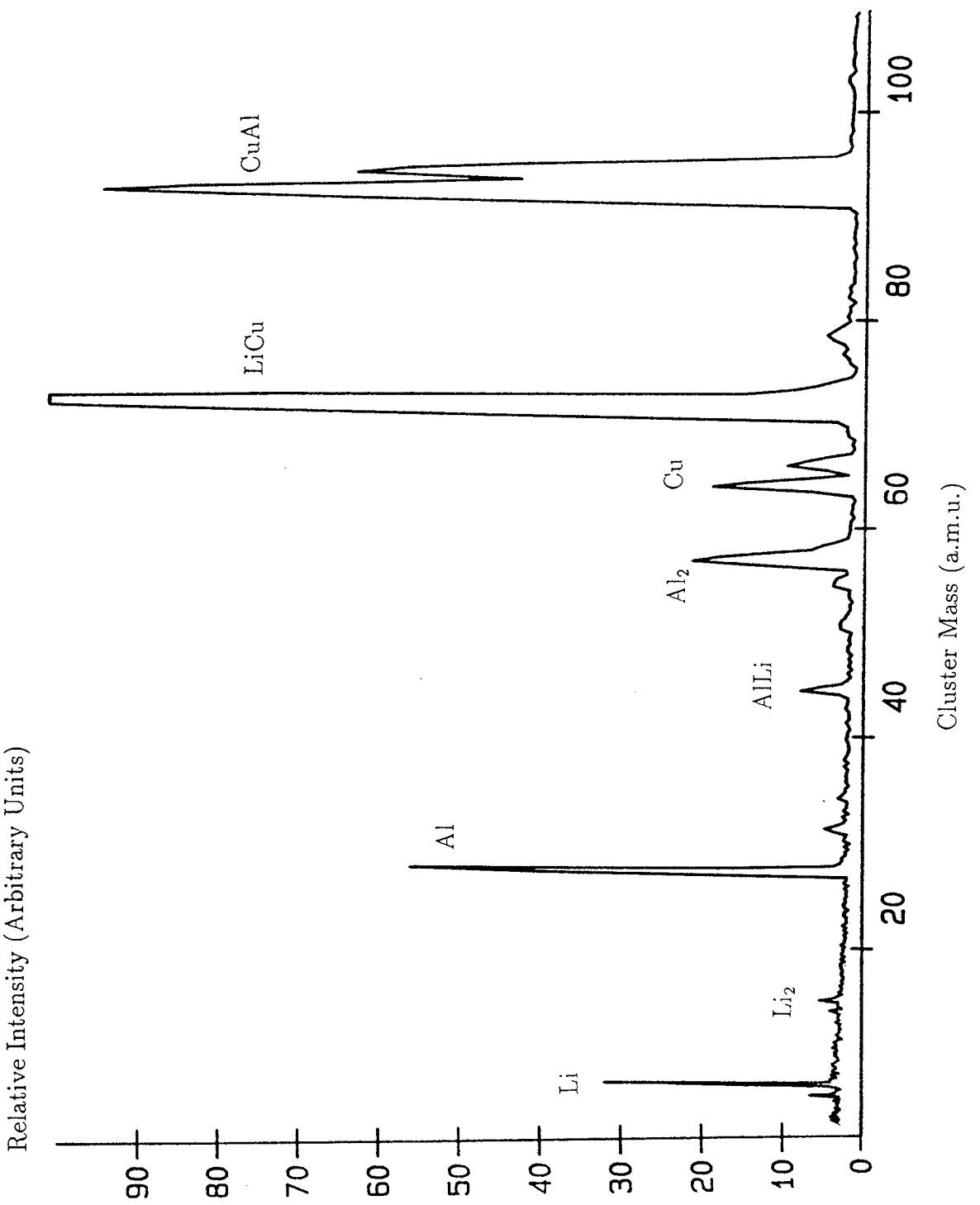

Figure 3–20: Mass Spectrum of the LiAlCu Disc

Bibliography

[1] Dietz T.G., Duncan M.A., Powers D.E. and Smalley R.E., J. Chem. Phys., 1981, **74**, 6511.

[2] Ready J.F., *Industrial Applications of Lasers*, Academic Press, New York, 1978.

[3] Ready J.F., *Effects of high power laser radiation*, Academic Press, New York, 1971.

[4] Bernholc J. and Phillips J.C., J. Chem. Phys, 1986, **85**, 3258.

[5] Hagena O.F., Surf. Sci., 1981, **106**, 101.

[6] Ryali S.B. and Fenn J.B., Ber. Bunsenges. Phys. Chem., 1984, **88**, 245.

[7] Smalley R.E., Wharton L. and Levy D.H., Acc. Chem. Res., 1977, **10**, 139.

[8] Kantrowitz A. and Grey J., Rev. Sci. Instrum., 1951, **22**, 328.

[9] Kistiakowsky G.B. and Slichter W.P., Rev. Sci. Instrum., 1951, **22**, 333.

[10] Engelking P.C., Chem. Rev., 1991, **91**, 399.

[11] Toennies J.P. and Winkelmann K., J. Chem. Phys., 1977, **66**, 3965.

[12] Levy D.H., Ann. Rev. Phys. Chem., 1980, **31**, 197.

[13] Lubman D.M., Rettner C.T. and Zare R.N., J. Phys. Chem., 1982, **86**, 1129.

[14] Lossing F.P. and Tanaka I., J. Chem. Phys., 1956, **25**, 1031.

[15] Atkins P.W., *Molecular Quantum Mechanics*, Second Edition, Oxford University Press, 1983.

[16] Hollas J.M., *High Resolution Spectroscopy*, Butterworths, London, 1982.

[17] Johnson P.M. and Otis C.E., Ann. Rev. Phys. Chem., 1981, **32**, 139.

[18] Rohlfing E.A., Cox D.M. and Kaldor A., J. Chem. Phys., 1984, **81**, 3322.

[19] Göppert-Mayer M., Ann. Phys., 1931, **9**, 273.

[20] Parker D.W., *Ultra Sensitive Laser Spectroscopy*, Edited by Kliger D.S., Academic Press, New York, 1983.

[21] Demtröder W., *Laser Spectroscopy - Basic Concepts and Instrumentation*, Springer Series in Chemical Physics 5, Springer-Verlag, Berlin, 1984.

[22] Campara J.E., Anal. Instrum., 1987, **16**, 1.

[23] Opsal R.B., Owens K.G. and Reilly J.P., Anal. Chem., 1985, **57**, 1884.

[24] Wiley W.C. and M^{c}Laren I.H., Rev. Sci. Instrum., 1955, **26**, 1150.

[25] Mamyrin B.A., Karataev V.I., Shmikk D.V. and Zagulin V.A. Sov. Phys. JETP, 1973, **37**, 45.

[26] Karataev V.A., Mamyrim B.A. and Shmikk D.V., Sov. Phys. Tech. Phys., 1972, **16**, 1177.

[27] Mamyrin B.A. and Shmikk D.V., Sov. Phys. JETP, 1979, **49**, 762.

[28] Lubman D.M., Bell W.E. and Kronick M.N., Anal. Chem., 1983, **55**, 1437.

[29] Hellsing M., Karlsson L., Andren H-O. and Norden H., J. Phys. E: Sci. Instrum., 1985, **18**, 920.

[30] Treglia G., Legrand B. and Maugain P., Surf. Sci., 1990, **225**, 319.

[31] Fu Z-W. and Morse M.D., J. Chem. Phys., 1989, **90**, 3417.

[32] Efremov Y.M., Samoilova A.N. and Gurvich L.V., Chem. Phys. Lett., 1976, **44**, 108.

[33] Spain E.M., Behm J.M. and Morse M.D., Chem. Phys. Lett., 1991, **179**, 411.

[34] Morse M.D., Chem. Rev., 1986, **86**, 1049.

[35] Bishea G.A., Marak N. and Morse M.D., J. Chem. Phys., 1991, **95**, 5618.

[36] Mrozek P. and Jablonski A., Surf. Sci., 1989, **208**, 351.

[37] Cai M.F., Tsay S.J., Dzugan T.P., Pak K. and Bondybey V.E., J. Phys. Chem., 1990, **94**, 1313.

[38] Uy O.M. and Drowart J., Trans. Faraday Soc., 1971, **67**, 1293.

[39] Bauschlicher C.W.Jnr., Langhoff S.R., Partridge H. and Walch S.P., J. Chem. Phys., 1987, **86**, 5603.

[40] Bär M. and Ahlrichs R., Chem. Phys. Lett., 1991, **178**, 241.

[41] Shi M., Grizzi O. and Rabalais J.W., Surf. Sci., 1990, **235**, 67.

[42] Beckmann H-O., Pacchioni G. and Jeung G-H., Chem. Phys. Lett., 1985, **116**, 423.

[43] Neubert A. and Zmbov K.F., J. Chem. Soc. Faraday Trans. I, 1974, **70**, 2219.

Chapter 4

R2PI Spectroscopy of Jet-Cooled Silver Dimer

4.1 Introduction

Much work has been carried out on the electronic spectroscopy of clusters of the coinage metals. In particular the diatomics, both homo and heteronuclear, have received considerable attention [1]. However, close analysis of these studies shows that it was not until quite recently that rotationally resolved spectra were recorded for many of these systems. The principal reason for this was the lack of a suitably general experimental approach for recording high resolution electronic spectra of such refractory species. However, as discussed fully in Chapter 1, the introduction of the laser vaporisation cluster source by Smalley and co-workers, coupled with the use of mass-resolved laser photoionisation spectroscopy, has now enabled considerable progress to be made in this field.

In the present work this combination of techniques has been employed to examine the A $(^1\Sigma_u^+) \leftarrow$ X $(^1\Sigma_g^+)$, B $(^1\Pi_u) \leftarrow$ X $(^1\Sigma_g^+)$ and C $(^1\Pi_u) \leftarrow$ X $(^1\Sigma_g^+)$ transitions of Ag_2.

4.2 Silver Dimer - Previous Spectroscopic Studies.

The previous spectroscopic studies on Ag_2 fell basically into two catagories; those employing matrix isolation techniques, and those carried out in the gas phase.

4.2.1 Matrix Isolation Studies

A variety of such studies have taken place over the past ten years [2] - [24]. Many of these have concentrated on the absorption features around 390 and 263 nm. Grinter et al. have shown in a magnetic circular dichroism (MCD) study that the upper and lower states involved in the 390 nm band system are non-degenerate, whilst the 263 nm band system has a degenerate upper state [5]. These two systems are believed to correspond to the A ($^1\Sigma_u^+$) and C ($^1\Pi_u$) states which are found in the gas phase at 435 nm and 266 nm respectively. The vacuum ultraviolet region has also been investigated, using synchrotron radiation, resulting in the identification of a number of new states [14]. Raman [13] [16] and resonance Raman [17], [18] studies have also been carried out, together with various time-resolved fluorescence studies which have allowed the lifetimes of some excited states to be determined [22] - [24].

4.2.2 Gas Phase Studies

Gas-phase electronic spectra of diatomic silver have been recorded, in both absorption and emission, by various research groups over the past forty years [25] - [41]. The spectroscopic constants derived from these studies are summarised in Table 4-1.

It is clear from the above table that a variety of states have been identified. Indeed, the vibronic analysis of each is well documented, with all the states having been observed in absorption, and all but one in emission. The first studies, carried

Table 4–1: Spectroscopic Constants for all known States of $^{107,109}Ag_2$.

State	T_e (cm^{-1})	ω_e (cm^{-1})	$\omega_e x_e$ (cm^{-1})	B_e (cm^{-1})
H $^1\Sigma_u^+$ (0_u^+)	58273.1	165.9	2.46	-
E $^1\Pi_u$ (0_u^+)	40158.6	146.4	1.59	0.04717
D $^1\Sigma_u^+$ (0_u^+)	39014.5	168.2	1.20	0.04866
C $^1\Pi_u$ (1_u)	37631.6	171.0	0.84	0.04858
B $^1\Pi_u$ (1_u)	35828.9	151.4	0.70	0.04541
A $^1\Sigma_u^+$ (0_u^+)	22996.4	154.6	0.59	0.04435
X $^1\Sigma_g^+$ (0_g^+)	0.0	192.4	0.64	0.04881

The above values were taken from reference [41].

out by Ruamps [25] [26], recorded many of the states in absorption. Subsequent studies have improved on the values of the constants for particular states; for example the A state is best represented by the work of Kleman and Lindqvist [27].

The rovibronic analysis also appears to be well advanced. These values, however, are all recent additions; the prior dearth of data being due primarily to the experimental reasons detailed in Chapter 1 of this thesis. Indeed, the only values offered prior to the advent of the experimental techniques described earlier in this work were an estimation from the measured separation of band heads by Brown and Ginter [31]. Since the advent of this new technique, several studies have taken place on the Ag_2 system [33] - [41]. Rotationally resolved spectra were recorded in this laboratory for the A $\leftarrow$ X system [33]. Although these spectra were of poor quality, they allowed rotational constants to be calculated. These values were then used in a laser-induced fluorescence (LIF) study to aid in the identification of particular spectral lines [39]. The combination of these two studies provided excellent values for the X and A states. This work has recently been extended by a further high resolution study, confirming the original analysis [37]. Of the higher excited states, only the B state has enjoyed a determination of its structure, with two recent studies. The earlier study reported rovibronic resolution, but the assignment of P lines in the analysis was in error by +3 J units, resulting in inaccurate constants [35]. This situation has since been corrected [36]. One point of note, however, is that no spectra were published alongside this analysis, and the transition designated as $\Delta\Lambda = 0$. The second study, offered both experimental spectra and a different analysis, such that $\Delta\Lambda = +1$ [40]. These points will be discussed further in a later section, permitting a consideration of the results reported here. Finally, while one other higher state of Ag_2 has been investigated under rovibronic resolution [41], it will not be considered further in this thesis.

4.3 Experimental Set-Up

While the experimental set-up was earlier described in a general sense, each experiment had a selection of nuances which were crucial for any successful outcome. The quality of the beam species was monitored and optimised using non-resonant excimer ionisation lasing on the ArF line. This excimer was positioned as close to the vacuum chamber window as possible to prevent losses from beam divergence (6 mrad). The excimer output could be focussed, defocussed, irised or attenuated as required. Once the quality of beam was assured, the spectroscopic investigation could begin. Excitation of the A $\leftarrow$ X transition was achieved by the excimer pumped dye laser, using Coumarin 120 in the 426 - 436 nm region. As the ionisation potential was known to lie in the 7.5 eV region, this initial step constituted a less than half way excitation. Hence the second, ionising, photon was required to be from a more energetic source. This was supplied by the previously described excimer laser, again operating on the ArF line. This set up is shown in Figure 4-1.

Temporal overlap of these two radiation sources is critical in states with short lifetimes, and the A state was known to have a lifetime of the order of 30 ns. Such overlap was maintained by monitoring both sources on oscilloscope (Tektronic 2445A 150 MHz.) via two fast, homebuilt photodiodes. The sources were prone to two types of movement: a shot-to-shot jitter of the order of 10 ns and a slower long term drift. While the first type was essentially unavoidable, the second could be minimised by constantly monitoring the timing delay control in the THOR program to bring both sources back together in time. Spatial overlap was also crucial. This was achieved by means of a pair of razor blade slits and adjustable iris on the excimer beam, resulting in a short horisontal strip of radiation. This was subsequently buried inside the circular profile of the dye laser output. In order to obtain good enhancement when on resonance, either or both of these beams were focussed, telescoped or filtered to give the best possible working conditions.

For the B $\leftarrow$ X and C $\leftarrow$ X work a slightly simpler system could be used. It is shown in Figure 4-2.

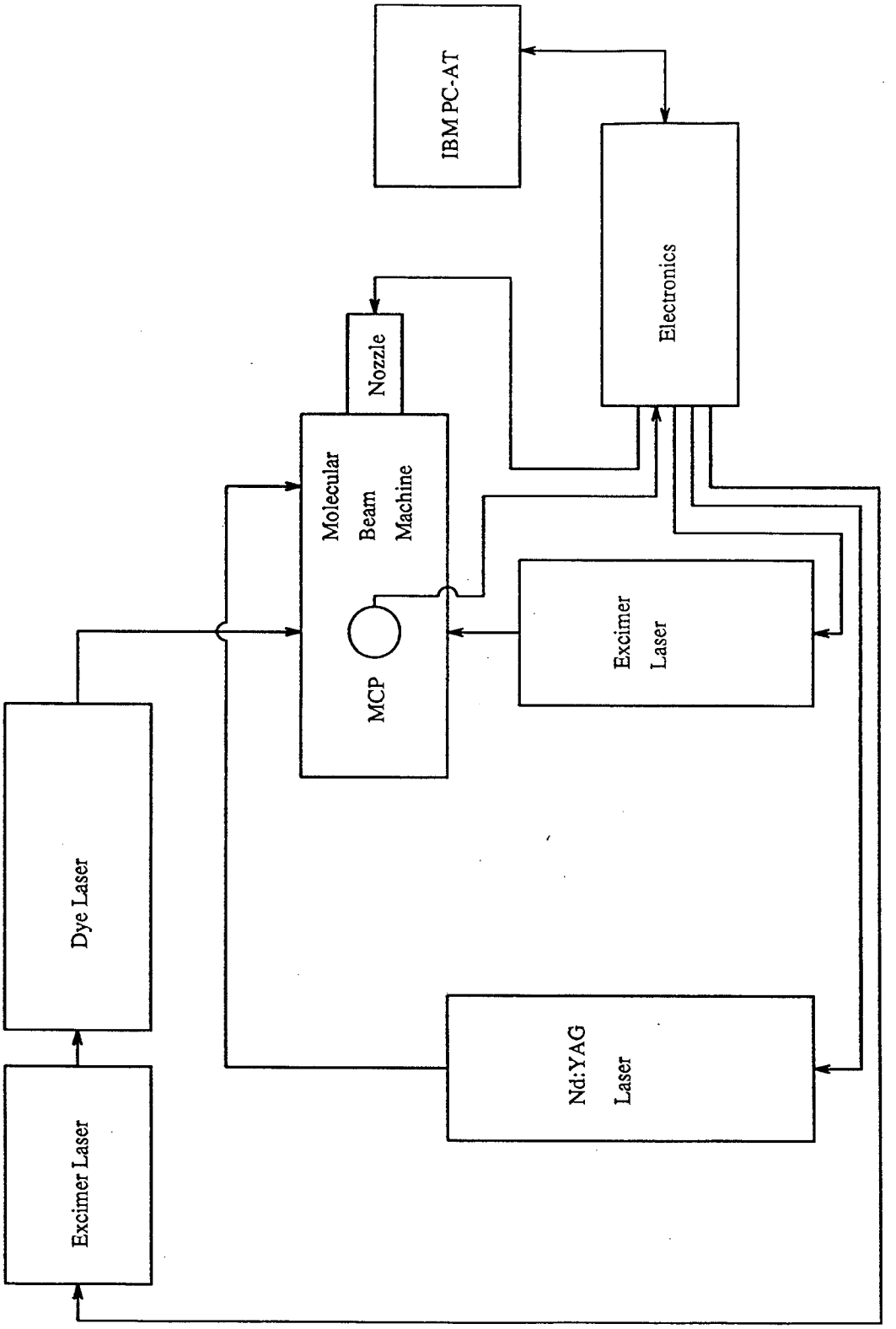

Figure 4–1: Experimental Set-Up for the Investigation of the Ag_2 A $\leftarrow$ X System

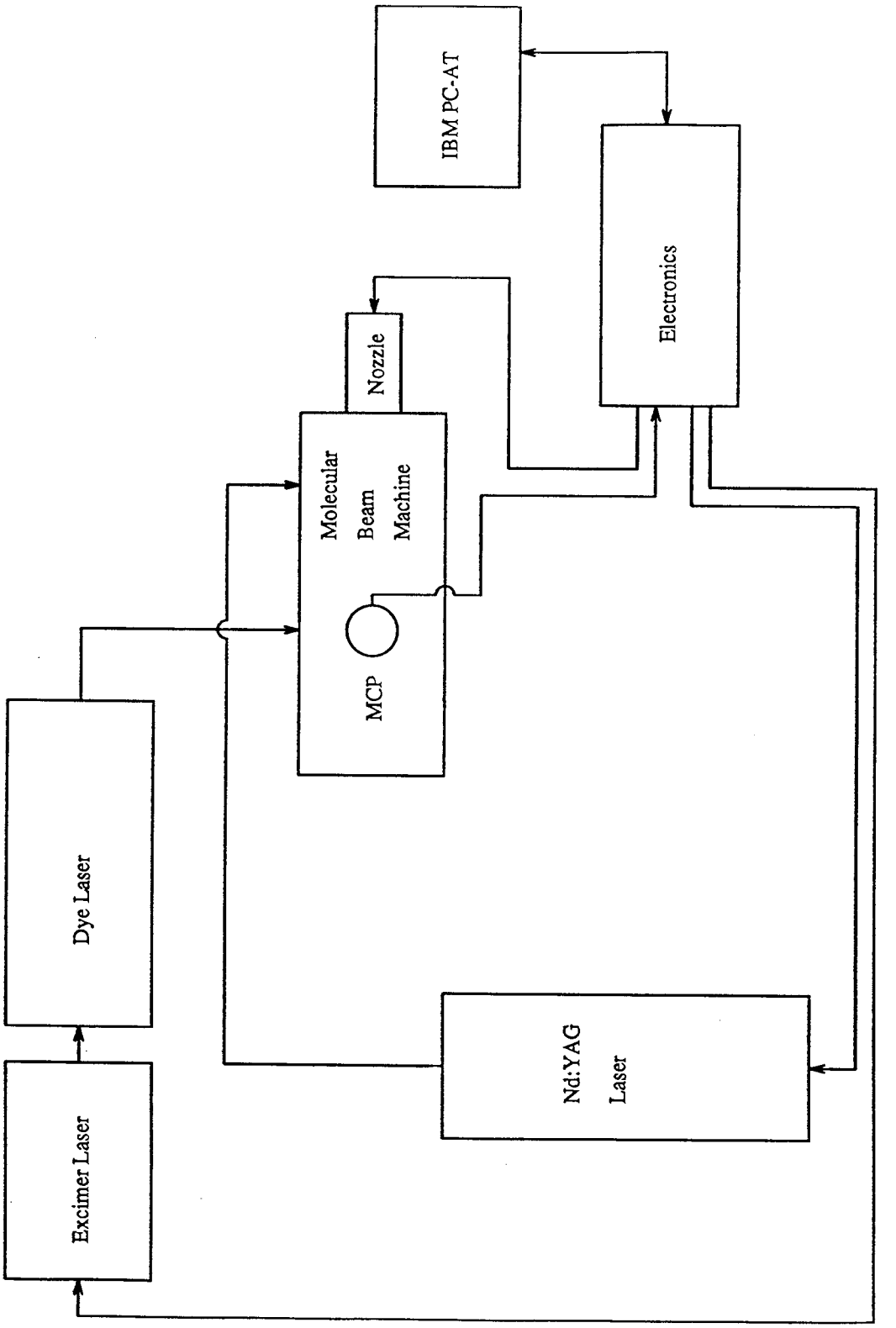

Figure 4–2: Experimental set-up for the Investigations of the Ag_2 B $\leftarrow$ X and C $\leftarrow$ X Systems

For investigations of these systems, only the dye laser was required, as the intermediate state lay more than halfway to the ionisation limit. Hence the second, ionising photon could come from the same source, and the timing problem was effectively removed. One drawback of this system, however, was that lifetime measurements were no longer possible by delaying the second photon. Also, as these states required the dye laser output to be frequency doubled, the effective laser bandwidth was also doubled, resulting in spectra of reduced resolution.

4.4 The A ← X System

This was the first transition in the Ag_2 molecule to be studied, and has had the greatest volume of subsequent work. The initial gas phase studies carried out on this system used a hot oven source, and recorded the transition in emission, achieving vibronic resolution [25] [26]. A second vibronic study was able to record many more band positions and so led to more accurate vibrational constants [27]. A previous study carried out in this group, used an identical experimental set up to investigate this system and achieved rovibronic analysis [33]. However, the quality of the spectra was rather poor, due to a laser timing jitter of up to 30 ns shot to shot, as described previously. This problem has since been resolved, and it was felt that by repeating that work, a more accurate analysis could be achieved. Another member of this group has since been able to perform some laser induced fluorescence work [39]. While this work suffered from the spectral congestion of the various isotopic combinations, it was able to use the rotational constants calculated in the earlier work to assign P branch members and improve the accuracy of the rotational constants. Finally, in a very recent paper [37], this state has been recorded under resolution such that individual members of the R head are fully resolved. Using the accurate ground state constants from these previous investigations, values are given for the upper state constants which are in good agreement with those obtained in this study.

4.4.1 Vibronic Resolution

Figure 4-3 shows the intensity variations occurring in the ion signal of one of the Ag_2 mass channels when the dye laser was scanned from 426 - 436 nm with a 0.1 nm step.

The spectrum shows one strong progression in which $v'' = 0$, and a weaker progression from $v'' = 1$. There are no transitions from higher levels of the lower state, confirming that extensive vibronic cooling has taken place during expansion. All bands are red degraded, indicating an increase in bond length upon excitation. Table 4-2 shows the measured band head positions. These were obtained directly from the digital diffraction grating readout of the dye laser. Table 4-2 also shows the accepted literature values for the corresponding bands of the 107 - 109 combination, taken from the most extensive of the earlier studies. Excluding the (3-0) band, the average deviation is some 7.8 cm^{-1}. This corresponds to around 0.15 nm at 426 nm. Despite this absolute error, the relative error between the (0-0), (1-0) and (2-0) features is very small.

The vibronic peaks were assigned from the literature values of Kleman and Lindkvist [27]. For comparison, they were both used in a vibrational line fitting program, written in the FORTRAN 77 language, using the REGRESS routine [42]. This program performed a least squares fit to the familiar vibronic formula

$$\nu = T_e' + G(\nu') - [T_e'' + G(\nu'')] \tag{4.1}$$

where;

ν = band position,
T_e = electronic term value and
$G(\nu) = \omega_e(\nu + 1/2) - \omega_e x_e(\nu + 1/2)^2$.

These results are shown in Table 4-3. They were achieved using the above formula in conjunction with the ground state literature values. Although good agreement was achieved, care has to be exercised here as only a few lines were fitted, and so the least squares process is of limited reliability. Despite this, good ω_e'' and

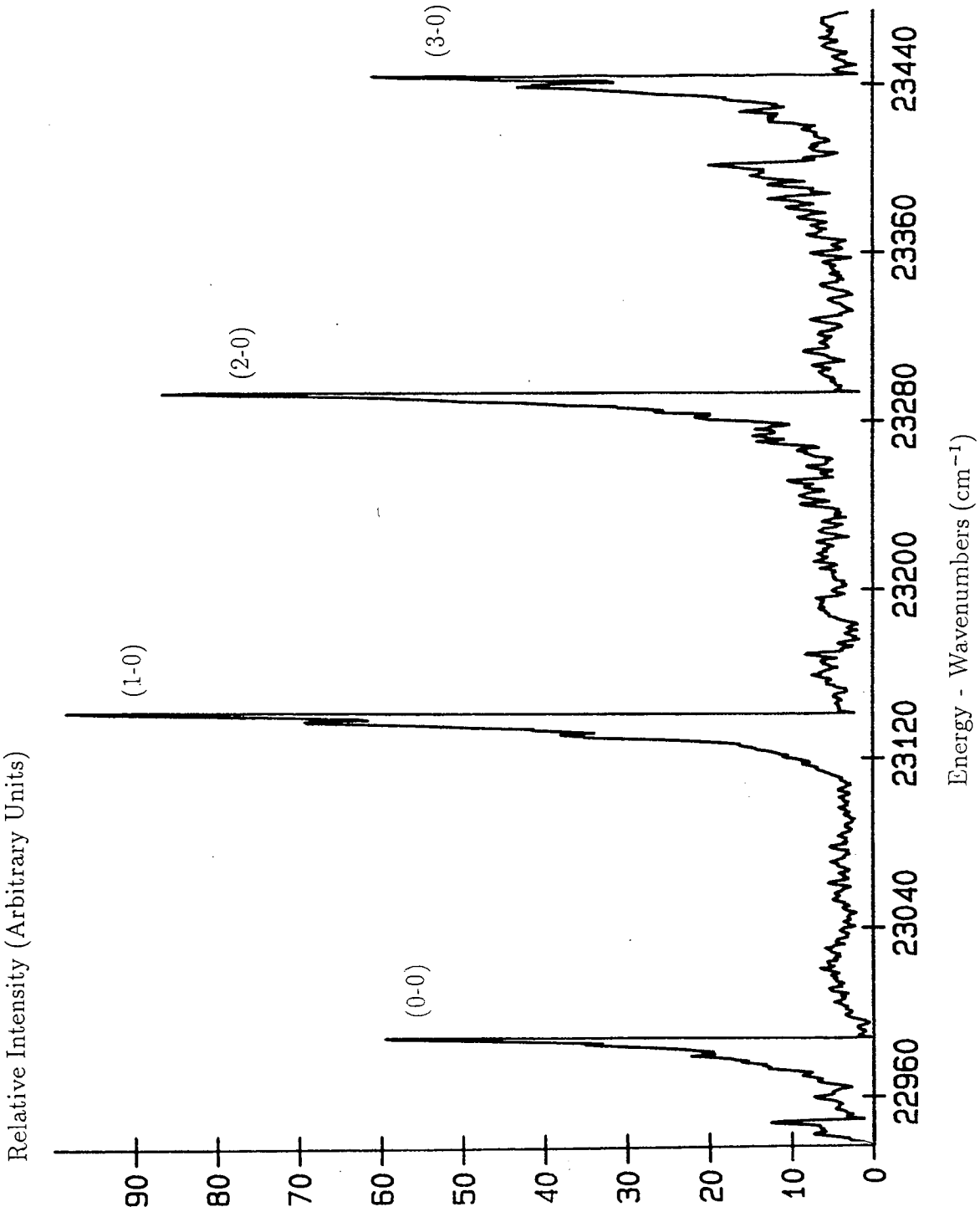

Figure 4–3: Vibronic Scan of the $^{107,109}Ag_2$ A $\leftarrow$ X System

Table 4–2: Vibronic Line Positions for Ag_2 A $\leftarrow$ X

Isotopomer	v′	v″	Value (cm^{-1})
107 - 107	0	0	22985.8 ± 0.6
107 - 107	1	0	23138.8 ± 0.6
107 - 107	2	0	23291.0 ± 0.6
107 - 107	3	0	23443.1 ± 0.6
107 - 107	4	1	23402.9 ± 0.6
107 - 107	1	1	22947.2 ± 0.6
107 - 109	0	0	22985.8 ± 0.6
107 - 109	1	0	23138.4 ± 0.6
107 - 109	2	0	23290.8 ± 0.6
107 - 109	3	0	23441.6 ± 0.6
107 - 109	4	1	23400.7 ± 0.6
107 - 109	1	1	22947.4 ± 0.6
109 - 109	0	0	22985.9 ± 0.6
109 - 109	1	0	23138.0 ± 0.6
109 - 109	2	0	23289.7 ± 0.6
109 - 109	3	0	23438.4 ± 0.6
109 - 109	4	1	23399.2 ± 0.6
109 - 109	1	1	22947.4 ± 0.6

ω_e' values were obtained, particularly when one considers that the literature value was in fact obtained from Kleman and Lindkvist using a larger selection of lines.

4.4.2 Rovibronic Resolution

An intra-cavity etalon was now inserted to reduce the bandwidth of the excitation laser from 0.18 cm^{-1} to 0.04 cm^{-1}. Both these values are as given in the manufacturers handbook, and are for radiation of 480 nm. Figures 4-4 to 4-15 show rotationally resolved spectra of the two strongest features of this system, namely the (0-0) and (1-0) bands. These systems have P and R bands only, confirming the previous assignments of the transition as $\Delta\Omega = 0$. They also show the R branch reversing quite sharply to form a head at around J = 9. This is consistent with an increase in bond length on excitation. The correct rovibronic line assignment for the homonuclear species was aided by the expected intensity alteration between transitions originating from odd or even levels of the ground state. From nuclear spin statistics, $I_{Ag} = 1/2$, and thus the expected ratio of (I+1)/I = 3 : 1 for odd : even J'' levels. No such alteration was expected from the heteronuclear species, where no centre of symmetry existed.

The line positions are listed in Tables 4-4 to 4-9. These were calculated by assigning the first fine etalon fringe as an arbitrary zero point and counting the line positions in terms of etalon fringes. These line positions were then used, along with their P or R line assignment to calculate rotational constants for the upper and lower states. This was done by means of another least squares program, again written in FORTRAN 77, but now fitting the data to the familiar rovibronic expression

$$\nu = \nu_0 + B'J(J+1) - D'J^2(J+1)^2 - B''J(J+1) + D''J^2(J+1)^2 \qquad (4.2)$$

where;

ν = band position,

ν_0 = rotationless transition energy,

B' = upper state rotational constant,

Table 4–3: Vibronic Constants for $^{107,109}Ag_2$ A $\leftarrow$ X

Quantity	Value 1 (cm^{-1})	Value 2 (cm^{-1})
ω''_e	192.4	192.4
error	-	-
$\omega_e x''_e$	0.643	0.643
error	-	-
ω'_e	152.9	154.0
error	1.4	1.4
$\omega_e x'_e$	0.217	0.377
error	0.260	0.260
T''_e	23006.5	22997.6
error	1.4	1.4

Value 1: This work

Value 2: Kleman and Lindqvist

D′ = upper state centrifugal term,

B″ = lower state rotational constant,

D″ = lower state centrifugal term and

J = rotational line number.

This program was run twice for each data set. Initially, both the upper and lower state values were allowed to assume any value, or 'floated' as it was called. It was found that the resulting D values had little meaning at this level of accuracy - their error bars were an order of magnitude larger than the values themselves. The fits were then repeated with only the B values being calculated. It is these fits that are detailed in Tables 4-4 to 4-9, with their corresponding constants and reduced χ^2 values. This fitting process was then repeated, using the literature ground state constants [39]. The upper state values obtained under these conditions are given in Table 4-10.

The values obtained for v′ = 0 and v′ = 1 have also been used to calculate the equilibrium value using the equation

$$B_v = B_e - \alpha_e(v + 1/2). \tag{4.3}$$

These values are also given in the Table 4-10. The corresponding ground state values could not be calculated as only one level, B_0, of the ground state had been evaluated. However, if the potential energy curve for the ground state is assumed to be well represented by a Morse function [44], then the corresponding α_e value can be calculated from the Pekeris relation [45]

$$\alpha_e = 6(\omega_e x_e B_e^3)^{1/2}/\omega_e - 6B_e^2/\omega_e \tag{4.4}$$

where;

B_e is assumed to equal B_0,

ω_e is the vibrational frequency and

$\omega_e x_e$ is the anharmonicity constant.

Table 4–4: Rovibronic line positions of (0-0) band of Ag_2 A $\leftarrow$ X

Isotopomer	Branch	J″	Data (FSR)	Fitted (FSR)	Residual (FSR)
107 - 107	P	21	1.96	2.10	-0.14
107 - 107	P	20	5.20	4.87	0.33
107 - 107	P	19	7.60	7.54	0.06
107 - 107	P	18	10.00	10.13	-0.13
107 - 107	P	17	12.61	12.62	-0.01
107 - 107	P	16	14.90	15.03	-0.12
107 - 107	P	15	17.27	17.34	-0.07
107 - 107	P	14	19.46	19.57	-0.10
107 - 107	P	13	21.81	21.71	0.10
107 - 107	P	12	23.75	23.76	-0.01
107 - 107	P	11	25.82	25.72	0.10
107 - 107	P	10	27.56	27.59	-0.03
107 - 107	P	9	29.48	29.37	0.11
107 - 107	P	8	31.00	31.06	-0.06
107 - 107	P	7	32.66	32.66	-0.00
107 - 107	P	6	34.23	34.18	0.05
107 - 107	P	5	35.58	35.60	-0.02
107 - 107	P	4	36.90	36.94	-0.04
107 - 107	P	3	38.16	38.19	-0.03
107 - 107	P	1	40.27	40.42	-0.15
107 - 107	R	0	42.46	42.29	0.17
107 - 107	R	2	43.86	43.80	0.06
107 - 107	R	9	46.25	46.30	-0.05

All line positions are accurate to $\pm$ 0.17 FSR

$B''_0 = 0.4901 \pm 0.0233$ FSR

$B'_0 = 0.4456 \pm 0.0257$ FSR

Reduced $\chi^2 = 0.01427$

$\Delta T_e = 41.39657 \pm 0.32706$ FSR

FSR = 0.100606 cm^{-1}

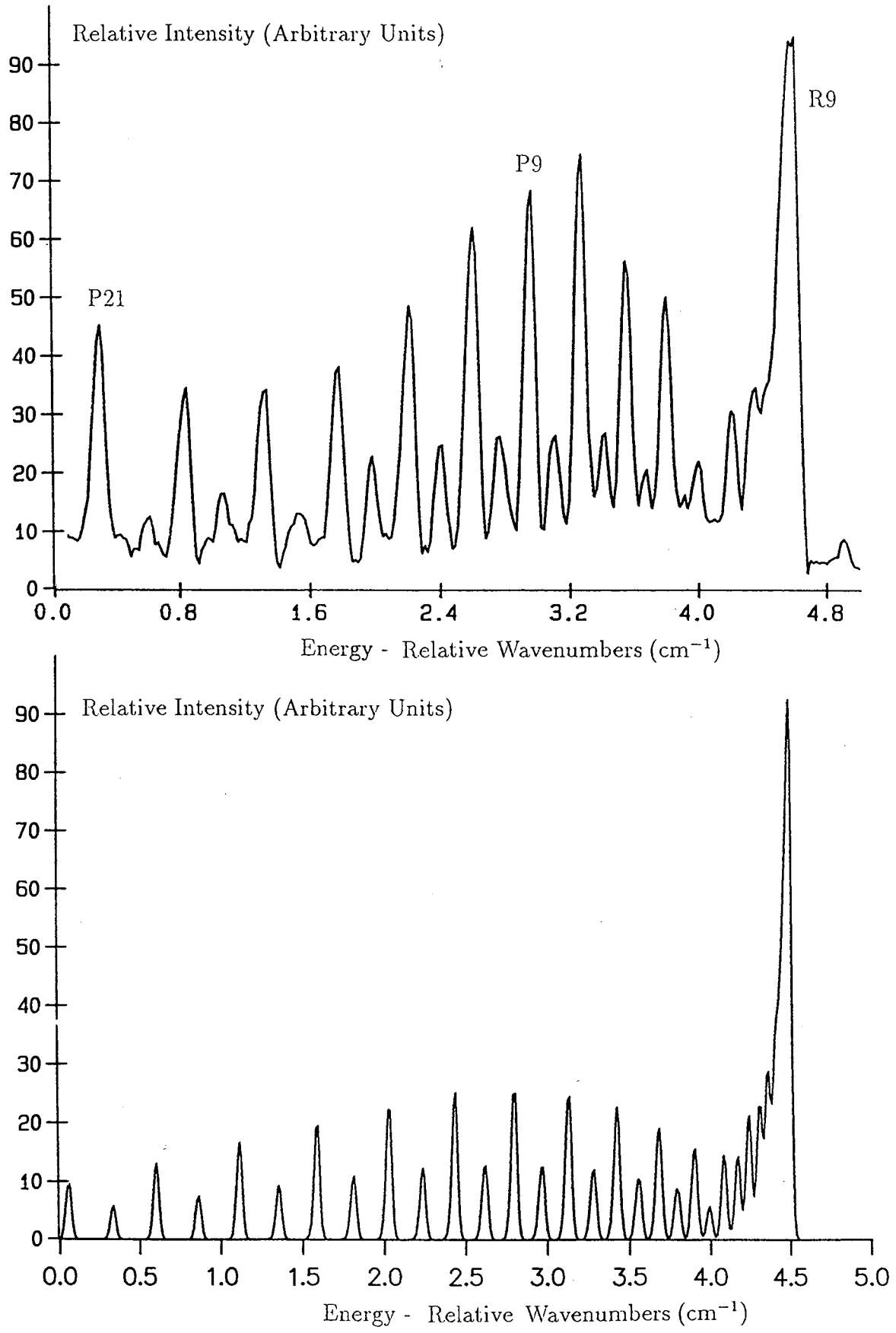

Figure 4–4: Rovibronic scan and simulation of $^{107}Ag_2$ A $\leftarrow$ X (0-0)

Table 4–5: Rovibronic Line Positions of the (0-0) Band of Ag_2 A $\leftarrow$ X

Isotopomer	Branch	J″	Data (FSR)	Fitted (FSR)	Residual (FSR)
107 - 109	P	22	0.41	0.36	0.05
107 - 109	P	21	3.17	3.21	-0.04
107 - 109	P	20	5.93	5.97	-0.04
107 - 109	P	19	8.69	8.64	0.05
107 - 109	P	18	11.14	11.21	-0.07
107 - 109	P	17	13.64	13.70	-0.06
107 - 109	P	16	16.12	16.10	0.02
107 - 109	P	15	18.43	18.40	0.03
107 - 109	P	14	20.64	20.62	0.02
107 - 109	P	13	22.72	22.75	-0.03
107 - 109	P	12	24.87	24.79	0.08
107 - 109	P	11	26.81	26.73	0.08
107 - 109	P	10	28.57	28.59	-0.02
107 - 109	P	9	30.42	30.36	0.06
107 - 109	P	8	32.10	32.04	0.06
107 - 109	P	7	33.60	33.62	-0.02
107 - 109	P	6	35.13	35.12	0.01
107 - 109	P	5	36.47	36.53	-0.06
107 - 109	P	4	37.82	37.85	-0.03
107 - 109	P	3	39.01	39.08	-0.07
107 - 109	P	2	40.13	40.21	-0.08
107 - 109	P	1	41.25	41.26	-0.01
107 - 109	R	18	42.44	42.50	-0.06
107 - 109	R	1	43.85	43.87	-0.02
107 - 109	R	4	45.86	45.81	0.05
107 - 109	R	9	46.97	46.86	0.11

All line positions are accurate to $\pm$ 0.17 FSR

$B''_0 = 0.4792 \pm 0.0098$ FSR

$B'_0 = 0.4342 \pm 0.0104$ FSR

Reduced $\chi^2 = 0.00342$

$\Delta T_e = 42.22102 \pm 0.30733$ FSR

FSR = 0.100606 cm^{-1}

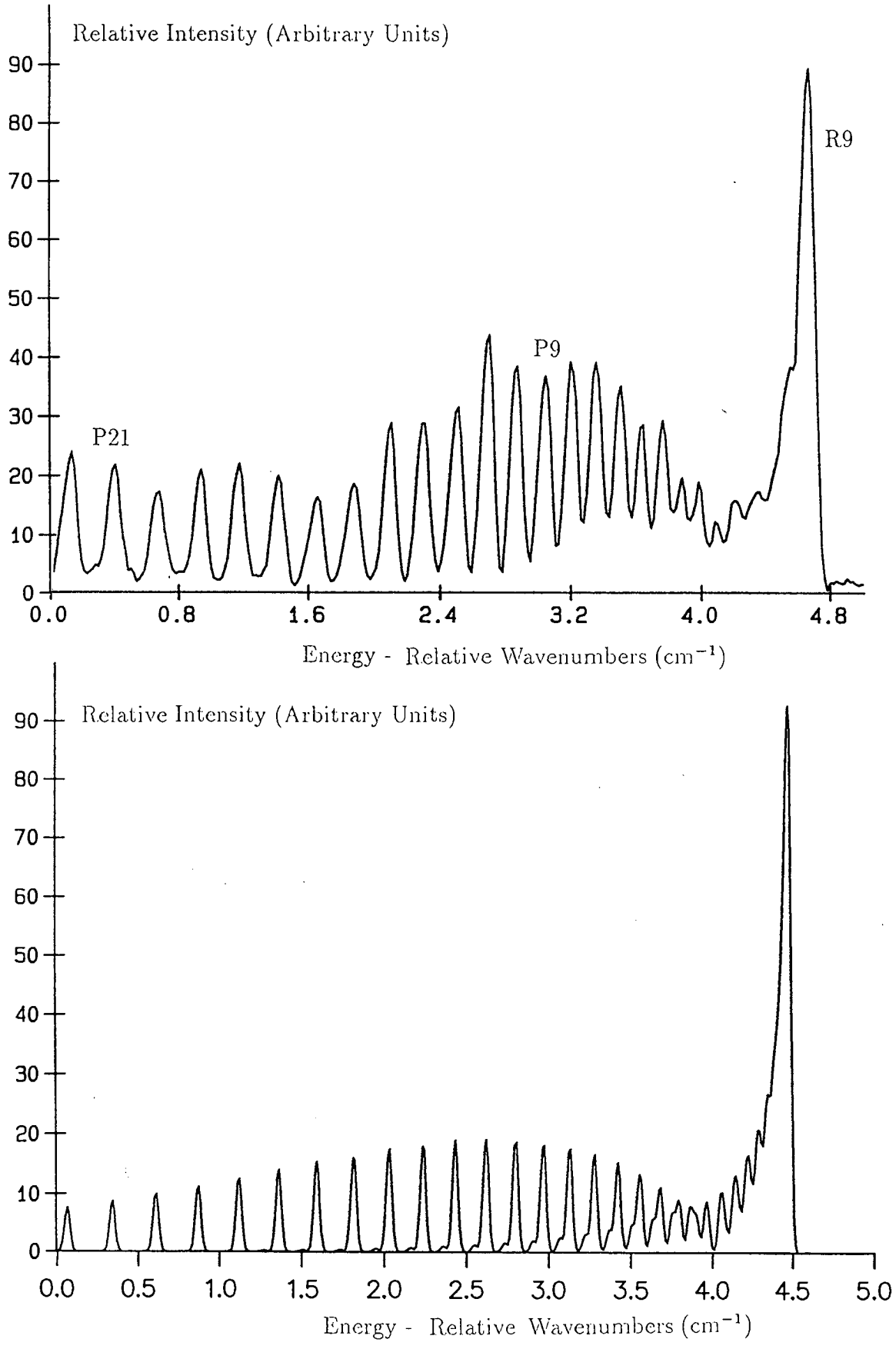

Figure 4–5: Rovibronic scan and simulation of $^{107,109}Ag_2$ A $\leftarrow$ X (0-0)

Table 4–6: Rovibronic Line Positions of the (0-0) Band of Ag_2 A $\leftarrow$ X

Isotopomer	Branch	J″	Data (FSR)	Fitted (FSR)	Residual (FSR)
109 - 109	P	22	1.48	1.53	-0.05
109 - 109	P	21	4.30	4.35	-0.05
109 - 109	P	20	7.12	7.09	0.03
109 - 109	P	19	9.75	9.73	0.02
109 - 109	P	18	12.25	12.28	-0.03
109 - 109	P	17	14.83	14.75	0.08
109 - 109	P	16	17.06	17.13	-0.07
109 - 109	P	15	19.36	19.42	-0.06
109 - 109	P	14	21.70	21.62	0.08
109 - 109	P	13	23.78	23.73	0.05
109 - 109	P	12	25.77	25.75	0.02
109 - 109	P	11	27.76	27.68	0.08
109 - 109	P	10	29.67	29.53	0.14
109 - 109	P	9	31.31	31.28	0.03
109 - 109	P	8	32.92	32.95	-0.03
109 - 109	P	7	34.44	34.53	-0.09
109 - 109	P	6	35.89	36.02	-0.13
109 - 109	P	5	37.44	37.42	0.02
109 - 109	P	4	38.63	38.73	-0.10
109 - 109	P	3	39.81	39.96	-0.15
109 - 109	P	2	41.21	41.09	0.12
109 - 109	P	1	42.28	42.14	0.14
109 - 109	R	0	43.89	43.97	-0.08
109 - 109	R	9	47.83	47.80	0.03

All line positions are accurate to $\pm$ 0.17 FSR

$B''_0 = 0.4789 \pm 0.0241$ FSR

$B'_0 = 0.4345 \pm 0.0264$ FSR

Reduced $\chi^2 = 0.00762$

$\Delta T_e = 43.09826 \pm 0.33397$ FSR

FSR = 0.100606 cm^{-1}

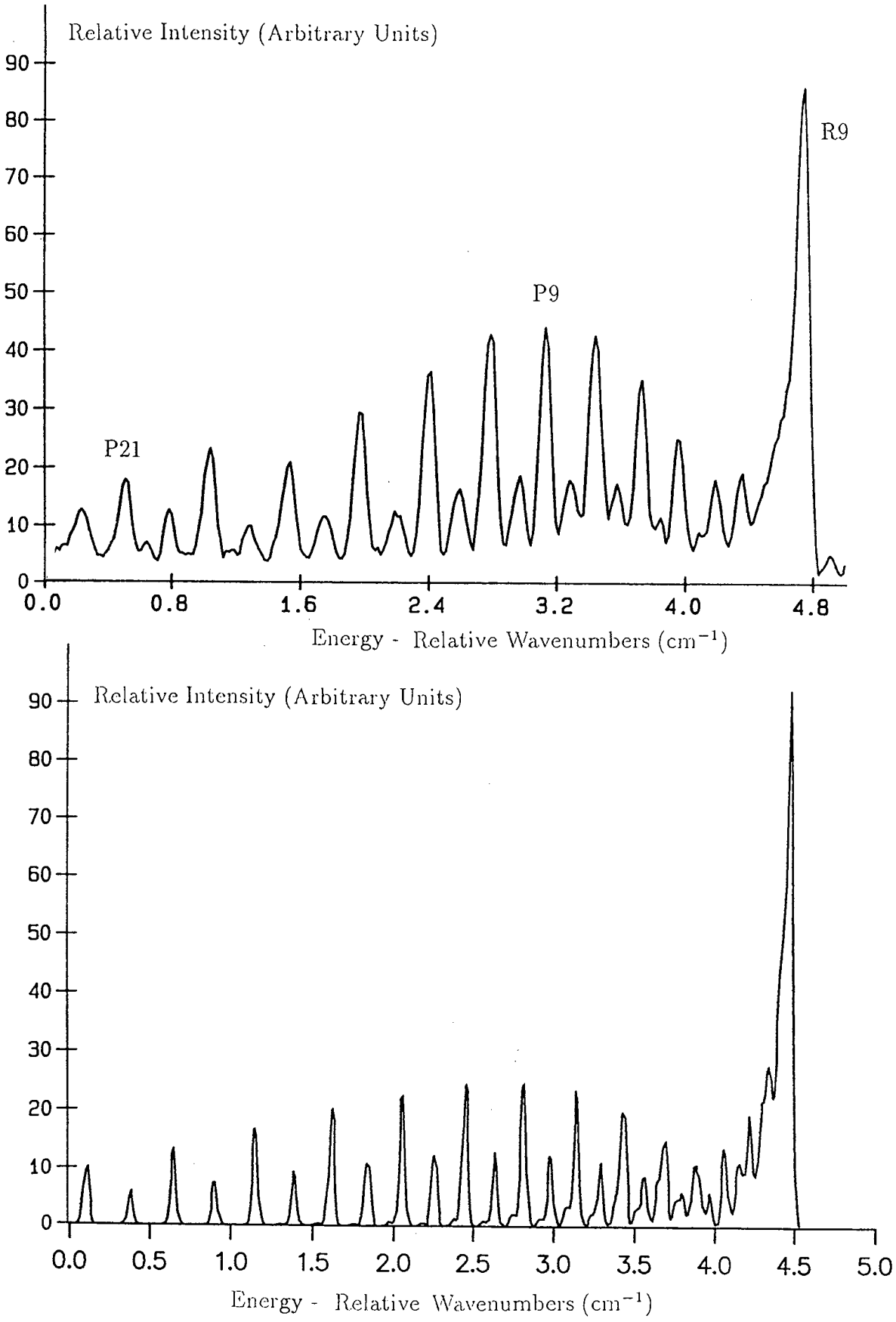

Figure 4–6: Rovibronic scan and simulation of $^{109}Ag_2$ A $\leftarrow$ X (0-0)

Table 4–7: Rovibronic Line Positions of the (1-0) Band of Ag_2 A $\leftarrow$ X

Isotopomer	Branch	J″	Data (FSR)	Fitted (FSR)	Residual (FSR)
107 - 107	P	31	0.56	0.11	0.45
107 - 107	P	30	3.34	3.94	-0.60
107 - 107	P	29	8.00	7.68	0.32
107 - 107	P	28	11.20	11.31	-0.11
107 - 107	P	27	15.11	14.86	0.25
107 - 107	P	26	17.77	18.30	-0.53
107 - 107	P	25	21.90	21.65	0.25
107 - 107	P	24	24.56	24.91	-0.35
107 - 107	P	23	28.17	28.07	0.10
107 - 107	P	22	30.94	31.14	-0.20
107 - 107	P	21	34.35	34.14	0.21
107 - 107	P	20	37.07	36.98	0.09
107 - 107	P	19	40.07	39.76	0.31
107 - 107	P	18	42.24	42.45	-0.21
107 - 107	P	17	45.06	45.03	0.03
107 - 107	P	16	47.40	47.53	-0.13
107 - 107	P	15	50.00	49.93	0.07
107 - 107	R	9	78.87	78.88	-0.01

All line positions are accurate to $\pm$ 0.13 FSR

$B''_0 = 0.4837 \pm 0.0236$ FSR

$B'_1 = 0.4361 \pm 0.0251$ FSR

Reduced $\chi^2 = 0.09939$

$\Delta T_e = 74.45228 \pm 0.61110$ FSR

FSR = 0.101434 cm^{-1}

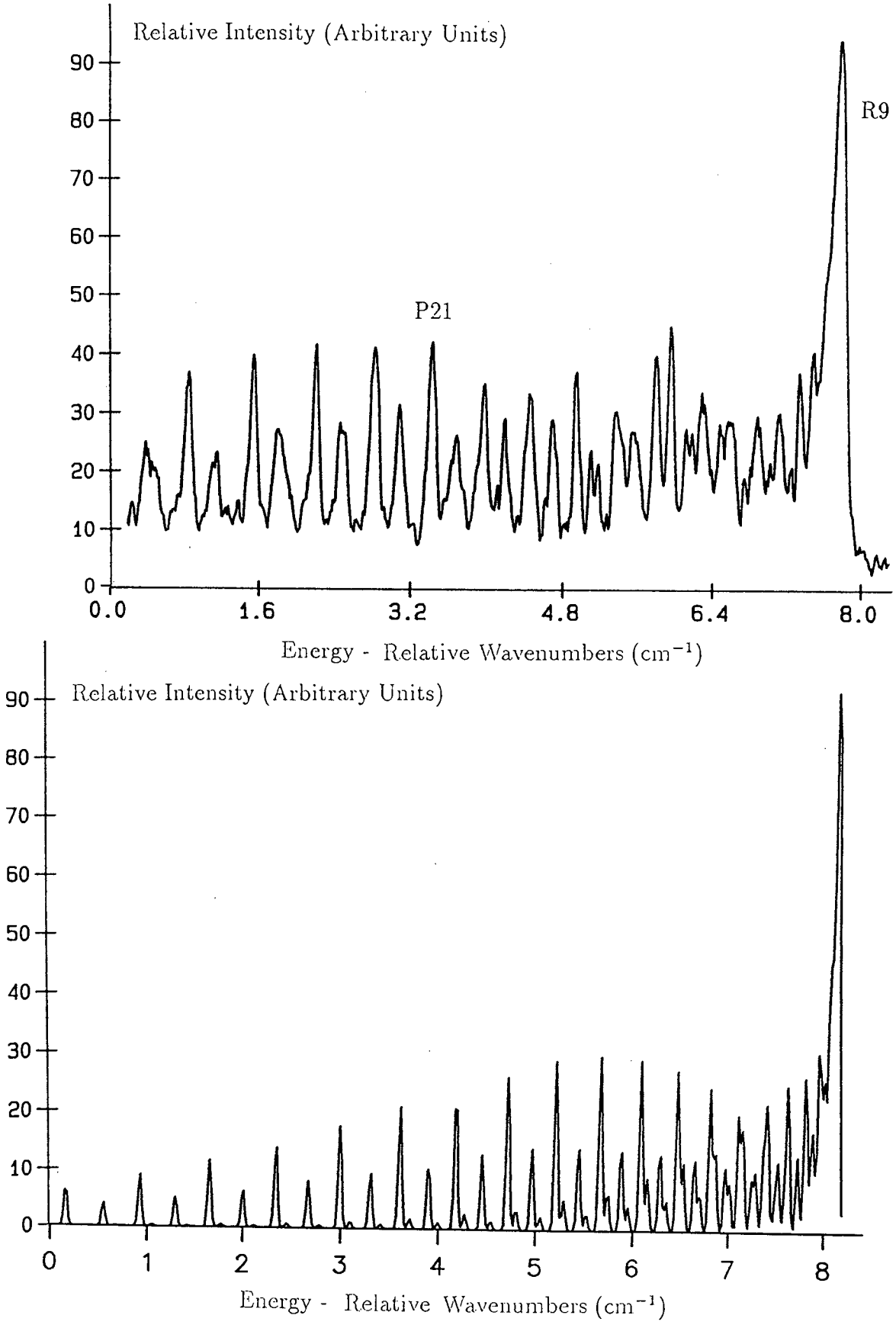

Figure 4–7: Rovibronic scan and simulation of $^{107}Ag_2$ A $\leftarrow$ X (1-0)

Table 4–8: Rovibronic Line Positions of the (1-0) Band of Ag_2 A $\leftarrow$ X

Isotopomer	Branch	J″	Data (FSR)	Fitted (FSR)	Residual (FSR)
107 - 109	P	29	2.44	2.22	0.22
107 - 109	P	28	5.79	5.82	-0.03
107 - 109	P	27	9.34	9.32	0.02
107 - 109	P	26	12.49	12.73	-0.24
107 - 109	P	25	16.22	16.04	0.18
107 - 109	P	24	19.25	19.26	-0.01
107 - 109	P	23	22.27	22.38	-0.11
107 - 109	P	22	25.22	25.41	-0.19
107 - 109	P	21	28.32	28.35	-0.03
107 - 109	P	20	31.17	31.19	-0.02
107 - 109	P	19	34.08	33.94	0.14
107 - 109	P	18	36.50	36.59	-0.09
107 - 109	P	17	39.11	39.15	-0.04
107 - 109	P	16	41.38	41.62	-0.24
107 - 109	P	15	44.46	43.99	0.47
107 - 109	R	9	72.67	72.69	-0.02

All line positions are accurate to $\pm$ 0.13 FSR

$B''_0 = 0.4798 \pm 0.0245$ FSR

$B'_1 = 0.4327 \pm 0.0263$ FSR

Reduced $\chi^2 = 0.03861$

$\Delta T_e = 68.26940 \pm 0.64606$ FSR

FSR = 0.101434 cm^{-1}

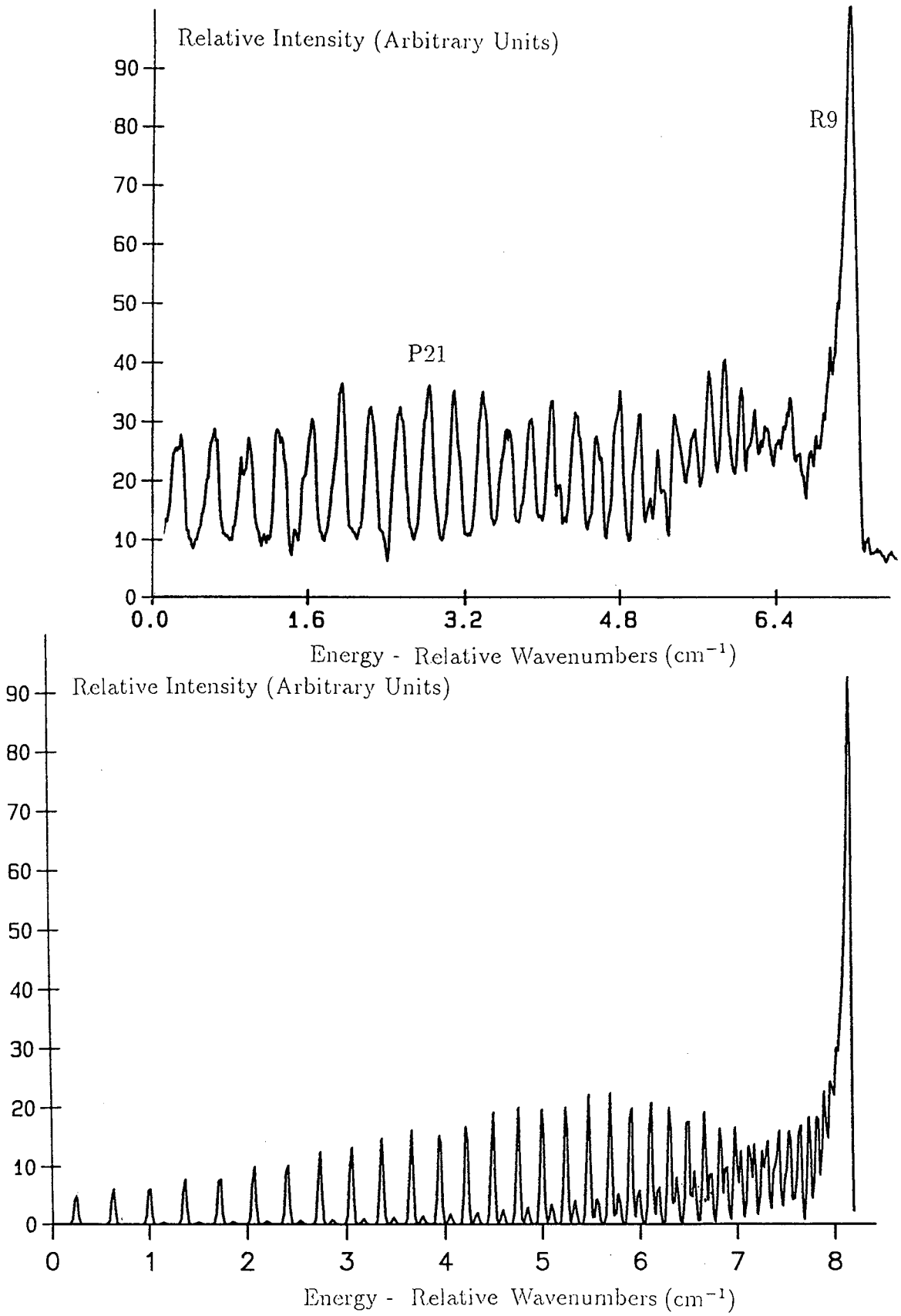

Figure 4–8: Rovibronic scan and simulation of $^{107,109}Ag_2$ A $\leftarrow$ X (1-0)

Table 4–9: Rovibronic Line Positions of the (1-0) Band of Ag_2 A $\leftarrow$ X

Isotopomer	Branch	J″	Data (FSR)	Fitted (FSR)	Residual (FSR)
109 - 109	P	27	3.61	3.47	0.14
109 - 109	P	26	6.43	6.85	-0.42
109 - 109	P	25	10.45	10.15	0.30
109 - 109	P	24	13.18	13.34	-0.16
109 - 109	P	23	16.59	16.45	0.14
109 - 109	P	22	19.19	19.46	-0.27
109 - 109	P	21	22.70	22.38	0.32
109 - 109	P	20	24.97	25.20	-0.23
109 - 109	P	19	28.13	27.93	0.20
109 - 109	P	18	30.63	30.57	0.06
109 - 109	P	17	33.35	33.11	0.24
109 - 109	P	16	35.26	35.56	-0.30
109 - 109	P	15	37.91	37.92	-0.01
109 - 109	P	14	40.17	40.18	-0.01
109 - 109	P	13	42.56	42.35	0.21
109 - 109	P	12	44.40	44.43	-0.03
109 - 109	P	11	46.49	46.41	0.08
109 - 109	P	10	48.03	48.30	-0.27
109 - 109	R	9	66.49	66.47	0.02

All line positions are accurate to $\pm$ 0.13 FSR

$B''_0 = 0.4775 \pm 0.0242$ FSR

$B'_1 = 0.4307 \pm 0.0259$ FSR

Reduced $\chi^2 = 0.05503$

$\Delta T_e = 62.05624 \pm 0.53279$ FSR

FSR = 0.101434 cm^{-1}

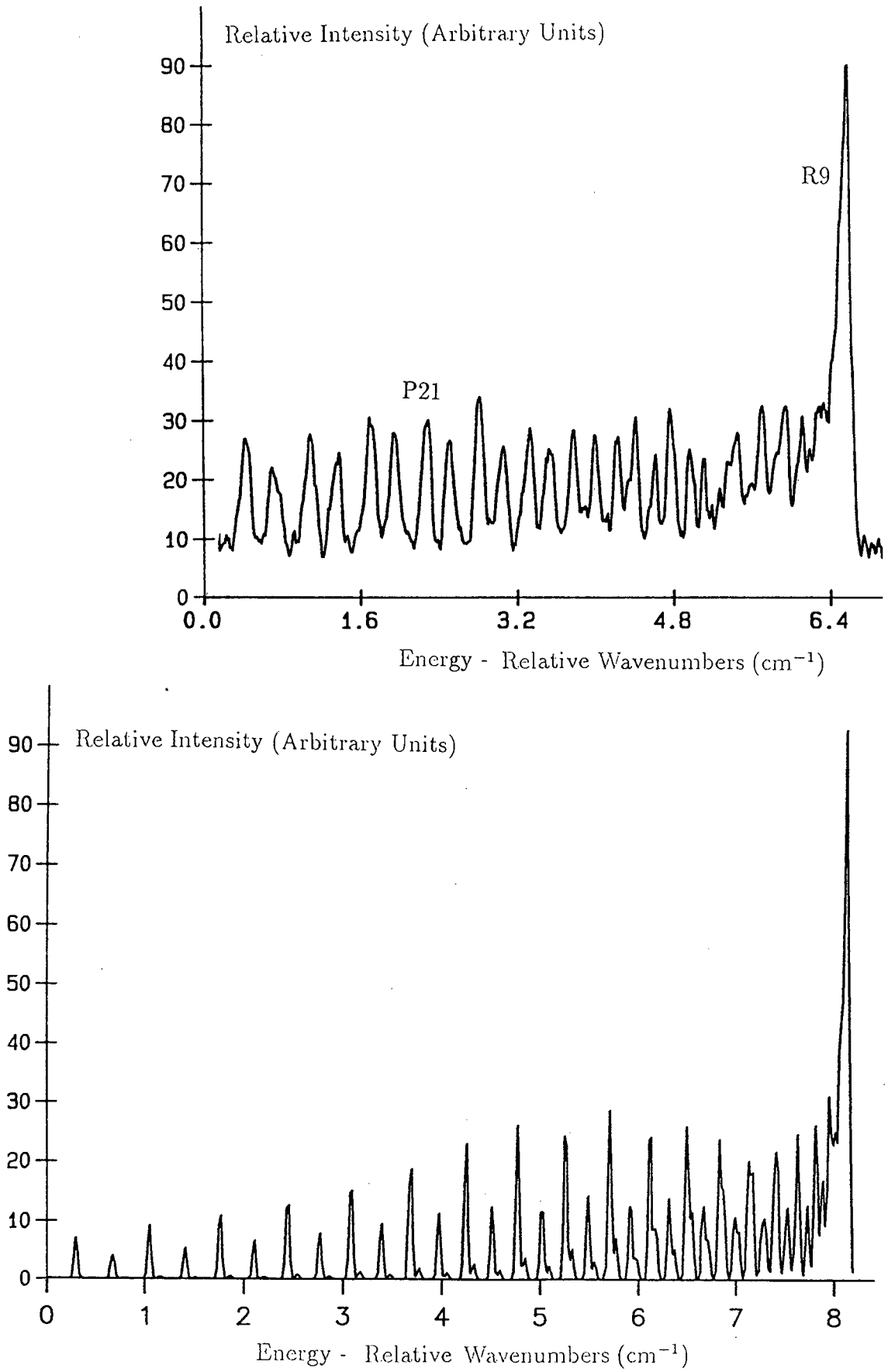

Figure 4–9: Rovibronic scan and simulation of $^{109}Ag_2$ A $\leftarrow$ X (1-0)

The α_e value calculated in this way is also reported in Table 4-10. Although the value lies in the expected area, care must be exercised over the accuracy which can be attached to it, due to the method of calculation.

4.4.3 Spectral Simulations

The simulated spectra displayed above were prepared using a computer program written in house using the FORTRAN 77 language. The ground and upper state constants obtained from the earlier tables were used to calculate the positions of the lines themselves. The intensities of the rotational lines were calculated using the Hönl-London formulae for $\Delta\Lambda = 0$ [46]. The population distribution over the ground state was assumed to follow Boltzmann statistics. In order to match the intensity distribution of the observed spectra, the temperature had to be estimated; in this case at 15 K. The spectra were generated by a convolution of the calculated line positions and intensities with a Gaussian function describing the finite bandwidth of the dye laser (0.04 cm^{-1}). In these experiments the Doppler width could be effectively ignored as it was only of the order of 5% of the laser bandwidth at these temperatures. The even/odd alteration of the homonuclear species was achieved by including a consideration of nuclear spin statistics, where the ratio of odd to even species is (I+1)/I.

4.4.4 Lifetime Measurement

An estimation of the upper state lifetime value was also made using this apparatus. The dye laser, without the intracavity etalon, was tuned such that it excited a particular band of the upper state, in this case the (0-0) transition. Spectra were then recorded using the time scan mode. The parameter being varied was that of the time delay between the pump laser and the ionising laser. Clearly, as the delay between pumping and ionising photons was increased, the ion signal fell away due to the depletion of the upper state. Such a spectra is shown in Figure 4-16.

Caution has to be exercised here, however. This spectra is a convolution of the two laser pulse profiles and the lifetime of the state. In order to obtain the true

Table 4–10: Rotational constants for the A ← X system of Ag_2

(0-0)	107-107 (cm^{-1})	107-109 (cm^{-1})	109-109 (cm^{-1})
B_0''	0.04913	0.04868	0.04823
B_0'	0.04464	0.04418	0.04377
(1-0)			
B_1'	0.04430	0.04391	0.04348
A State			
B_e	0.04480	0.04432	0.04392
α_e	0.00034	0.00027	0.00030
X State[a]			
B_e	0.04923	0.04878	0.04860
α_e	0.00019	0.00019	0.00018

[a]From the Pekeris relationship

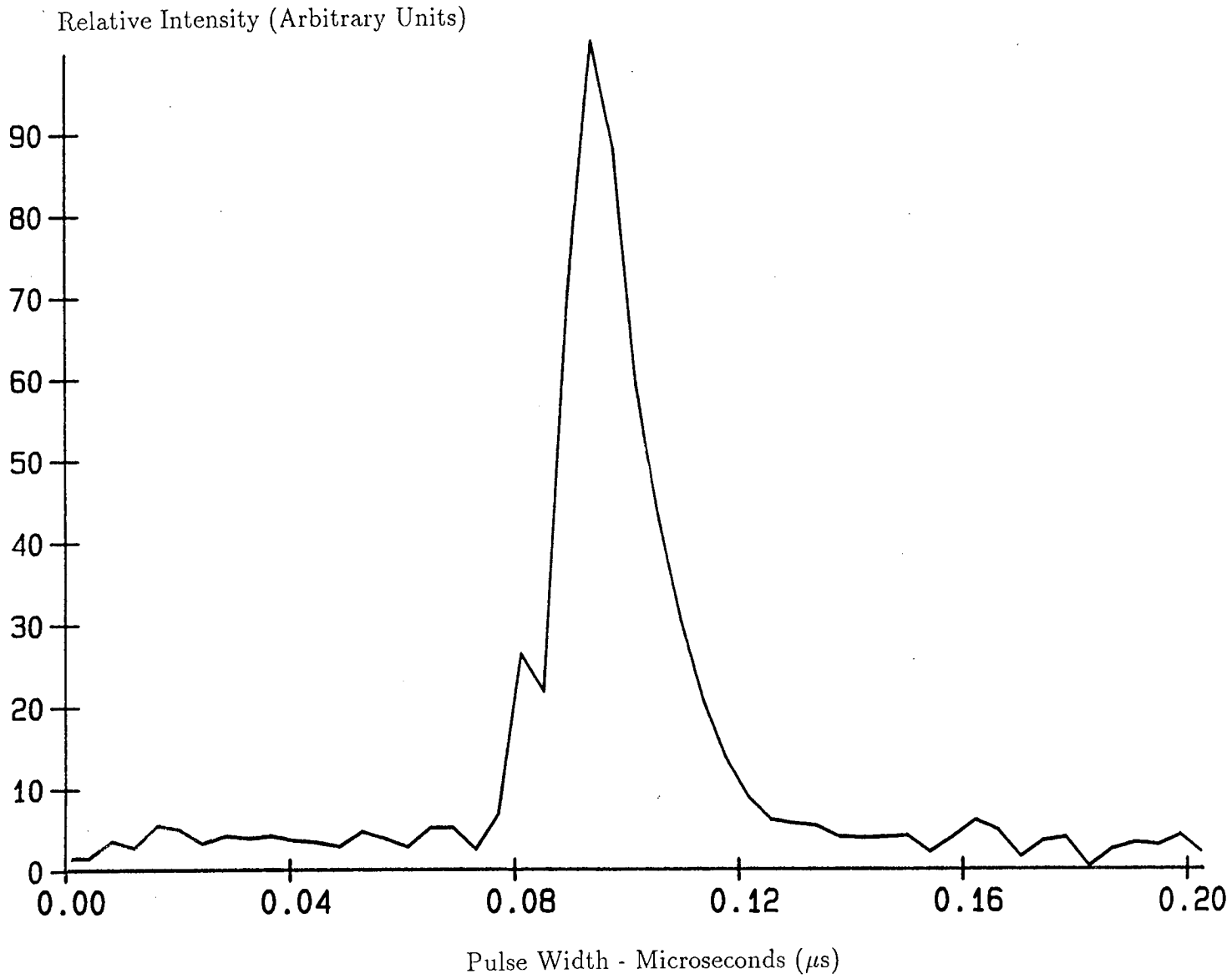

Figure 4–10: Lifetime Scan of the Ag_2 A State

lifetime, either study with much shorter laser pulses or a process of deconvolution is required. Neither has yet been undertaken. It is possible, however, to obtain an approximate upper limit value by ignoring the laser widths and regarding the decay curve as a single exponential. Such a calculation has been carried out recently, and yielded a value of 32 $\pm$ 2 ns [39]. This is in broad agreement with a crude estimation from an earlier study [33] ($\leq$ 40 ns) and the work carried out here. This short life time is indicative of a strongly allowed transition, and the absence of any enhanced signal in the Ag atom channel confirms that predissociation is not a dominant pathway in this system.

4.4.5 Spectral Calibration

The method of calibration normally applied to such spectra is that of coincident recording of a reference spectrum, commonly from an optogalvanic lamp or iodine cell. A portion of the excitation beam would be split off and directed into the lamp or cell. When radiation corresponding to a transition in the neon gas or iodine vapour was incident on the particular device, an enhanced signal would be produced. The relative intensities of these signals allowed spectra to be calibrated. However, in the region analysed above, only a few neon lines of weak intensity were available, and the method could not be used. The lack of iodine cell meant that another method of calibration was required. It has already been shown that the relative error between the band positions measured during this work and those in the literature is small. This fact was used to calibrate the free spectral range (FSR) of the fused silica etalon (Technical Optics finesse = 7) in this region. The number of FSR's between these known points was used to calculate an average FSR. This was accomplished by using a computer program written in the FORTRAN 77 language. This program accepted the positions of the etalon fringes in both wavenumbers and bin numbers, and used this data to fit a polynomial of selected degree to the data. The constants from such a fit not only allowed an average FSR for the region to be calculated, but also indicated how linear the pip spacings were in terms of wavenumber. The following results were obtained;

Using the POLFIT program

$23474.17 - 0.551(x) + 1.25\times10^{-5}(x^2)$ 1

$23466.32 - 0.552(x) + 1.31\times10^{-5}(x^2)$ 2

where;

1 - This work

2 - Kleman & Lindqvist

By then assuming that the air spaced etalon, used below, had a constant free spectral range over the area of a scan (1 nm), an average value could be obtained by simple arithmetic. The free spectral range of the air spaced etalon had to be calculated in this way for each scan. The values calculated for the A $\leftarrow$ X work are shown below;

From the experimental values of Kleman and Lindqvist

FSR of the solid state etalon = 3.3137246 cm^{-1}

FSR of the air spaced etalon = 0.100606 cm^{-1} (0-0)

0.101434 cm^{-1} (1-0)

The value for the solid state etalon reported here is in agreement with an earlier calibration of this component which gave a range of values; FSR = 3.372 cm^{-1} (600 nm) - 3.336 cm^{-1} (480 nm) [43]. Although this value should have been wavelength independent, the etalon itself was held in a sealed, fixed volume mount. As the temperature in the laboratory was known to fluctuate quite sharply, hence so did the pressure in the closed system. Pressure is related to refractive index which in turn is related to FSR. The temperature variations, therefore, had a direct bearing on the FSR value. It did not prove possible to obtain a pressure dependence curve from the etalon manufacturers, and so it was impossible to calculate the effect on the FSR value. However, over all scans, the FSR values varied by around 1% maximum, and thus this process could have made an important contribution to this variation.

4.5 The B ← X System

While not as heavily studied as the A state, various experiments have been performed in this area. Two early gas phase studies of this system recorded it with vibronic resolution. Although the exact line position values of the two studies are not coincident, the vibrational constants obtained are in good agreement. To date, only two previous studies at rovibronic resolution have been carried out. In the earlier of these [35], the initial analysis of the system was in error by +3J numbers, but this has since been corrected in line with the ground state work given above. The second study [40] is very much in agreement with the work reported here. As this work had been carried out before the above papers appeared in the literature, the comparison of results and interpretations should be a good test of their reliability and accuracy.

In terms of theoretical work, only one study has tackled this state [89], and predicted a weak state, resulting from spin-orbit coupling.

4.5.1 Vibronic Resolution

The apparatus for this study has already been shown in Figure 4-2. The dye laser was scanned using the Coumarin 153 medium over the region 560 - 550 nm with a 0.01 nm step. The dye output was then doubled via a non-centrosymmetric crystal such that the effective scan was from 280 nm - 275 nm. Figure 4-11 shows the intensity variations in ion signal for this region.

Again, a similar spectrum was obtained for all isotopomer combinations. The bands all appear to be red degraded, as for the A ← X work, indicating an increase in bond length on excitation, with an extended P branch and sharp R head. The line positions for all the measured lines are given in Table 4-11, along with the corresponding lines from the previous studies of the region.

As with the A ← X system, these line positions were used in a least squares vibrational fitting program. As the two previous data sets only offered values for

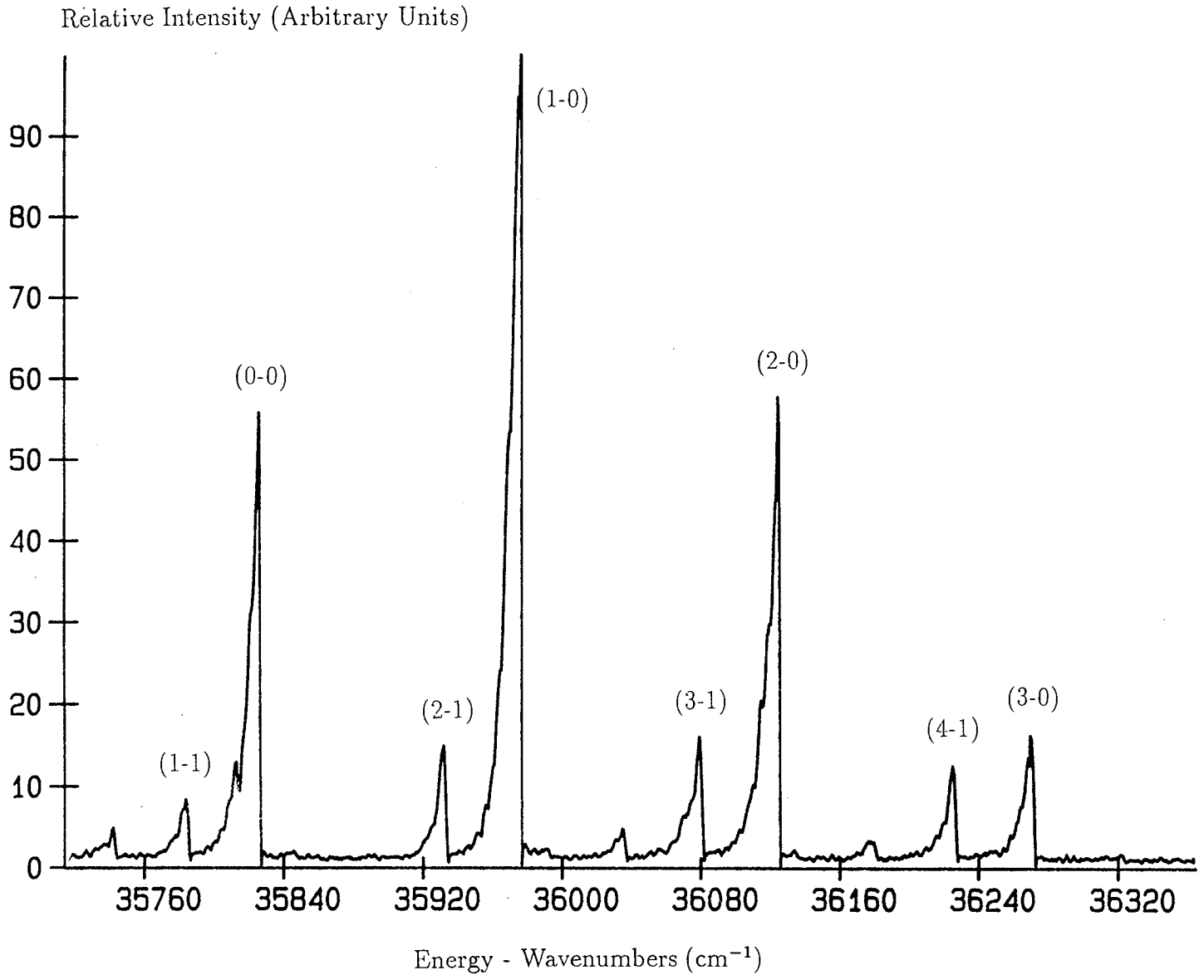

Figure 4–11: Vibronic Scan of $^{107,109}Ag_2$ B $\leftarrow$ X

Table 4–11: Vibronic Line Positions for the B ← X System of Ag_2

Isotopomer	v′	v″	Value (cm^{-1})
107 - 107	0	0	35823.3 ± 0.7
107 - 107	1	0	35974.5 ± 0.7
107 - 107	2	0	36123.3 ± 0.7
107 - 107	3	0	36271.1 ± 0.7
107 - 107	4	0	36418.6 ± 0.7
107 - 107	5	0	36563.0 ± 0.7
107 - 107	2	1	35931.8 ± 0.7
107 - 107	3	1	36079.8 ± 0.7
107 - 107	4	1	36225.8 ± 0.7
107 - 107	5	1	36370.6 ± 0.7
107 - 107	4	2	36030.9 ± 0.7
107 - 107	5	2	36181.0 ± 0.7
107 - 107	6	2	36324.5 ± 0.7
107 - 107	1	1	35783.6 ± 0.7
107 - 107	2	2	35741.2 ± 0.7
107 - 109	0	0	35823.7 ± 0.7
107 - 109	1	0	35973.2 ± 0.7
107 - 109	2	0	36122.3 ± 0.7
107 - 109	3	0	36269.4 ± 0.7
107 - 109	4	0	36414.3 ± 0.7
107 - 109	5	0	36558.0 ± 0.7
107 - 109	2	1	35930.8 ± 0.7
107 - 109	3	1	36078.1 ± 0.7
107 - 109	4	1	36224.2 ± 0.7
107 - 109	5	1	36368.6 ± 0.7
107 - 109	4	2	36034.3 ± 0.7
107 - 109	5	2	36176.2 ± 0.7
107 - 109	6	2	36322.4 ± 0.7
107 - 109	1	1	35783.6 ± 0.7
107 - 109	2	2	35741.5 ± 0.7

Table 4-11 (cont.)

109 - 109	0	0	35823.8 ± 0.7
109 - 109	1	0	35972.6 ± 0.7
109 - 109	2	0	36120.9 ± 0.7
109 - 109	3	0	36266.7 ± 0.7
109 - 109	4	0	36413.4 ± 0.7
109 - 109	5	0	36556.4 ± 0.7
109 - 109	2	1	35930.7 ± 0.7
109 - 109	3	1	36077.4 ± 0.7
109 - 109	4	1	36222.5 ± 0.7
109 - 109	5	1	36365.8 ± 0.7
109 - 109	4	2	36032.9 ± 0.7
109 - 109	5	2	36176.1 ± 0.7
109 - 109	6	2	36318.9 ± 0.7
109 - 109	1	1	35784.0 ± 0.7
109 - 109	2	2	35741.4 ± 0.7

the mixed 107 - 109 species, only the corresponding lines were used for fitting and comparison. While using all of the measured lines may have given a better set of fitted constants, the real interest was in comparing this work with the previous studies and ultimately in calibrating the air spaced etalon for future work. The results of these fitting exercises are detailed in Table 4-12.

The first set of values were obtained by floating both upper and lower state constants, where the second set are from a fit where the accepted ground state values were used. Clearly the fit of Ruamps is much better than that of this work. This was to be as expected due to the greater number of lines available. Despite this, the experimental lines have clearly been assigned correctly, and give constants within about 1 cm^{-1} of the accepted figures. A comparison with the A $\leftarrow$ X spectra shows that many more lines are recorded in this system, particularly those with excited ground state values $v'' = 1, 2$. A precise explanation of this feature has yet to be developed. Clearly the ground state is not as vibronically cold as it was previously, but the reason for this is unclear. Gas pressures and vaporisation powers were very similar in both studies, but the performance of the valve itself may have resulted in an effective reduction of gas and hence collisional cooling. Unfortunately the reproducibility of this scan was not tested, due to time constraints.

4.5.2 Rovibronic Resolution

The air spaced etalon was now placed inside the laser cavity as before, such that the reduction in bandwidth allowed single features of the system to be investigated. At the time of carrying out these experiments, the B state had not been investigated in this detail and so rovibronic scans were made of as many features as possible. Figures 4-12 to 4-16 show the scans and simulations for some of the (0-0) and (2-0) bands. All other features of the earlier vibronic scan proved too weak to be investigated. These spectra confirm that the system features P and R branches, with the rapid reversal to form an R head confirming a longer bond in the upper state. However, the existence of a Q branch is also suggested by these spectra.

Table 4–12: Vibronic Constants for $^{107,109}Ag_2$ B $\leftarrow$ X

ω_e'' (cm^{-1})	$\omega_e x_e''$ (cm^{-1})	ω_e' (cm^{-1})	$\omega_e x_e'$ (cm^{-1})	Source
191.1	0.24	151.8	0.83	- This work
193.9	0.81	153.0	0.89	- Ruamps
192.6	1.20	151.6	0.89	- Brown and Grinter
192.4	0.643	153.2	0.954	- This work
192.4	0.643	152.0	0.527	- Ruamps
192.4	0.643	150.5	0.409	- Brown and Grinter

The region around the low J value members of the P branch is almost without resolution, and has an increased intensity to that expected for a simple P branch. The inclusion of a Q branch would explain both of these points and this idea will be discussed fully in a later section.

The line positions of all features are given in Tables 4-13 to 4-21, again in units of free spectral range. The same program as before was used to fit these lines to a least squares fit of the familiar rotational energy expression given in an earlier section.

These rotational constants were then used, as before, to calculate the equilibrium values for the B state. Once again, the actual values used were not those from the above fits, but rather those from fits where the literature ground state constants [39] were included, as was done in the A state calculations. These values are given in Table 4-22, along with the calculated equilibrium constants. From the equation relating B_v and B_e given earlier, it is apparent that three sets of values were possible, dependent upon which pair of simultaneous equations were solved. All three are shown in the table.

4.5.3 Spectral Simulations

These were carried out using the same procedure as described for the A state, but with the transition now described as $\Delta\Lambda = 1$.

4.5.4 Spectral Calibration

As before, it was necessary to obtain accurate values for the etalon free spectral range in the areas of interest. This was carried out in a similar manner as before, only now there were two previous studies that could be used as guides. It was decided to use both in parallel and then compare and contrast the results obtained;

From the experimental values of Ruamps

FSR of solid state etalon = (6.7634 ± 0.0584) cm^{-1}

Table 4–13: Rovibronic Line Positions of the (0-0) Band of Ag_2 B $\leftarrow$ X

Isotopomer	Branch	J″	Data (FSR)	Fitted (FSR)	Residual (FSR)
107 - 107	P	37	0.46	0.60	-0.14
107 - 107	P	36	2.40	2.30	0.10
107 - 107	P	35	3.92	3.98	-0.06
107 - 107	P	34	5.62	5.62	0.00
107 - 107	P	33	7.22	7.22	-0.00
107 - 107	P	32	8.84	8.79	0.05
107 - 107	P	31	10.41	10.33	0.08
107 - 107	P	30	11.85	11.84	0.01
107 - 107	P	29	13.47	13.31	0.16
107 - 107	P	28	14.75	14.74	0.01
107 - 107	P	27	16.08	16.15	-0.07
107 - 107	P	26	17.36	17.52	-0.16
107 - 107	R	13	44.62	44.62	0.00

All line positions are accurate to $\pm$ 0.10 FSR

$B''_0 = 0.2459 \pm 0.0220$ FSR

$B'_0 = 0.2290 \pm 0.0237$ FSR

Reduced $\chi^2 = 0.00947$

$\Delta T_e = 41.27461 \pm 0.96077$ FSR

FSR = 0.20075 cm^{-1} (Ruamps) or

0.19806 cm^{-1} (Brown & Ginter)

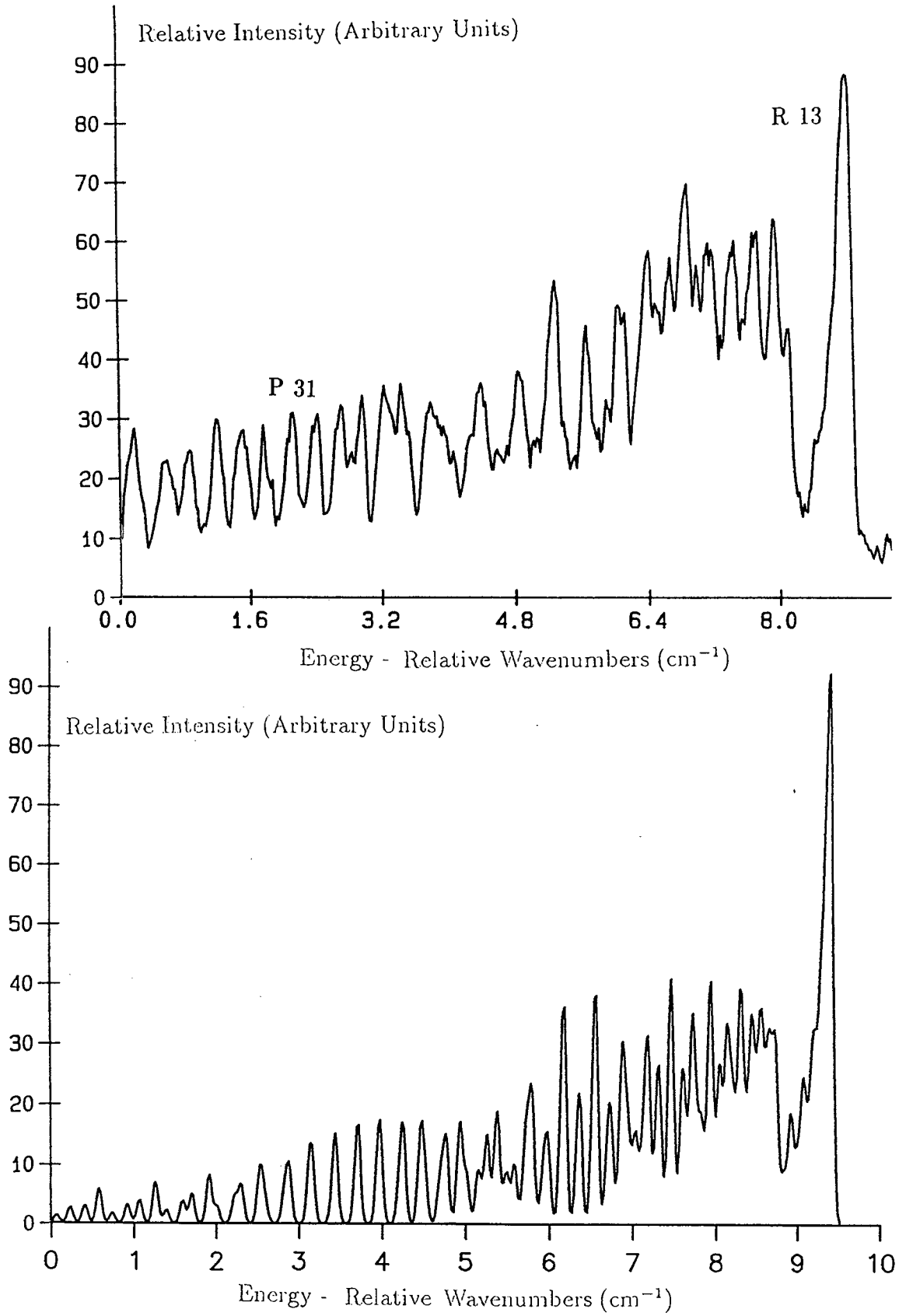

Figure 4–12: Rovibronic scan and simulation of $^{107}Ag_2$ B $\leftarrow$ X (0-0)

Table 4–14: Rovibronic Line Positions of the (0-0) Band of Ag_2 B $\leftarrow$ X

Isotopomer	Branch	J″	Data (FSR)	Fitted (FSR)	Residual (FSR)
107 - 109	P	37	1.46	1.44	0.02
107 - 109	P	36	3.05	3.12	-0.07
107 - 109	P	35	4.77	4.77	0.00
107 - 109	P	34	6.30	6.39	-0.09
107 - 109	P	33	8.07	7.97	0.10
107 - 109	P	32	9.53	9.53	0.00
107 - 109	P	31	11.10	11.04	0.06
107 - 109	P	30	12.36	12.53	-0.17
107 - 109	P	29	14.10	13.98	0.12
107 - 109	P	28	15.56	15.40	0.16
107 - 109	P	27	16.62	16.79	-0.17
107 - 109	P	26	18.17	18.14	0.03
107 - 109	P	25	19.50	19.46	0.04
107 - 109	P	5	38.85	38.87	-0.02
107 - 109	P	3	40.06	40.09	-0.03
107 - 109	R	13	45.04	45.02	0.02

All line positions are accurate to $\pm$ 0.10 FSR

$B''_0 = 0.2448 \pm 0.0200$ FSR

$B'_0 = 0.2282 \pm 0.0212$ FSR

Reduced $\chi^2 = 0.00999$

$\Delta T_e = 41.65348 \pm 0.55190$ FSR

FSR = 0.20075 cm^{-1} (Ruamps)

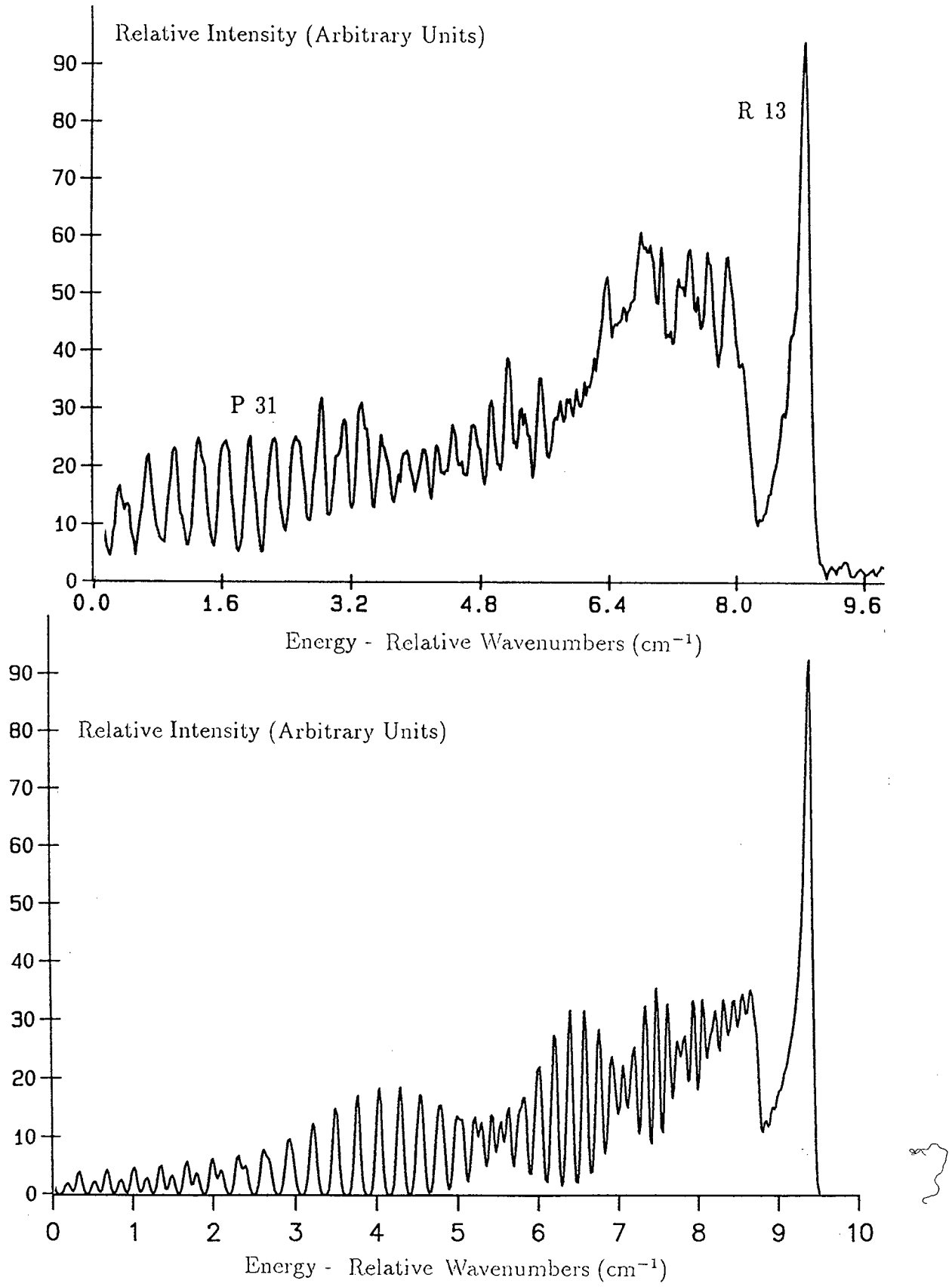

Figure 4–13: Rovibronic scan and simulation of $^{107,109}Ag_2$ B $\leftarrow$ X (0-0)

Table 4–15: Rovibronic Line Positions of the (0-0) Band of Ag_2 B $\leftarrow$ X

Isotopomer	Branch	J″	Data (FSR)	Fitted (FSR)	Residual (FSR)
109 - 109	P	38	0.73	0.65	0.08
109 - 109	P	37	2.23	2.32	-0.09
109 - 109	P	36	3.99	3.97	0.02
109 - 109	P	35	5.56	5.58	-0.02
109 - 109	P	34	7.33	7.16	0.17
109 - 109	P	33	8.52	8.71	-0.19
109 - 109	P	32	10.17	10.22	-0.05
109 - 109	P	31	11.72	11.71	0.01
109 - 109	P	30	13.04	13.16	-0.12
109 - 109	P	29	14.75	14.58	0.17
109 - 109	R	13	45.38	45.38	0.00

All line positions are accurate to $\pm$ 0.10 FSR

$B''_0 = 0.2463 \pm 0.0266$ FSR

$B'_0 = 0.2303 \pm 0.0288$ FSR

Reduced $\chi^2 = 0.01601$

$\Delta\ T_e = 41.84606 \pm 1.2128$ FSR

FSR = 0.20075 cm^{-1} (Ruamps)

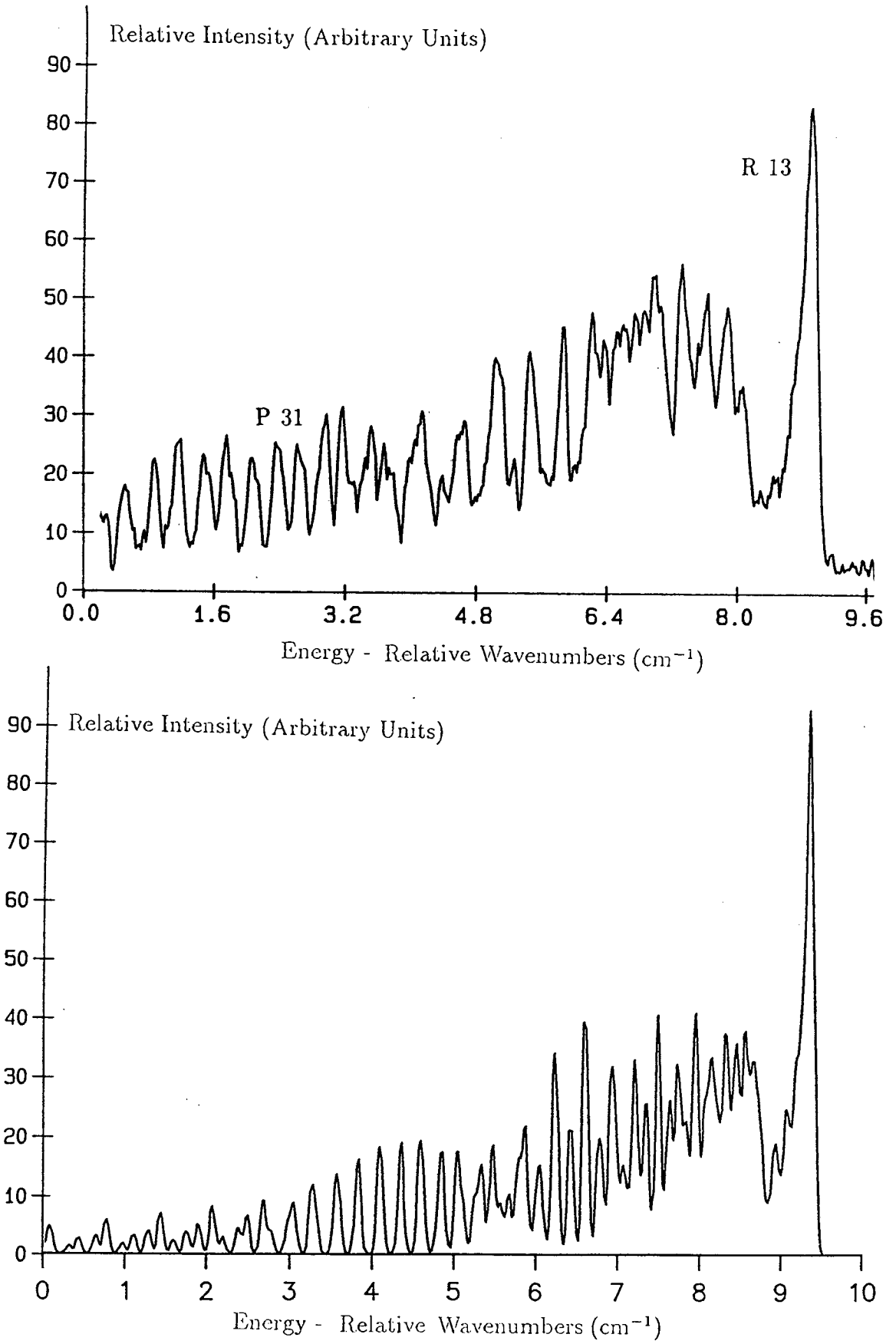

Figure 4–14: Rovibronic scan and simulation of $^{109}Ag_2$ B $\leftarrow$ X (0-0)

Table 4–16: Rovibronic Line Positions of the (1-0) Band of Ag_2 B $\leftarrow$ X

Isotopomer	Branch	J″	Data (FSR)	Fitted (FSR)	Residual (FSR)
107 - 107	P	45	0.48	0.46	0.02
107 - 107	P	43	4.59	4.64	-0.05
107 - 107	P	41	8.67	8.68	-0.01
107 - 107	P	39	12.47	12.56	-0.09
107 - 107	P	37	16.18	16.31	-0.13
107 - 107	P	35	19.92	19.90	0.02
107 - 107	P	31	26.97	26.65	0.32
107 - 107	P	30	28.20	28.24	-0.04
107 - 107	P	29	29.94	29.80	0.14
107 - 107	P	27	32.88	32.81	0.07
107 - 107	P	26	34.45	34.26	0.19
107 - 107	P	25	35.71	35.67	0.04
107 - 107	P	23	38.17	38.38	-0.21
107 - 107	P	21	40.90	40.95	-0.05
107 - 107	P	19	43.16	43.37	-0.21
107 - 107	R	13	62.20	62.17	0.03

All line positions are accurate to $\pm$ 0.10 FSR

$B''_0 = 0.2481 \pm 0.0168$ FSR

$B'_1 = 0.2298 \pm 0.0176$ FSR

Reduced $\chi^2 = 0.02263$

$\Delta\ T_e = 59.06786 \pm 0.58899$ FSR

FSR = 0.20286 cm^{-1} (Ruamps)

Table 4–17: Rovibronic Line Positions of the (1-0) Band of Ag_2 B $\leftarrow$ X

Isotopomer	Branch	J″	Data (FSR)	Fitted (FSR)	Residual (FSR)
107 - 109	P	35	17.38	17.69	-0.31
107 - 109	P	34	19.56	19.37	0.19
107 - 109	P	33	21.11	21.01	0.10
107 - 109	P	32	22.82	22.62	0.20
107 - 109	P	31	24.13	24.19	-0.06
107 - 109	P	30	25.77	25.73	0.04
107 - 109	P	29	27.10	27.23	-0.13
107 - 109	P	28	28.60	28.70	-0.10
107 - 109	P	27	30.12	30.13	-0.01
107 - 109	P	26	31.46	31.53	-0.07
107 - 109	P	25	33.08	32.89	0.19
107 - 109	P	24	34.20	34.22	-0.02
107 - 109	P	23	35.53	35.51	0.02
107 - 109	P	22	36.69	36.77	-0.08
107 - 109	P	21	38.01	38.00	0.01
107 - 109	R	13	58.83	58.83	0.00

All line positions are accurate to $\pm$ 0.10 FSR

$B''_0 = 0.2453 \pm 0.0189$ FSR

$B'_1 = 0.2278 \pm 0.0201$ FSR

Reduced $\chi^2 = 0.02027$

$\Delta\ T_e = 55.62943 \pm 0.73473$ FSR

FSR = 0.20286 cm^{-1} (Ruamps)

Table 4–18: Rovibronic Line Positions of the (1-0) Band of Ag_2 B $\leftarrow$ X

Isotopomer	Branch	J″	Data (FSR)	Fitted (FSR)	Residual (FSR)
109 - 109	P	31	21.51	21.43	0.08
109 - 109	P	30	22.80	22.98	-0.18
109 - 109	P	29	24.56	24.48	0.08
109 - 109	P	28	26.04	25.96	0.08
109 - 109	P	27	27.38	27.39	-0.01
109 - 109	P	26	28.78	28.79	-0.01
109 - 109	P	25	30.27	30.16	0.11
109 - 109	P	24	32.63	32.79	-0.16
109 - 109	P	23	33.91	34.05	-0.14
109 - 109	P	21	35.32	35.28	0.04
109 - 109	P	19	37.70	37.62	0.08
109 - 109	P	17	39.86	39.83	0.03
109 - 109	R	13	56.02	56.02	0.00

All line positions are accurate to $\pm$ 0.10 FSR

$B''_0 = 0.2436 \pm 0.0194$ FSR

$B'_1 = 0.2260 \pm 0.0210$ E-02 FSR

Reduced $\chi^2 = 0.01166$

$\Delta\ T_e = 52.89231 \pm 0.77305$ FSR

FSR = 0.20?86 cm^{-1} (Ruamps)

Table 4–19: Rovibronic Line Positions of the (2-0) Band of Ag_2 B $\leftarrow$ X

Isotopomer	Branch	J″	Data (FSR)	Fitted (FSR)	Residual (FSR)
107 - 107	P	43	3.56	3.58	-0.02
107 - 107	P	42	5.67	5.69	-0.02
107 - 107	P	41	7.93	7.76	0.17
107 - 107	P	39	11.72	11.79	-0.07
107 - 107	P	37	15.76	15.67	0.09
107 - 107	P	35	19.54	19.39	0.15
107 - 107	P	34	21.21	21.20	0.01
107 - 107	P	33	22.44	22.97	-0.53
107 - 107	P	32	24.48	24.69	-0.21
107 - 107	P	31	26.29	26.38	-0.09
107 - 107	P	30	28.34	28.04	0.30
107 - 107	P	29	29.88	29.65	0.23
107 - 107	R	13	62.90	62.90	0.00

All line positions are accurate to $\pm$ 0.10 FSR

$B''_0 = 0.2529 \pm 0.0197$ FSR

$B'_2 = 0.2338 \pm 0.0208$ FSR

Reduced $\chi^2 = 0.05421$

$\Delta\ T_e = 59.83336 \pm 0.82040$ FSR

FSR = 0.19806 cm^{-1} (Ruamps)

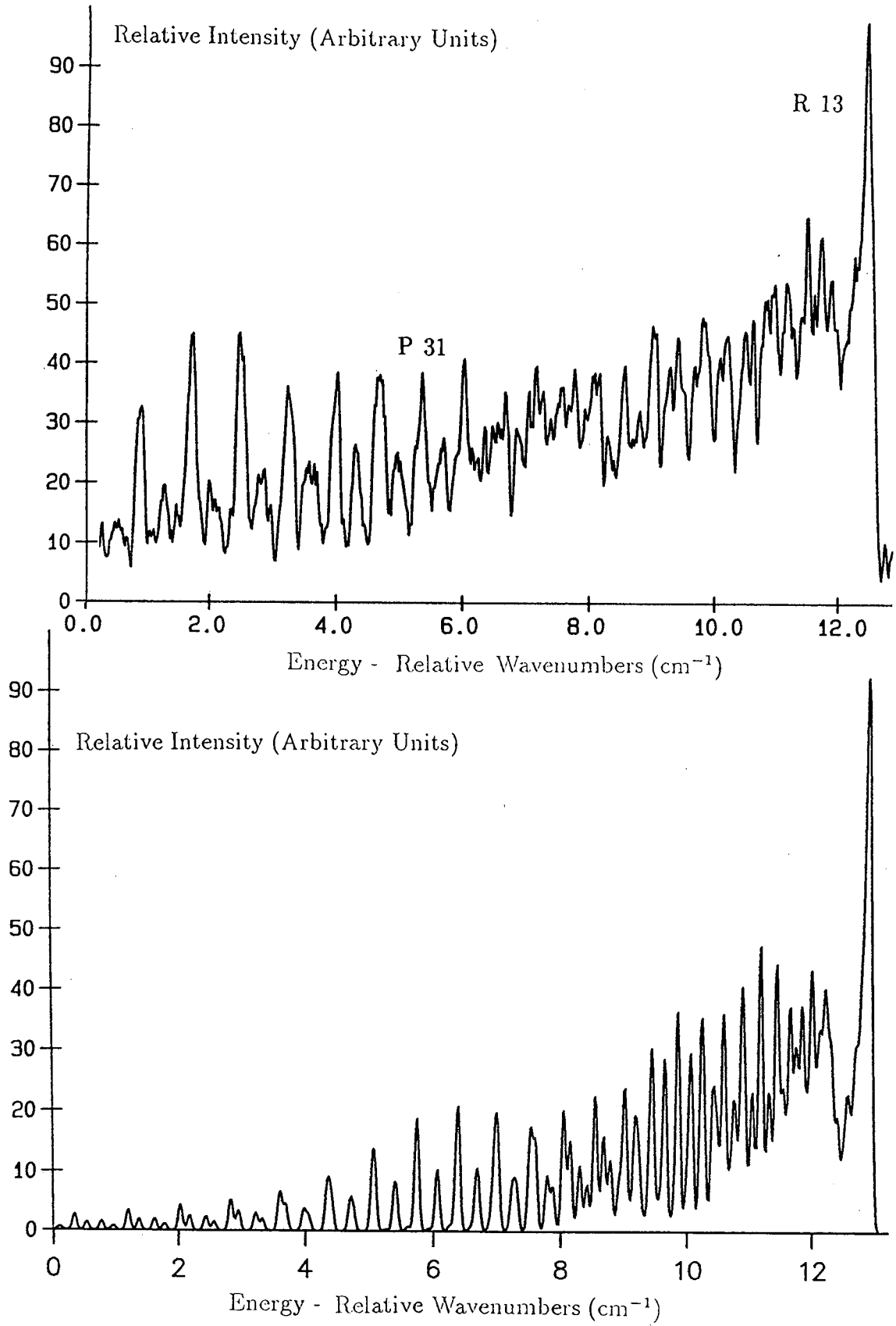

Figure 4–15: Rovibronic scan and simulation of $^{107}Ag_2$ B $\leftarrow$ X (2-0)

Table 4–20: Rovibronic Line Positions of the (2-0) Band of Ag_2 B $\leftarrow$ X

Isotopomer	Branch	J″	Data (FSR)	Fitted (FSR)	Residual (FSR)
107 - 109	P	42	-0.05	-0.03	-0.02
107 - 109	P	41	2.04	2.02	0.02
107 - 109	P	40	3.98	4.03	-0.05
107 - 109	P	39	6.08	6.01	0.07
107 - 109	P	38	7.96	7.94	0.02
107 - 109	P	37	9.76	9.84	-0.08
107 - 109	P	36	11.71	11.70	0.01
107 - 109	P	35	13.48	13.53	-0.05
107 - 109	P	34	15.47	15.31	0.16
107 - 109	P	33	17.10	17.06	0.04
107 - 109	P	32	18.91	18.77	0.14
107 - 109	P	31	20.35	20.44	-0.09
107 - 109	P	30	22.00	22.08	-0.08
107 - 109	P	29	23.46	23.68	-0.22
107 - 109	P	28	25.22	25.23	-0.01
107 - 109	P	27	26.73	26.75	-0.02
107 - 109	P	26	28.42	28.24	0.18
107 - 109	R	13	56.46	56.46	0.00

All line positions are accurate to $\pm$ 0.10 FSR

$B''_0 = 0.2486 \pm 0.0182$ FSR

$B'_2 = 0.2296 \pm 0.0191$ FSR

Reduced $\chi^2 = 0.01064$

$\Delta\ T_e = 53.48092 \pm 0.71698$ FSR

FSR = 0.19806 cm^{-1} (Ruamps)

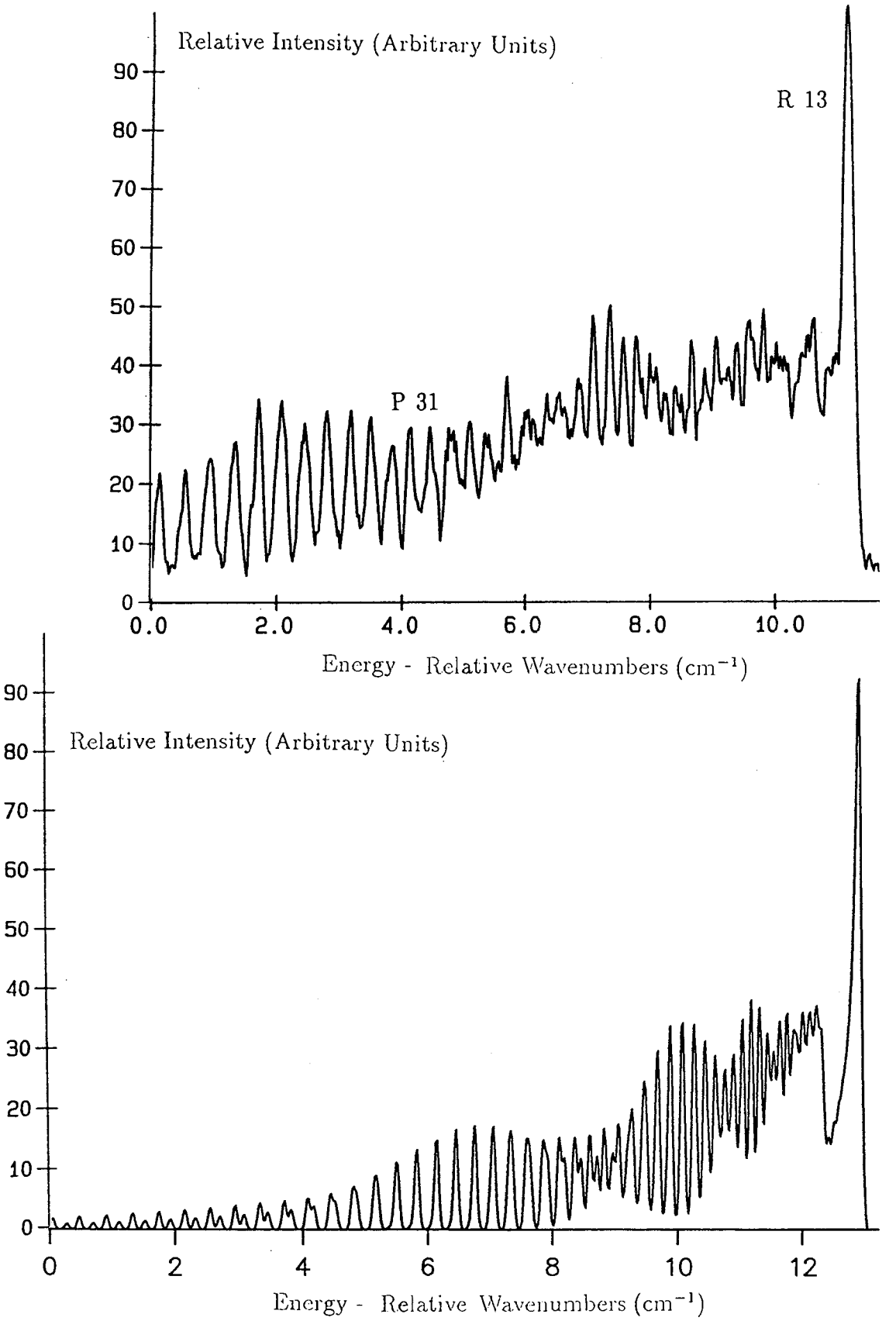

Figure 4–16: Rovibronic scan and simulation of $^{107,109}Ag_2$ B $\leftarrow$ X (2-0)

Table 4–21: Rovibronic Line Positions of the (2-0) Band of Ag_2 B $\leftarrow$ X

Isotopomer	Branch	J″	Data (FSR)	Fitted (FSR)	Residual (FSR)
109 - 109	P	41	0.22	0.04	0.18
109 - 109	P	40	2.06	1.98	0.08
109 - 109	P	39	3.88	3.88	0.00
109 - 109	P	38	5.60	5.74	-0.14
109 - 109	P	37	7.47	7.57	-0.10
109 - 109	P	36	9.21	9.36	-0.15
109 - 109	P	35	11.12	11.11	0.01
109 - 109	P	34	12.72	12.82	-0.10
109 - 109	P	33	14.46	14.49	-0.03
109 - 109	P	32	16.19	16.12	0.07
109 - 109	P	31	17.80	17.72	0.08
109 - 109	P	29	20.90	20.80	0.10
109 - 109	R	13	50.05	50.06	-0.01

All line positions are accurate to $\pm$ 0.10 FSR

$B''_0 = 0.2418 \pm 0.0222$ FSR

$B'_2 = 0.2226 \pm 0.0238$ FSR

Reduced $\chi^2 = 0.01250$

$\Delta\ T_e = 47.31687 \pm 0.95877$ FSR

FSR = 0.19806 cm^{-1} (Ruamps)

Table 4–22: Rotational constants for the B $\leftarrow$ X system of Ag_2

Transition	Constant	107-107 (cm^{-1})	107-109 (cm^{-1})	109-109 (cm^{-1})
(0-0)	B''_0	0.04913	0.04868	0.04823
	B'_0	0.04573	0.04532	0.04492
(1-0)	B'_1	0.04537	0.04507	0.04457
(2-0)	B'_2	0.04529	0.04490	0.04446

Table 4–23: Equilibrium constants for the B $\leftarrow$ X system of Ag_2.

B_v pair	Constant	107-107 (cm^{-1})	107-109 (cm^{-1})	109-109 (cm^{-1})
(0,1)	B_e	0.04591	0.04545	0.04510
	α_e	0.00036	0.00025	0.00035
(1,2)	B_e	0.04547	0.04533	0.04475
	α_e	0.00007	0.00017	0.00012
(0,2)	B_e	0.04584	0.04543	0.04504
	α_e	0.00022	0.00021	0.00023

FSR of air spaced etalon = 0.20075 cm^{-1} (0-0)
0.20286 cm^{-1} (1-0)
0.19806 cm^{-1} (2-0)

From the work of Brown and Ginter:

FSR of solid state etalon = (6.6728 ± 0.0454) cm^{-1}
FSR of air spaced etalon = 0.19806 cm^{-1} (0-0)
0.20014 cm^{-1} (1-0)
0.19541 cm^{-1} (2-0)

Clearly, these values are different from those used in the A ← X work. The free spectral range of the solid state etalon is expected to vary with wavelength as it is the refractive index of the material which determines its value. Indeed, a previous member of this group calibrated this etalon over a wide range of frequencies [43], and this work is consistent with the earlier findings.

The air spaced etalon, on the other hand, should have a free spectral range that is independent of wavelength. However, in this case, the etalon was mounted in a sealed volume. This point was discussed fully during the A state calibrations. A final point of note is that the values are approximately twice those stated in an earlier section. This is simply due to the action of the doubling crystal and its positioning relative to the point of investigation by the etalons. The light entering the etalons is not doubled by the crystal, and so appears to have a value of twice that expected.

4.6 The C ← X System

The C state of silver dimer lies close to the B state in energetic terms. It is also similar in that only vibronically resolved spectra were available from the literature, as no true rovibronic analysis had been performed. One paper, however, offered an analysis on the basis of a ground state value assumed to be the arithmetic average of the copper and gold values, in conjunction with the observed band head separations [32]. In theoretical terms, several studies have been made of this system. All agree that the upper state is of $^1\Pi_u$ (1_u) symmetry. They differ, however, in that most authors assign the state to a pure Π state where Grinter again explains it as a mixture of states with shared intensities. In the light of the conclusions drawn in the previous section, it may be that such a mixture needs to be invoked to fully describe this state.

4.6.1 Vibronic Resolution

The apparatus for this study was identical to that used in the B state work. The dye laser was now scanned over the 528 - 538 nm region of coumarin 153. After doubling, this resulted in an effective scan of the 264 - 269 nm region. Figure 4-16 shows the resulting spectrum.

Very few vibronic bands were recorded for this system. However, this was in agreement with Srdanof and Pešić, who stated that intenstiy was only appreciable in the $v'' = v'$ sequence. As the experimental technique used here only permits effective population of the lowest members of any system, it should be of little surprise that only the (0-0), (1-0) and (1-1) bands were observed with any intensity. Due to this lack of data, no real significance can be placed on the resulting vibronic fit. However, comparing this work with these previous studies gave an appreciable amount of agreement in terms of constants. The measured lines are shown in Table 4-23, with the results of the various fitting attempts displayed in Table 4-24.

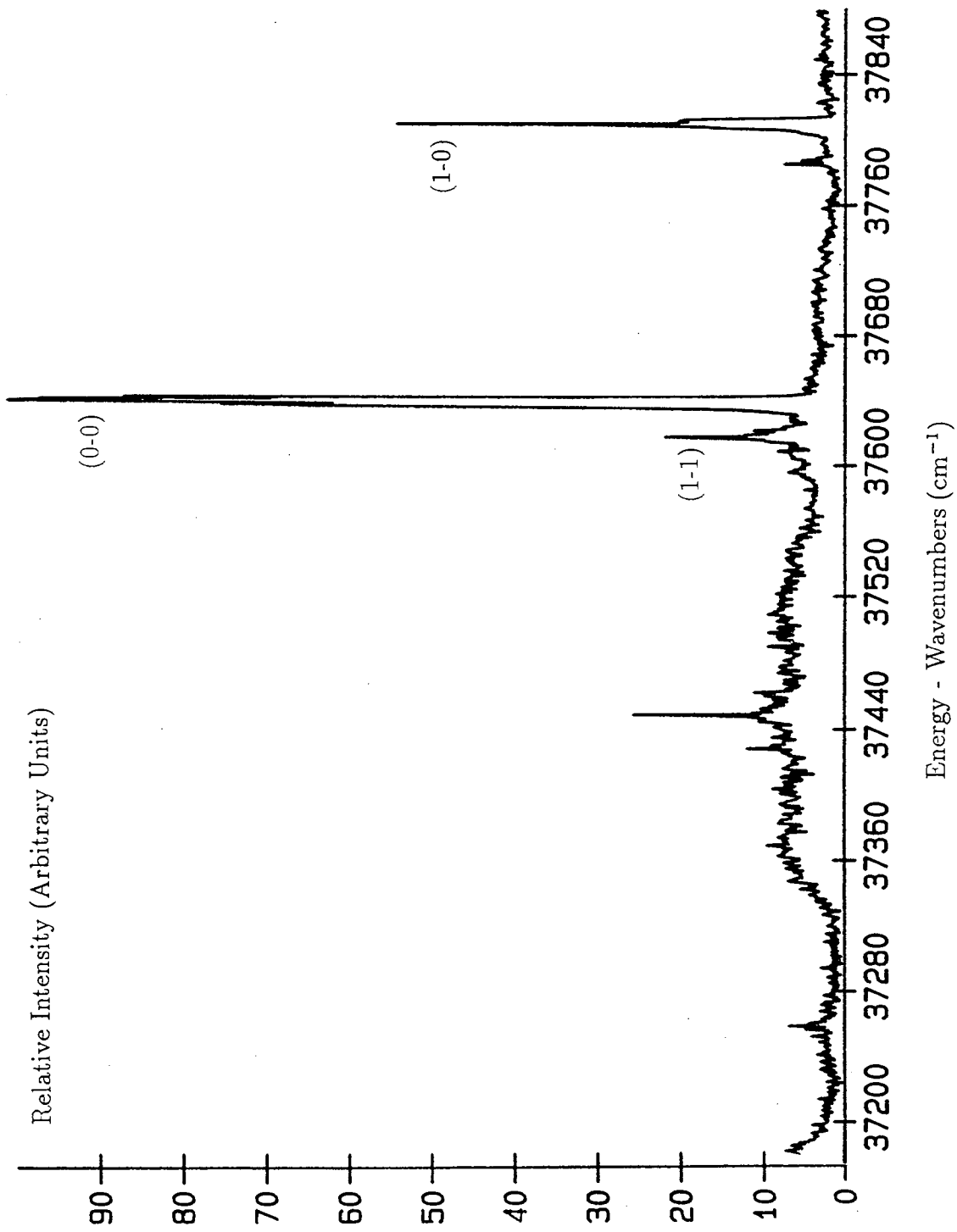

Figure 4–17: Vibronic Scan of $^{107,109}Ag_2$ C $\leftarrow$ X

Table 4–24: Vibronic Band Positions of the C ← X System of Ag_2

Isotopomer	v′	v″	Value (cm^{-1})
107 - 107	0	0	37637.5 ± 0.7
107 - 107	1	0	37808.5 ± 0.7
107 - 107	0	1	37446.7 ± 0.7
107 - 107	1	1	37615.7 ± 0.7
107 - 107	2	1	37785.4 ± 0.7
107 - 107	0	2	37256.7 ± 0.7
107 - 109	0	0	37638.0 ± 0.7
107 - 109	1	0	37807.9 ± 0.7
107 - 109	0	1	37446.8 ± 0.7
107 - 109	1	1	37616.6 ± 0.7
107 - 109	2	1	37784.9 ± 0.7
107 - 109	0	2	37257.8 ± 0.7
109 - 109	0	0	37637.4 ± 0.7
109 - 109	1	0	37807.2 ± 0.7
109 - 109	0	1	37447.0 ± 0.7
109 - 109	1	1	37616.6 ± 0.7
109 - 109	2	1	37783.7 ± 0.7
109 - 109	0	2	37259.9 ± 0.7

Table 4–25: Vibronic Constants for $^{107,109}Ag_2$ C $\leftarrow$ X

ω_e'' (cm^{-1})	$\omega_e x_e''$ (cm^{-1})	ω_e' (cm^{-1})	$\omega_e x_e'$ (cm^{-1})	Source
190.5	-	168.1	-	Brown & Ginter
192.4	0.6	173.0	1.1	
191.4	-	169.5	-	This work
192.4	0.6	169.6	0.1	

The Brown & Ginter work was based on measured positions of the Q - heads.

4.6.2 Rovibronic Resolution

The intracavity etalon was once again inserted. Due to the lack of intensity of most of the previously recorded bands, only the (0-0) feature proved intense enough to analyse further. The resulting spectra are shown in Figures 4-18 to 4-20, while the measured line positions are given in Tables 4-25 to 4-27.

It is clear from these spectra that this is not the simple $\Pi \leftarrow \Sigma$ transition that was expected. While there appears to be a strong Q branch in all of the spectra, the P and R branches are sparsely populated; each isotopomer has a mixture of strong and weak lines, with each species having a unique combination of such lines, in terms of relative FSR positions. Because of this, it has not proved possible to make a definitive assignment of these lines. What has been done, as shown in the above tables, was to assume that the ratio of ground to upper state constants was as given by Srdanof and Pešić. Using this ratio, in conjunction with the known ground state values of James, tentative assignments of these features were made. The constants resulting from these fits are given in Table 4-28. As only the (0-0) system was investigated, no experimentally derived equilibrium constants were available.

4.6.3 Spectral Simulations

These were carried out as for the B state with Hönl-London factors calculated for a $\Delta\Lambda = 1$ transition. As can be seen from the resulting spectra, this gave no reproduction of the intensity alterations present in the P and R branches of the experimental work.

4.6.4 Lifetime Measurements

Despite lying more than halfway to ionisation, it proved possible to scan this state such that an indication of its lifetime was obtained. This was achieved by attenuation of the excitation laser such that two-photon absorption from this source was less likely than excimer ionisation. The resulting spectra is shown in Figure 4-21.

Table 4–26: Rovibronic Line Positions of the (0-0) Band of Ag_2 C $\leftarrow$ X

Isotopomer	Branch	J″	Data (FSR)	Error (FSR)	Fitted (FSR)	Residual (FSR)
107 - 107	P	28	10.5823	0.0719	10.6074	-0.0252
107 - 107	P	17	16.6723	0.0719	16.6413	0.0311
107 - 107	Q	6	25.4647	0.0719	25.4218	0.0428
107 - 107	R	8	29.8365	0.0719	29.8920	-0.0554
107 - 107	R	19	35.0659	0.0719	35.0703	-0.0044
107 - 107	R	36	42.5839	0.0719	42.5728	0.0111

All line positions are accurate to ± 0.10 FSR

$B''_0 = 0.251143 \pm 1.025$ E-02 FSR

$B'_0 = 0.250092 \pm 9.905$ E-03 FSR

Reduced $\chi^2 = 0.00222$

$\Delta T_e = 25.46599 \pm 0.60711$ FSR

FSR = 0.197067 cm^{-1} (Brown & Ginter - R heads)

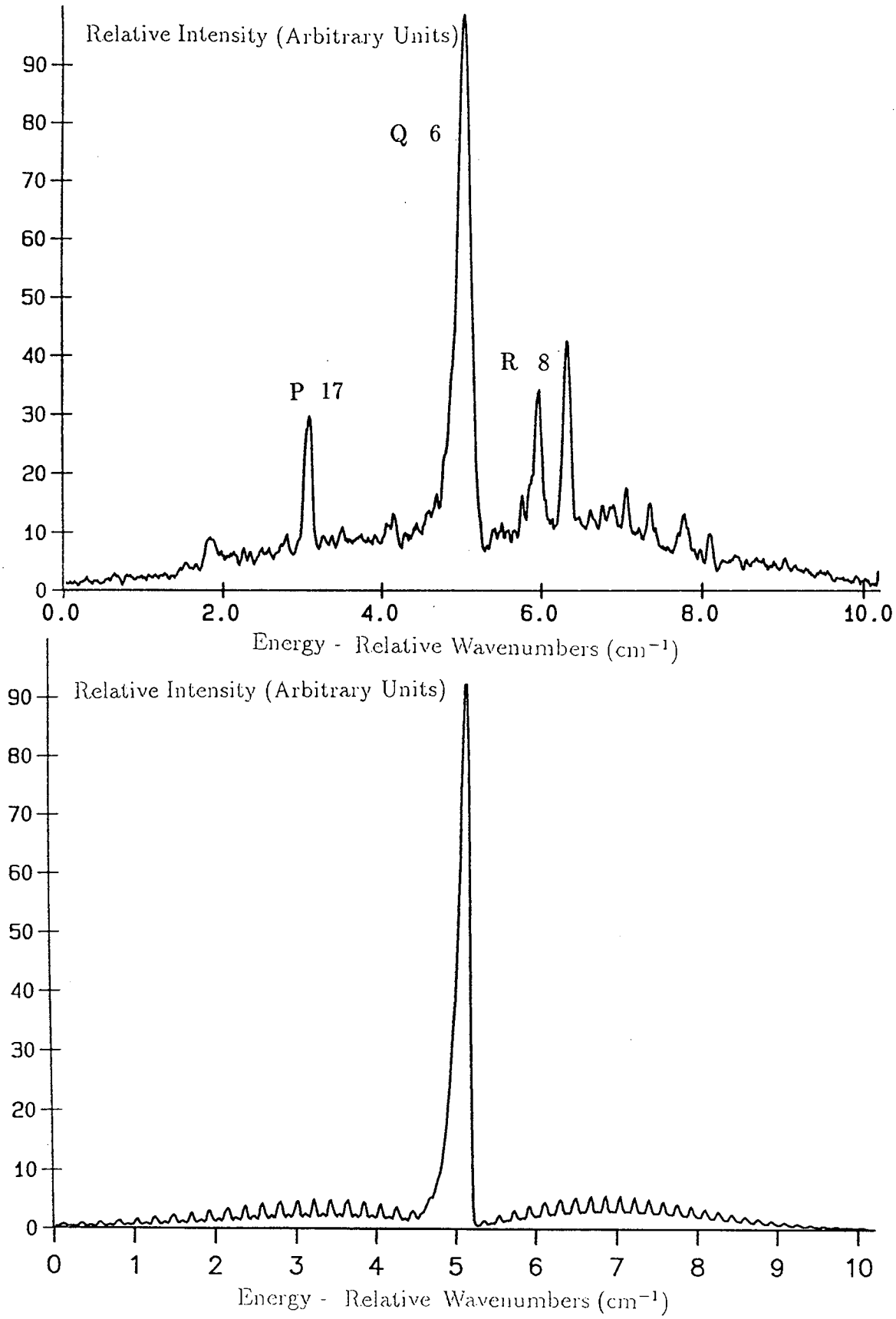

Figure 4–18: Rovibronic scan and simulation of $^{107}Ag_2$ C $\leftarrow$ X (0-0)

Table 4–27: Rovibronic Line Positions of the (0-0) Band of Ag_2 C $\leftarrow$ X

Isotopomer	Branch	J″	Data (FSR)	Error (FSR)	Fitted (FSR)	Residual (FSR)
107 - 109	P	31	9.1793	0.0719	9.1699	0.0094
107 - 109	P	19	15.6278	0.0719	15.6700	-0.0422
107 - 109	P	9	20.9075	0.0719	20.8828	0.0247
107 - 109	Q	6	25.4596	0.0719	25.3769	0.0829
107 - 109	R	9	30.2146	0.0719	30.2763	-0.0618
107 - 109	R	13	32.0710	0.0719	32.1686	-0.0976
107 - 109	R	21	35.8394	0.0719	35.8643	-0.0248
107 - 109	R	24	37.3604	0.0719	37.2195	0.1409
107 - 109	R	29	39.4948	0.0719	39.4412	0.0536
107 - 109	R	33	41.1003	0.0719	41.1852	-0.0849

All line positions are accurate to $\pm$ 0.10 FSR

$B_0'' = 0.248125 \pm 8.064$ E-03 FSR

$B_0' = 0.247198 \pm 7.831$ E-03 FSR

Reduced $\chi^2 = 0.00760$

$\Delta\ T_e = 25.41579 \pm 0.51306$ FSR

FSR = 0.197067 cm^{-1} (Brown & Ginter - R heads)

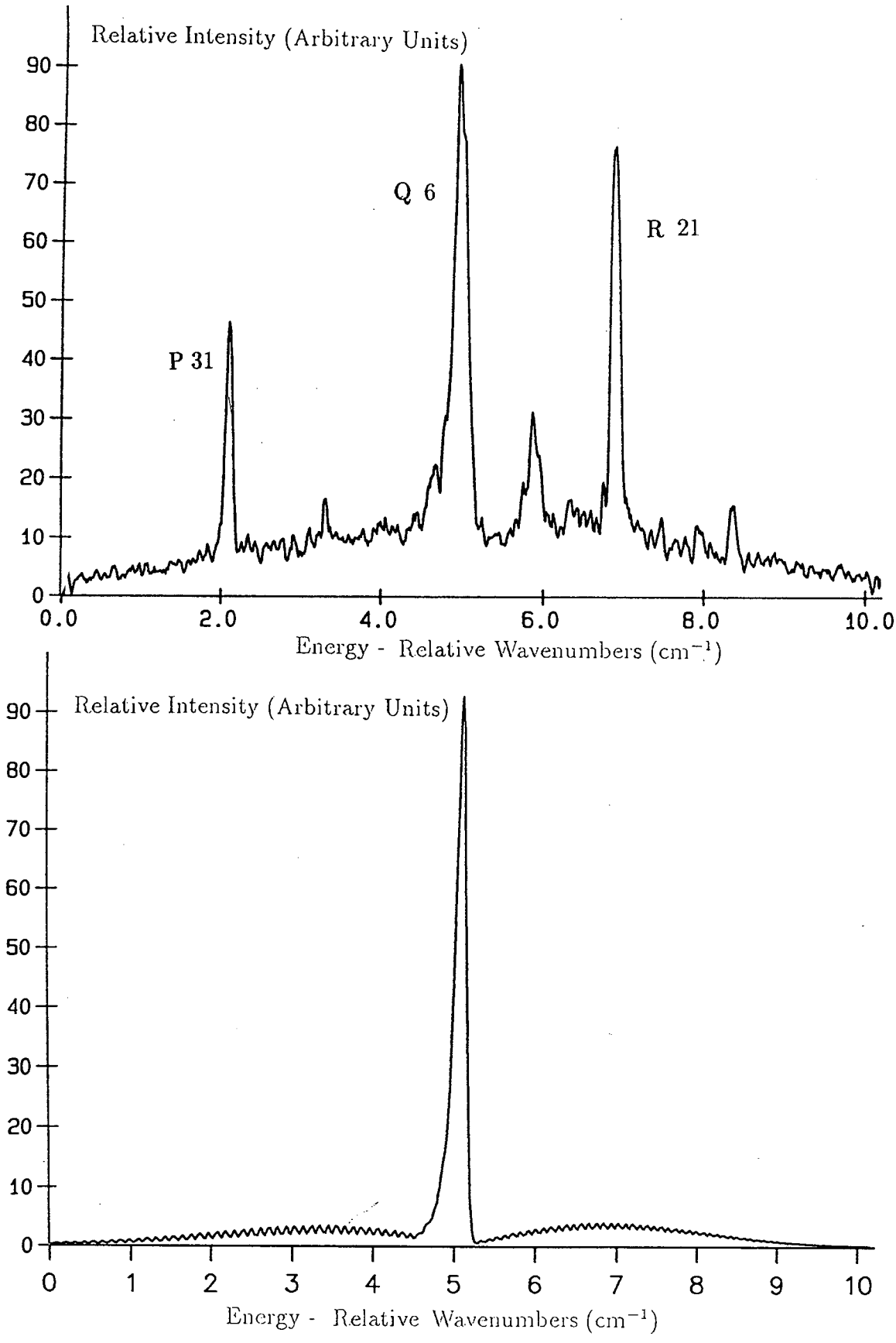

Figure 4–19: Rovibronic scan and simulation of $^{107,109}Ag_2$ C $\leftarrow$ X (0-0)

Table 4–28: Rovibronic Line Positions of the (0-0) Band of Ag_2 C $\leftarrow$ X

Isotopomer	Branch	J″	Data (FSR)	Error (FSR)	Fitted (FSR)	Residual (FSR)
109 - 109	P	29	10.6071	0.0719	10.5630	0.0441
109 - 109	P	26	12.1545	0.0719	12.1741	-0.0195
109 - 109	P	7	21.8253	0.0719	21.9870	-0.1617
109 - 109	Q	0	25.5404	0.0719	25.4324	0.1080
109 - 109	R	4	27.8452	0.0719	27.8374	0.0078
109 - 109	R	8	29.8019	0.0719	29.7277	0.0742
109 - 109	R	13	32.0410	0.0719	32.0486	-0.0076
109 - 109	R	18	34.2976	0.0719	34.3228	-0.0252
109 - 109	R	23	36.5303	0.0719	36.5504	-0.0201

All line positions are accurate to $\pm$ 0.10 FSR

$B''_0 = 0.243296 \pm 1.027$ E-02 FSR

$B'_0 = 0.242363 \pm 1.082$ E-02 FSR

Reduced $\chi^2 = 0.00780$

$\Delta\ T_e = 25.43240 \pm 0.51901$ FSR

FSR = 0.197067 cm^{-1} (Brown & Ginter - R heads)

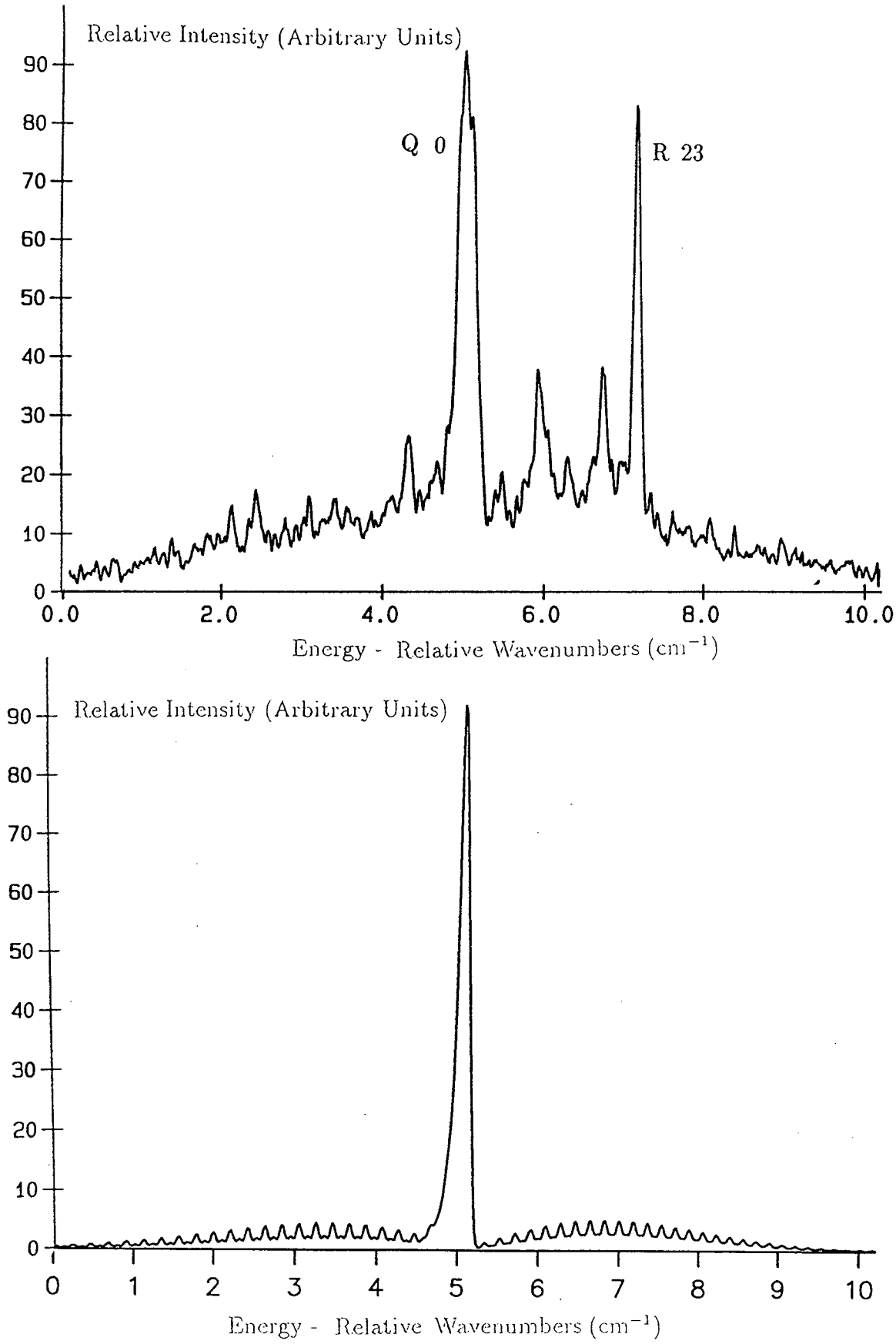

Figure 4–20: Rovibronic scan and simulation of $^{109}Ag_2$ C $\leftarrow$ X (0-0)

Table 4–29: Rotational constants for the Ag_2 C $\leftarrow$ X (0-0) system

Transition	Constant	107-107 (cm^{-1})	107-109 (cm^{-1})	109-109 (cm^{-1})
(0-0)	B_0''	0.04913	0.04868	0.04823
	B'	0.04894	0.04851	0.04806

Again, accurate deconvolution of this work has not proved possible, but the lifetime can be estimated to be of the order of 150 ns. While longer than that of the A state, it indicates that the upper state is based on an allowed transition. There was also some evidence of increased signal in the Ag atom channel, indicating that predissociation may play an important part in the description of this state.

4.6.5 Spectral Calibration

As in the previous two sections, the free spectral ranges of the etalons had to be calibrated for the appropriate spectral region. This work was carried out as before, and gave the following values;

From the experimental values of Brown & Ginter
FSR of the solid state etalon = 6.55375 cm^{-1}
FSR of the air spaced etalon = 0.197067 cm^{-1} (0-0)

4.7 Discussion

4.7.1 The X state

Silver atom is known to have a ground state electronic configuration of [Kr] $4d^{10}5s^1$. Hence, one can imagine the diatomic species as having a single bond, with configuration [Kr][Kr] $4d\sigma_g^2$ $4d\pi_u^4$ $4d\delta_u^4$ $4d\pi_g^4$ $4d\sigma_u^2$ $5s\sigma_g^2$, resulting in a $^1\Sigma_g^+$ ground state. This assignment assumes the coupling of spin and orbital angular momenta to the internuclear axis according to Hund's case a. However, in species that contain heavy nucleii, it is more likely that Hund's case c would be invoked, where Δ and Σ are no longer 'good' quantum numbers, and it is only their resultant, Ω, along the axis that is meaningful. Hence the assignment becomes 0_g^+. Whichever of these cases is selected, the assumption that all twenty d electrons play no part whatsoever in terms of bonding has been made. This can be justified by considering two

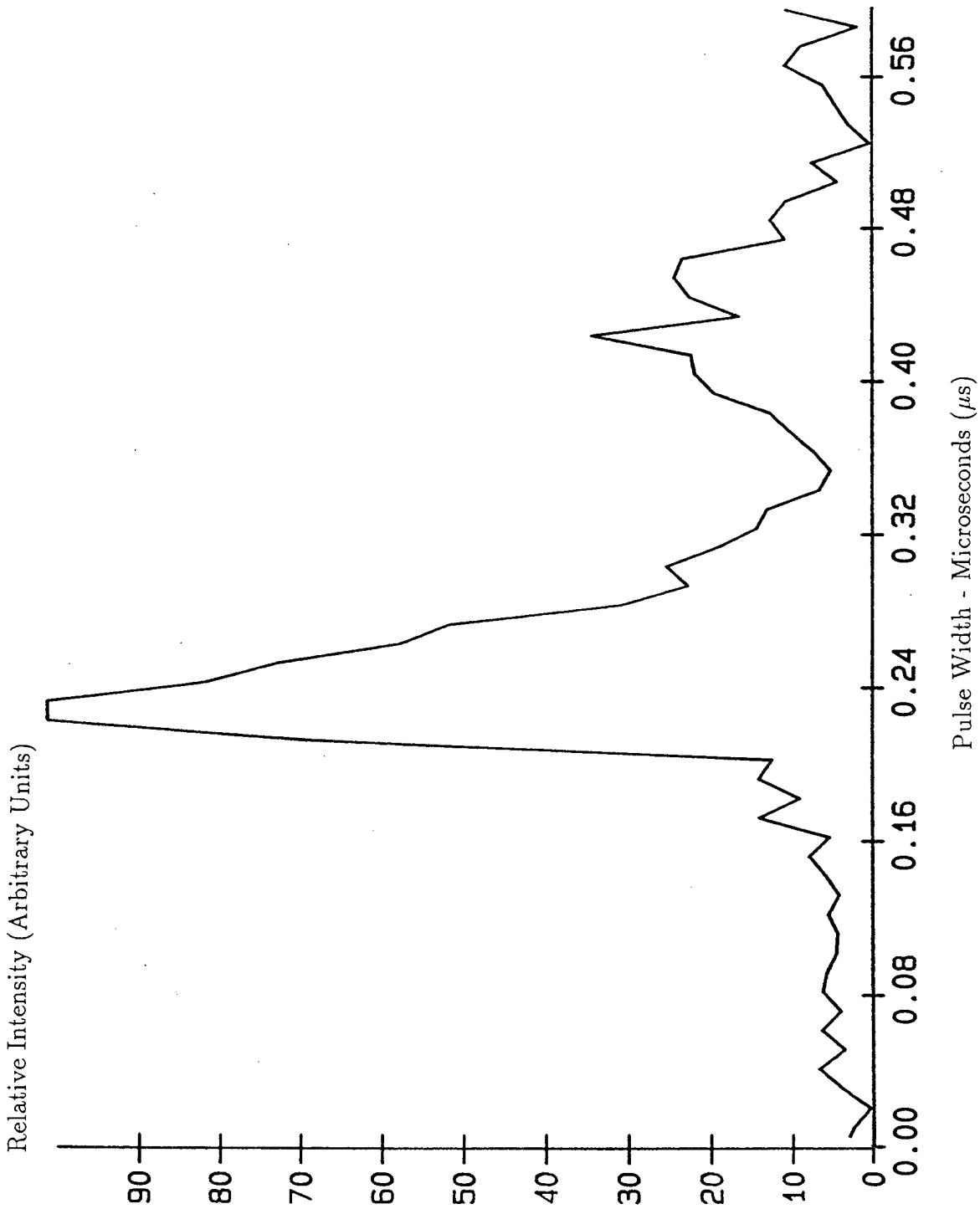

Figure 4–21: Lifetime Scan of the Ag_2 C State

pieces of information. Firstly, if d electrons are to take part, then the stable d shell atomic arrangement has to be broken. A consideration of the energy required to promote an electron from such an energetically stable configuration is of the order of 3.75 eV for the $4d^9\ 5s^2 \leftarrow 4d^{10}\ 5s^1$ promotion in silver. Hence it seems likely that the $4d^{10}\ 5s^1$ arrangement would be preserved on purely energetic grounds. Secondly, as one crosses a transition period, the nuclear charge increases while the additional electrons fill the particular d shell. Hence orbitals which have smaller principal quantum numbers will feel an increasingly attractive force, causing them to contract. In other words, for any given n, the nd level contracts more than the (n+1)s level. As silver lies to the far right of its period, the 4d orditals undergo far greater contraction than the 5s. Hence the likelihood of little d electron participation in the ground state. Due to this apparent simplicity, the coinage metals have been the subject of many theoretical studies, most of which have concentrated on the ground state.

The parameters that these studies concentrate upon are the vibrational constant, the dissociation constant and the molecular bondlength. While the work reported here concentrates upon the third of these parameters, it may be useful to briefly describe the evaluation of the other two. Experimentally, these parameters were measured via two different techniques. The vibrational constant was determined from an extensive analysis of emission data, and should therefore be well described for a large portion of the potential surface [27]. The dissociation energy was evaluated using Knudsen effusion mass spectrometry [47] - [54]. This so-called 'third-law' determination is dependent on spectroscopic constants and should therefore be quite accurate. In terms of theoretical work, the value of the vibrational constant is critical, as it determines the shape of the proposed potential surface. Also, these calculations tend to concentrate around quite small internuclear values. However, as the r values increase and the dissociation energy is approached, these calculated values are prone to some variation. While all three are of importance, a comparison of the bondlength values is of most relevance to the work reported here. The salient points of these studies are summarised in Table 4-29. While a detailed examination of this work will not be attempted here,

the experimentalist requires an appreciation of such studies, if they are to hold any useful predictive powers [55].

All electron *ab initio* studies have been performed by several groups [64] [66]. Although the resulting bondlength values are typically too high, when relativistic effects are incorporated they can approach experimental values quite closely. These studies have been particularly useful in demonstrating how little hybridisation takes place in ground state bond formation : the $s\sigma_g$ bond has around 95% s character.

Pseudopotential methods have proved useful for heavy species, due to the fact that an explicit treatment of the filled inner shell orbitals is avoided. Instead, a potential which represents the M^+ atomic core is defined. Many studies have been carried out on the silver system, with the core potential allowing for more subtle effects such as core - core overlap and polarisation [75] - [77] [82] [83]. The remaining valence electrons can be considered using configuration interaction (CI) or local spin density (LSD) methods [77] [78] [81]. Such studies have achieved a high level of accuracy.

The use of effective core potentials, with or without relativistic considerations, have also been widely used, with RECP calculations giving very good results [68] [69] [71] [72] [84] - [86]. Here, many of the electrons are considered together as a core, with only the $4d^{10}\ 5s^1$ or $4s^2\ 4p^6\ 4d^{10}\ 5s^2$ electrons of Ag to be considered in the valence space. Although generally too high by 0.1 Å, the inclusion of configuration interactions gives very good agreement for bondlength values [68].

4.7.2 The A state

Due to the $+ \leftrightarrow +$ and $g \leftrightarrow u$ selection rules that apply to homonuclear systems, the upper state symmetry of any single photon transition from the ground state should be $0_u^+(^1\Sigma_u^+)$, for a parallel or $\Delta\Omega = 0$ transition. Although few theoretical studies have been performed for this system, the $A \leftarrow X$ transition has universally been assigned as a $5s\sigma_u \leftarrow 5s\sigma_g$ promotion [8]. When one considers the large energy separation of the 5s, 5p and 4d levels, this is certainly the least energetic

Table 4–30: Theoretical Calculations on the Ground State of the Ag_2 molecule

Calculation	Relativistic (R/NR)	Bond Length (Å)	Reference
VB	NR	3.09	[56]
GVB/CI	NR	2.80	[57]
LCAO/SCF	NR	2.79	[58]
EH/CNDO	NR	2.10 - 3.00	[59] - [62]
H-F-S	NR	2.70	[63]
H-F/CI	NR	2.67 - 2.75	[64]
H-F-S	NR	2.67	[65]
H-F-S	R	2.52	[65]
MCSCF/CI	NR	2.72	[66]
SCF - Xα - SW	NR	2.84	[3]
SCF - Xα - DSW	NR	2.47	[67]
RECP/CI	R	2.52	[68]
RECP/CI	R	2.71	[69]
RECP/CI	R	2.68	[70]
RECP/CI	R	2.62	[71]
RECP/CI	R	2.58	[72]
RECP/CI	R	2.66	[73]
RECP/CI	R	2.66	[74]
PP/CI	NR	2.69	[75]
PP/LSD	NR	2.57	[76]
PP/LSD	NR	2.55	[77]
PP/LSD	NR	2.51	[78]
PP/LSD	NR	2.48	[79]
RPP/CEPA	R	2.58 - 2.61	[80]
MP/LSD	NR	2.48 - 2.55	[81]
Expt (Cu_2/Au_2)	-	2.48	[32] [31]

GVB = Generalised valence bond

LCAO = Linear combination of atomic orbitals

EH = Extended Hückel

H-F-S = Hartree-Fock-Slater

SCF = Self consistent fields

RECP = Relativistic effective core potential

PP = Pseudopotential

CI = Configuration Interaction

LSD = Local spin density

CEPA = Coupled electron pair approximation

[3]. Hence it should be a strongly allowed transtion, as it does not break any of the selection rules ($\Delta L = 0, \pm 1$ and $\Delta S = 0$). This is demonstrated by the short lifetime of the upper state (40 ns). There is also a small increase in bond length on excitation of around 0.1 Å.

The study of Basch [70] offered no quantitive description of any molecular parameters, but calculated the transition energy to be of the order of 2.59 eV, a good agreement with the experimental value of 2.85 eV. Ozin and Klotzbucher [87] used extended Hückel methods and an internuclear distance of 2.6 Åto assign the transition as $s\sigma^* \leftarrow s\sigma$, while a third study used SCF - Xα calculations for a bondlength of 2.47 Å, and predicted a transition energy of 3.19 eV [3]. One other point of note is that Ozin also calculated the energy of promotion for a transition from the 4d molecular orbitals. The $5s\sigma_u^* \leftarrow 4d\pi_g$ promotion required 5.65 eV, confirming the stable nature of the 4d shell.

This transition gives rise, formally, to an ion pair state in Hund's case a, derived from the ion pair limit at 63883 cm^{-1}. In Hund's case c, however, it can undergo avoided crossings with other 0_u^+ states, correlating with lower lying neutral atom asymptotes.

These atomic limits can arise from one of two promotions within the molecule. ^2S and ^2P arise from a fully allowed p $\leftarrow$ s promotion in one of the atoms. ^2S and ^2D, on the other hand, can be achieved by a forbidden 5s $\leftarrow$ 4d promotion, facilitated by a spin-orbit coupling mechanism. Table 4-30 shows the lowest energy atomic limits that can arise from these promotions, while Table 4-31 shows some symmetry combinations that these limits can give rise to. Of these, some are suitable as upper states. From the $^2P + {}^2S$ limits there are two possibilities;

$$^1\Sigma_u^+ \quad (4d^{10})(4d^{10})\ (5s\sigma_g)^1(5p\sigma_u^*)^1$$
$$^3\Pi(0_u^+) \quad (4d^{10})(4d^{10})\ (5s\sigma_g)^1(5p\pi_u)^1$$

The $^1\Sigma_u$ state reduces the formal bond order to zero, resulting in a weak bond [85]. Also, the pσ^* orbital is the most highly excited 5p derived molecular orbital. It seems unlikely that this configuration plays an extensive part in upper state

Table 4–31: Lowest Atomic Limits for the Ag atom

Configuration	Term	J	Energy (cm^{-1}) (a)	Splitting (cm^{-1})
$4d^{10}5s$	^2S	1/2	0.00	-
$4d^{10}5p$	^2P	1/2	29552.05	920.66
		3/2	30472.71	
$4d^95s^2$	^2D	5/2	30242.26	4471.90
		3/2	34714.16	
$4d^{10}6s$	^2S	1/2	42556.15	-
$4d^{10}6p$	^2P	1/2	48297.38	203.39
		3/2	48500.77	

(a) All values from reference [88]

Table 4–32: Symmetry correlations in Ag_2

Atomic Limits	Hunds Case a (**L**,**S**)	Hunds Case c (*j*,*j*)
$^2S + {}^2S$	$^1\Sigma^+, {}^3\Sigma^+$	$0^+,0^-,1$
$^2S + {}^2P$	$^1\Sigma^+, {}^3\Sigma^+, {}^1\Pi, {}^3\Pi$	$0^+, 0^-, 0^+, 0^-, 1, 1, 1, 2$
$^2S + {}^2D$	$^1\Sigma^+, {}^3\Sigma^+, {}^1\Pi, {}^3\Pi, {}^1\Delta, {}^3\Delta$	$0^+, 0^-, 0^+, 0^-, 1,1,1,1,2,2,2,3$

All the above have g and u pairs for the homonuclear species $^{107}Ag_2$ and $^{109}Ag_2$.

bonding. The $^3\Pi$ state is generated by spin-orbit coupling of sσ and pπ. It has been calculated that this state lies some 2.72 eV from the atomic limits. This is close to the experimentally measured value of 2.85 eV, and indicates a strongly bound state. The small electronic isotope shift measured in this work and elsewhere [33] is also consistent with a state dominated by filled d shells. However, the ^{2}P spin-orbit multiplets are only 920.7 cm^{-1} apart, whereas the observed transition, $^3\Pi$ $(0_u^+) \leftarrow$ X $(^1\Sigma_g^+)$ is intense and would require greater splitting. The ^{2}D + ^{2}S limits provide the following options;

$$^1\Sigma_u^+ \quad (d\sigma_g)^1\,(d\pi_u)^4\,(d\delta_g)^4\,(d\pi_g^*)^4\,(d\sigma_u^*)^2\,(s\sigma_g)^2\,(s\sigma_u^*)^1$$
$$^3\Pi(0_u^+) \quad (d\sigma_g)^2\,(d\pi_u)^4\,(d\delta_g)^4\,(d\pi_g^*)^3\,(d\sigma_u^*)^2\,(s\sigma_g)^2\,(s\sigma_u^*)^1$$

These species arise from spin-orbit coupling and contain a d core vacancy. The atomic spin-orbit coupling in ^{2}D is large - of the order of 4471.9 cm^{-1}. This favours an $0^+ \leftarrow 0^+$ promotion. However, the atomic transition ^{2}D $\leftarrow$ ^{2}S is very weak, and the resulting bond order falls from 1 to 1/2, resulting in a weak bond. Clearly, while each of these configurations has some positive aspects, each also contains at least one point that is inconsistent with the observed A state. While the work reported here has improved the quality of the available spectra, these have not allowed any definitive insight into the make-up of the state itself and, at present, the best estimate of this state is an admixture of the 0_u^+ states and the ion pair state.

4.7.3 The B state

Clearly, the rovibronic spectra recorded for the B state are not of as high resolution as those shown earlier for the A state, due to the fact that the dye laser output had to be frequency doubled in order to access the required region. This resulted in an effective doubling of the laser bandwidth. Hence for low J values the bandwidth (0.08 cm^{-1}) was of the order of the spacing between adjacent lines and resolution was lost. This problem resolved itself at higher J values where the spacing between adjacent lines increased sufficiently. Hence the P branches of these spectra have

areas of resolved (high J) and non-resolved (low J) lines. This proved to be a great hurdle in the accurate assignment of the resolved J lines, where an error of 1 or 2 J numbers could easily have passed undetected. However, this problem was reduced because the ratio of the upper and lower constants remained fairly constant over this range. As the lower state constants were known, then the upper state values could be approached with some confidence. Another feature of these spectra was an apparent 'hump' of enhanced intensity in the non-resolved region. This was originally thought to be simply a consequence of the low resolution in this area - after all, the B $\leftarrow$ X transition had been well documented as $\Sigma \leftarrow \Sigma$ [25] [26] [35]. However, on further consideration of the experimental evidence, alongside some simulations of likely transitions, it was apparent that this hump was in fact due to the existence of a Q-branch. Not only did this assumption explain the loss of resolution in the low J values, but also the 'beating' interference pattern that was evident in the mid J range.

As a result of this work, the B $\leftarrow$ X spectra are now believed to contain P, Q and R branches, and therefore appear to show a perpendicular transition. While this analysis is at odds with many of the earlier studies, most of these did not have the necessary resolution to identify the transition beyond reasonable doubt. Also, the first rovibronic study did not identify the Q-branch, as the limited resolution available prevented the region around the bandhead(s) being properly investigated. The most recent rovibronic study, however, is in agreement with this analysis to such an extent that both constants and spectra are in excellent agreement [40].

Having identified the symmetry of the B state, this transition needs to be defined in terms of electronic promotions. As stated earlier, only one theoretical study has made any attempt to explain the B $\leftarrow$ X transition. In his general analysis of silver dimer below 5.5 eV, Grinter highlighted the fact that there are too few allowed transitions in this area to support all the observed gas phase spectra [89]. A simple molecular orbital diagram offers only three allowed transitions below 40,000 cm^{-1}, where five have been observed. This situation was resolved by invoking second order spin-orbit coupling to permit the mixing of states with different symmetries, as well as the more common spin-orbit coupling for states of

different multiplicities. Both these processes result in intensity being transferred from forbidden to allowed transitions. In this way, the B state was described as a mixture of two states, $^3\Sigma_1$ and $^1\Pi_1$, in nearly equal quantities. Here, the intensity of the transition was supplied by the allowed π component. The sources of these states can again be investigated by way of their atomic limit configurations. The $^2S + {}^2P$ limits give;

$$^3\Sigma \quad (4d^{10})(4d^{10})(5s\sigma)(5p\sigma^*) \text{ and } (4d^{10})(4d^{10})(5s\sigma)(5s\sigma^*)$$
$$^1\Pi \quad (4d^{10})(4d^{10})(5s\sigma)(5p\pi)$$

The first of the $^3\Sigma$ representations is that of the highest promotion within the p levels. The singlet equivalent was described in the A state analysis. Again, this is a highly energetic promotion to an anti-bonding orbital and would be unlikely to offer much to a bonding molecular state. The second $^3\Sigma$ scheme is the triplet equivalent of the ion pair excitation from the A state. Again anti-bonding, there seems little to recommend this configuration. The $^1\Pi$, on the other hand, is a fully allowed, bonding scheme. Clearly, this is one way in which the required intensity could be transferred. However, if this were the only upper state involved, then the transition would be $\Delta\Omega = +1$, and the resulting spectra should show a Q branch. While the author of this analysis believed otherwise, it now seems likely that this component is indeed the B state. As $\Omega = 1$ for the upper state, no such mixing is required to explain this state.

The upper states arising from $^2S + {}^2D$ atomic limits are;

$$^3\Sigma \quad (4d^{10})(4d^{9})(5s\sigma^2)(5s\sigma^*)$$
$$^1\Pi \quad (4d^{10})(4d^{9})(5s\sigma^2)(5s\sigma^*)$$

Both these configurations arise from d shell promotions to the anti-bonding 5s level, resulting in a weakening of the bond. The first involves a $d\sigma$ electron, while the second uses a $d\pi$. The same arguments apply as in the A state work; large spin-orbit coupling favouring promotion, but weak d $\leftarrow$ s atomic transition resulting in an inconclusive result. It seems most likely that a simple $\Pi \leftarrow \Sigma$ description is sufficient to describe this state.

4.7.4 The C state

No rotational work has previously been done on this state. However, from some of the vibronic studies the symmetry has been assigned as Π. Indeed, the $^1\Pi$ element from $^2S + {}^2P$ atomic limits, which was discussed as part of the B state work, has generally been considered an ideal candidate for this state. However, as this symmetry element was used earlier in a description of the B state, some alternative description of this state is now required.

In an earlier study [32] an estimate of the respective bond lengths was made from an average of the ground state values of Cu_2 and Au_2. This value was then used, in conjunction with the measured band head separations of some C $\leftarrow$ X members, to calculate the bond length in the upper state. Care must be taken here as no account was taken of the relativistic contraction that occurs as mass increases. Electrons that populate orbitals which penetrate close to the nucleus undergo increasingly attractive fields as nuclear mass increases. They are accelerated to speeds close to that of light, and the corresponding Lorentz contraction results in a smaller effective orbital [90]. Indeed, such is this effect, that it is now known that the bond length in gold is actually less than that in silver. However, if we assume that the *ratio* of the bond lengths transcends this problem, then the analysis offered here may yet be correct. All of this does nothing to explain the intensity profiles of these spectra. One possible explanation would be that the C state is perturbed by another, as yet unidentified, state of the diatomic silver species. If this interaction resulted in predissociation of all but a few J levels, the resulting spectra could be sparce in nature. A similar, if inverted, situation has been reported in several papers on the Cr_2 system [91] - [93]. Here the P branch envelope was almost sinusoidal in intensity, with two distinct regions of reduced intensity. This was rationalised as being due to two predissociating states crossing at specific J levels. With this in mind, the C state spectra was re-examined. Unfortunately, no such explanation is plausible. The spectra reported here do not so much have periods of lesser intensity, but have sharp, single J lines, with very little intensity elsewhere. While no firm conclusions have been reached

as to the nature or origin of this state, the work reported here provides a firm basis for future studies, as further analysis of this system is clearly required.

4.8 Future Work

In this chapter some analyses of the X, A, B and C states of the silver dimer molecule have been shown. Some of this work has proved to be more conclusive than the rest. Much work has been done on the X and A states of silver dimer, and much is now known about these systems. The B state has recently been studied by two other groups, and good agreement has been obtained between the results of one of those groups and this work. However, the quality of the spectra shown here is such that they would benefit from being recorded at higher resolution. This would accomplish two things. Firstly, the numbering of particular J lines could be confirmed beyond any doubt. Secondly, the 'hump' nature of the low J values would be resolved into individual rovibronic lines, which could then be measured and assigned. This work could be carried out in two ways. The dye system used in this work has the facility for further bandwidth reduction via a pressure tuning grating block. Alternatively, a continuous wave (CW) dye laser would permit the resolution of the R head and the P and Q lines giving unambiguous spectra for this state. The work reported here on the C state requires reinvestigation. Although increased resolution is always advantageous, it did not appear to be the main reason behind the quality of spectra reported here. Indeed, it may be that these spectra are sufficient and that it is our understanding of the silver dimer system in this region which needs to be improved. By way of conclusion, Figure 4-22 shows the present understanding of the states of Ag_2 calculated by RKR methods. This calculation was achieved by use of a program written in the FORTRAN 77 language, and the various spectroscopic constants that were available at that time. While the work reported in this thesis has added to the overall picture of this molecule, there is clearly still much that has to be discovered.

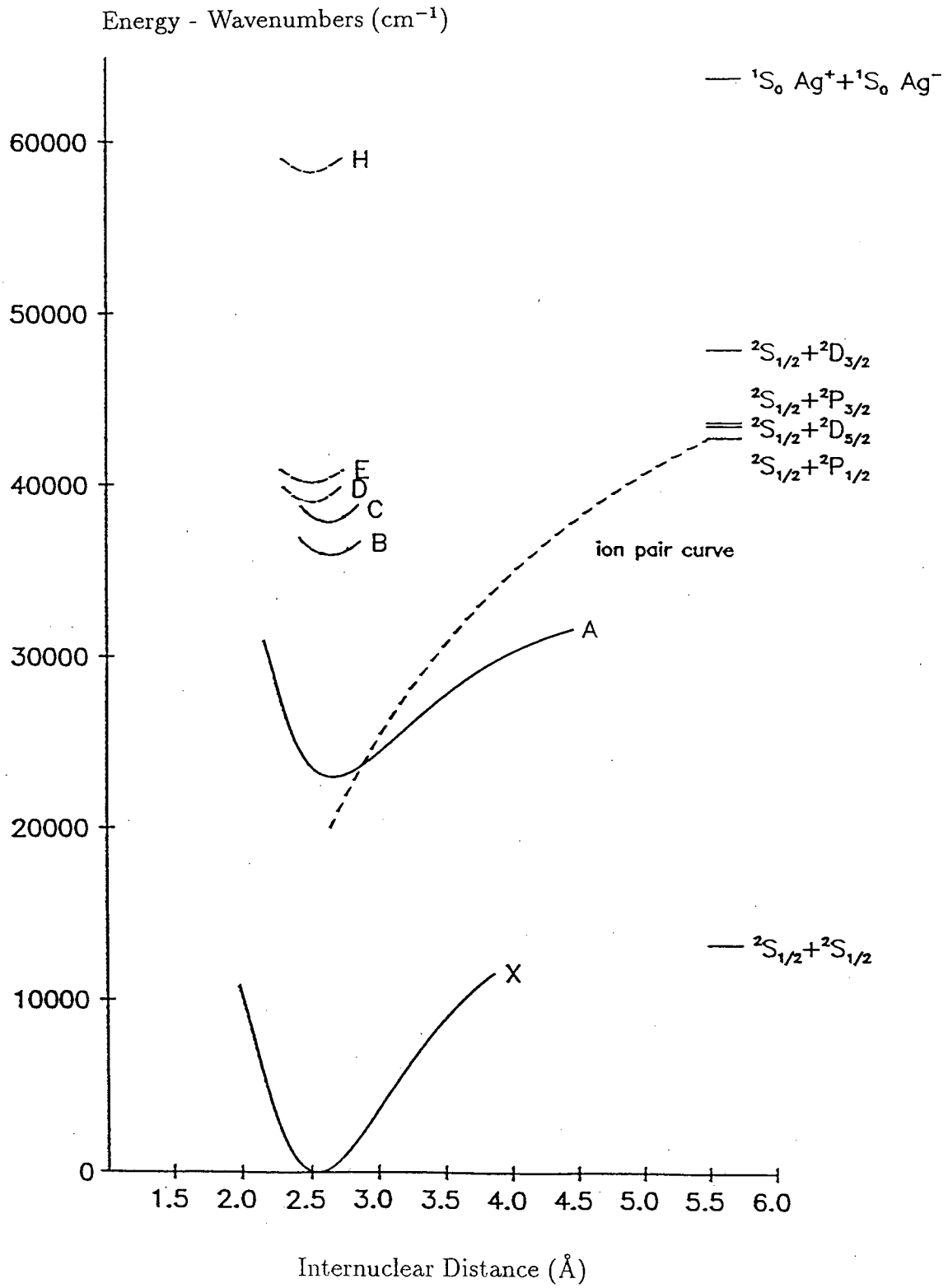

Figure 4–22: RKR Curves of the Ag_2 Molecule

Bibliography

[1] Morse M.D., Chem. Rev., 1986, **86**, 1049.

[2] Ozin G.A., Appl. Spectrosc., 1976, **30**, 573.

[3] Ozin G.A., Huber H., McIntosh D., Mitchell S., Norman J.G.Jnr. and Noodleman L., J. Am. Chem. Soc., 1979, **101**, 3504.

[4] Frank F., Schulze W., Tesche B., Urban J. and Winter B., Surf. Sci., 1985, **156**, 90.

[5] Grinter R., Armstrong S., Jayasooriya U.A., McCombie J., Norris D. and Springall J.P., Faraday Symp. Chem. Soc., 1980, **14**, 94.

[6] Mitchell S.A. and Ozin G.A., J. Am. Chem. Soc., 1978, **100**, 6776.

[7] Ozin G.A. and Huber H., Inorg. Chem., 1978, **17**, 155.

[8] Mitchell S.A., Kenney-Wallace G.A. and Ozin G.A., J. Am. Chem. Soc., 1981, **103**, 6030.

[9] Mitchell S.A. and Ozin G.A., J. Phys. Chem., 1984, **88**, 1425.

[10] Ozin G.A., Faraday Symp. Chem. Soc., 1980, **14**, 7.

[11] Welker T. and Martin T.P., J. Chem. Phys., 1979, **70**, 5683.

[12] Schulze W., Becker H.U. and Abe H., Chem. Phys., 1978, **35**, 177.

[13] Schulze W. and Abe H., Faraday Symp. Chem. Soc., 1980, **14**, 87.

[14] Schrittenlacher W., Rotermund H.H., Schroeder W. and Kolb D.M., Surf. Sci., 1985, **156**, 777.

[15] Gruen D.M. and Bates J.K., Inorg. Chem., 1977, **16**, 2450.

[16] Schulze W., Becker H.U., Minkwitz R. and Manzel K., Chem. Phys. Lett., 1978, **55**, 59.

[17] Bechthold P.S., Kettler U. and Krasser W., Solid State Commun., 1984, **52**, 347.

[18] Bechthold P.S., Kettler U. and Krasser W., Surf. Sci., 1985, **156**, 875.

[19] Leutloff D. and Kolb D.M., Ber. Bunsenges. Phys. Chem., 1979, **83**, 666.

[20] Harbich W., Fedrigo S., Meyer F., Lindsay D.M., Lignieres J., Rivoal J.C and Kreisle D., J. Chem. Phys., 1990, **93**, 8535.

[21] Montano P.A., Zhao J., Ramanathan M., Shenoy G.K., Schulze W. and Urban J., Chem. Phys. Lett., 1989, **164**, 126.

[22] Wiggenhauser H., Schroeder W. and Kolb D.M., J. Chem. Phys., 1988, **88**, 3434.

[23] Herbert T., Wiggenhauser H. and Kolb D.M., J. Chem. Phys., 1989, **91**, 1417.

[24] Herbert T., Kolb D.M., Rotermund H.H., Schriever U. and Wiggenhauser H., Chem. Phys. Lett., 1990, **166**, 101.

[25] Ruamps J., Compt. Rend. Hebd. Seances Acad. Sci., 1954, **238**, 1489.

[26] Ruamps J., Ann. Phys. (Paris), 1959, **4**, 1111.

[27] Kleman B. and Lindqvist S., Arkiv För Fysik, 1955, **9**, 385.

[28] Maheshwari R.C., Indian J. Phys., 1963, **37**, 368.

[29] Choong S-P., Wang L-S. and Lim Y-S., Nature (London), 1966, **209**, 1300.

[30] Choong S-P. and Wang L-S., Nature (London), 1964, **204**, 276.

[31] Brown C.M. and Ginter M.L., J. Mol. Spectrosc., 1978, **69**, 25.

[32] Srdanov V.I. and Pešić D.S., J. Mol. Spectrosc., 1981, **90**, 27.

[33] Butler A.M., *PhD. Thesis*, University of Edinburgh, 1989.

[34] Simard B., Hackett P.A., James A.M. and Langridge-Smith P.R.R., Chem. Phys. Lett., 1991, **186**, 415.

[35] Pešić D.S. and Vujisić B.R., J. Mol. Spectrosc., 1991, **146**, 516.

[36] Pešić D.S. and Vujisić B.R., J. Mol. Spectrosc., 1992, **151**, 269.

[37] Krämer H-G., Beutel V., Weyers K. and Demtröder W., Chem. Phys. Lett., 1992, **193**, 331.

[38] Hopkins J.B., Langridge-Smith P.R.R., Morse M.D. and Smalley R.E., unpublished results.

[39] James A.M., *PhD. Thesis*, University of Edinburgh, 1991.

[40] Beutel V., Kuhn M. and Demtröder W., J. Mol. Spectrosc., 1992, **155**, 343.

[41] Beutel V., Krämer H.-G., Bhale G.L., Kuhn M., Weyers K. and Demtröder W., J. Chem. Phys., 1993, **98**, 2699.

[42] Bevington P.R., *Data Reduction and Error Analysis for the Physical Sciences*, McGraw-Hill, New York, 1969.

[43] Brown M.A., *PhD. Thesis*, University of Edinburgh, 1987.

[44] Morse P.M., Phys. Rev., 1929, **34**, 57.

[45] Pekeris C.L., Phys. Rev., 1934, **45**, 98.

[46] Herzberg G., *Molecular Spectra and Molecular Structure.* I: *Spectra of diatomic molecules*, Second Edition, van Nostrand, Princeton, 1950.

[47] Drowart J. and Honig R.E., J. Phys. Chem., 1957, **61**, 980.

[48] Drowart J. and Honig R.E., J. Chem. Phys., 1956, **25**, 581.

[49] Ackerman M., Stafford F.E. and Drowart J., J. Chem. Phys., 1960, **33**, 1784.

[50] Schissel P., J. Chem. Phys., 1957, **26**, 1276.

[51] Hilpert K. and Gingerich K.A., Ber. Bunsenges. Phys. Chem., 1980, **84**, 739.

[52] Gingerich K.A., J. Cryst. Growth, 1971, 9, 31.

[53] Gingerich K.A., Chimia, 1972, **26**, 619.

[54] Gingerich K.A., Faraday Symp. Chem. Soc., 1980, **14**, 109.

[55] Simons J., J. Phys. Chem., 1991, **95**, 1017.

[56] Boeyens J.C.A. and Lemmer R.H., J. Chem. Soc. Faraday Trans. 2, 1977, **73**, 321.

[57] McAdon M.H. and Goddard W.A.III, J. Phys. Chem., 1988, **92**, 1352.

[58] Biagini Cingi M., Clemente D.A. and Foglia C., Mol. Phys., 1984, **53**, 301.

[59] Baetzold R.C., J. Chem. Phys., 1971, **55**, 4355.

[60] Baetzold R.C., J. Chem. Phys., 1971, **55**, 4363.

[61] Baetzold R.C. and Mack R.E., J. Chem. Phys., 1975, **62**, 1513.

[62] Baetzold R.C., J. Chem. Phys., 1978, **68**, 555.

[63] DeKock R.L., Zee R.D.v and Ziegler T., Inorg. Chem., 1987, **26**, 563.

[64] Shim I. and Gingerich K.A., J. Chem. Phys., 1983, **79**, 2903.

[65] Ziegler T., Snijders J.G. and Baerends E.J., J. Chem. Phys., 1981, **74**, 1271.

[66] McLean A.D., J. Chem. Phys., 1983, **79**, 3392.

[67] Rabii S., Yang C.Y., Chem. Phys. Lett., 1984, **105**, 480.

[68] Martin R.L., J. Chem. Phys., 1987, **86**, 5027.

[69] Ross R.B. and Ermler W.C., J. Phys. Chem., 1985, **89**, 5202.

[70] Basch H., J. Am. Chem. Soc., 1981, **103**, 4657.

[71] Hay P.J. and Martin R.L., J. Chem. Phys., 1985, **83**, 5174,

[72] Walch S.P., Bauschlicher C.W.Jnr. and Langhoff S.R., J. Chem. Phys., 1986, **85**, 5900.

[73] Bauschlicher C.W.Jnr., Langhoff S.R. and Partridge H., J. Chem. Phys., 1989, **91**, 2412.

[74] Partridge H., Bauschlicher C.W.Jnr. and Langhoff S.R., Chem. Phys. Lett., 1990, **175**, 531.

[75] Stoll H., Fuentealba P., Schwerdtfeger P., Flad J., Szentpaly L.v. and Preuß H., J. Chem. Phys., 1984, **81**, 2732.

[76] Flad J., Igel-Mann G., Preuß H. and Stoll H., Chem. Phys., 1984, **90**, 257.

[77] Stoll H., Fuentealba P., Dolg M., Flad J., Szentpaly L.v., Preuß H., J. Chem. Phys., 1983, **79**, 5532.

[78] Martins J.L. and Andreoni W., Phys. Rev. A, 1983, **28**, 3637.

[79] Ballone P. and Galli G., Phys. Rev. B., 1990, **42**, 1112.

[80] Andrae D., Häußermann U., Dolg M., Stoll H. and Preuß H., Theor. Chim. Acta., 1991, **78**, 247.

[81] Andzelm J., Radzio E. and Salahub D.R., J. Chem. Phys., 1985, **83**, 4573.

[82] Flad J., Igel G., Preuß H. and Stoll H., Ber. Bunsenges. Phys. Chem., 1984, **88**, 241.

[83] Flad J., Igel-Mann G., Preuß H. and Stoll H., Surf. Sci., 1985, **156**, 379.

[84] Klobukowski M., J. Comput. Chem., 1983, **4**, 350.

[85] Basch H., Faraday Symp. Chem. Soc., 1980, **14**, 149.

[86] Bauschlicher C.W.Jnr., Langhoff S.R. and Partridge H., J. Chem. Phys., 1990, **93**, 8133.

[87] Ozin G.A. and Klotzbücher W.E., Inorg. Chem., 1979, **18**, 2101.

[88] Moore C.E., *Atomic Energy Levels N.B.S. Circular 467 Vol.*III, Washington D.C., 1971.

[89] Grinter R., Chem. Phys., 1986, **102**, 187.

[90] Balasubramanian K., J. Phys. Chem., 1989, **93**, 6585.

[91] Bondybey V.E. and English J.H., Chem. Phys. Lett., 1983, **94**, 443.

[92] Riley S.J., Parks E.K., Pobo G. and Wexler S., J. Chem. Phys., 1983, **79**, 2577.

[93] Michalopoulos D.L., Geusic M.E., Hansen S.G., Powers D.E. and Smalley R.E., J. Phys. Chem., 1982, **86**, 3914.

Chapter 5

Threshold Photoionisation Spectroscopy of Silver Dimer

5.1 Introduction

The ionisation potential (I.P.) is one of the most important parameters of any molecular system. It is a direct measure of the amount of energy required to remove one of the valence electrons, and is therefore a pointer to not only the electronic structure of the neutral species, but also to the chemical reactivity of the species; chemistry is concerned with reactions, and reactions are influenced by the availability of charged participants.

As described in Chapter 1, a great deal of recent interest has been focussed on how molecular parameters change between the atomic value and the bulk phase. The bulk ionisation value, known as the work function, has been measured for many metallic systems. For the transition metals, it has been found that typical values fall by as much as 3 eV from atom to bulk [1]. An understanding of why and how this change takes place would allow further insight into the electronic structure of such species. Although these processes are understood in broad terms, a more detailed study of the relationships between neighbouring clusters is required.

Several studies have taken place on the ionisation potentials of clusters of alkali [2] [3] and transition metals [4] [8]. In general, the results point to a gradual reduction in value, which is related inversely to the cluster radius, with the bulk value being approached assymptotically [9]. Within this transformation scheme, however, subtle local inconsistencies can be observed. In the cases of copper and

silver, a distinct even/odd alteration is observed for the early members of the progression [4]. This can be attributed to the single s electron of the silver or copper atoms, which results in clusters with an odd number of atoms having an unpaired outer electron and hence a lower ionisation value than their neighbouring, even numbered species. As the cluster size, n, increases, the isolated molecular orbitals evolve into the bulk band structure, and these alterations decrease to zero. It was the aim of this work to investigate the ionisation potential of the silver dimer species with a greater precision than had previously been achieved. This quantity had been evaluated many times as part of theoretical studies, and this work is summarised in Table 5-1. However, only one experimental determination of the ionisation potential had been achieved [10], using the dependence of ion yield on laser fluence. This involved the monitoring of ion intensity as a series of intermediate levels were pumped. As ionisation was achieved via a fixed frequency laser, the value of ionisation potential could be found to within one vibrational quanta of the intermediate level. While this technique had provided an experimental measure of the I.P. it was rather crude, and it was hoped that a more accurate value could be obtained by the use of a more suitable technique.

This chapter begins with a consideration of the techniques that were available for such studies, followed by a description of the experimental apparatus used in this work. There follows a short discussion of factors which can influence the actual values recorded in such studies, namely autoionisation pathways. The results obtained are then presented. This section consists of two distinct studies; one recorded under the influence of a steady state potential, and the other with field free observation. The final discussion section compares these results to previous work and attempts to assign the rich post-threshold fine structure to particular Rydberg series.

Table 5–1: Theoretical Estimations of the Ionisation Potential of Ag_2

Calculation	Value (eV)	Reference
EH/CNDO	8.51,9.86/7.23	[11]
EH/CNDO	7.74	[12]
PP/LSD	7.93, 8.05 [a]	[13]
PP/LSD	7.91, 8.03 [a]	[14]
PP/CI	7.65	[15]
HF/CI	5.45	[16]
MCSCF/RCI	6.7	[17]
RECP/MRSDCI	7.44	[18]
RECP/MCPF	6.74, 7.35/7.55 [b]	[19]
RECP/MCPF	6.74, 7.35/7.55 [b]	[20]
RPP/CEPA	7.11	[21]
OVGF	6.75	[22]
SCF - Xα - DSW	7.78	[23]
Experimental Value	7.56	[10]

EH = Extended Hückel

CNDO = Complete Neglect of Differential Overlap

(R)PP = (Relativistic) Pseudopotential

LSD = Local Spin Density

(R)CI = (Relativistic) Configuration Interaction

HF = Hartree-Fock

MCSCF = Multi Configurational Self Consistent Fields

RECP = Relativistic Effective Core Potential

MRSDCI = Multi Reference Singles + Doubles CI

MCPF = Modified Coupled-Pair Function

CEPA = Coupled Electron Pair Approximation

OVGF = Outer Valence Green's Function

DSW = Dirac-Scattered-Wave

a) The first value is adiabatic, the second vertical

b) The first value is the theoretical, the second and third are scaled by an estimated error.

5.2 Photoelectron Spectroscopy

The conventional route to ionisation potential measurements is that of photoelectron spectroscopy (PES) [24], and such measurements have been made on the coinage dimers [25] - [27]. The source, which is typically laser or discharge in nature, supplies enough energy to remove either valence (UPES) or core (XPES) electrons. These free electrons are energy analysed and the resulting intensity alterations give the structural information. There are several drawbacks with this approach. As ionisation is a single photon process, the area of the molecular ion ground state potential surface that can be accessed is very dependent on the particular Franck-Condon overlap of the system. In order to measure the adiabatic IP, the transition required is that between the lowest energies of both the molecule and molecular ion ground states; the (0-0) transition. Consider the situation where the equilibrium bond lengths in these two states are quite different. A vertical transition will not result in the lowest energy promotion possible but rather to a highly excited vibrational level in the molecular ion. Hence the single photon nature of the technique is open to problems. The accuracy with which values can be recorded using this method is defined by the spectroscopic width of the radiation source. Typical values are of the order of 15 meV [28].

Two related techniques which are more able to provide transition metal measurements are multiphoton ionisation photoelectron spectroscopy (MPI-PES) and excited state photoelectron spectroscopy (ES-PES) [29] - [34]. Both these methods employ REMPI techniques, with kinetic energy analysis of the electrons produced, resulting in a conventional spectrum. As a result of accessing the ionisation continuum via an intermediate state the need for a VUV source is removed. Perhaps more importantly, by careful selection of intermediate level, a wide portion of the ionic potential energy surface can be probed. Hence the likelihood of measuring the adiabatic IP is enhanced. These techniques are ideally suited to pulsed sources, the principal limitation being a resolution of typically 10 meV.

A further increase in resolution is offered by zero kinetic energy photoelectron

spectroscopy (ZEKE - PES), here limited only by the laser bandwidth [35] - [39]. Tunable laser radiation is used to excite distinct levels in the molecular ion. When this energy is in resonance with a real eigenstate, the resulting electron is ejected with no kinetic energy (save that of random thermal motion). When not in resonance, the electrons possess the residual energy as translational motion. As this ionisation takes place in the source region of a time-of-flight mass spectrometer incorporating delayed extraction optics, these two types of electrons undergo differing fortunes. The non-zero species drift out of the extraction region, while the others feel the full extraction pulse. Hence they each extract different energies from the source and by monitoring the zero energy flight time the vibronic structure in the ion can be recorded. While it has proved possible to study some lighter species with rotational resolution, the transition metals should be amenable to vibrational investigation.

In the course of this work, the technique employed was that of threshold ionisation spectroscopy (TIS) [40] - [47]. This required no major modifications to the existing apparatus as it is simply a variant of the two-colour R2PI technique described earlier. This method used two dye lasers; one to pump a specific intermediate level of the molecule and a second to scan over the ionisation threshold. By monitoring the photoion signal as a function of ionising laser wavelength, a photoionisation efficiency (PIE) curve was generated. This technique is analogous to the MPI-PES and ES - PES described earlier in that provided there exists some *a priori* knowledge relating to the geometry and electronic nature of the molecule, there is a free choice of intermediate level and hence greater experimental flexibility. It should also be noted that the supersonic cooling of these molecules defines the initial level of such experiments as $v'' = 0$, hence paving the way for access to the measurement of the adiabatic I.P. As well as the IP measurement, the rich post threshold structure can also give an insight into autoionising processes. Although not as accurate as ZEKE-PES, a limit of around 2 cm^{-1} can be achieved.

5.3 Autoionisation

These are processes by which neutral eigenstates of any molecule, which lie above an ionisation limit, can give rise to spontaneous ionisation [48]. This is due to the coupling of such energy into the kinetic energy of a particular electron, resulting in ionisation. This coupling can occur using excess energy from a variety of sources. The most important as far as this work is concerned is that of field ionisation, whereby an external electric field is the source, but others include electronic, vibronic and rotational energies.

Electronic autoionisation was observed initially in atomic systems [49] - [51]. It is possible for the electrons to adopt a configuration such that the total energy of the system is greater than the ionisation potential. The ejection of an electron is accompanied by a rearrangement of the remaining electrons to provide the required excess energy. This rearrangement often takes the form of a valence electron dropping down to fill a core electron hole, but can be a spin orbit rearrangement for species that are close to threshold.

For molecular systems which lie above the ionisation limit, it is possible for ionisation to be achieved by the coupling of vibrational energy to the ejected electron, so called vibrational autoionisation [41], [48], [51]. Here, the molecule 'loses' one or more quanta of vibrational energy as ionisation is achieved.

Rotational autoionisation is a similar process to that described immediately above. The coupling now involves rotational energy and subsequent energy transfer. Clearly, the species undergoing this type of process need to be much closer to ionisation, as rotational quanta are much smaller than vibrational [48] [52] - [55]. The alternative is for a highly rotationally excited species to lose many quanta consecutively, but this is not a favourable process.

All of the above processes have been identified in a variety of molecular situations. They will, however, play little part in the following discussion as they involve systems with a total energy greater than that required to achieve ionisa-

tion. The main process of interest here is one in which the system is below this required threshold.

5.4 Field Ionisation

Field ionisation differs from the ionisation processes described previously in that the total energy of the system now lies below the ionisation threshold. However, the presence of an external electrostatic field has the effect of reducing the energy that is required to achieve ionisation [49] [56] - [62]. Thus the value of the measured ionisation potential is red shifted by the field. The extent of this field shift can be explained with simple electrostatic considerations.

The coulombic attraction between a nucleus and an orbiting Rydberg electron is given by the following relationship [63],

$$U(r) = -Ze^2/4\pi\epsilon_0 r \tag{5.1}$$

where;

Z = effective nuclear mass,
e = electronic charge,
ϵ_0 = vacuum permittivity and
r = separation of electron and nucleus.

This conforms to the established tradition of a zero value at infinite separation. If an external electric field is now introduced the resulting equation becomes;

$$U(r) = Eer - Ze^2/4\pi\epsilon_0 r \tag{5.2}$$

The interaction of these two functions of r give a resultant parabola, as shown in Figure 5-1.

The point at which the external field exactly balances the internal attraction of the nucleus and electron is easily calculated. Differentiation of the above equation

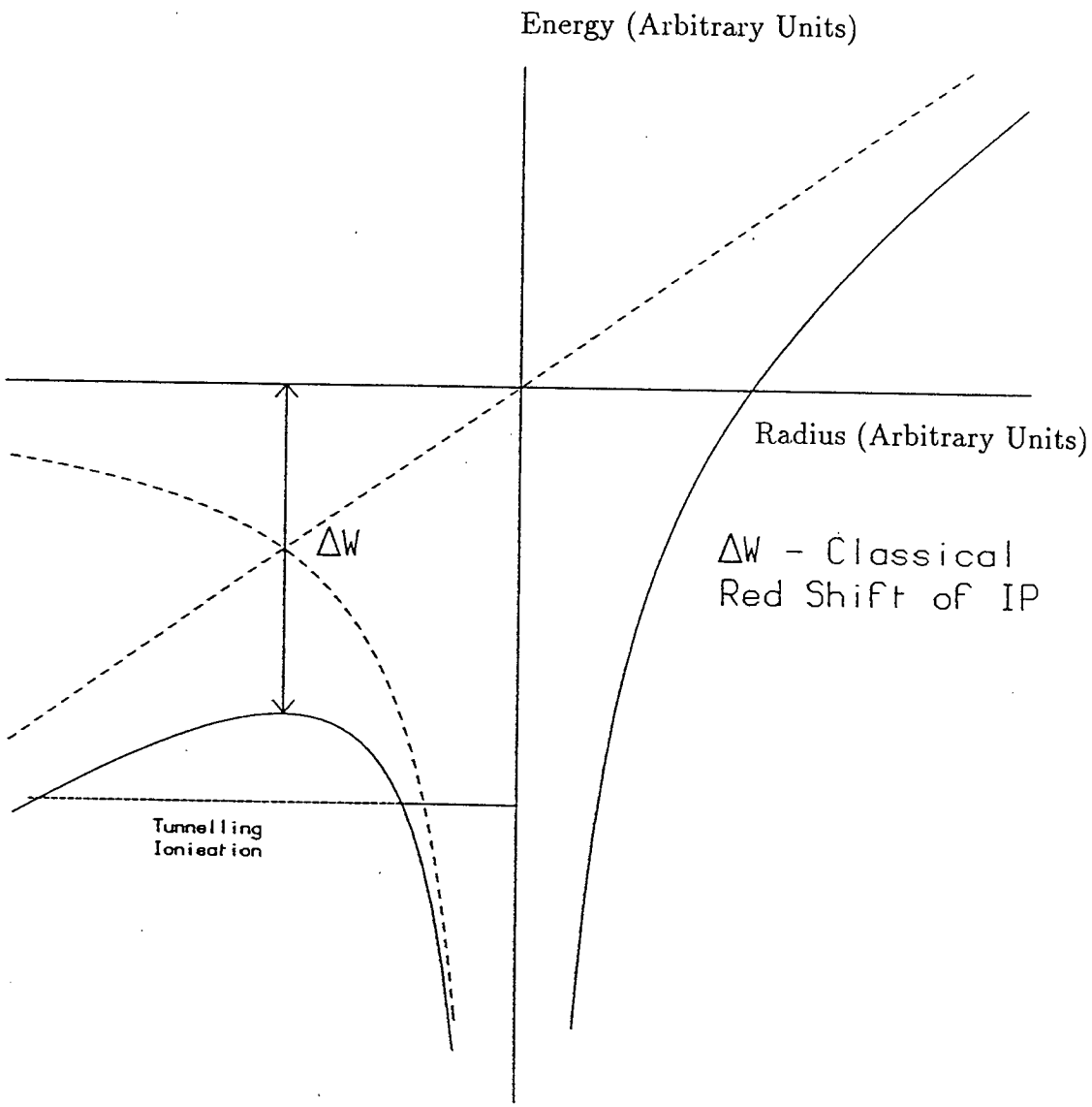

Figure 5–1: Potential Interactions from Coulombic and External Static Fields

with respect to radius gives

$$dU(r)/dr = Ee + (Ze^2/4\pi\epsilon_0) \times 1/r^2 \tag{5.3}$$

For turning points, this expression is equal to zero;

$$dU(r)/dr = 0 \tag{5.4}$$

resulting in

$$r_0 = (-Ze/4\pi\epsilon_0 E)^{1/2} \tag{5.5}$$

At this point, the ionisation potential has been reduced by the external field to the tune of

$$\Delta W = EeR = -(Ze^3/4\pi\epsilon_0)^{1/2} E^{1/2} \tag{5.6}$$

which can be expressed in more convenient units as

$$-6.13 \times [E(Vcm^{-1})]^{1/2} \tag{5.7}$$

As the typical working voltages in these studies were of the order;

$$V_{Rep} = 3015 \text{ V}$$
$$V_{DOG} = 2500 \text{ V}$$

where

$$d_{Rep-DOG} = 30 \text{ mm}$$

it follows that the static field in the source region was typically of the order of 170 Vcm^{-1}, which resulted in a reduction of some 80 cm^{-1} in the measured appearance potential (AP) of intensity in the photoionisation spectrum. This quantity is related to the true ionisation potential (IP) by the above equation such that

$$AP = IP - 6.13 \times [E(Vcm^{-1})]^{1/2} \tag{5.8}$$

This relationship was verified in an exhaustive series of measurements carried out in this group [64]. The appearance potential was scanned for a range of source field values. This information was then used in a variety of plots to evaluate the field free ionisation potential and confirm the value of the constant. The molecules studied in this earlier work were Cu_2 and CuAg, while the work reported here deals with another member of the coinage triad, namely Ag_2.

5.5 Experimental

The apparatus used to perform this work was very similar to that employed in the previous chapter. The main difference was that two dye lasers were required for these studies. The experimental set-up is shown in Figure 5-2.

The intermediate state selected for this work was the A $^1\Sigma_u^+$ (0_u^+) state of Ag_2, described in Chapter 4. In these experiments, the (0-0) band of the A $\leftarrow$ X transition was pumped by the first dye laser (PDL-2). This instrument, with its broad bandwidth of 0.4 cm^{-1}, was parked on the R-head of this state to ensure that a strong signal was achieved by exciting many rovibronic lines simultaneously; from Chapter 4, it may be recalled that the R-head formed at around J = 9. The second, etalon narrowed dye laser (FL3002EC), was then scanned over the predicted ionisation region, and the resulting PIE spectra used to determine the threshold value.

This threshold region had been identified in earlier work [10], thus allowing a suitable spectral range to be selected for investigation. In this previous study, resonant two-photon ionisation methods, similar to those described earlier in this thesis, were used. The difference in the two techniques, however, was that the second, ionising photon in this earlier work came from a fixed frequency laser. By observation of the resulting vibronic structure, the value of the ionisation potential could be bracketed as (7.56 $\pm$ 0.02) eV. However, as no allowance was described for the contribution of the extraction field, and as the value of such a field was unstated, the initial scans performed in this work covered a wide area to ensure that the required threshold region was identified.

A previous study in this group contained a section on the relationship between measured threshold position and the ionisation source field strength [64]. Here, threshold photoionisation spectra were recorded for a number of source field conditions and these were used to evaluate both the adiabatic I.P. value by extrapolation and to verify the equation relating these values, as given earlier. While both these objectives were achieved, the quality of spectra obtained became increasingly poor

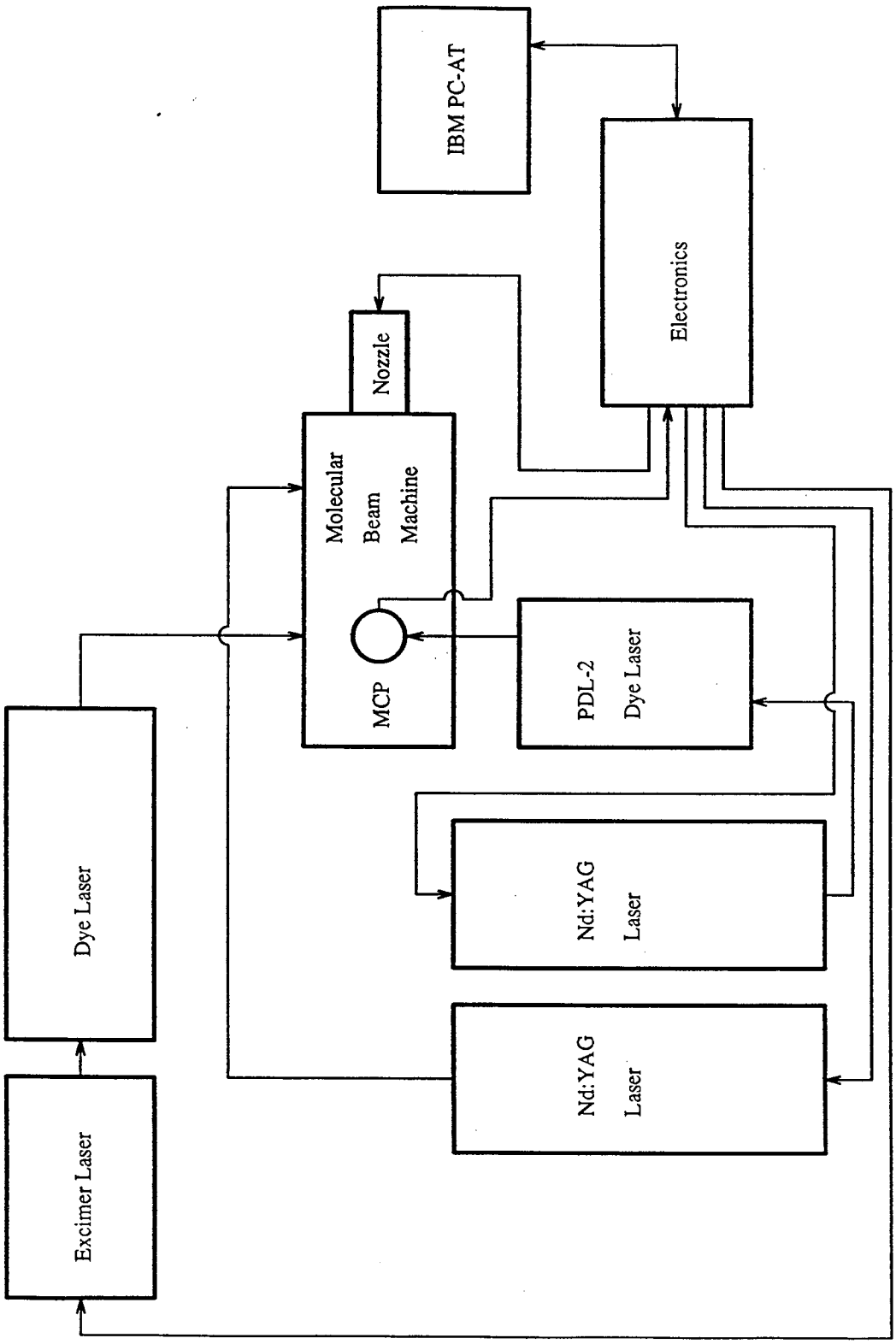

Figure 5–2: Experimental Set-up for I.P. Measurements

when lower field values were used. This was due mainly to the increased flight times encountered under these conditions, which resulted in any off-axis velocity components reducing the intensity in the particular mass channels. Such problems could not be overcome by the use of deflector plates. However, as these experiments were carried out primarily to allow a field-free evaluation to be made, the need for such work was removed by the availability of a voltage pulser suitable for such studies.

Once these initial, static field scans had been completed, therefore, the pulsed ion optics were introduced [65]. While the details of the instrument used in this work are unavailable, the following general description can be offered. The pulser was driven by a pulse (10 μs, TTL level) from the LeCroy 4222 pulse generator in the same way as the other pieces of apparatus. The voltage from a stabilised d.c. supply (0.067 % ripple) was stepped by a 1:300 transformer to generate the high voltage required, in this case 3000 V. The electronics then produced a pulse of 25 ns rise time and 100 μs duration, with excellent reproducibility. Two output ports were provided, supplying 3000 V and 2000 V, and these were used for the repeller and draw out grids respectively. This instrument allowed a considerable reduction in the field ionisation effect described earlier. This was achieved by allowing a time delay between the ionising photon and the subsequent extraction. This delay meant that only Rydberg states of lifetimes greater than 150 ns were in the source region at the time of extraction. Ideally, this delay would have been made as long as possible. However, a balance had to be struck between length of delay and the fact that the translational motion of the beam species removed them from the ionisation region. A delay of 150 ns resulted in a movement of around 1 mm of the beam species, such that they were still well within the source region when ionised.

One other experimental modification was introduced in the course of this work. Under ordinary operating conditions, the molecular beam contains a significant number of plasma-generated ions. These are usually removed from any subsequent consideration by the potential field they encounter as they move towards the source region. In a pulsed system, however, these species would be able to enter the source region along with the neutral species, and be subsequently accelerated towards the

detector. This would result in a masking of the true ionisation profile by some background signal and would prevent the evaluation of the required parameters. To prevent this, a pair of Ni-Al ion scavenging plates, separated by some 5.6 cm, were mounted downstream of the cluster source extender channel. While these did not appear to disrupt formation of the molecular beam, they were able to scavenge all ions of mass less than 230 a.m.u., and deflect any heavier species, with a potential difference of some 60 V across them. This was supplied by a dry cell battery pack.

5.6 Results

The following section is readily split into two areas of study. The first is concerned with the work completed with static extraction fields and the second with the more accurate measurements taken in the field free work.

5.6.1 Static Field Measurements

The apparatus was optimised as for all previous experiments. The position of the pump dye laser was verified by performing a short scan while ionising with an excimer source. The result is shown in Figure 5-3.

The dye laser was then parked on the most intense region of this feature, the R head, and the threshold spectra recorded by scanning the second dye laser over the required area. Some typical scans of this region are shown in Figures 5-4 and 5-5.

It is quite clear that the second of these spectra is split into two distinct regions, those with and without ionisation intensity. However, it is a non-trivial problem to accurately measure the onset of ionisation [66]. The expected sharpness of the threshold is masked by both the superimposed molecular structure and the width of the threshold itself; that is to say, a decision has to be made as to whether the point of ionisation should be taken as the top, middle or base of the

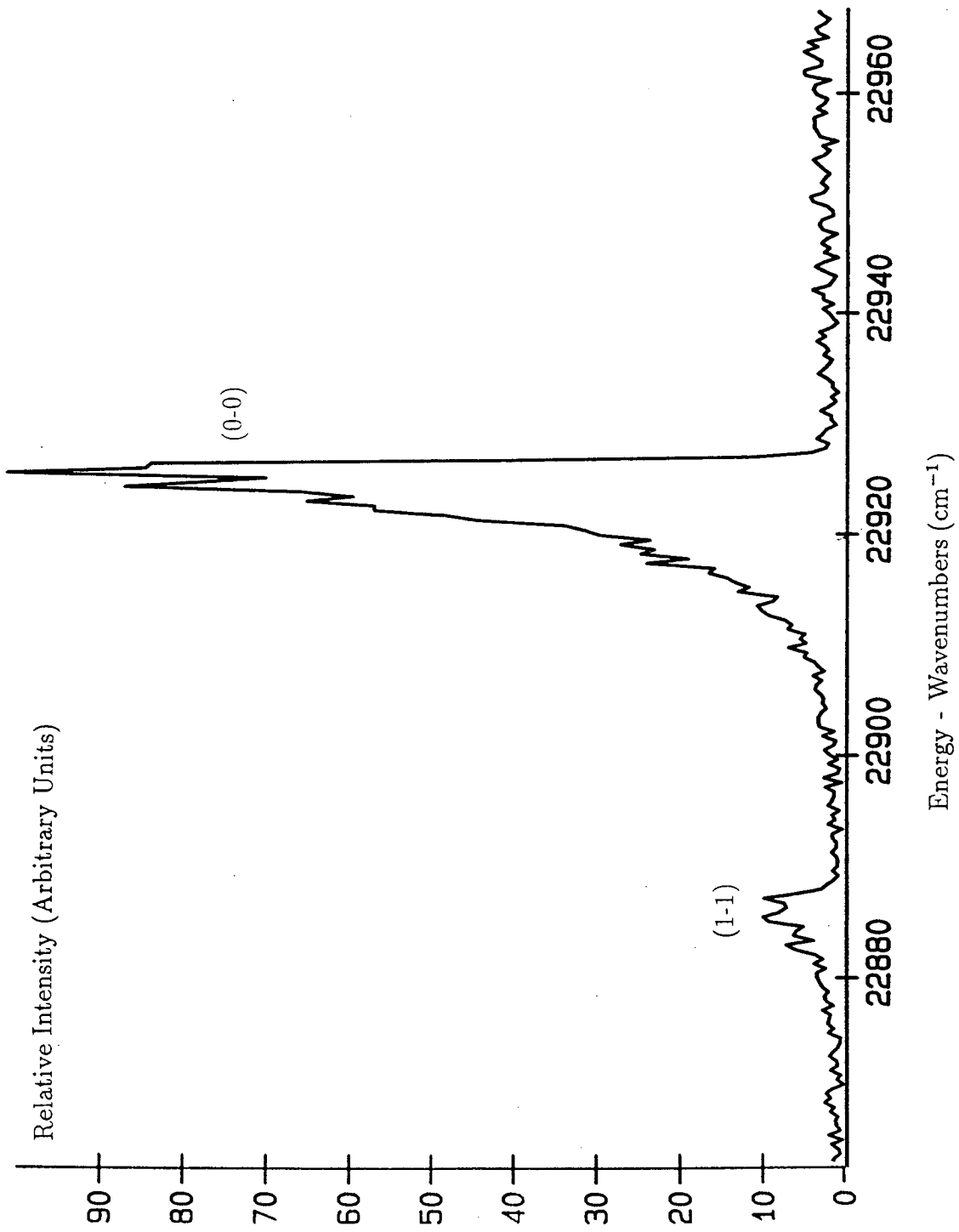

Figure 5–3: Scan of PDL-2 laser, with nonresonant excimer ionisation, over the (0-0) band of the Ag_2 A state

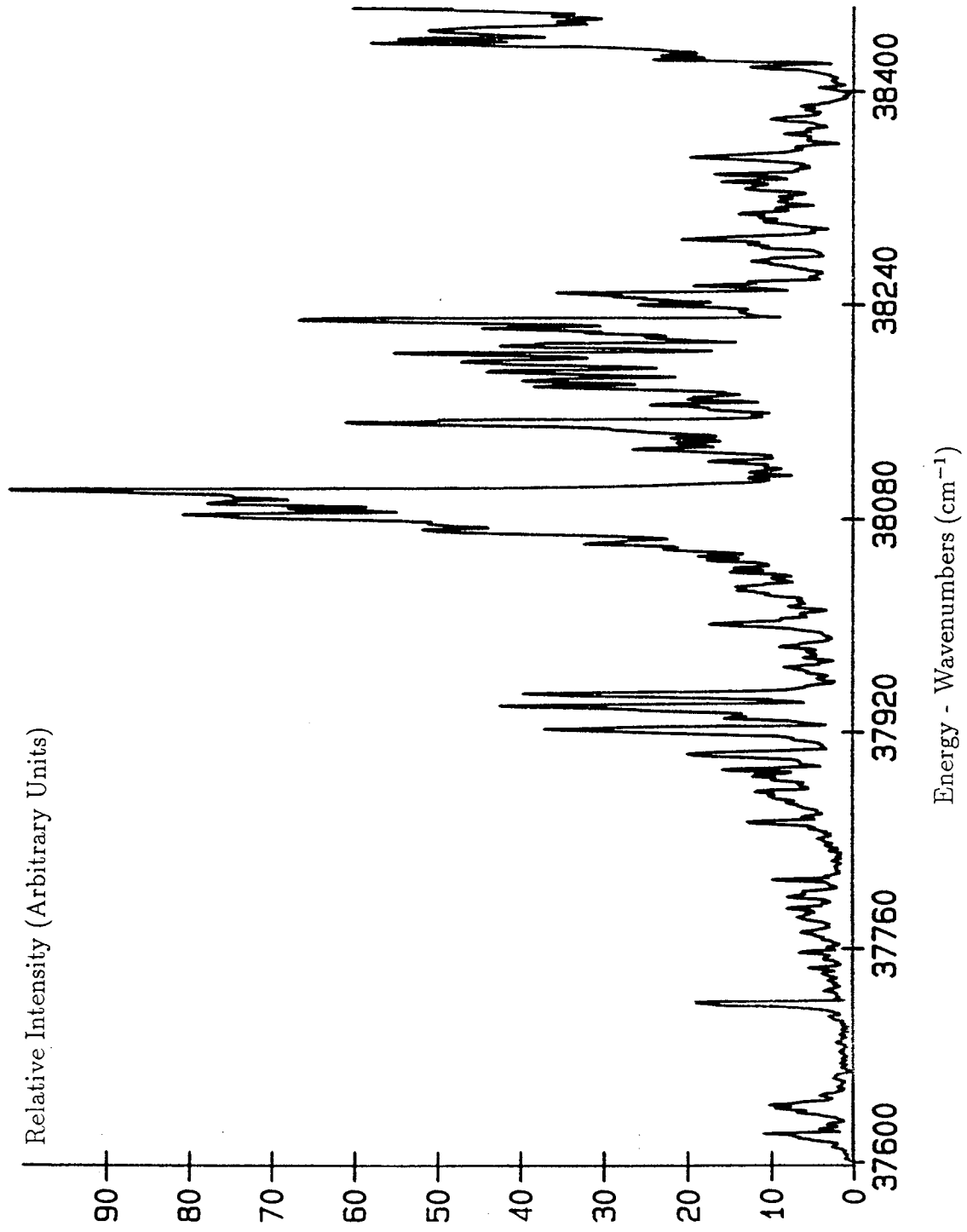

Figure 5–4: Scan over pre-threshold region of Ag_2 via the (0-0) level of the A state

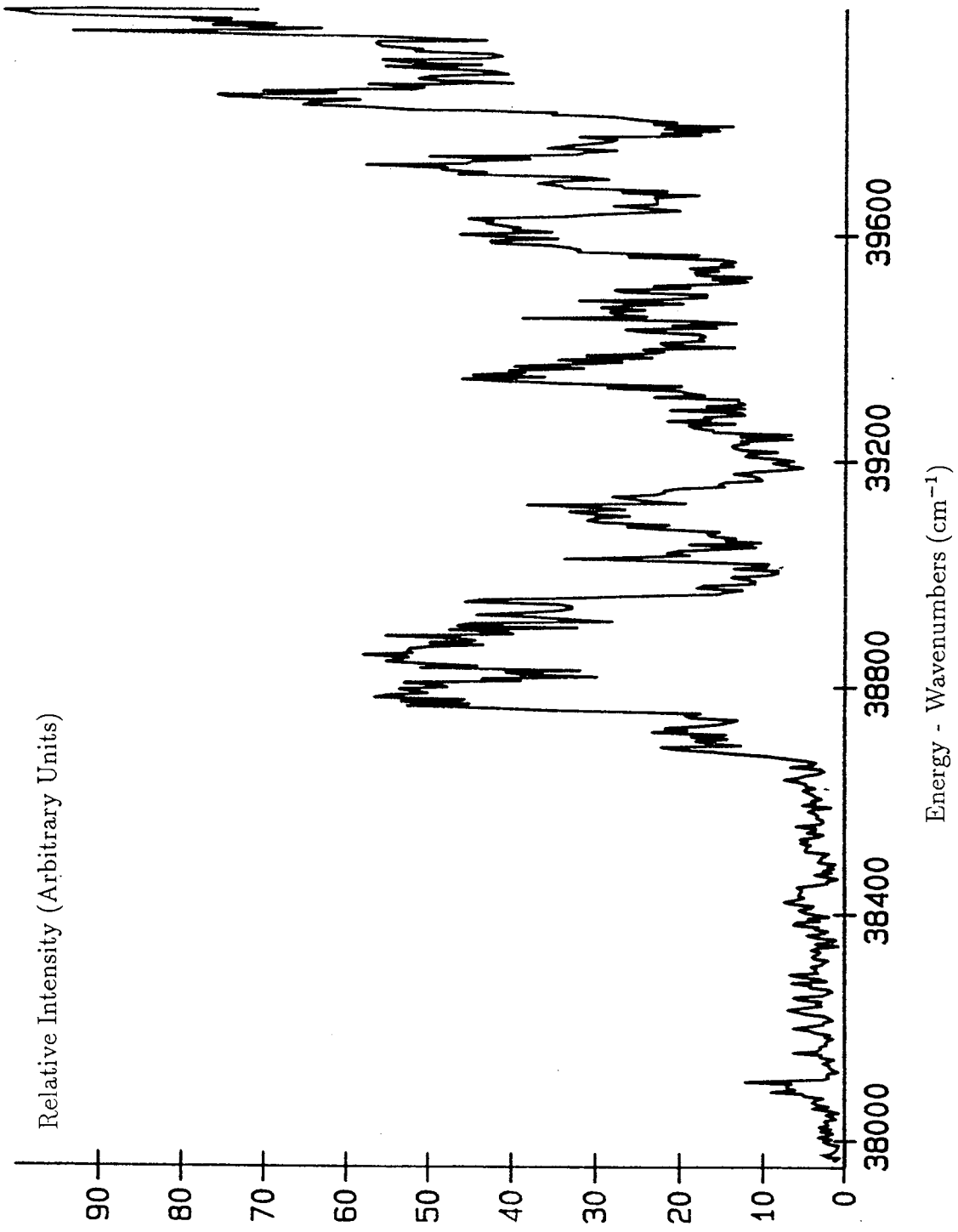

Figure 5–5: Scan over threshold region of Ag_2 via the (0-0) level of the A state

rising edge. One, perhaps surprising, feature of these spectra is the amount of structure to the low energy side of threshold. Ionisation takes place in a static potential field of some 170 Vcm^{-1}. From the earlier considerations, any Rydberg states lying within 80 cm^{-1} of the true threshold would be field-ionised by this region; equivalent to a red shift in the ionisation potential of that magnitude. However, the observed spectra have features much further down the energetic ladder; Figure 5-4 shows features extending to at as much as 1000 cm^{-1} below the measured threshold. These can be explained by considering the long lifetimes and high collisional cross-sections of Rydberg states thus supporting the possibility of three-photon ionisations, such as those observed. The results obtained from this work are shown in Table 5-2.

From the 'Static' column of Table 5-2, the measured IP value is some 7.65 eV. This is some 0.1 eV, or 800 cm^{-1}, higher than the previous experimental value. There is no single explanation for this discrepancy, but an evaluation of experimental conditions allows several possible sources to be identified. Considering again the spectra in Figure 5-5, the slope of the curve in the region of the threshold is such that an accurate determination of its value is difficult. This arises in part from the phenomena described earlier such as rotational autoionisation and tunnelling through the potential barrier, as well as a contribution from the finite bandwidths of the lasers. Also, the values of the two photons involved in the ionisation process are known only approximately. The first photon, $h\nu_1$, was taken from the R head value of the A $\leftarrow$ X (0-0) band. As this lies some 0.4 cm^{-1} above the ν_{00} value, which is well known, the energy of this photon can be considered as measured quite accurately. The second photon, $h\nu_2$, however, was measured from the digital readout of the dye laser itself. While this instrument had been recently calibrated, and shown to remain accurate over a wide spectral region, no absolute measurement of these values were made. This may have resulted in an error of the order of some 15 cm^{-1}. Finally, the true value of any static field would have to be measured to allow a more accurate calculation of its effect. While this has probably the least effect of the errors detailed here, it is important to include it for completeness. Despite these discrepancies, the experimental work reported here is

Table 5–2: Ionisation Potential Measurements for Ag_2 in Static and Pulsed Fields

Isotopomer	107-109 (cm^{-1})	107-109 (cm^{-1})	107-109 (cm^{-1})
$h\nu_1$	22977.1	22977.1	23132.1
$h\nu_2$	38681.3	38762.9	38615.0
IP	61658.4	61740.0	61747.1
Corrections	80	0	0
True IP	61738.4	61740.0	61747.1
Field	Static	Pulsed	Pulsed

still some way from agreement with the previous experimental determination described earlier. It was hoped, however, that the next stage of investigation would allow such agreement to be reached.

5.6.2 Field Free Measurements

The scans recorded in the above work were now repeated with the pulsed extraction optics in place. Initially the delay was set such that the conditions of extraction were identical to those of the earlier work. Indeed, the resulting spectra were very similar; a typical scan is shown in Figure 5-6.

The delay between ionisation and extraction was then increased in multiples of 50 ns such that a series of scans was produced. These showed the threshold moving to higher energy, until a point was reached where no subsequent increase was recorded, and the so-called field free ionisation potential had been attained. Figure 5-7 shows a scan recorded under these conditions.

The energetics of this work are also included in Table 5-1. It was found that the three field free values - one calculated and two measured directly - were in very good agreement with each other. Hence while it might remain desirable to actually measure the field free value by experiment, there would appear to be no need to do so as long as the static field in use is well understood. Also, given that these values are in agreement, it would appear that the earlier experimental evaluation may be in error. However, considering the earlier discussion with regard to the difficulty of spectral interpretation, it would be prudent to wait for a third, independent evaluation to confirm the value.

Considering the spectra themselves, all are qualitatively similar, with no apparent alterations imposed by their respective environments. The threshold widths appear similar, which was surprising as the field free spectra should have been free from tunnelling and rotational autoionisation, but this may simply be an artefact of the experimental process itself.

The lack of structure to the red of the ionisation threshold is of interest; one might have expected to observe the sharp features of long-lived molecular Rydberg

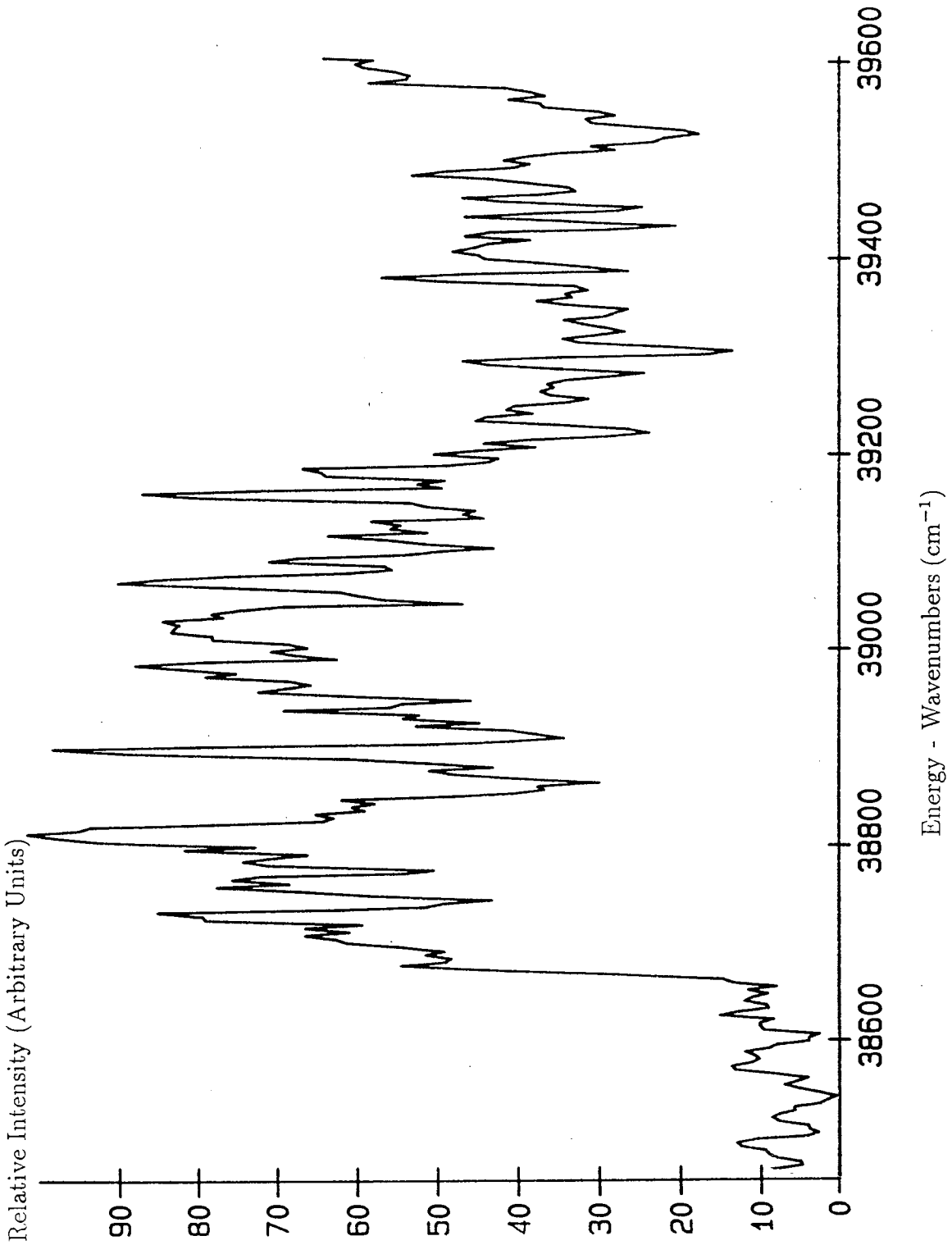

Figure 5–6: Field free scan of threshold area via the (0-0) level of the A state with short pulser delay

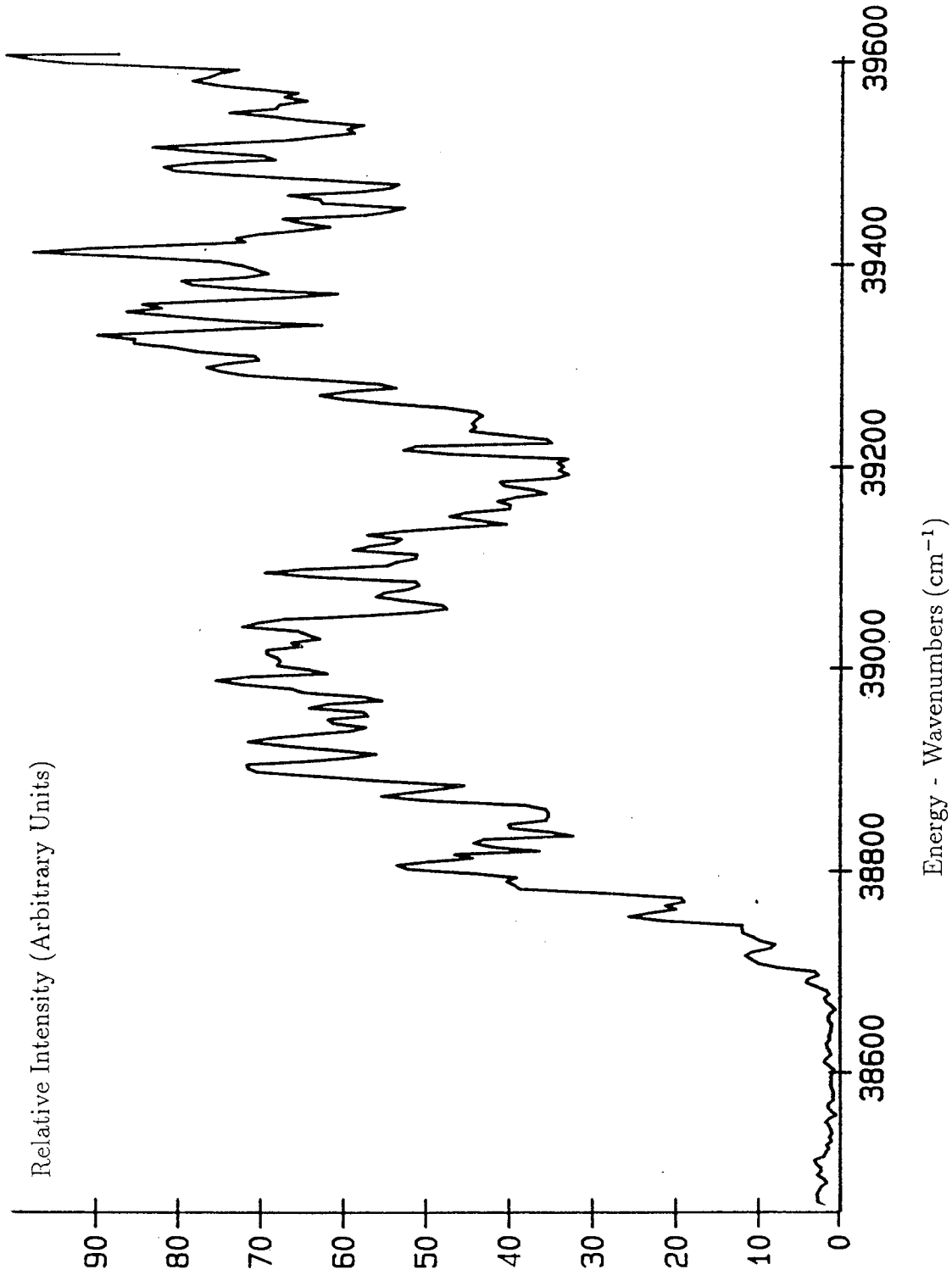

Figure 5–7: Field free scan of threshold area via (0-0) level of A state with long pulser delay

states which were field ionised by the pulsed voltage. Application of some 1000 V across this area would permit the observation of features some 110 cm^{-1} below threshold, providing that they do not decay during the time delay between excitation and extraction. This delay, of some 150 ns, is not long in terms of Rydberg state lifetimes and we have therefore assumed that some predissociation channel, which correlates with excited atomic limits, is responsible for their removal.

The shape of the PIE spectra themselves should give an indication of whether the measured transition is the adiabatic I.P. or some other threshold due to geometric considerations. The spectra themselves are essentially a single step; the observed dip in intensity being an artefact of the doubling crystal efficiency in that region. No "staircase" like structure is observed, whereby the photoion signal intensity increases as successive vibrationally-excited ion thresholds are crossed. While these may simply be masked by the superimposed structure, it is of note that their relative intensities, and hence Franck-Condon factors, are equal as far as these spectra are concerned. These two facts, coupled to the significant intensity increase recorded on these spectra indicate that we have in fact recorded the adiabatic threshold; assuming the geometry in the excited state and the ion to be similar, it would be unlikely to produce such a profile if the v = 0 level of the ion were not accessed, and if the geometries were significantly different, a stepped profile would be expected.

In Chapter 4, it was argued that the A state of Ag_2 was an admixture of several configurations, with both the $d^{20}(s\sigma)^1(s\sigma^*)^1$ and $d^{19}(s\sigma)^2 9s\sigma^*)^1$ configurations playing important roles. While this work has not established with any certainty the nature of the molecular orbital from which the electron is removed in these experiments, given that the above work demonstrates a strong vertical correlation between excited state and ion it can at least suggest a significant involvement of both the s and d hole configurations in the ion ground state.

5.6.3 Rydberg Analysis

The determination of the first ionisation potential of a system by locating the onset of photoionisation is a non-trivial assignment. The absorption of light just below this critical frequency results in an electron of very high principle quantum number. These states, collectively called Rydberg states, can be thought of as an electron orbiting an effectively atomic core - so large can be the radius of orbit [63]. Such systems are then susceptible to a variety of ionising phenomena, leading to a false IP value; the preceding section dealt with one such pathway, namely that of field ionisation. This problem was overcome, to a great extent, by the use of pulsed extraction fields. However, this technique cannot overcome long lived Rydberg states which can make the accurate threshold identification difficult. Other sources of error also exist; for example, collisional ionisation, which further complicate such analyses. Even excluding all such phenomena, the problem of the finite width of the threshold itself is the source of an error of the order of 10 cm^{-1}.

The most accurate method for the determination of the molecular ionisation potential is based on the measurement of different series of autoionising Rydberg levels. The term values of such series obey the general relationship,

$$T(n, v^*) = IP(v^*) - R/[n - \delta(v^*)]^2 \tag{5.9}$$

where;

T(n,v*) = term value
IP(v*) = ionisation potential of v^{th} level
R = Rydberg constant (= 109737.2 cm^{-1})
n = principle quantum number of Rydberg electron and
δ(v*) = quantum defect

Clearly then, these levels converge, as n $\rightarrow \infty$, towards the level $v^+ = v^*$ of the ion ground state. Measurement of a selection of such series allows not only the vibrational constants of the ion ground state to be calculated, but also in turn

the ionisation potential itself. However, the assignment of specific Rydberg lines to particular experimental peaks is also prone to error. As these series converge to high energy, and only contain certain middle order members, any assignment can easily be in error by an arbitrary integer value. This is amplified by the fact that with so many lines in these spectral areas, it is always possible to fit a series of lines through them. Several such analyses have been performed, but a satisfactory interpretation has not yet proved possible; each attempt at such a procedure merely resulting in near arbitrary values being attached to such peaks. A typical spectrum recorded in this area is shown in Figure 5-8. Clearly, such spectra contain large numbers of closely packed features making definitive assignments near impossible, and hence care must be exercised in the use of such data.

The Ag_2^+ ion has been studied in a variety of theoretical work [13] [21] [68] - [71]. For the purposes of this comparison, the important parameters are bond length, vibrational constant and dissociation energy. These are summarised in Table 5-3.

5.6.4 Dissociation Energy of Ag_2

Having determined what is believed to be the adiabatic ionisation potential of Ag_2, it is possible to calculate the dissociation energy of the ionic ground state using the following thermochemical cycle equation

$$D_0(Ag_2^+) = I.P.(Ag) + D_0(Ag_2) - I.P.(Ag_2) \tag{5.10}$$

where D_0 refers to the dissociation energies measured with respect to zero point levels. The value obtained is included in Table 5-4, but is of the order of 95 % of the neutral ground state dissociation energy. This is a substantial fraction, and has important implications for the bonding in the ion. It would appear that there are important contributions from $d^{19}(s\sigma)^2$ configurations. Were the ion predominantly described by the $d^{20}(s\sigma)^1$ configuration, one would expect the ion to be weakly bound, as this would correspond to a halving of bond order upon ionisation. As the neutral and ion have very similar dissociation values, there is evidence to say

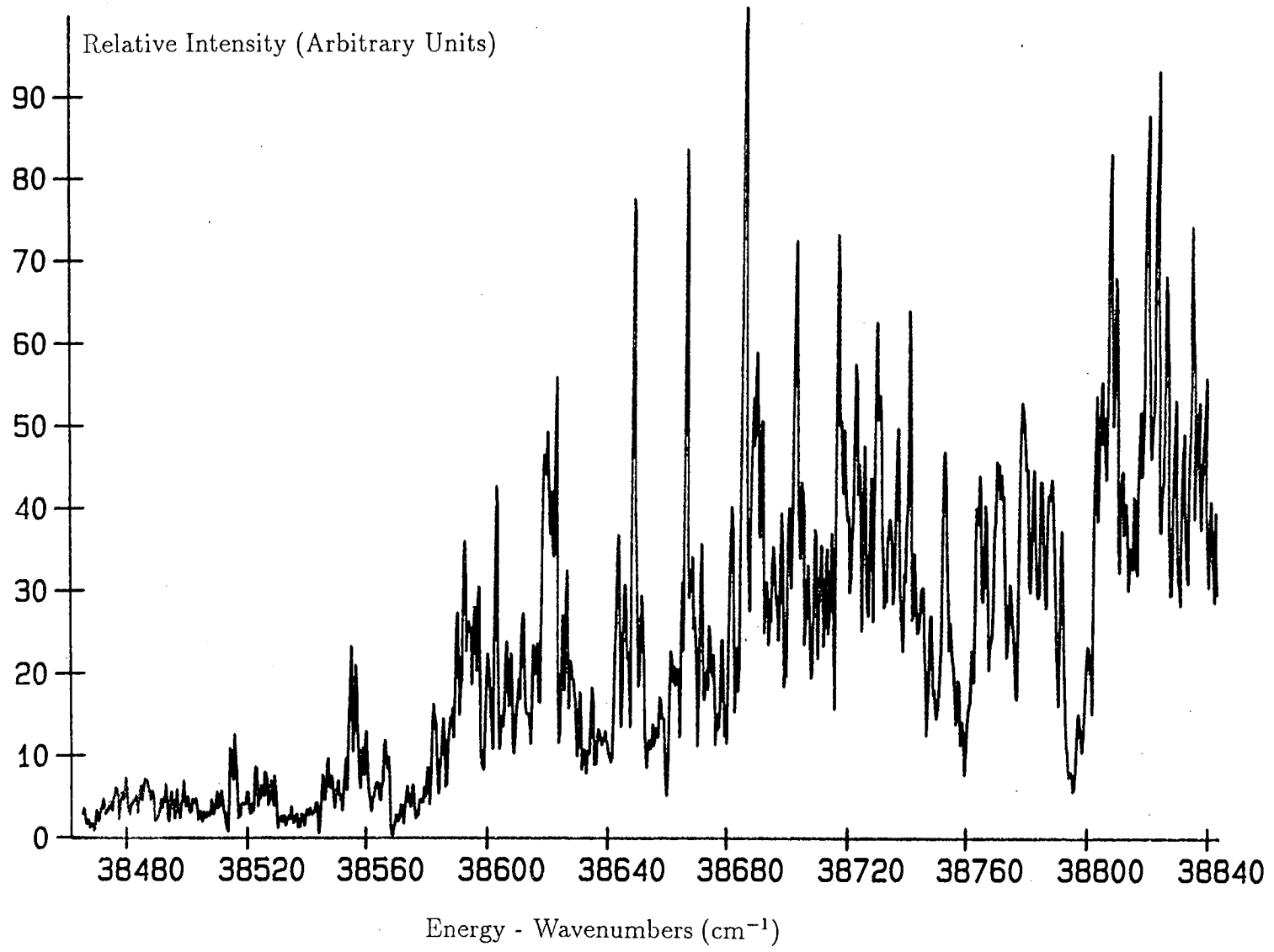

Figure 5–8: Post-threshold structure in Ag_2

Table 5–3: Summary of theoretical work published on Ag_2^+

Calculation	r_e (Å)	ω_e (cm^{-1})	D_e (eV)	Reference
PP/LSD	5.34	83	1.33	[13]
	5.63	94	1.27	
	5.30	113	1.40	
PP/LSD	2.59	161.1	2.24	[67]
RECP/CI	2.99	100.0		[68]
	3.02	96.4		
	2.92	107.1		
RECP/CI	2.922	93	1.20	[69]
PP/LSD	5.37		1.30	[70]
RECP/MCPF	5.469	106	1.36	[20]
RPP/CEPA	5.274	116	1.41	[21]
RPP/CI(SD)	5.363	108	1.33	

All methods are as described in Table 5-1.

that the $(s\sigma)^2$ bond is preserved on ionisation, with the creation of a 'd hole' from a weakly bonding orbital.

A previous experimental determination of the Ag_2^+ dissociation energy, using effusion mass spectrometry, gave a value of 1.66 eV [72]. While not in complete agreement with the value calculated here, the subsequent discussion of the ion ground state is valid for either figure, with the value and description obtained from this work appearing to have greater validity.

5.7 Recent Developments

The very recent publication of a new and independent evaluation of the I.P. of Ag_2 has allowed a certain amount of retro analysis to take place [74].

Despite the simplification of not having to accurately determine the ionisation potential itself, it has not yet proved possible to assign the Rydberg structure with any certainty, due to their inherent complexity. Although the spectra recorded during this work are very likely to be in agreement with that of the published material, it has simply not proved possible to verify this to date.

Some comparitive work has proved possible, however. A direct comparison of the two ionisation potential values shows very good agreement indeed. Also, it has been possible to assign some of the steps on the vibrational ladder, using the reported values.

5.8 Future Work

The first ionisation potential of the Ag_2 molecule has been measured. The value obtained is in good agreement with an independently published value, and would therefore appear to be of some accuracy. The stated aim of this work was to follow molecular parameters through to their bulk values. A previous study in this group measured ionisation potentials for Cu_2 and CuAg [64]. It would seem logical, then,

Table 5–4: Dissociation Energy Data

Constant	Value (eV)	Source
I.P.(Ag)	7.57	[73]
I.P.(Ag_2	7.65	This work
D_0(Ag_2	1.65	[72]
$D_0(Ag_2^+)$	1.66	[72]
$D_0(Ag_2^+)$	1.57	This work

to continue with this work for the higher coinage clusters. Moving through the triatomics towards bulk would be the longterm goal of this work. However, due to the two-photon nature of such work, there is a need to understand the energetics of any such system, via spectroscopy, before any studies can utilise the intermediate levels as above.

Bibliography

[1] Morse M.D., Chem. Rev., 1986, **86**, 1049.

[2] Schumacher E., Kappes M., Marti K., Radi P., Schär M. and Schmidhalter B., Ber. Bunsenges. Phys. Chem., 1984, **88**, 220.

[3] Kappes M., Schär M., Radi P. and Schumacher E., J. Chem. Phys., 1986, **84**, 1863.

[4] Powers D.E., Hansen S.G., Geusic M.E., Michalopoulos D.L. and Smalley R.E., J. Chem. Phys., 1983, **78**, 2866.

[5] Rohlfing E.A., Cox D.M. and Kaldor A., J. Phys. Chem., 1984, **88**, 4497.

[6] Rohlfing E.A., Cox D.M., Kaldor A. and Johnson K.H., J. Chem. Phys., 1984, **81**, 3846.

[7] Cheeseman M.A. and Eyler J.R., J. Phys. Chem., 1992, **96**, 1082.

[8] Whetten R.L., Zakin M.R., Cox D.M., Trevor D.J. and Kaldor A., J. Chem. Phys., 1986, **85**, 1697.

[9] Wood D.M., Phys. Rev. Lett., 1981, **46**, 749.

[10] Hopkins J.B., Langridge-Smith P.R.R., Morse M.D. and Smalley R.E., unpublished results.

[11] Baetzold R.C., J. Chem. Phys., 1971, **55**, 4355.

[12] Baetzold R.C., J. Chem. Phys., 1978, **68**, 555.

[13] Stoll H., Fuentealba P., Dolg M., Flad J., Szentpaly L.v. and Preuß H., J. Chem. Phys., 1983, **79**, 5532.

[14] Flad J., Igel G., Preuß H. and Stoll H., Ber. Bunsenges. Phys. Chem., 1984, **88**, 241.

[15] Stoll H., Fuentealba P., Schwerdtfeger P., Flad J., Szentpaly L.v. and Preuß H., J. Chem. Phys., 1984, **81**, 2732.

[16] Shim I. and Gingerich K.A., J. Chem. Phys., 1983, **79**, 2903.

[17] Balasubramanian K., J. Phys. Chem., 1989, **93**, 6585.

[18] Balasubramanian K. and Feng P.Y., Chem. Phys. Lett., 1989, **159**, 452.

[19] Bauschlicher C.W.Jnr., Langhoff S.R. and Partridge H., J. Chem. Phys., 1990, **93**, 8133.

[20] Partridge H., Bauschlicher C.W.Jnr. and Langhoff S.R., Chem. Phys. Lett., 1990, **175**, 531.

[21] Andrae D., Häußermann U., Dolg M., Stoll H. and Prueß H., Theor. Chim. Acta., 1991, **78**, 247.

[22] Niessen W.v., J. Chem. Phys., 1986, **85**, 337.

[23] Rabii S. and Yang C.Y., Chem. Phys. Lett., 1984, **105**, 480.

[24] Hollas J.M., *High Resolution Spectroscopy*, Butterworths, London, 1982.

[25] Ho J., Ervin K.M. and Lineberger W.C., J. Chem. Phys., 1990, **93**, 6987.

[26] Ganteför G.F., Gausa M., Meiwes-Broer K-H. and Lutz H.O., J. Chem. Soc. Faraday Trans., 1990, **86**, 2483.

[27] Taylor K.J., Pettiette-Hall C.L., Cheshcovsky O. and Smalley R.E., J. Chem. Phys., 1992, **96**, 3319.

[28] Reisler H. and Wittig C., Adv. Chem. Phys., 1985, **60**, 1.

[29] Parker D.H., *Ultrasensitive Laser Spectroscopy*, Editor Kliger D.S., Academic Press, New York, 1983.

[30] Kimura K., Adv. Chem. Phys., 1985, **60**, 161.

[31] Meck J.T., Jones R.K. and Reilly J.P., J. Chem. Phys., 1980, **73**, 3503.

[32] Compton R.N., Miller J.C., Carter A.E. and Kruit P., Chem. Phys. Lett., 1980, **71**, 87.

[33] Achiba Y., Hiraya A. and Kimura K., J. Chem. Phys., 1984, **80**, 6047.

[34] O'Halloran M.A., Pratt S.T., Dehmer P.M. and Dehmer J.L., J. Chem. Phys., 1987, **87**, 3288.

[35] Chewter L.A., Sander M., Muller-Dethlefs K. and Schlag E.W., J. Chem. Phys., 1984, **86**, 4737.

[36] Muller-Dethlefs K., Sander M. and Schlag E.W., Z. Naturforsch Teil A, 1984, **39**, 1089.

[37] Reiser G., Habenicht W., Muller-Dethlefs K. and Schlag E.W., Chem. Phys. Lett., 1988, **152**, 119.

[38] Tonkyn R.G., Winniczek J.W. and White M.G., Chem. Phys. Lett., 1989, **164**, 137.

[39] Ganteför G.F., Cox D.M., Kaldor A., 5^{th} *Int. Symp. on Small Particles and Inorganic Clusters*, Konstanz, 1990.

[40] Broyer M., Chevaleyre J., Delacretaz G., Martin S. and Wöste L., Chem. Phys. Lett., 1983, **99**, 206.

[41] Leutwyler S., Herrmann A., Wöste L. and Schumacher E., Chem. Phys., 1980, **48**, 253.

[42] Smith M.A., Hager J.W. and Wallace S.C., J. Chem. Phys., 1984, **80**, 3097.

[43] Duncan M.A., Dietz T.G. and Smalley R.E., J. Chem. Phys., 1981, **75**, 2118.

[44] Lemaire J., Dimicoli I., Piuzzi F. and Botter R., Chem. Phys., 1987, **115**, 119.

[45] Morse M.D., in *Advances in Metal and Semiconductor Clusters Vol. 1: Spectroscopy and Dynamics.*

[46] Morse M.D., Hopkins J.B., Langridge-Smith P.R.R. and Smalley R.E., J. Chem. Phys., 1983, **79**, 5316.

[47] Cheng P.Y. and Duncan M.A., Chem. Phys. Lett., 1988, **152**, 341.

[48] Berry R.S., J. Chem. Phys., 1966, **45**, 1228.

[49] Brandsen B.H. and Joachain C.J., *Physics of Atoms and Molecules*, Longman, London, 1983.

[50] Guyon P.M., Baer T. and Nenner I., J. Chem. Phys., 1983, **78**, 3665.

[51] Fujii M., Ebata T., Mikami N. and Ito M., Chem. Phys. Lett., 1983, **101**, 578.

[52] Eyler E.E. and Pipkin F.M., Phys. Rev. A., 1983, **27**, 2462.

[53] Jaffe S.M., Kachru R., van Linden van den Heuvell H.B. and Gallagher T.F., Phys. Rev. A., 1985, **32**, 1480.

[54] Bordas C., Brevet P-F., Broyer M., Chevaleyre J. and Labastie P., Europhys. Lett., 1987, **3**, 789.

[55] Berkowitz J. and Ruscie B., J. Chem. Phys., 1990, **93**, 1741.

[56] Atkins P.W., *Molecular Quantum Mechanics*, Second Edition, Oxford University Press, 1983.

[57] Robertson H.P. and Dewey J.M., Phys. Rev., 1928, **31**, 973.

[58] Lanczos C., Z. Physik., 1930, **62**, 518.

[59] Callender C.L., Hackett P.A. and Rayner D.M., J. Opt. Soc. Am. B., 1988, **5**, 614.

[60] Rayner D.M., Mitchell S.A., Bourne O.L. and Hackett P.A., J. Opt. Soc. Am. B., 1987, **4**, 900,

[61] Persson J.L. and Whetten R.L., Chem. Phys. Lett., 1988, **147**, 168.

[62] Halliday D. and Resnick R., *Physics*, Third Edition, John Wiley, New York, 1978.

[63] Mulliken R.S., J. Am. Chem. Soc., 1964, **86**, 3183.

[64] James A.M., *PhD. Thesis*, University of Edinburgh, 1991.

[65] Gandhi S.R. and Bernstein R.B., J. Chem. Phys., 1990, **93**, 4024.

[66] Guyon P.M. and Berkowitz J., J. Chem. Phys., 1971, **54**, 1814.

[67] Ballone P. and Galli G., Phys. Rev. B., 1990, **42**, 1112.

[68] Ross R.B. and Ermler W.C., J. Phys. Chem., 1985, **89**, 5202.

[69] Basch H., J. Am. Chem. Soc., 1981, **103**, 4657.

[70] Flad J., Igel-Mann G., Preuß H. and Stoll H., Chem. Phys., 1984, **90**, 257.

[71] Benard M., Chem. Phys. Lett., 1983, **96**, 183.

[72] Gingerich K.A., J. Cryst. Growth, 1971 9, 31.

[73] Moore C.E., *Atomic Energy Levels N.B.S. Circular 467 Vol.*III, Washington D.C., 1971.

[74] Beutel V., Bhale G.L., Kuhn M. and Demtröder W., Chem. Phys. Lett., 1991, **185**, 313.

Appendix 1

Courses and Conferences Attended

In accordance with the regulations of the Department of Chemistry, University of Edinburgh, I have attended the following courses during my period of study;

1. Laser Physics
2. Reaction Dynamics
3. Theoretical Chemistry
4. Recent Developments in Physical Chemistry
5. Scientific German

I have also attended a variety of computing courses including EMAS, SCRIBE, UNIX, FORTRAN and C.
This thesis was composed using the LaTeX package available via the University of Edinburgh UNIX system.

The following conferences were attended;

Faraday Division High Resolution Spectroscopy Group Birmingham 1988
Faraday Division High Resolution Spectroscopy Group Nottingham 1989
Faraday Division High Resolution Spectroscopy Group Heriot-Watt 1992

I have also attended laser chemistry research group meetings, departmental evening seminars and a joint Edinburgh - Heriot-Watt laser chemistry group meeting 1989.

FACULTY OF ARTS

NON-GRADUATION CERTIFICATE

CLASS OF GERMAN

(INTRODUCTORY READING COURSE)

I hereby certify that James Macdonald

attended the above Class during the session 1988-89

with regularity, and that he *performed the work of the Class*,

passing a test in translation from German into English in accordance with Ph.D. regulations.

W. T. Webster

(Lecturer)